Improving the Determination of the Dynamic Modulus of Asphalt Concrete for Mechanistic-Empirical Pavement Design

by

Ghareib Harran

A Thesis submitted to the Faculty of Graduate Studies of

The University of Manitoba

in partial fulfilment of the requirements of the degree of

Doctor of Philosophy

Department of Civil Engineering

University of Manitoba

Winnipeg, Manitoba, Canada

Improving the Determination of the Dynamic Modulus of Asphalt Concrete for Mechanistic-Empirical Pavement Design

By

Ghareib Harran

A Thesis/Practicum submitted to the Faculty of Graduate Studies of The University of Manitoba in partial fulfillment of the requirement of the degree

Of

Doctor of Philosophy

Abstract

The reliability of asphalt pavement design depends on the accuracy of material characterization. The dynamic modulus ($|E^*|$) of asphalt concrete is the main parameter in both structural and performance models of asphalt layer, and its accuracy contributes significantly to the reliability of pavement analysis. This thesis deals with the determination of $|E^*|$ for mechanistic-empirical pavement design. Published studies have clearly identified three issues that may affect the accuracy of $|E^*|$. Firstly, predictive techniques for estimating $|E^*|$ from mixture volumetric properties are widely used in pavement design and evaluation when the measured values are not available. The reliability of these techniques is lowest at high service temperatures above 35°C. Rutting is one of the major distresses in asphalt pavements and is considered highly sensitive to $|E^*|$ at high temperatures. Secondly, $|E^*|$ is measured or predicted as a function of frequency. Since the vehicular pulse loads are represented in the time domain, the correctness of the selected $|E^*|$ for the multilayered elastic analysis depends on the accuracy of the conversion from pulse loading time to the testing frequency. The mechanistic-empirical pavement design guide (MEPDG) assumes that the loading frequency is the inverse of the pulse time. This approach overestimates the frequency and leads to unconservative pavement design. Finally, the asphalt mixtures are conveniently characterized with $|E^*|$ master curves developed from values measured at a wide range of temperature and frequency. However, stiffness of in-service asphalt concrete is limited to the resilient or backcalculated moduli because the thickness of the asphalt layer, in most cases, is less than the required height of $|E^*|$ specimens. The objective of this thesis is to

improve the reliability of pavement design and evaluation through the followings: improving the prediction of $|E^*|$ at high temperature; determining the $|E^*|$ master curve from the resilient modulus; and proposing a method to determine the frequency of the pulse loading to assign $|E^*|$ for the multilayered elastic analysis.

The relationship between $|E^*|$ at high temperature and the aggregate gradation represented with a new gradation parameter is examined. The correlation between $|E^*|$ at high temperatures and the gradation parameter improved when it was carried out independently on fine- and coarse-graded mixtures. The new parameter shows the ability to describe the effect of aggregate gradation on the stiffness at high temperatures even for as-constructed asphalt concrete. Reasonable results were predicted for the calibration data and a validation dataset from the literature. For fine-graded mixtures, a linear regression model is developed to predict $|E^*|$ at 40°C and it is used to adjust the $|E^*|$ master curve obtained with the predictive techniques. The adjustment improved the predicted moduli at high temperatures.

A viscoelastic method is proposed to calculate the frequency of a pulse load to determine the applicable $|E^*|$ for pavement design. The method can be used to calculate the frequency of any shape of loading pulse and to investigate the effect of the mixture type. Conversion equations from loading time to the frequency are developed for both field and laboratory pulses. The loading frequencies of the M_R pulse that has a loading period of 0.1 second and the FWD pulse load are 5 Hz and 15.7 Hz, respectively. The MEPDG approach overestimates the loading frequency up to 173%.

A method is proposed for predicting $|E^*|$ from M_R measured. The method applies a conversion equation to determine the frequency of the loading pulse, the parabolic interpolation function to determine $|E^*|$ at various temperatures, and the shift factor of the binder to substitute the shift factor of the mixture. Predicted $|E^*|$ values at various temperatures and frequencies are an acceptable substitution for measured $|E^*|$ values at these conditions.

Acknowledgement

Special thank goes to Professor Dr. A. Shalaby, my PhD advisor, for his continuous support, advice and valuable comments. I would like also to thank my PhD committee, Professor A. Clayton, Professor Dr. N. Richards, and Dr. N. Rattanawangcharoen, for their valuable comments during my research.

The laboratory work of the thesis was completed under a research project to characterize the paving materials in Manitoba. The laboratory assistance received from Manitoba Infrastructure and Transportation is acknowledged. The technical assistance of Dr. Gani Ganapathy during the research project is gratefully acknowledged. I would like to thank Mr. Scott Sparrow for his technical assistant during the preparation of the testing setup.

I would like to acknowledge the financial support from the Egyptian Government and from the Department of Civil Engineering of the University of Manitoba in completing the research presented in this thesis.

Finally but not the least, I am thankful to my parents for their support especially my mother who died after struggling with cancer. She insisted to stay beside my research and not to be beside her during her sickness. I would like to thank my wife for her support and encourage during my research, and my fifteen-month daughter, Mariam, for the inspiration.

Table of Contents

List of Figures

List of Tables

List of Symbols and Abbreviations

E^*	: Complex dynamic modulus
$\|E^*\|$	: Dynamic modulus
ϕ	: Phase angle
$\|E^*_{40}\|$	: Dynamic modulus at 40°C and 1 Hz
f	: Frequency (Hz)
ω	: Angular frequency (rad/s); $\omega=2\pi f$
M_R	: Resilient modulus
GR	: Gradation Ratio of aggregate, the ratio of % passing of 4.75 mm sieve to % passing of No. 200 sieve
AC	: Asphalt concrete
$\varepsilon(t)$	: Strain-time history
$\sigma(t)$	: Stress-time history
D_0, D_1 and m	: Parameters of creep compliance
R	: Universal gas constant = 8.314472 J/°K-mol
T_0	: Reference temperature (°C)
A and VTS	: Parameters of viscosity-temperature susceptibility of binder
η	: Viscosity of binder
G^*	: Complex shear modulus of binder
δ	: Phase angle of binder
ΔE_a	: Activation energy, J/mol
$D(t)$	: Creep compliance
$E(t)$	: Relaxation modulus
D^*	: Complex creep compliance
$\|D^*\|$	: Magnitude of creep compliance
$D', D'(f)$	: Storage creep compliance
$D'', D''(f)$	: Loss creep compliance
$E', E'(f)$	: Storage complex dynamic modulus

$E^{"}, E^{"}(f)$	: Loss complex dynamic modulus
VE	: Viscoelastic property
LVE	: Linear viscoelastic property
VP	: Viscoplastic property
f	: Frequency (Hz)
ω	: Angular frequency (rad/s); $\omega=2\pi f$
t_p	: Pulse loading time (s)
t	: Time (s)
T	: Temperature (°C)
$a(T)$	: Shift factor at Temperature of T
$\delta, \alpha, \beta, \gamma$	: Regression parameters of $\lvert E^* \rvert$ master curve
σ_0	: Constant applied stress
ε_0	: Constant resilient strain
$\hat{\sigma}$	: Peak-to-peak sinusoidal stress
$\hat{\varepsilon}$	: Peak-to-peak sinusoidal strain
σ_a	: Applied repeated pulse stress
ε_r	: Resilient strain
ε_i	: Instantaneous resilient strain
ε_t	: Total resilient strain
M_i	: Instantaneous resilient modulus
M_t	: Total resilient modulus
V	: Vehicle speed (km/h)
T_g	: Glass transition temperature
τ	: Time variable
TRS	: Thermo-rheologically simple
DSR	: Dynamic shear rheometer
S_e	: Standard error
S_y	: Standard deviation
EICM	: Enhanced Integrated Climatic Model
SGC	: SuperPave gyratory compactor

SPT	: Simple performance test
ALF	: Accelerated Loading Facility
NMPS	: Nominal maximum particle size
a_{fa}, n_{fa}	: Fine aggregate gradation parameters
a_{ca}, n_{ca}	: Coarse aggregate gradation parameters
$\Gamma(m)$	: Gamma function
CV	: Coefficient of variation
CV_w	: Within specimen coeffecient of variation
CV_b	: Between specimens coeffecient of variation
LVDT	: Linear Variable Defrential Traneducer
V_{beff}	: Percentage effective bitumen content, by volume
V_a	: Percentage air content
VMA	: Voids in mineral aggregate, %
VFA	: Voids filled with asphalt, %
f_{eq}	: Equivalent frequency
PTH	: Provincial Trunk Highway
PR	: Provincial Road
RAP	: Reclaimed Asphalt Pavement
MDL	: Maximum density line
PG	: Performance grade of binder
MTSG	: Maximum theoretical specific gravity
AADT	: Annual average daily traffic
AADTT	: Average annual daily truck traffic
$\lvert E^*_{40} \rvert$	: Dynamic modulus at 40°C and 1 Hz
RMSE	: Root Mean Square Error
MEPDG	: Mechanistic-Empirical Pavement Design Guide
MEPD	: Mechanistic-Empirical Pavement Design
NCHRP	: National Cooperative Highway Research Program
AASHTO	: *American Association of State Highway and Transportation Officials*
SHRP	: Strategic Highway Research Program

FHWA	: Federal Highway Administration
FWD	: Falling Weight Deflectometer
ANN	: Artificial Neural Network
FFT	: Fast Fourier Transformation
IFFT	: Inverse Fast Fourier Transformation
LTPP	: Long Term Pavement Performance

1 Introduction and Problem Statement

1.1 Introduction

Asphalt concrete (AC) is a composite material consisting of fine and coarse aggregates and asphalt binder. AC is used for paving roads and parking lots to provide a smooth, quiet, and skid-resistant surface. The loading response of aggregates is considered nonlinear elastic. The asphalt binder, on the other hand, is sensitive to temperature and loading rate, and it ages with time due to exposure to ultraviolet rays and extreme temperatures. Thus, factors governing the loading response of AC are the responses of its component materials, temperature, loading rate and strain level.

AC pavements exhibit deterioration due to a number of distresses such as rutting, fatigue cracking and low temperature (thermal) cracking. The deterioration affects the serviceability and structural integrity of pavements, thus increasing the maintenance costs and reducing the pavement service life. An accurate and representative characterization and design of asphalt concrete under a diverse range of traffic and climatic conditions is essential to reduce the deterioration and to improve the prediction of pavement performance.

Yoder and Witczak (1975) identified three essential elements for any rational pavement design procedure: (1) the theory used to predict the failure or distress

parameter; (2) the evaluation of the pertinent material properties necessary for the theory; and (3) the determination of the relationship between these material properties and the failure or distress parameter. According to Uzan (1996), the load-based deformation of AC consists of elastic, plastic, viscoelastic (VE) and viscoplastic (VP) components. The elastic and plastic components are time-independent deformations, while the VE and VP components are time-dependent deformations. He also found that a VE component is present at any temperature and loading rate. Based on the strain level and the number of loading cycles, Di Benedetto et al. (2001) classified VE behaviour of asphalt concrete to three typical domains. The first domain is the linear viscoelastic (LVE) with strain of less than 100 microstrains and less than a few hundred cycles. The second domain is the nonlinear viscoelastic with high strain and low number of loading cycles. The third domain is fatigue with strain below the LVE limit and a high number of load cycles ($>10^6$). Asphalt pavement is designed to fail within the fatigue domain to sustain traffic loads with high number of repetitions.

A complex dynamic modulus (E^*) is a stress-strain relationship of LVE materials, such as AC at small strains, under a continuous sinusoidal load. Due to the viscous property, the strain lags behind the stress with a phase angle (ϕ); therefore, E^* is a complex number that can be represented by its magnitude ($|E^*|$) and ϕ. $|E^*|$ is the ratio of the sinusoidal stress amplitude to the recoverable strain amplitude. $|E^*|$ is measured at a number of temperature and frequency, and it is used to develop the $|E^*|$ master curve, which is unique curve for each mixture.

$|E^*|$ is an important AC parameter for mixture evaluation and pavement design. The

panel of the National Cooperative Highway Research Program (NCHRP) project 9-19, "SuperPave Support and Performance Models Management," selected $|E^*|$ as a primary simple performance candidate to be used with SuperPave mix design method (NCHRP 2007). That is because $|E^*|$ is highly correlated to rutting and fatigue cracking (Witczak et al., 2002a, 2002b). Furthermore, $|E^*|$ is a required input in the Mechanistic-Empirical Pavement Design Guide (MEPDG) developed in NCHRP project 1-37A, "Development of the 2002 Guide for the Design of New and Rehabilitated Pavement Structures" (NCHRP 2004). $|E^*|$ is incorporated in both pavement structural and pavement performance models to calculate the stress, strain and displacement and to predict rutting and fatigue cracking. Through the $|E^*|$ master curve, the effect of traffic speed, temperature and aging can be integrated in pavement models. Moreover, $|E^*|$ as a fundamental AC property has relationships, through the viscoelastic theory, with the time-dependent AC stiffnesses such as creep compliance $D(t)$, and relaxation modulus $E(t)$ that are determined under constant stress and strain, respectively. $D(t)$ is efficiently used to predict low-temperature distress, and $E(t)$ is used in LVE analysis of asphalt pavement.

There are two methods to determine $|E^*|$: laboratory testing and predictive models. MEPDG recommends measuring $|E^*|$ in the advanced pavement design (level 1) and using the predictive models that can estimate $|E^*|$ in the less sophisticated and less reliable designs (level 2 and level 3). The complexity of the laboratory testing as well as the limited capability of AC testing systems forces pavement engineers to rely on level 2 and level 3 to characterize AC (Zeghal et al., 2005 and Zeghal and Mohamed, 2008).

In addition to $|E^*|$, a resilient modulus (M_R) of AC is used for mixture characterization and in-service pavement evaluation. M_R is obtained from a repeated test in the indirect tensile (IDT) mode by applying a pulse load followed with a rest period. In the IDT mode, cylindrical specimens are loaded diametrically between two curved loading strips and the deformations are collected along the loading direction and perpendicular to it. The M_R test may be carried out on laboratory compacted specimens and field AC cores. Generally specimen preparation is easier in M_R test than in $|E^*|$ test, however M_R specimens can be damaged more easily due to cracking at the contact area between loading strips and the specimen. In addition, the $|E^*|$ test is more reliable and results in more consistent data compared to the M_R test.

1.2 Problem Statement

The accurate determination of $|E^*|$ of asphalt concrete is imperative for more reliable pavement design and evaluation. Three issues will be addressed to improve determination of $|E^*|$ for mechanistic-empirical pavement design.

1. Improving $|E^*|$ prediction at high temperatures

There has been significant progress in developing predictive models that rely on material and mixture volumetric properties to determine $|E^*|$. The Witczak $|E^*|$ predictive model (Witczak and Fonseca, 1996) is perhaps the most used one since it is incorporated in MEPDG (NCHRP 2004). Pellinen (2001) evaluated the model and concluded that "*the Witczak et al. model needs further evaluation to accurately predict the volumetric components influenced upon* $|E^*|$". Dongré et al. (2005) found

that the model can not detect the deviation of the mixture volumetric properties, aggregate gradation or binder content, from the mix design levels, and that the current methods of predicting $|E^*|$ are least reliable at high service temperatures such as those close to 40°C. The low reliability of $|E^*|$ prediction reduces the reliability in the forecasted pavement performance and its estimated service life. In this thesis, the relationship between $|E^*|$ at 40°C, $|E^*_{40}|$, and the aggregate gradation of mixtures is investigated using a new gradation ratio (GR). In addition, a $|E^*_{40}|$-GR model has been developed for fine-graded mixtures to improve $|E^*|$ predicted from models such as the Witczak model.

AC pavements in cold climate regions such as Manitoba exhibit low temperature cracking and rutting that are related to temperature. The resistance of AC to low temperature cracking depends mainly on the temperature susceptibility of the asphalt binder. This cracking can be reduced by using binder with lower stiffness than the one used at hot climate regions. The low stiffness binder allows AC to shrink at cold temperatures without building critical tensile stress causing the cracking but makes AC more susceptible to rutting at high temperatures. AC pavements at cold climate regions experience rutting at lower service temperatures than those temperatures at hot climate regions. The resistance of AC to rutting as a high temperature distress depends mainly on aggregate characteristics in asphalt mixtures.

According to MEPDG, $|E^*|$ is an essential AC parameter in modeling of AC rutting and improving its prediction especially at high temperatures increases the reliability

in prediction of rutting. Modeling of low temperature cracking does not require $|E^*|$ but parameters of the indirect tensile creep compliance at temperatures -30°C to 0°C.

2. Pulse Loading Time-Frequency Conversion for Representative $|E^*|$ for Elastic Analysis Asphalt Concrete

$|E^*|$ is obtained from laboratory measurements and predictive models as a function of frequency (f). For an elastic AC pavement analysis, the pulse loading time (t_p) is used to calculate f (Hz) at which $|E^*|$ is considered as an elastic stiffness. MEPDG, which utilizes a multilayer elastic analysis for the pavement system, has adopted an approach considering that f (Hz) is the inverse of t_p (s). Dongré et al. (2006) concluded that the MEPDG approach does not have scientific support and suggested using the angular frequency (ω) (rad/s) instead of the frequency (Hz) for the conversion. Both approaches have been under examination due to the high modulus they estimate (Underwood and Kim, 2009). This issue was discussed by the Federal Highway Administration (FHWA) and Expert Task Group (ETG) on Asphalt Fundamental Properties and Advanced Modeling in its 2006 and 2007 meetings (FHWA and ETG minutes, 2006 and 2007). Al-Qadi (FHWA and ETG minutes, 2007) concluded that the two approaches are incorrect and further investigation for the relationship between the testing frequency and the loading time was recommended. Recently, Al-Qadi et al. (2008b) used Fast Fourier Transformation (FFT) to determine the frequency content of field measured stresses. They calculated f (Hz) as the dominant frequency obtained from the weight centres of the frequency spectrum. Although FFT can determine the frequency content of the pulse stress, the

dominant frequency does not account for the viscoelastic property of AC. The thesis has contributed a pulse time-frequency conversion approach that is based on the viscoelastic theory and equal recoverable strains resulting from both pulse and sinusoidal stresses. The approach can be applied to determine the equivalent frequency of either laboratory or field loading pulses. Adopting this approach in pavement design may result in equal critical AC strains from both the viscoelastic and elastic analysis thus predicting more realistic load-related pavement performance.

3. Predicting the dynamic modulus from the resilient modulus

According to AASHTO TP62-03 "Standard Method of Test for Determining Dynamic Modulus of Hot-Mix Asphalt Concrete Mixtures", the $|E^*|$ test is carried out on gyratory compacted specimens that are cored and sawed to a 100 mm diameter and a 150 mm height. The required specimen height restricts the test to laboratory compacted specimens, and even if it is possible to extract 150 mm cores from in-service pavement, in most cases, they will be composed of two or more AC layers having different properties. Since $|E^*|$ is a required input for pavement evaluation and rehabilitation, its determination is imperative for in-service pavement.

The in-situ layer modulus is determined using the falling weight deflectometer (FWD) and back-calculation analysis (NCHRP 1-37A). This methodology provides the stiffness value at one single pavement temperature for an AC layer. For complete characterization of AC as a viscoelastic material, stiffness is required at a wide range of temperature and loading rate.

Recently, Lacroix et al. (2008) used an artificial neural network (ANN) to predict $|E^*|$ from M_R. The ANN was trained with a database containing $|E^*|$ of mixtures and M_R that is calculated from this database. Using the trained ANN for predicting $|E^*|$ of in-service asphalt concrete from M_R may result in significant errors since the training data is from laboratory compacted mixtures. The accuracy of ANN depends on the range of the training data. Harran and Shalaby (2007a) concluded that the compaction type has a significant effect on AC stiffness where different $|E^*|$ values were obtained from laboratory compacted specimens and field cores. In this thesis, a method to predict $|E^*|$ from M_R has been introduced and can be applied to laboratory compacted specimens or extracted field cores.

1.3 Objectives of the Thesis

1. To evaluate methods of determining $|E^*|$ including the shifting techniques required for constructing the $|E^*|$ master curve.
2. To improve the reliability in the prediction of $|E^*|$ at high temperatures through evaluating the relationship between $|E^*|$ at 40°C and the aggregate gradation, developing the $|E_{40}^*|$-GR model and using it to adjust the predicted $|E^*|$ master curves.
3. To convert the pulse loading time to testing frequency to assign $|E^*|$ as an AC elastic modulus in the pavement elastic analysis. The pulse time-frequency conversion approach will be based on the viscoelastic theory, and it can calculate frequency of field and laboratory pulse stresses.

4. To predict $|E^*|$ from M_R of asphalt concrete. The pulse loading time of M_R is converted to an equivalent frequency using the conversion approach proposed to fulfil the third objective of this thesis. An interpolation function will be examined to determine $|E^*|$ required for developing the entire master curve.

1.4 Scope and Research Methodology

The scope of the thesis is limited to fine-graded AC mixtures, which are the prevailing type of mixtures in Manitoba. The research program consists of testing specimens prepared in the laboratory and AC cores extracted from in-service pavements. The mixtures were prepared from aggregates and binder samples that were obtained from recent highway projects in Manitoba and the cores were extracted from recent paved highways. Some of these mixtures were specified for wear-resistant surface courses and others were specified for binder courses.

$|E^*|$ and ϕ of AC were measured in the axial compression mode according to AASHTO TP62-03 from specimens compacted in the laboratory . M_R is measured according to the protocol of the long-term pavement performance (LTPP) project 07 from laboratory compacted mixtures and in-service AC cores that are extracted from pavements immediately after construction. $|E^*|$ and M_R are measured in the linear viscoelastic range where the strain does not exceed 150 microstrains.

2 Literature Review

2.1 Rheology of Asphalt Concrete

Asphalt concrete (AC) is a composite material consisting of mineral aggregates and an asphalt binder. Mechanical properties of AC vary with composition, temperature, loading rate (frequency) and strain level. Goodrich (1991) evaluated the influence of the following factors on the rheology of AC: the composition of AC, the effect of aggregates and the effect of binder, using a dynamic mechanical analyzer (DMA). He found that the contribution of each factor to the rheology of asphalt mixtures largely depends on temperature whereas:

- At low temperature (below 10°C), the binder rheology has the dominant influence.
- At medium temperature (10 to 50°C), the change in the binder rheology has small effect on the magnitude of the rheology of AC.
- At high temperature (above 50°C), aggregate properties dominate the rheology of AC and the rheological differences of the binders are not apparent. Thus mixture stability at high temperatures should be achieved with good mix design rather than binder rheology change.

Goodrich (1991) concluded that properties of AC change from linear viscoelastic (LVE) with hereditary characteristics at low temperatures, low loading times or high loading frequencies and low strain levels, to nonlinear elasto-visco-plastic at high temperatures,

low frequencies and high strain levels.

Uzan (1996) evaluated the response of AC to the applied load using the repetitive axial creep test and concluded that:

- The deformation of AC under loads consists of four components, elastic, plastic, viscoelastic (VE) and viscoplastic (VP), as shown in Figure 2.1. The elastic and the plastic deformations are time-independent while the VE and VP components are time-dependant. The elastic component rebounds completely after removing the load while the plastic one accumulates producing permanent deformation. The VE deformation is recoverable while the VP component is a rate-dependant plasticity.
- The dominant deformation component depends on temperature and loading time.

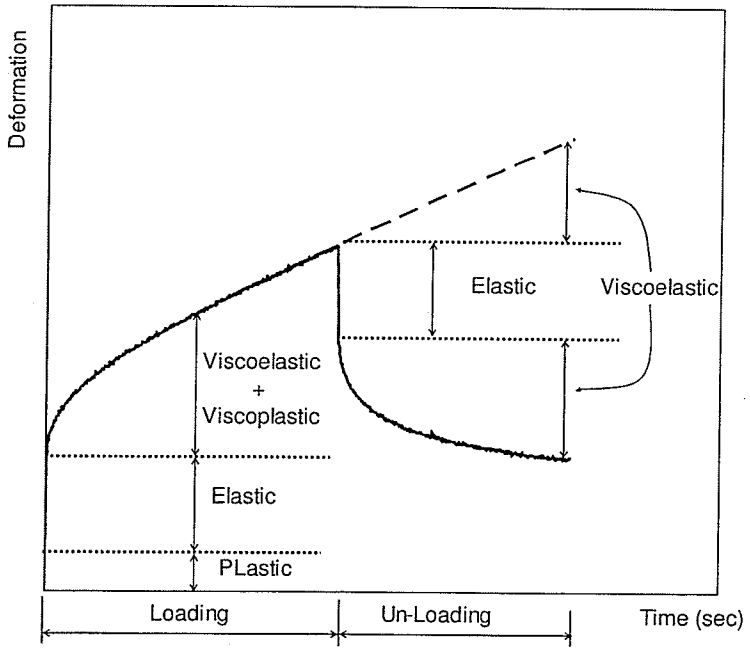

Figure 2.1: Components of asphalt concrete deformation (Uzan, 1996)

- The VE component is present at all temperatures and loading times and should be considered in any constitutive law for an accurate characterization of asphalt concrete to calculate the state of stress and the strain in the pavement structure.

Di Benedetto et al. (2001) classified AC behaviour based on the magnitude of strain and the number of loading cycles to three typical domains. (1) The linear viscoelastic (LVE) domain is relevant to the small strain ($<10^{-4}$) and few hundreds of loading cycles. Christensen and Anderson (1992) described AC behaviour as LVE when small strain remains small. (2) The nonlinear viscoelastic domain is pertinent to high strain magnitudes and few loading cycles. (3) The fatigue domain is related to the small strain ($<10^{-4}$), LVE strain, combined with a high number of load cycles ($>10^{6}$). Asphalt concrete is designed to fail within the fatigue domain to sustain traffic loads with high number of cycles.

2.2 Linear Viscoelastic Response Functions of Asphalt Concrete

The relaxation modulus ($E(t)$), creep compliance ($D(t)$) and complex modulus (E^*) are fundamental response parameters that have been used to characterize LVE behaviour of asphalt concrete. While $E(t)$ and $D(t)$ are measured in the time domain, E^* is measured in frequency domain. Using one of these response parameters for AC characterization depends on the loading application and the condition under which the material is characterized and difficulty of determining the response in the laboratory.

2.2.1 Time –Dependent Response Function

$D(t)$ is determined by applying a constant stress (σ_0) and simultaneously measuring the corresponding strain history ($\varepsilon(t)$) while $E(t)$ is obtained by applying a constant strain, ε_0, and measuring the stress history, $\sigma(t)$. $D(t)$ and $E(t)$ can be defined respectively as follows:

$$D(t) = \frac{\varepsilon(t)}{\sigma_0} \tag{2.1}$$

$$E(t) = \frac{\sigma(t)}{\varepsilon_0} \tag{2.2}$$

$D(t)$ and $E(t)$ are not the inverse of one another and the relationship between them can be obtained from the following Equation(2.3)

$$\int_0^1 E(t-\tau)\frac{dD(\tau)}{d\tau}d\tau = 1 \tag{2.3}$$

where τ is the integration variable.

Christensen (1992) stated that, at low temperatures and low strain levels, $D(t)$ and $E(t)$ tests can be accurately used to model the VE property of AC . At high temperatures and high strain levels, the plastic deformation of AC is much higher than the VE deformation, thus the $D(t)$ and $E(t)$ tests may produce unrealistic characterization of AC and should not be used at these conditions. Generally, $D(t)$ is used for modeling cold temperature distresses while $E(t)$ is used to determine the stresses and strains under applied loads. The E^* and cyclic creep compliance (D^*) tests have been used efficiently to characterize AC especially at small loading times.

$D(t)$ can be expressed with the power law that has three material constants (D_0, D_1 and m)

as follows:

$$D(t) = D_0 + D_1 t^m \tag{2.4}$$

The D_0, represents the elastic compliance while D_1 and m represent the long time loading (creep). Kim et al. (2005) introduced an approach to determine these constants accurately from the results of the dynamic and static creep tests. D_0 is obtained from results of the cyclic creep test and then used to determine D_1 and m from results of the static creep test. When both the stress and strain are changing with time, which is the case for the traffic loading, Equations (2.1 and 2.3) are not valid. For unaged material, the uniaxial stress and strain are related through the following convolution integrals:

$$\sigma(t) = \int_0^t E(t-\tau)\frac{\partial \varepsilon(\tau)}{\partial \tau} d\tau \tag{2.5}$$

$$\varepsilon(t) = \int_0^t D(t-\tau)\frac{\partial \sigma(\tau)}{\partial \tau} d\tau \tag{2.6}$$

2.2.2 Dynamic (Complex) Modulus (Frequency-Dependent Response Function)

The complex modulus of AC is a LVE property that depends on temperature and loading frequency. It is a stress-to-strain relationship under a continuous sinusoidal load. Due to the viscous property of AC, the strain lags behind the stress, Figure 2.2(a), (Witczak et al., 2002a). The stress and the corresponding strain are sinusoidal whereas strain are represented as follows:

$$\sigma = \hat{\sigma}\sin(\omega t) \tag{2.7}$$

$$\varepsilon = \hat{\varepsilon}\sin(\omega t - \phi) \tag{2.8}$$

where: $\hat{\sigma}, \hat{\varepsilon}$ = peak-to-peak stress and strain respectively,

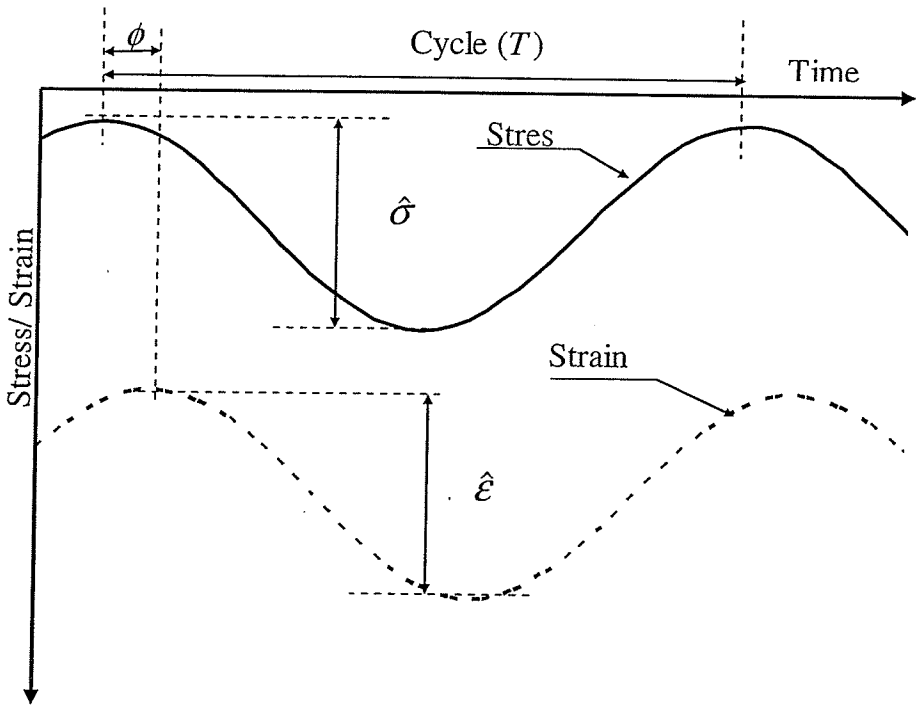

(a)

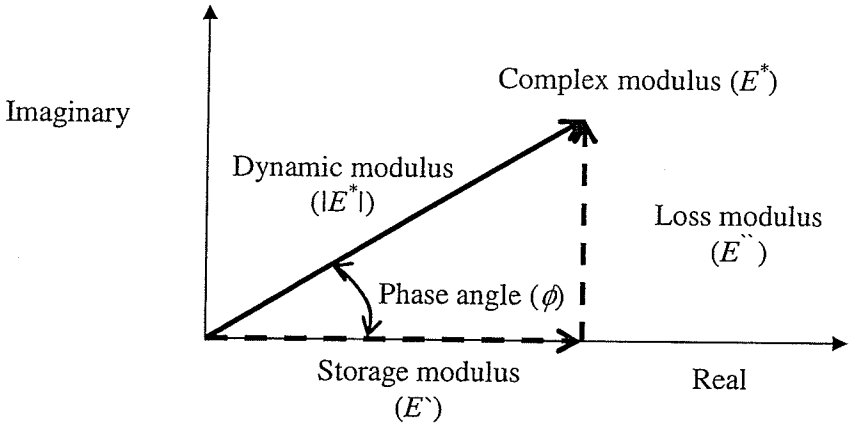

(b)

Figure 2.2: Parameters of the dynamic modulus test

(a) Stress-strain relationship. (b) Complex modulus components.

t = time, s

ω = angular velocity; rad/s, where $\omega = 2\pi f$ and f is the frequency of the load, Hz

ϕ = phase angle, degree.

Thus the complex modulus (E^*) can be represented by the following:

$$E^* = \frac{\sigma_o \sin(\omega t)}{\varepsilon_o \sin(\omega t - \phi)} = \frac{\sigma_o}{\varepsilon_o}\cos\phi + i\frac{\sigma_o}{\varepsilon_o}\sin\phi \tag{2.9}$$

E^* can be written in the following form:

$$E^* = E' + iE'' \tag{2.10}$$

Equation (2.10) represents a complex plane, Figure 2.2(b), where the real and imaginary parts are the storage (E') and loss (E'') moduli, respectively. Furthermore, E^* can be represented by a polar coordinate system including a radial coordinate, which is the dynamic modulus ($|E^*|$), and a polar angle, ϕ. $|E^*|$ can be obtained as follows:

$$\left|E^*\right| = \sqrt{(E')^2 + (E'')^2} = \frac{\hat{\sigma}}{\hat{\varepsilon}} \tag{2.11}$$

Both $|E^*|$ and ϕ characterize the viscoelastic behaviour of AC. For a given $|E^*|$ and ϕ, E' and E'' can be calculated as follows:

$$E' = |E^*| \cos\phi \text{; and} \tag{2.12}$$

$$E'' = |E^*| \sin\phi \tag{2.13}$$

Generally, a material can be described based on ϕ as follows:

- ϕ = 0; elastic material,

- ϕ = 90; viscous material, and

- ϕ = 0 - 90; viscoelastic (VE) material such as AC.

2.3 Thermo-rheologically Simple Principle

Asphalt concrete is a thermo-rheologically simple (TRS) material in the linear viscoelastic stage (Kim and Lee, 1995). The TRS means that the VE properties at a given temperature and loading rate can be obtained either at lower temperatures and longer loading times or at higher temperatures and shorter loading times (Chehab et al., 2002). By applying TRS, which is also called the time-temperature superposition principle, a viscoelastic property measured at various temperatures and loading times/frequencies can be represented with either temperature or loading time/frequency while holding the other one constant. For example the dynamic modulus measured at various temperatures and frequencies, $|E^*|$ (f, T), is represented with one continuous curve, known a master curve, at a given reference temperature (T_0). The $|E^*|$ master curve is a unique relationship between $|E^*|$ and frequency at the reference temperature and can be represented as follows:

$$|E^*|\ (f_r) = |E^*|\ (f, T) \text{ at the reference temperature } (T_0) \qquad (2.14)$$

where: f_r is the reduced frequency and can be calculated as follows:

$f_r = \dfrac{f}{a(T)}$, and $a(T)$ is the shift factor at temperature (T)

Figure 2.3 illustrates the typical procedure of constructing the $|E^*|$ master curve. $|E^*|$ at each temperature is shifted a specific value, shift factor, to align the master curve at T_0. The master curve represents the time dependency of AC and the shift factor is a function of temperature and represents the AC temperature dependency. Both the $|E^*|$ master curve and the shift function are required for complete VE characterization over a wide range of frequencies (times) and temperatures.

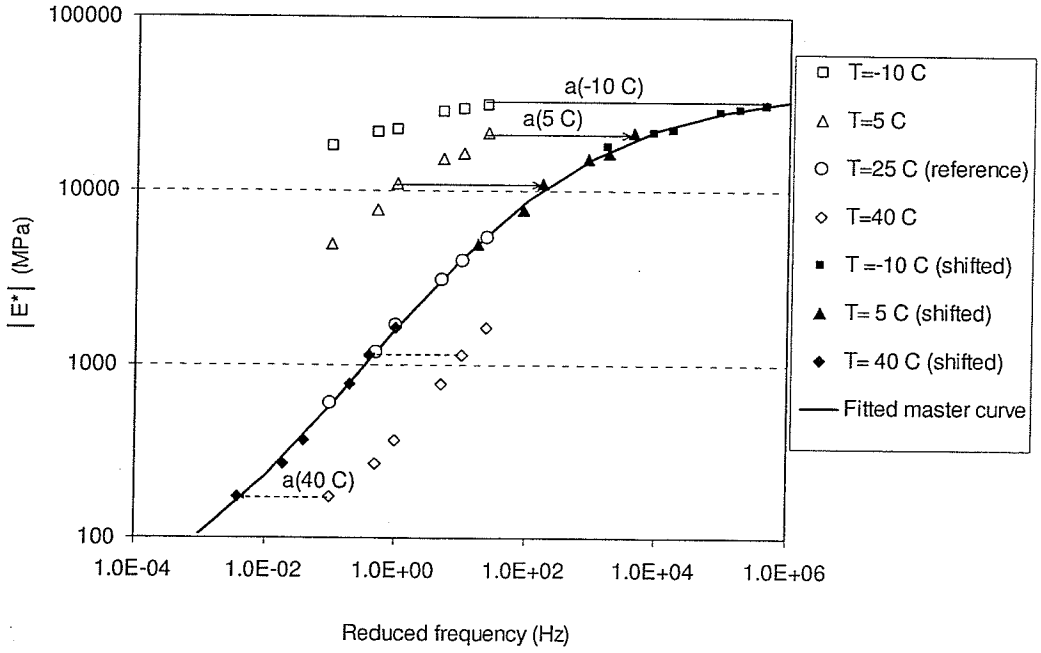

(a)

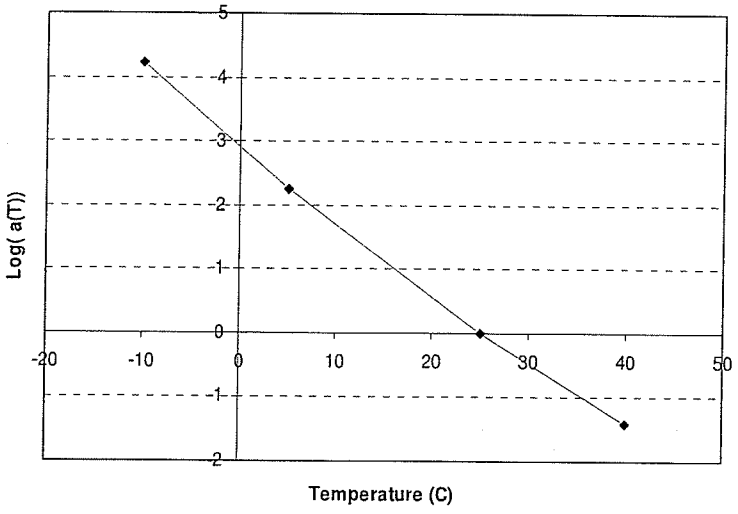

(b)

Figure 2.3: Construction of the |E*| master curve

(a) $|E^*|$ master curve, (b) Shift factor-temperature relationship

2.4 Shifting Techniques

Two ways have been used to obtain the shift factors of asphalt mixtures for constructing a $|E^*|$ master curve: using the shift equations of binders and an experimental method proposed by Pellinen et al. (2004). These shifting equations are as follows:

- Williams, Landel and Ferry (WLF) equation,
- Viscosity-temperature susceptibility (VTS) equation,
- Arrhenius equation,
- Log-linear equation.

2.4.1 WLF Equation

The WLF equation defines the shift factor at a temperature above the glass transition state, the change from a viscous or rubbery condition to a hard and relatively brittle condition, of the binder. The WLF equation is represented by Equation (2.15).

$$\log[a(T)] = \frac{-C_1(T - T_g)}{C_2 + T - T_g} \tag{2.15}$$

where:

$a(T)$ = shift factor

T_g = glass transition temperature, °C

T = temperature, °C, where T > T_g

C_1, C_2 = constants

The WLF equation describes the temperature susceptibility of the asphalt binder over temperatures -20°C to 60°C. Pellinen et al. (2004) found that constants of the WLF equation, C_1 and C_2, vary from a mixture to another.

2.4.2 Arrhenius Equation

The Arrhenius equation assumes that the relaxation time of the creep behaviour of binder is proportional to the thermal energy ($R.T$) required to overcome the activation energy barrier (ΔE_a).

$$\log[a(T)] = \frac{\Delta E_a}{2.303R}\left(\frac{1}{T} - \frac{1}{T_0}\right) \tag{2.16}$$

where:

ΔE_a = activation energy, J/mol

R = universal gas constant = 8.314472 J/°K-mol,

T, T_0 = temperature and reference temperature, °K

Dongre' et al. (2005) found that activation energy, ΔE_a, depends on the binder type where the binder was characterized by a Useful Temperature Range (UTR), which is the algebraic sum of the high and low temperatures for continuous performance grade (PG) of asphalt binders. For example, UTR of PG 51-27 binder is 78°C, which is the sum of 51 and 27. ΔE_a was correlated well (R^2 = 0.90) to UTR and the relationship was shown by Equation (2.17).

$$\Delta E_a = 2484.7\ UTR - 43168.0 \tag{2.17}$$

where

UTR = Useful Temperature Range, °C

2.4.3 Log-linear Equation

The Log-linear equation assumes that the relationship between the logarithm of the shift

factor at a given temperature is proportional to the difference between the given and reference temperatures. It can be represented by Equation (2.18):

$$\log[a(T)] = \beta(T - T_0) \tag{2.18}$$

where

β = constant, and

T, T_o = given and reference temperatures (°C) respectively

2.4.4 VTS Equation

The temperature susceptibility model of binders can be used to calculate the shift function using Equation (2.19):

$$Log[a(T)] = C(10^{A+VTS\log(T_R)} - 10^{A+VTS\log(T_{oR})}) \tag{2.19}$$

where

C =constant,

A, VTS= viscosity-temperature susceptibility parameters of the binder

T_R, =temperature, Rankin (°R)

T_{oR} = reference temperature, Rankin (°R)

The constants A and VTS can be obtained from the viscosity-temperature relationship, which is defined by:

$$\log(\log(\eta)) = A + VTS\ \log(T_R) \tag{2.20}$$

where

η = viscosity (cpoise)

The viscosity (η) is obtained by conducting the dynamic shear rheometer (DSR) test on

binders at an angular velocity (ω) of 10 rad/second. It can be calculated from the DSR test parameters, the complex shear modulus (G^*) and phase angle (δ), using Equation (2.21):

$$\eta = \frac{G^*}{10}\left(\frac{1}{\sin\delta}\right)^{4.8628} \tag{2.21}$$

Using Equation (2.21) to calculate the shift factor enables one to integrate the binder rheological property in the $|E^*|$ master curve, for example integrating the aging effect into the AC stiffness. MEPDG incorporates A-VTS model to predict $|E^*|$ (NCHRP, 2004).

2.4.5 Experimental Method

The experimental method is a shifting technique in which no shift function is used to obtain the shift factor. The method applies the nonlinear fitting technique to determine the shift factors and parameters of a master curve simultaneously. Pellinen et al. (2004) compared the five shift techniques. The experimental method produced master curves with the best goodness of fit, which is represented with the ratio of the standard error to the standard deviation (S_e/S_y), compared to the other shifting techniques. The reason is that the method has the most flexibility because no function is assigned. The method was recommended for shifting $|E^*|$ values. The shift factor calculated from Arrhenius Equation was found to be comparable to the one obtained from the experimental method.

Chehab et al. (2002) demonstrated that AC is thermorheologically simple (TRS) in tension even with growing damage, thus the shifting technique is applicable even with growing damage. The time-temperature superposition principle can be applied with growing damage and viscoplastic straining. Chehab et al. stated that this principle helps

to reduce the testing program, develop strength and corresponding strain master curves as a function of reduced time, predict stress-strain curves obtained from the crosshead strain test, and simplify the thermorheological analysis of a pavement structure.

2.5 Complex Modulus Representation

2.5.1 Dynamic Modulus Master Curve

The $|E^*|$ master curve of an AC mixture is a unique curve for each mixture and has the following benefits:

- To characterize AC over a wide range of temperatures and loading frequencies for pavement design and evaluation.
- To compare AC mixtures over a wide range of frequencies and temperatures.
- To determine $|E^*|$ of AC beyond the sensitivity range of the test setup and to reduce the testing program.
- To integrate factors influencing the stiffness and the performance of AC. The factors include loading time, temperature, and AC aging.

Pellinen and Witczak (2004) constructed $|E^*|$ master curves by fitting the sigmoidal function, Equation (2.22), to the measured compressive $|E^*|$ test data using nonlinear least square regression.

$$\log|E^*| = \delta + \frac{\alpha}{1+e^{\beta-\gamma\log f_r}} \tag{2.22}$$

where: δ, α, β and γ = regression parameters

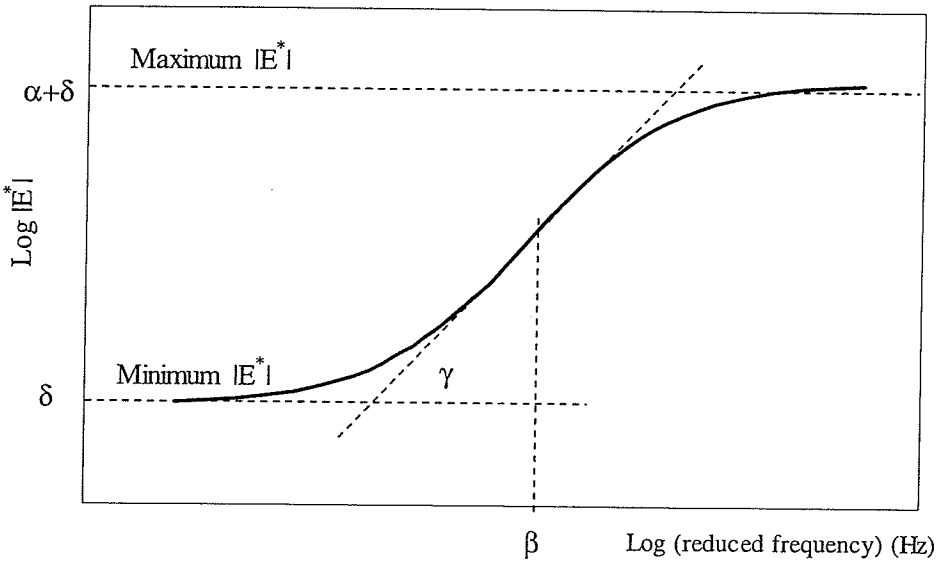

Figure 2.4: Sigmoidal function of |E*| master curve, after Pellinen et al. 2004

Figure 2.4 illustrates the sigmoidal function shown by Equation (2.22). δ and α are location parameters where δ represents the minimum $|E^*|$ and α represents the range of change in $|E^*|$ values. Sum of the two location parameters is the maximum $|E^*|$ value of an AC mixture. β represents location of the turning point of the master curve and γ represents the steepness of the master curve. Pellinen et al. (2004) justified using the sigmoidal function based on the physical behaviour of $|E^*|$ through the entire temperature range. $|E^*|$ at low temperatures are close to the maximum $|E^*|$ while, at high temperatures, get close to the minimum $|E^*|$. Pellinen et al. (2002) through using a k1-k3 non-linear elasticity model incorporated the stress dependency and non-linearity to the sigmoidal master curve.

2.5.2 Isothermal and Isochronal curves

The complex modulus (E^*) components, $|E^*|$ and ϕ, at various temperatures and frequencies can be illustrated using the family curves holding one variable constant (Pellinen, 2001). Isothermal curves, Figure 2.5(a), are family curves in which the temperature is held constant and isochronal curves, Figure 2.5(b), are family curves in which the frequency is held constant. The isothermal and isochronal curves are used to investigate the relationship between $|E^*|$ and the controlling variables. $|E^*|$ master curves are isothermal curves that are constructed at a reference temperature. Functions have been evaluated to represent the isochronal curve in chapter 7 to interpolate $|E^*|$ at various temperature.

2.5.3 Complex and black space planes

$|E^*|$ and ϕ can be represented using complex plane, known as Cole-Cole, and black space plane, Figure 2.6. In complex plane, the horizontal axis is the storage modulus ($E^{'}$) and vertical axis is the loss modulus ($E^{``}$). On the black space plane, $|E^*|$ and ϕ values are plotted on the horizontal and vertical axes; respectively. The complex and black space planes are unique smooth curves for the AC mixture independent of frequency and temperature factors. The planes are used for data quality control (Pellinen et al., 2004). The complex plane shows consistency of the dynamic modulus test data at low and intermediate temperatures while black space shows the consistency of the test data at high temperatures.

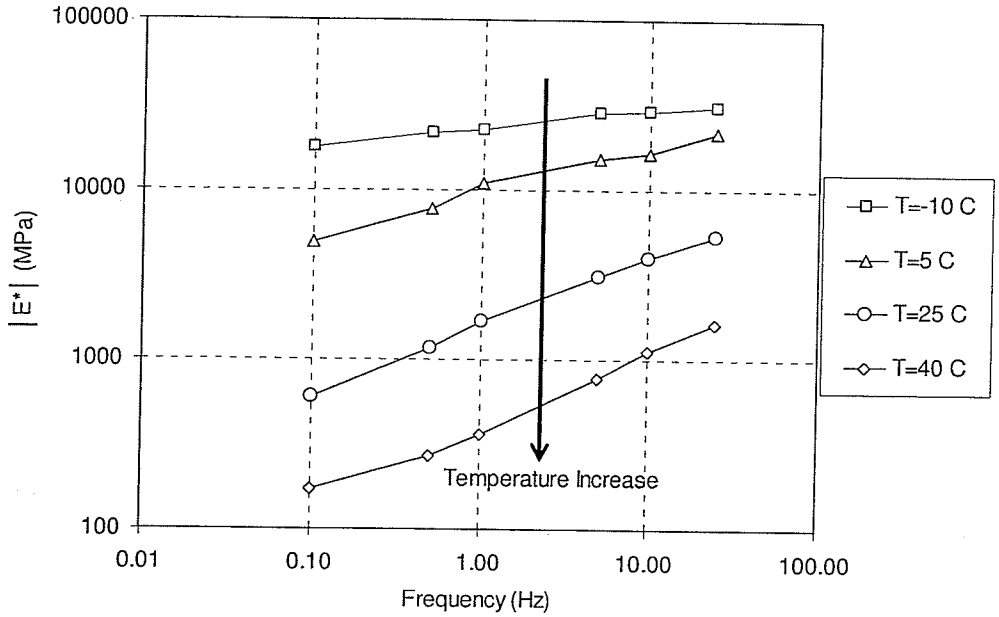

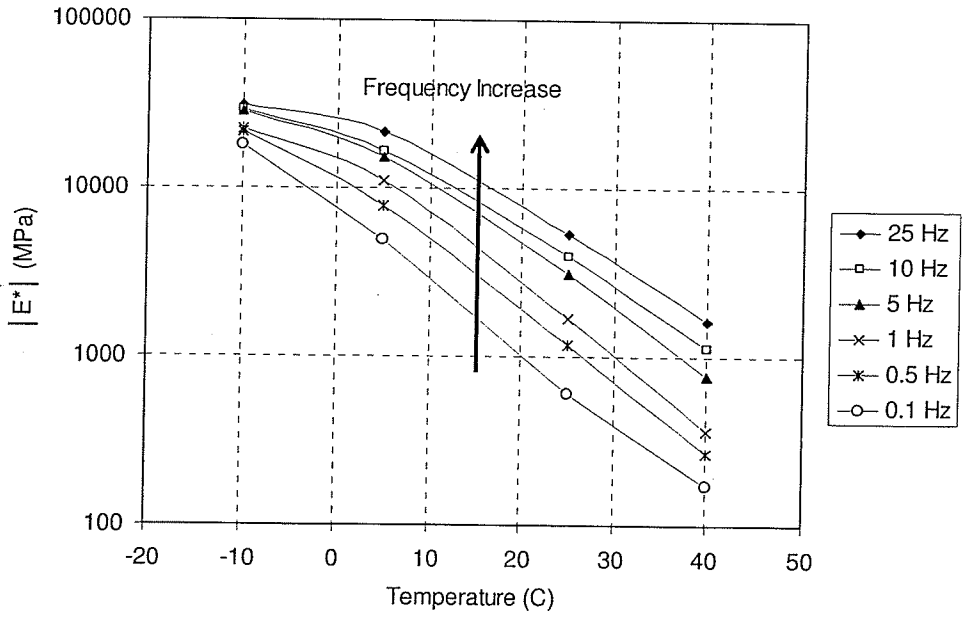

b) Isochronal curves of the complex modulus

Figure 2.5: Isothermal and Isochronal curves of the AC dynamic modulus

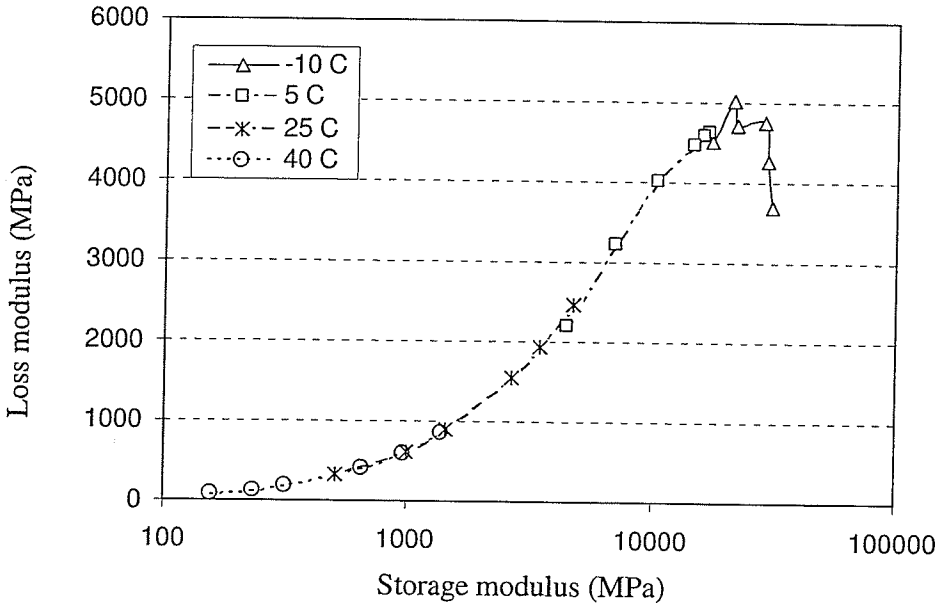

(a)

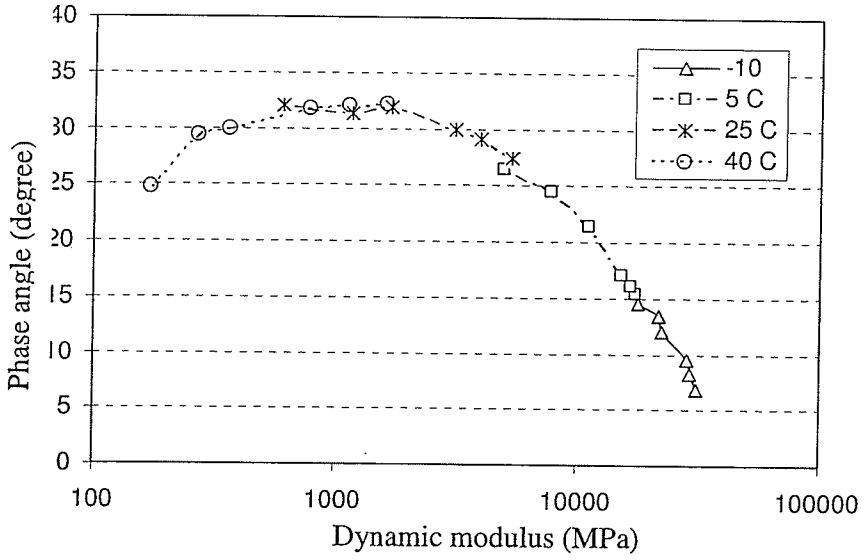

(b)

Figure 2.6: Frequency and temperature independent curves of asphalt concrete

(a) Complex plane. and (b) Black space plane

2.6 Significance of Dynamic Modulus

2.6.1 Modulus of Pavement Design and Evaluation

MEPDG is the first design procedure that incorporated the impact of aging of asphalt on mixture properties over short periods of time such as biweekly and/or monthly basis through the entire design life. The guide incorporates the effect of the pavement temperature and vehicular loading time and the binder properties on AC through the $|E^*|$ master curve and the shift factor. In MEPDG, the change of temperature is predicted with the Enhanced Integrated Climatic Model (EICM) through the pavement depth. The EICM is a one-dimensional coupled heat and moisture flow model that is used to predict the change in behaviour of pavement material over the service life. The EICM is out the scope of the thesis and more information can be found in Zapata and Huston (2008). On the other hand, the loading time, which is calculated based on the stress distribution in a pavement structure and a speed of the moving load, is used in MEPDG to calculate the loading frequency. $|E^*|$ is integrated in the pavement structure and performance models used in MEPDG. The structure model provides responses: the stress, strain and displacement. The critical structure model responses are the inputs of the performance prediction models such as fatigue cracking (alligator and longitudinal), permanent deformation (rutting), and low temperature cracking.

2.6.1.1 Fatigue Cracking

The fatigue cracking performance model predicts the number of load cycles until the fatigue failure. The transfer function of the fatigue cracking, alligator and longitudinal, incorporated in MEPDG is defined by Equation (2.23).

$$N_f = 0.00432\bar{k}_1 C\left(\frac{1}{\varepsilon_t}\right)^{3.9492}\left(\frac{1}{|E^*|}\right)^{1.281} \quad (2.23)$$

where,

N_f = number of repetitions until fatigue failure,

ε_t = max tensile strain at bottom of AC layers, and

$|E^*|$ = complex modulus of the material.

$\bar{k}_1$ = correction parameter of different asphalt layer thickness (H_{ac}) effects.

$\bar{k}_1$ depends on type of the fatigue cracking. For the alligator cracking, it is calculated as follows:.

$$\bar{k}_1 = \left(0.000398 + \frac{0.003602}{1 + e^{(11.02 - 3.49 H_{ac})}}\right)^{-1}$$

For the longitudinal cracking, $\bar{k}_1$ is calculated as follows:

$$\bar{k}_1 = \left(0.01 + \frac{12.00}{1 + e^{(15.676 - 2.8186 H_{ac})}}\right)^{-1}$$

where,

H_{ac} = total thickness of asphalt layers, inch,

C = laboratory to field adjustment factor, where

$C = 10^M$ in which

$$M = 4.84\left(\frac{V_b}{V_b + V_a} - 0.69\right)$$

V_b= percentage effective binder content.

V_a= percentage of air voids of the AC layer

2.6.1.2 Rutting

The transfer function of AC rutting is calculated of the Equation (2.24).

$$\frac{\varepsilon_p}{\varepsilon_r} = k_1 10^{-3.4488} T^{1.5606} N^{0.479244} \tag{2.24}$$

where,

ε_p = permanent strain at a depth from the pavement surface of "*depth*"

ε_r = resilient strain,

T = temperature, Fahrenheit (°F),

N = total number of load repetitions.

k_1 = factor accounts for the confining pressure at different depth

$$k_1 = (C_1 + C_2 depth)0.328196^{depth}$$

where,

$$C_1 = -0.1039 H^2_{ac} + 2.4868 H_{ac} - 17.342$$

$$C_2 = 0.0172 H_{ac} - 1.733 H_{ac} + 27.428$$

2.6.2 Simple Performance Indicator

The simple performance test (SPT) is defined in a NCHRP 9-19 report as "*A test method that measures a mixture response characteristic or a parameter that is highly correlated to the occurrence of the pavement distress (e.g., cracking and rutting) over a diverse range of traffic and climatic conditions*" (NCHRP 2002). Witczak et al. (2002b) listed specific requirements for developing the SPT:

- The SPT is to be used in support of the SuperPave volumetric mixture design

procedure.

- The SPT must test AC specimens compacted with SuperPave gyratory compactor (SGC).
- The SPT must accurately measure true fundamental responses and properties of AC mixtures.
- The SPT must be based on existing technology and equipments.
- Responses measured with the SPT need not predict the entire performance history.
- Properties determined from SPT should be tied to the advanced mixture characterization methods.

The NCHRP 9-19 research team performed an extensive test program to select a SPT for the most common distresses of asphalt concrete such as rutting, fatigue cracking and thermal cracking. The test program included over 80 test response parameters from eleven test types and mixtures and performance data from three experimental sites, the Minnesota Road (MnRoad) Project, the Federal Highway (FHWA) Accelerated Loading Facility study (ALF) and the FHWA Performance Related Specifications Study (WesTrack). The candidates for rutting were dynamic modulus, static creep, and the repeated load permanent deformation test. In a similar attempt, Witczak et al. (2002a) reported that the dynamic modulus test and the creep compliance test are the two top SPT candidates for fatigue and thermal cracking. The unconfined $|E^*|$ test in LVE was statistically the best SPT candidate for rutting, the parameters included $|E^*|/\sin\phi$, which is the highest recommended candidate performance parameter, and $|E^*|$. The analysis included unconfined and confined $|E^*|$ test at various confinement pressures, two

temperatures, 37.8°C and 54°C, and a frequency of 5 Hz. The parameters were measured in the linear and nonlinear viscoelastic regions.

2.6.3 Effect of Aggregate Gradation

Birgisson and Roque (2005) proposed a framework for optimizing aggregate gradation for high $|E^*|$ values. The framework relies on gradation factors proposed by Birgisson and Ruth (2002) and Ruth et al. (2002) and $|E^*|$ at high temperature (40°C). The gradation factors can be calculated for a given aggregate as follows:

1. For a given gradation with a nominal maximum particle size (NMPS), a control sieve point (P_c) is calculated from (0.22NMPS) and then rounded to the nearest sieve size. Control Point (P_c) separates the gradation of fine and coarse aggregates as shown in Figure 2.7.

2. The gradation factors of fine and coarse aggregates are the power law constants of the aggregate gradation curves of each, and are obtained as follows:

$$P = a_{fa} D^{n_{fa}} \text{ ; for fine aggregate} \quad (2.25)$$

$$P = a_{ca} D^{n_{ca}} \text{ ; for coarse aggregate} \quad (2.26)$$

where:

P: the percentage of aggregate passing at sieve diameter (D) (mm)

a_{fa}, n_{fa}: fine gradation parameters

a_{ca}, n_{ca}: coarse gradation parameters

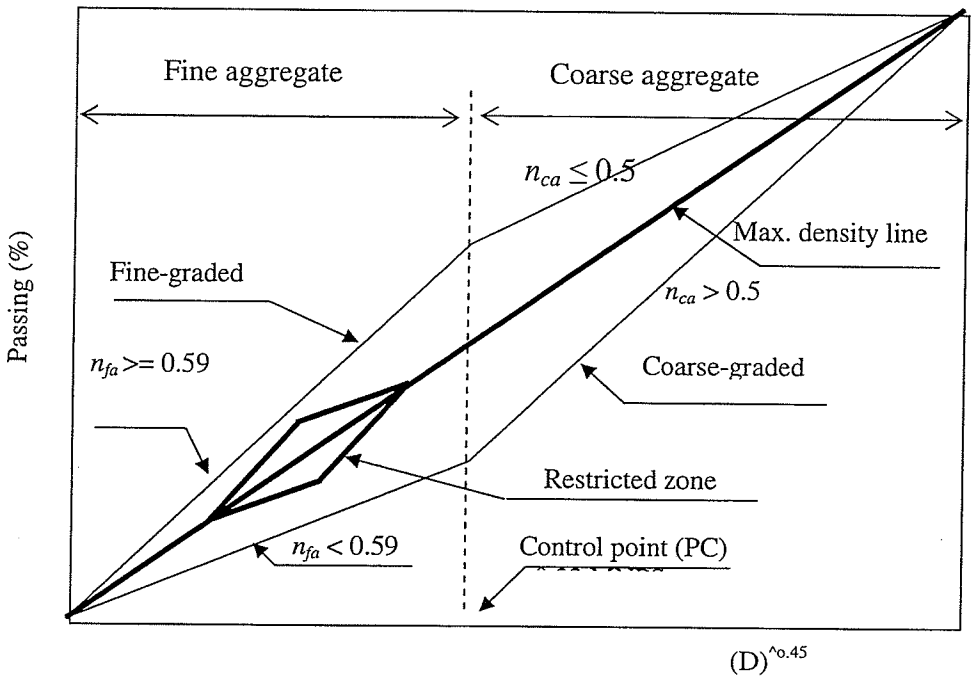

Figure 2.7: Gradation factors of aggregates

Gradations of fine-graded mixtures fall above the maximum density line (MDL) as given by the 0.45 power gradation chart while those of the coarse-graded mixtures are typically below the MDL. It was found that fine-graded aggregates have $n_{ca} \leq 0.5$ while coarse-graded aggregates have $n_{ca} > 0.5$. The aggregate gradations of asphalt mixtures were classified into four categories as shown in the framework in Figure 2.8:

Category 1: Fine-graded aggregate with $n_{ca} \leq 0.5$ and $n_{fa} \leq 0.59$, a high stiffness mix.

Category 2: Fine-graded aggregate with $n_{ca} \leq 0.5$ and $n_{fa} > 0.59$, a moderate to low stiffness mix

Category 3: Coarse-graded aggregate with $n_{ca} > 0.5$ and $n_{fa} \leq 0.59$, a moderate stiffness mix

Category 4: Coarse-graded aggregate with $n_{ca} > 0.5$ and $n_{fa} > 0.59$, a low stiffness mix

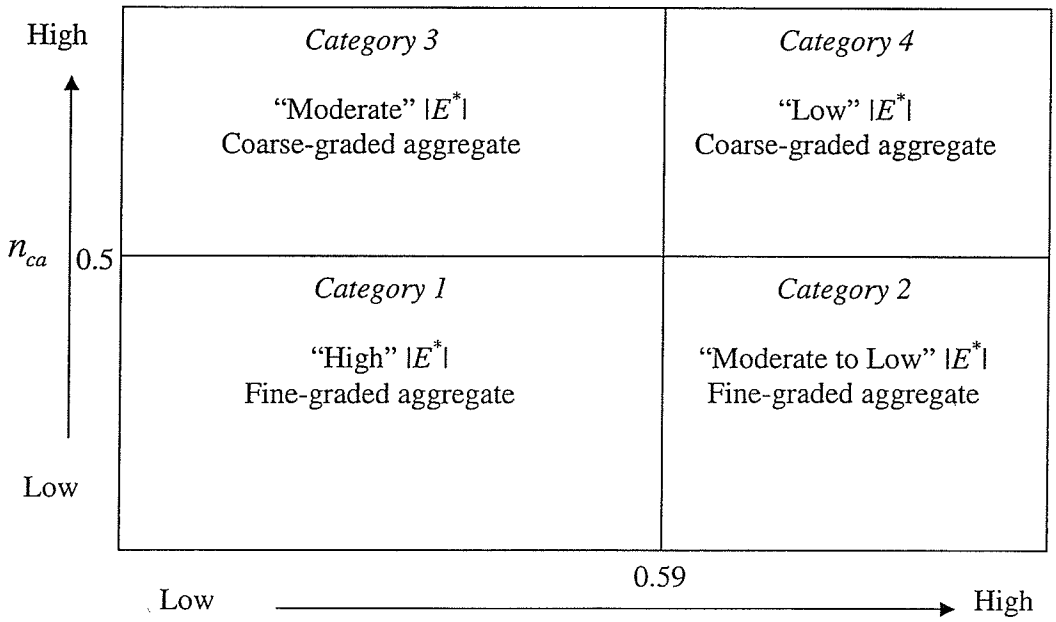

Figure 2.8: Framework for optimizing aggregate of asphalt mixtures for dynamic modulus (Birgisson and Roque, 2005)

The framework can be used to optimize the gradation for $|E^*|$ through the selection of aggregates. It classifies fine-graded and coarse-graded mixtures as optimal or non-optimal but it does not quantify the effect of the aggregate gradation on $|E^*|$. This framework implies that the aggregate gradation has a significant effect on $|E^*|$ at high service temperatures (40°C and above). In chapter 5, the relationship between $|E^*|$ at high temperatures and gradations is evaluated to determine a gradation parameter that can describe this relationship.

2.7 Relationship between Frequency-Dependent and Time-Dependent Viscoelastic Responses

The viscoelastic response of AC is required in both time and frequency domains. For the viscoelastic analysis, the response functions are required in the time domain to consider the load history in the analysis. On the other hand, MEPDG requires the dynamic modulus in the frequency domain where the pulse loading time is converted to loading frequency. The available methods to convert the responses between the two domains are discussed below.

Kim and Lee (1996) proposed an approach to determine $|E^*|$ from the static or complex creep compliance. The relationship between E^* and the complex creep (D^*) can be written in the frequency domain as follows:

$$E^* = \frac{1}{D^*} \tag{2.27}$$

where E^* is complex number that has storage and loss modulus as in Equation (2.12 and 2.13) and D^* is assumed as follows:

$$D^* = D' - iD'' \tag{2.28}$$

where D' and D'' are the storage and loss creep compliance respectively and can be calculated at a given f using Equations (2.12 and 13) as in Equations (2.29 and 2.30):

$$D' = \frac{E'}{|E^*|^2} \text{ and } D'' = \frac{E''}{|E^*|^2} \tag{2.29}$$

$$E' = \frac{D'}{|D^*|^2} \text{ and } E'' = \frac{D''}{|D^*|^2} \tag{2.30}$$

Applying the theory of viscoelasticity, D^* and $D(t)$ can be related to each other using Laplace transformation. If $D(t)$ is represented by Equation (2.4), D^* can be determined from Equation (2.31):

$$D^* = D_0 + D_1\Gamma(m+1)\left[\cos(\frac{m\pi}{2}) - i\sin(\frac{m\pi}{2})\right]\omega^{-m} \qquad (2.31)$$

where

$$\Gamma(m) = \int_0^\infty t^{m-1}e^{-t}dt \qquad (2.32)$$

where

$\Gamma(m)$ is Gamma function

$\omega = 2\pi f$ and it is the angular frequency (rad/second).

Comparing Equations (2.28) and (2.31), D' and D'' respectively are as follows:

$$D' = D_0 + D_1\Gamma(m+1)(2\pi f)^{-m}\cos(\frac{m\pi}{2}) \qquad (2.33)$$

$$D'' = D_1\Gamma(m+1)(2\pi f)^{-m}\sin(\frac{m\pi}{2}) \qquad (2.34)$$

The procedure described by Equations (2.29 to 2.34) is applied in chapter 6 to determine the creep compliance parameters, D_0, D_1 and m, from $|E^*|$ and ϕ of the tested materials at various temperatures. The parameters represent AC materials in an approach to determine the equivalent frequency for a loading time.

2.8 Pulse Loading Time –Testing Frequency Relationship

A major milestone of MEPDG is considering the effects of the pavement loading time (t_p) and temperature on AC behaviour (NCHRP 2004). MEPDG calculates t_p as a function of

the vehicle speed and pavement layer stiffness and thicknesses by applying the Odemark approach and the method of 45° influence zone of the vertical stress (NCHRP 2004). Equation (2.35) is used to calculate the design frequency (f) of $|E^*|$.

$$t_p = \frac{1}{f} \tag{2.35}$$

In an independent review of the MEPDG, NCHRP (2006) documented that "*In its present form, the Guide procedure for estimating complex modulus in the HMA layers results in unrealistic values, particularly for thick layers, showing a decrease in predicted modulus with depth in hot weather that is counterintuitive. This quandary results from the loading time/frequency effect overriding the temperature effect*". These shortcomings have motivated many researchers and discussions. Some of these discussions can be found in two consecutive meeting minutes of 2007 and 2008 of the FHWA Asphalt Fundamental Properties and Advanced Modeling Expert Task Group (FHWA and ETG minutes, 2006 and 2007).

Al-Qadi et al. (2008a) identified two major sources of the inaccuracy in the procedure adopted in MEPDG for estimation the frequency of $|E^*|$. The first source of inaccuracy is incapability of Odemark approach to account for the effect of the far-wheel loads. The second source is the conversion from the pulse loading time to the testing frequency.

Factors affecting the calculated loading time by applying the MEPDG approach according to Al-Qadi et al. (2008a) are

- The elastic solution to calculate the loading time can not account for the far-field effect of an approaching-leaving rolling wheel,

- The elastic solution does not consider the delayed response of AC,
- The accurate rheology of binder may not be captured in the MEPDG, and
- The accuracy of Odemark approach to calculate the loading time is uncertain and it requires validation since it is empirical.

Al-Qadi et al. (2008b) used 3-D Finite Element (FE) viscoelastic analysis to adjust the loading time calculated by Odemark approach. The viscoelastic properties of AC was calculated using $|E^*|$ and ϕ. A correction factor as a function of pavement depth and pavement functional class was proposed to adjust the MEPDG frequency. The correction factor was calculated as follows. First, the loading time at various pavement depths was calculated from the calculated history of the vertical stress at a given point. Then the FE loading frequency was calculated using Equation (2.35). The correction factor is the ratio between the FE frequency and the one calculated in accordance with the MEPDG.

The second source of the inaccuracy is the conversion method applied by MEPDG. Dongre et al. (2006) reviewed the common conversion methods between the time and frequency domains in the field of rheology and concluded the followings:

- No supporting reference other than MEPDG for Equation (2.35) was found.
- The angular frequency (ω) in rad/second is widely used and the conversion can be represented as in Equation (2.36). Using ω was explained as consequence of the Inverse Fast Fourier Transformation (IFFT) of the storage or loss modulus.

$$t_p = \frac{1}{\omega} = \frac{1}{2\pi f} \tag{2.36}$$

Underwood and Kim (2009) evaluated four solution techniques that are based on linear viscoelastic principles to determine $|E^*|$ that gives the same maximum response of AC subjected to a sinusoidal pulse stress. The solutions utilize the static and complex creep compliances that are calculated from $|E^*|$ and ϕ and they are as follows:

1. Linear viscoelastic analysis: in which, the maximum strain is calculated from the strain history and can be represented as in Equation (2.37)

$$\varepsilon_0 = \max\left[\int_0^t D(t-\tau)\frac{d(\frac{\sigma_0}{2}\sin(\omega\tau-\frac{\pi}{2})+\frac{\sigma_0}{2})}{d\tau}d\tau\right] \tag{2.37}$$

2. Quasi-static analysis, the maximum strain is calculated from Equation (2.38)

$$\varepsilon_0 = \max[D(t)\sigma(t)] \approx D(\frac{t_p}{2})\sigma_0 \tag{2.38}$$

3. Steady-state analysis, the maximum strain is calculated as follows:

$$\varepsilon_0 = \left|D^*\right|_{f=1/t_p}\sigma_0 \tag{2.39}$$

The source of error in adopting this approach is considering that the stress is steady-state sinusoidal input with zero mean stress. These conditions are not met by traffic loading (Underwood and Kim, 2009).

4. Superposition analysis; this approach separates the haversine pulse to a sinusoidal portion and constant loading portion. The maximum strain is calculated as follows:

$$\varepsilon_0 = \sigma_0\left(\frac{\left|D^*\right|_{f=1/t_p} + D(\frac{t_p}{2})}{2}\right) \tag{2.40}$$

These solutions provide considerable insight to calculate AC stiffness that account for the maximum strain instead of the recoverable strain. The maximum strain consists of the instantaneous recoverable strain and the creep strain, which releases within the rest period. The calculated stiffness at t_p is less than $|E^*|$ at frequency calculated according to MEPDG approach. These solutions have two main shortcomings:

- The solutions are based on a sinusoidal loading. Many equations as shown in Table 2.1 have been used to fit the measured or calculated stress to determine the pulse time. Al-Qadi et al. (2008b) found that haversine or bell-shape forms represent the normalized compressive stress for moving loads. Equations (2.41 and 2.42) represent the normalized haversine and bell-shape stresses; respectively

$$\sigma(t) = \sin^2(\frac{\pi}{2} + \pi\frac{t}{t_p}), \text{ where } -\frac{t_p}{2} \le t \le \frac{t_p}{2} \tag{2.41}$$

$$\sigma(t) = e^{-t^2/s^2} \tag{2.42}$$

where

s: standard deviation that control the shape of the curve.

Table 2.1: Different fitting functions used for pulse calculation (Al-Qadi et al., 2008b)

Approximation function	Source of AC stress distribution
Sinusoidal and triangular function	FE modeling and elastic theory
log (t_p)=0.5d-0.2-0.94 log (v)	Elastic layered theory
Square wave function	Proposed
Haversine and normalized bell-shape functions.	Field stress measurements

d = pavement depth (m), v = vehicle speed (km/h)

The solutions require both $|E^*|$ and ϕ to calculate the creep compliances. The current MEPDG version does not use ϕ in pavement design. Incorporating these solutions requires significant changes in MEPDG. Al-Qadi et al. (2008b) suggest that conversion of the field loading pulse to the frequency domain should be carried out using the Fast Fourier Transformation (FFT) for the following reasons:

- Conversion factors are based on the pulse shape in the time domain.
- There is no specific function to fit the field loading pulse under encountered conditions (pavement depth, material stiffness and vehicle speed).
- Symmetric functions can not account for the delayed AC response and the residual stress
- The pulse generated by vehicular loading includes complex frequency spectrum. The simple conversion forms shown by Equation (2.35 and 2.36) may not provide reliable conversion.

Al-Qadi et al. (2008b) used the dominant frequency to represent the frequency spectrum of a pulse stress. The dominant frequency was defined as the weight centre of the frequency spectrum. This definition neglects the property of the material that the stress is applied on. For example, the dominant frequency for a pulse is constant whether the material is elastic or viscoelastic.

A novel approach is introduced in chapter 6 of this thesis to determine the frequency of a pulse stress. The approach utilizes the viscoelastic theory to determine the frequency of $|E^*|$ that is calculated from normalized sinusoidal stress and the maximum strain of a normalized pulse stress.

2.9 Determination of AC Dynamic Modulus

2.9.1 Laboratory Testing

The $|E^*|$ test can be carried out according to ASTM 3497 (ASTM 2003) "Test Method for Dynamic Modulus of Asphalt Concrete" and AASHTO TP 62-03 (2005) "Determining Dynamic Modulus of Hot-Mix Asphalt Concrete Mixtures". There are some differences between ASTM 3497 and AASHTO TP 62-03. ASTM 3497 recommends conducting the test on cylindrical specimens with a height-to-diameter ratio of 2 to 1, a minimum specimen diameter of 101.6 mm (4 in) and four or more times the maximum nominal size of aggregate. It recommends carrying out the test at 5, 25 and 40°C and frequencies of 1, 4 and 16 Hz at each temperature. The major difference between the two test methods is that, the test based on ASTM 3497 can be carried on laboratory prepared specimens and field cores.

On the other hand, AASHTO TP 62-03 was developed during the National Cooperative Highway Research Program (NCHRP) projects 9-19 " SuperPave Support and Performance Models Management" and NCHRP 9-29 "Simple Performance Tester for SuperPave Mix Design". Figure 2.9 shows a schematic diagram for the test setup. AASHTO TP 62-03 requirements are as follows:

- Mixtures should be aged for 4 hours to represent the short-term aging that occurs for the mix during the mix placement and compaction
- The test specimens are prepared in the laboratory from 170-mm gyratory specimens by coring and sawing. Test specimens have dimensions of 100 mm diameter and 150 mm height with a height to diameter ratio of 1.5 to 1

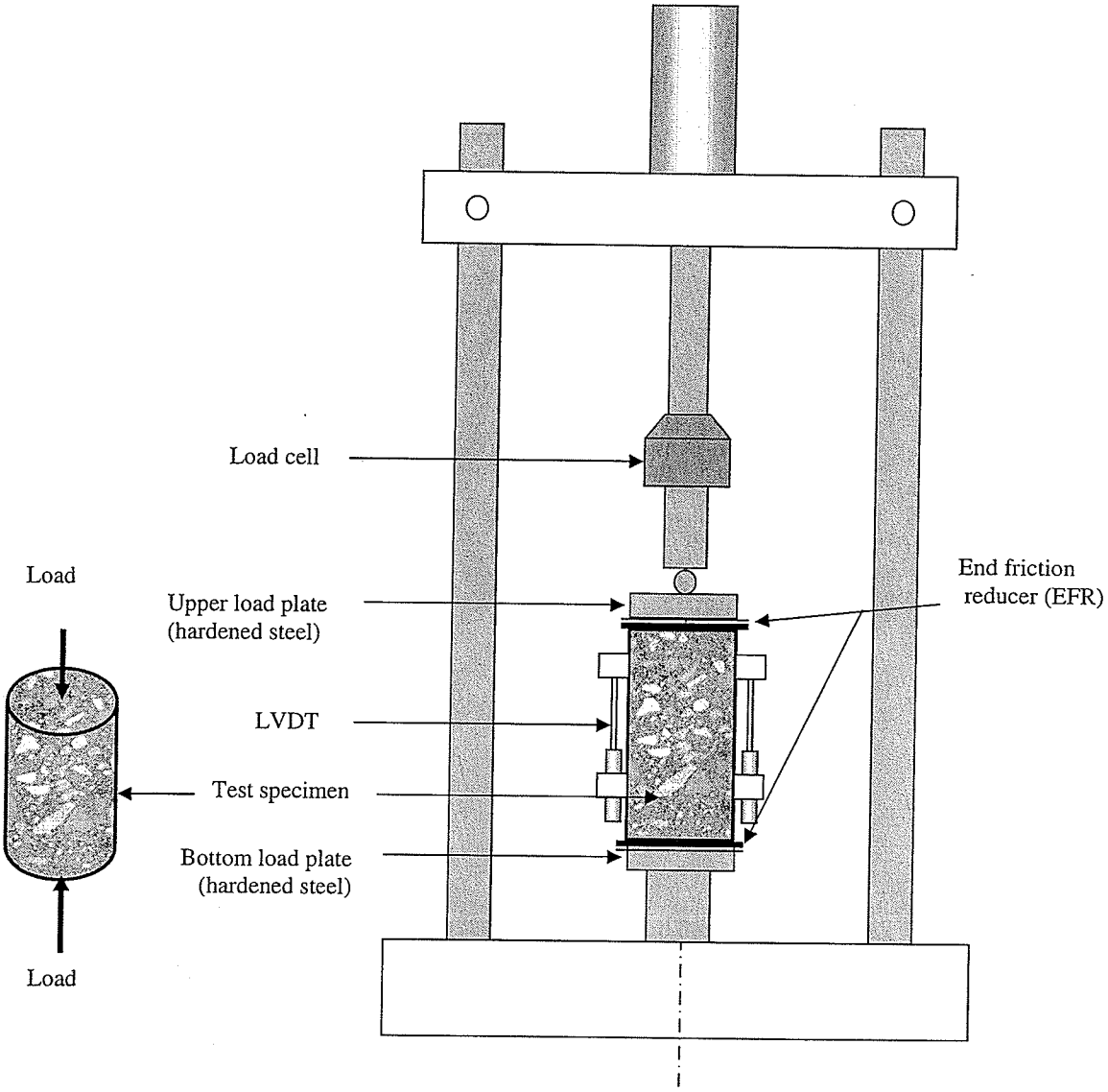

Figure 2.9: Schematic of dynamic modulus test (AASTHO TP 62-03)

- The test is conducted at temperatures of -10, 4.4, 37.8 and 54.4°C, and frequencies 0.1, 0.5, 1, 5, 10 and 25 Hz.
- End friction reducer (EFR) should be used to diminish the effect of friction developed between the specimen ends and the loading platens. EFR consists of

two latex sheets filled with silicon grease.

- Amplitude of the sinusoidal stress shall be adjusted at each test sequence to produce resilient axial strain between 50 and 150 micro-strains.

AASHTO TP 62-03 has been recommended to determine $|E^*|$ and ϕ of asphalt mixtures for pavement design and evaluation under MEPDG and under the SPT.

2.9.2 Indirect Tensile Testing Mode

Kim et al. (2004) presented a linear viscoelastic (LVE) solution to determine $|E^*|$ and ϕ using indirect tensile (IDT) testing mode. In IDT testing, the cylindrical specimen is instrumented with two transducers on each face to measure horizontal and vertical deformations and loaded diametrically via two loading strips with the sinusoidal load. Figure 2.10 shows schematic of the IDT testing. $|E^*|$ is measured in IDT testing mode, $IDT|E^*|$, is calculated using Equation (2.43).

$$IDT\left|E^*\right| = \frac{2P_0}{\pi a d}\frac{\beta_1\gamma_2 - \beta_2\gamma_1}{\gamma_2 V_o - \beta_2 U_0} \tag{2.43}$$

where;

P_0 = amplitude of the sinusoidal load.

a = loading strip width, m

d = thickness of the specimen, m

V_0, U_0 = amplitude of the vertical and horizontal displacements.

$\beta_1, \beta_2, \gamma_1, \gamma_2$ = coefficients that depend on the specimen diameter and gauge length as shown in Table 2.2.

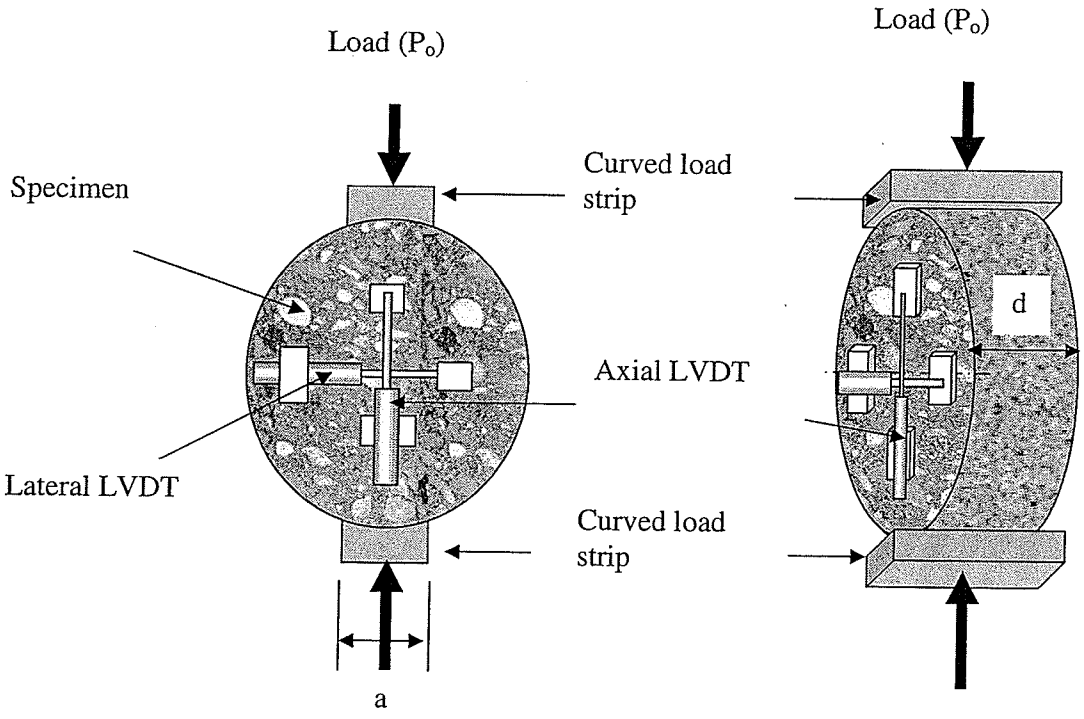

Figure 2.10: Schematic of indirect tension (IDT) test

Table 2.2: Coefficients of dynamic modulus and Poisson's ratio from indirect tensile method; specimen diameter of 150 mm

Gauge Length (mm)	β_1	β_2	γ_1	γ_2
25.4	-0.0065	-0.0021	0.002	0.0062
38.1	-0.0099	-0.0032	0.0029	0.0091
50.8	-0.0134	-0.0042	0.0037	0.0116

Harran and Shalaby (2007b) found that the variability in $|E^*|$ obtained from the uniaxial testing carried out according to AASHTO TP62-03 is higher than the variability of $|E^*|$

measured from IDT testing.

Kim et al. (2004) recommended to carry out *IDT*$|E^*|$ at 5, 25 and 40°C and eight frequencies at each temperature. Although the approach was verified for laboratory compacted specimens, it may not be feasible for extracted AC cores from in-service pavement. The high number of the test sequences on the cores may produce significant damage especially for cores collected from damaged pavement.

Pellinen et al. (2006) used composite $|E^*|$ testing to determine stiffness of thin surface layers. This testing is carried out on rectangular specimens that are sawed from the surface layer cores, and then stacked horizontally without bonding. The ends are hydrostone caped to provide flat and smooth loading area and to bond the blocks. The complexity of the specimen preparation may affect the viability of this approach (Biswas and Pellinen, 2007). In chapter 7, predicting $|E^*|$ master curve from M_R is introduced and can be used for predicting $|E^*|$ of in-service from laboratory measurements.

2.10 Variability of Dynamic Modulus

The sources of variability of $|E^*|$ are material, mixing and compaction process, preparation of test specimens and specimen instrumentation. AASHTO TP62-03 recommends an accuracy limit that depends on the number of test specimens and the number of the transducers required to measure the axial strain of the specimen. In general, AASHTO TP 62-03 recommends maximum limits of the accuracy of ±15% of the mean values.

$|E^*|$ test data depends on the two test parameters, temperature and frequency. Tran and

Hall (2006) used the variability of measured $|E^*|$ to evaluate different test protocols using different number of specimens and instruments to measure deformation. The variance is applied to measure the variability in $|E^*|$. The variability in measurements of the $|E^*|$ test is measured with both "within" the specimen and "between" the test specimens. The variability within the test specimen at given conditions is defined by Equation (2.44)

$$S_w^2 = \frac{1}{m-1}\sum_{i=1}^{m}(X_{is} - \overline{X}_s)^2 \tag{2.44}$$

where:

S_w^2 = "within" specimen variance

X_{is} = dynamic modulus of the specimen at position of the transducer (i)

$\overline{X}_s$ = average of the dynamic modulus at the transducers within the specimen

m = number of the transducers on the test specimen

The "between" specimen variance at given test conditions is calculated from Equation (2.45)

$$S_b^2 = \frac{1}{n-1}\sum_{j=1}^{n}(\overline{X}_{sj} - \overline{X})^2 \tag{2.45}$$

where:

S_b^2 = "between" specimens variance

$\overline{X}_{sj}$ = average dynamic modulus of specimen (j)

$\overline{X}$ = average of three samples

n = number of specimens

The variance of the dynamic modulus is sensitive to the test conditions: temperature and frequency. Coefficient of variation (CV) which is the normalized value of the variance is used to represent the variation. The average of the "within" specimen coefficient of variation (CV_w) and the "between" coefficient of variation (CV_b) are as follows:

$$CV_w = \frac{1}{n}\sum_{j}^{n}\frac{S_{wj}}{\overline{X}_{sj}} \tag{2.46}$$

$$CV_b = \frac{S_b}{\overline{\overline{X}}} \tag{2.47}$$

where:

S_{wi}= the variance within specimen i

Accuracy of the measured $|E^*|$ in terms of standard error (S_e) is defined using "within" specimen and "between" specimen variances by the relation:

$$s_e = \sqrt{\frac{CV_w^2}{m} + \frac{CV_b^2}{n}} \tag{2.48}$$

Tran and Hall (2006) found that number of test specimens and the number of measurement instruments affixed on each specimen significantly affect the variability of $|E^*|$ but the accuracy limit specified with AASHTO TP62-03, 15%, can be reached by using two specimens and two LVDTs on each specimen.

2.11 Dynamic Modulus Predictive Models

The dynamic modulus is best estimated from non-destructive laboratory testing at various loading frequencies and test temperatures (NCHRP 2004). On the other hand, there has

been significant progress in developing predictive models that can estimate $|E^*|$ without the need for testing. Such models rely on material and mixture volumetric properties to predict $|E^*|$. The models such as the Witczak model and Hirsch model are widely used in planning and design of projects in which laboratory testing is unavailable.

2.11.1 Witczak $|E^*|$ Model

The model was developed through comprehensive work initiated by Shook and Kallas (1969) and completed by Witczak and his associate research team at the University of Maryland since the early 1970s until 1990s (Pellinen 2001). The database includes $|E^*|$ test data conducted at the Asphalt Institute, University of Maryland, and Federal Highway Administration (FHWA). The revised Witczak model can be found in Witczak and Fonseca (1996). The revised Witczak model is shortly called the Witczak model and it is as shown by Equation (2.49).

$$\begin{aligned}\log|E^*| = {} & 3.750063 + 0.02932\,p_{200} - 0.001767\,(p_{200})^2 - 0.002841\,p_4 \\ & - 0.058097\,V_a - 0.802208\left(\frac{V_{beff}}{V_{beff}+V_a}\right) \\ & + \frac{3.871977 - 0.0021\,p_4 + 0.003958\,p_{38} - 0.000017\,(p_{38})^2 + 0.00547\,p_{34}}{1+e^{-0.603313-0.31335\log(f)-0.393532\log(\eta)}}\end{aligned} \tag{2.49}$$

where,

$|E^*|$ = dynamic modulus, psi,

P_{200} = percentage passing sieve #200,

P_4 = cumulative percentage retained on the 4.75-mm (#4) sieve,

P_{38} = cumulative percentage retained on the 9.5-mm (#3/8) sieve,

P_{34} = cumulative percentage retained on the 19-mm (#3/4) sieve,

V_{beff} = percentage effective bitumen content, by volume,

V_a = percentage air content,

f = frequency, Hz, and

η = bitumen viscosity, 10^6 Poise.

The viscosity (η) is incorporated in the predicting $|E^*|$ models to represent the effect of temperature and the asphalt aging. The viscosity-temperature relationship is shown by Equation (2.20). The regression constants, A and VTS, are determined by two methods. In the first method, the constants are obtained by regression analysis between viscosity and temperature using Equation (2.20). The viscosity of the binder at various temperatures is calculated from complex shear modulus, G^*, and phase angle, δ, of binder using Equation (2.50).

$$\eta = \frac{G^*}{10}\left(\frac{1}{\sin\delta}\right)^{4.8628} \tag{2.50}$$

In the second method, A and VTS are typical values for a given PG grade binder and they can be found in NCHRP 1-37A.

Several researchers, such as Dongré et al. (2005), Birgisson et al. (2005) and Schwartz (2005), evaluated the Witczak $|E^*|$ predicting model. Generally, the predicted and measured $|E^*|$ values are in good agreement. Pellinen (2001) reported that the Witczak model does not capture the mixture performance with sufficient accuracy, for the model to be used as a simple performance test, and that additional mixture volumetric evaluation is required to predict $|E^*|$ accurately. Schwartz (2005) concluded that the model understates the influence of the mixture parameters, and can not differentiate the performance of different mixtures under identical conditions. Dongré et al. (2005)

evaluated the Witczak model for hot mix asphalt plant mixtures, and concluded that the model loses accuracy if the mixture volumetric properties, aggregate gradation and binder content, deviate from the mix design levels. They found that the accuracy of the Witczak model was lowest at high temperature and that below an $|E^*|$ value of 125,000 psi (862 MPa) the model over-predicts $|E^*|$. Therefore, they recommended measuring $|E^*|$ if the expected value is below 125,000 psi (862 MPa). Rutting, one of the major pavement distresses, is considered highly sensitive to $|E^*|$ at high service temperatures. The low reliability of the $|E^*|$ predictive models at high temperatures devalues the reliability of the predicted rutting. Therefore, considering the difficulty of obtaining high quality measurements of $|E^*|$, it is essential to improve the prediction models at high temperature.

Birgisson and Roque (2005) proposed a framework for optimizing aggregate gradation for high values of $|E^*|$. This framework implies that aggregate gradation has a significant effect on the dynamic modulus at high temperatures. It ranks the mixtures according to their stiffness at high temperature but it does not quantify the effect of the aggregate gradation on $|E^*|$.

Schwartz (2005) performed a sensitivity analysis on the predicted $|E^*|$ for the input parameters of the Witczak model. The analysis was performed with the same data used to calibrate the Witczak model. The analysis showed that the aggregate gradation parameters have the strongest influence and, between the gradation parameters, the percent retained on the 4.75 mm sieve and the percent passing the 0.075 mm sieve have the strongest influence on the predicted $|E^*|$.

In chapter 5, a regression model has been developed to adjust the predicted $|E^*|$ master curve using an aggregate gradation parameter. The model was developed from $|E^*|$ test results of mixtures tested at the University of Manitoba and other tests that are available in the published literature.

2.11.2 Hirsch model

The Hirsch model can be used to predict properties of composite materials, such as AC, from their phases and volume fractions. Christensen et al. (2003) modified the Hirsch model to estimate $|E^*|$ and ϕ of AC. The modified model serves as a tool for analyzing the effect of the changes in volumetric mix factors of AC. They reported that the model is rational and simple. The Hirsch model uses three parameters, namely, the complex shear modulus of binder ($|G^*|$), the void in mineral aggregate (VMA), and the void filled with asphalt (VFA) to predict $|E^*|$ and ϕ. The calibrated Hirsch model is shown by Equation (2.51).

$$|E^*| = P_c\left[4.2\times10^6\left(1-\frac{VMA}{100}\right)+3|G^*|_{binder}\left(\frac{VFA\times VMA}{10^4}\right)\right] + (1-P_c)\left[\frac{1-\frac{VMA}{100}}{4.2\times10^6}+\frac{VMA}{3VFA|G^*|_{binder}}\right]^{-1} \quad (2.51)$$

where

$|E^*|$ = dynamic modulus, psi

$|G^*|_{binder}$ = complex shear modulus of binder, psi

VMA = voids in the mineral aggregate, %

VFA = voids filled with asphalt, %

P_c = aggregate contact factor where

$$P_c = \frac{\left(20 + \frac{VFA \times 3|G^*|_{binder}}{VMA}\right)^{0.58}}{650 + \left(\frac{VFA \times 3|G^*|_{binder}}{VMA}\right)^{0.58}} \tag{2.52}$$

$|G^*|$ is measured at various temperatures and frequencies using the DSR test. A model was proposed to predict phase angle at various temperatures and frequencies using the aggregate contact factor, P_c, Equation (2.53).

$$\phi = -21(\log P_c)^2 - 55\log P_c \tag{2.53}$$

They compared the Hirsch model shown by Equation (2.51) with the Witczak model shown by Equation (2.49). $|E^*|$ calculated from the two models are in good agreement and of similar accuracy. The Witczak model is used in pavement design and evaluation by MEPDG, therefore it has been evaluated by researchers. In chapter 4, the evaluation is carried out on the Witczak model for asphalt mixtures used in Manitoba because Manitoba, which is in a cold region, uses low stiffness binders to reduce thermal cracking due to cold temperatures (<5°C).

2.12 Resilient Modulus

The resilient modulus of asphalt concrete is an elastic property that is defined by the ratio

of the applied repeated stress (σ_a) to the resilient strain (ε_r) as follow.

$$M_R = \frac{\sigma_a}{\varepsilon_r} \tag{2.54}$$

M_R is obtained from the cyclic test in indirect tensile (IDT) mode by applying a pulse load followed by a rest period. In the IDT mode, cylindrical specimens are loaded diametrically against two loading strips and the horizontal and vertical deformations are measured simultaneously at centres of the specimen ends over a specific gauge length, Figure 2.11. According to ASTM D4123, M_R test may be carried out on laboratory compacted specimens as well as AC cores. LTPP 07 recommends a haversine pulse with a loading time of 0.1 s followed by rest period of a 0.9 s to determine M_R. Other pulse forms and loading times may be applied according to ASTM D4123. Table 2.3 lists differences between $|E^*|$ test and M_R test.

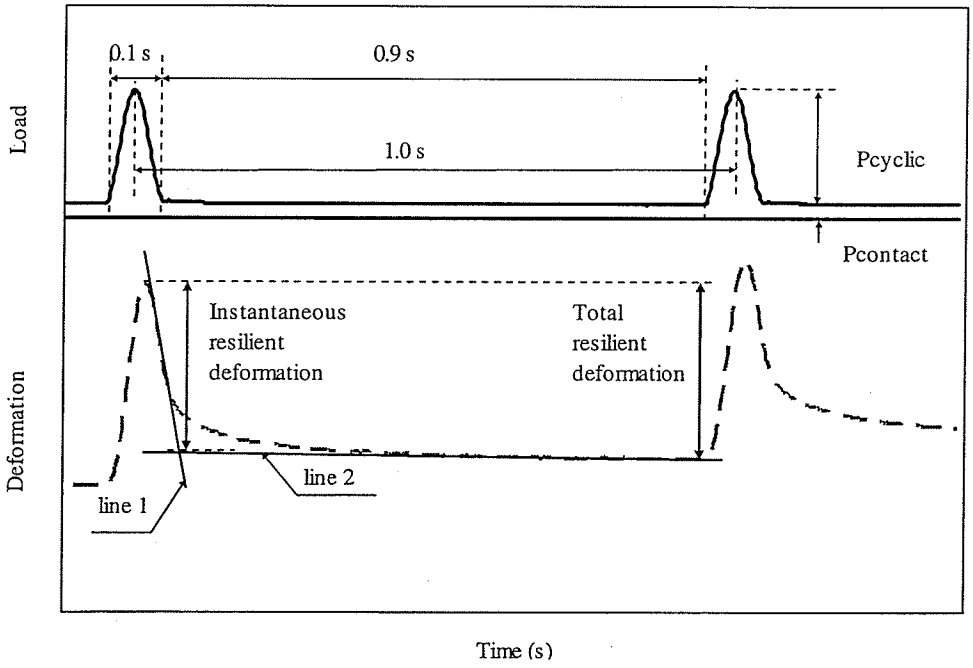

Figure 2.11: Typical load and deformation of resilient modulus test

Table 2.3: Comparison between resilient modulus and dynamic modulus

Criteria	Dynamic modulus ($\|E^*\|$)	Resilient modulus (M_R)
Test standards	ASTM 3497, AASHTO TP 62-03	ASTM D4123, SHRP P07, NCHRP 1-28 and 1-28A
Response range	Linear viscoelastic	Elastic
Load form	Continuous sinusoid	Pulse load
Loading time/frequency	25, 10, 5, 1, 0.5 and 0.1 Hz	One loading time (0.1 s)
Rest period	None	0.9 s
Testing mode	Axial compression	Indirect tensile (IDT)
Test specimen size	100 mm diam × 150 mm height	150 mm diam × 50 mm thickness
Specimen preparation	Lab compacted specimens	Lab compacted specimens and field cores
Compaction method	Gyratory	Marshall and Gyratory
Pavement design guide	NCHRP 1-37A	AASHTO1993
Relation to pavement performance	Correlated to rutting and fatigue cracking (Witczak et al. 2002a and 2002b)	Was not investigated
Measures creep compliance, relaxation modulus:	Yes (Daniel and Kim, 1998)	None

While M_R test can be performed on field cores, the required height of 150 mm restricts the $|E^*|$ test to laboratory compacted specimens. Even if it is possible to extract 150 mm cores from in-service pavement, in most cases they will be composed of two or more courses having different properties. Generally speaking, specimen preparation is easier in M_R test than in $|E^*|$ test , however M_R specimens can be damaged more easily due to cracking at the contact points between loading strips and specimens. In addition the $|E^*|$ test is more reliable, resulting in less variance compared to the M_R test.

A method to convert M_R to $|E^*|$ is useful for testing as-built and in-service pavements. This method can support using the M_R test for quality control (QC) since the M_R test is cheaper and faster to conduct, and for level 2 mix design, large improvements without the need to create new mixes or carry out the $|E^*|$ test. Furthermore, the method can be beneficial for adapting the existing asphalt pavement databases, such as the LTPP database, to MEPDG.

Any reliable method to convert M_R to $|E^*|$ should address the following three differences: the test configuration, load form and definition of the recoverable deformation.. First, the $|E^*|$ test is carried out in the axial compressive mode while the M_R test is performed in the IDT mode. Second, the load of $|E^*|$ is sinusoidal applied at multi frequencies while the load of M_R is pulsed and carried out at one loading time. Finally, the deformation history of $|E^*|$ specimens is a continuous sinusoid and the recoverable deformation is its amplitude. In contrast, the deformation history of M_R specimens consists of two components resulting during the pulse load and the rest period. The recoverable

deformation of the M_R testing is defined with empirical process by using a method illustrated by ASTM 4123 and LTPP 07 as in Figure 2.11 with line 1 and line 2.

Kim et al. (2004) introduced an analytical linear viscoelastic solution to determine $|E^*|$ in the IDT mode. The solution was verified with experimental measurements obtained from the axial compression mode. The verification implies that the test configuration does not have an impact on the stiffness when the applied stress is in the viscoelastic range.

Nunn (1996) suggested the equivalent frequency (f_{eq}) at which the stiffness modulus under a continuous sinusoidal load is determined is equivalent to the modulus determined under a pulse load. To calculate f_{eq}, the viscoelastic property of asphalt concrete was represented with the Burgers model, which includes three elements connected in series: spring, dashpot and Kelvin elements. Although this model represents well the behaviour of the viscoelastic material under a constant load, it does not capture exactly the strain over long-term loading. Loulizi et al. (2006) calculated f_{eq} from the pulse loading time (t_p) by using the following relationship.

$$f_{eq} = \frac{1}{2\pi\omega} = \frac{1}{2\pi t_p} \tag{2.55}$$

This approach treats the asphalt concrete as an elastic material and neglects the influence of the rest period on the recoverable deformation.

Lacroix et al. (2008) used an artificial neural network (ANN) to predict $|E^*|$ from M_R. The ANN was trained with $|E^*|$ of the Witczak database and M_R calculated from this database using an approach proposed by Lacroix et al. (2007). Since the accuracy of

ANN depends on the range of the training data, errors could result from extrapolating M_R. Using the trained ANN for predicting $|E^*|$ of in-service asphalt concrete could result in significant errors since the training data was based on laboratory compacted mixtures only. In chapter 6, a numerical approach is proposed to determine the equivalent frequency for the loading time of pulse. This approach was used to predict $|E^*|$ from M_R in chapter 7.

3 Materials and Experimental Program

3.1 Testing Plan

The research program required the determination of the $|E^*|$, ϕ and M_R of laboratory asphalt mixtures and in-service asphalt concrete. Figure 3.1 shows the testing plan. This testing plan is a part of a comprehensive testing plan of a project carried out at the University of Manitoba in cooperation with Manitoba Infrastructure and Transportation (MIT). In this project, test procedures were established for the first time in Manitoba to measure $|E^*|$, ϕ, M_R, $D(t)$ and IDT strength of asphalt concrete according to the current standards (Harran and Shalaby, 2008) .

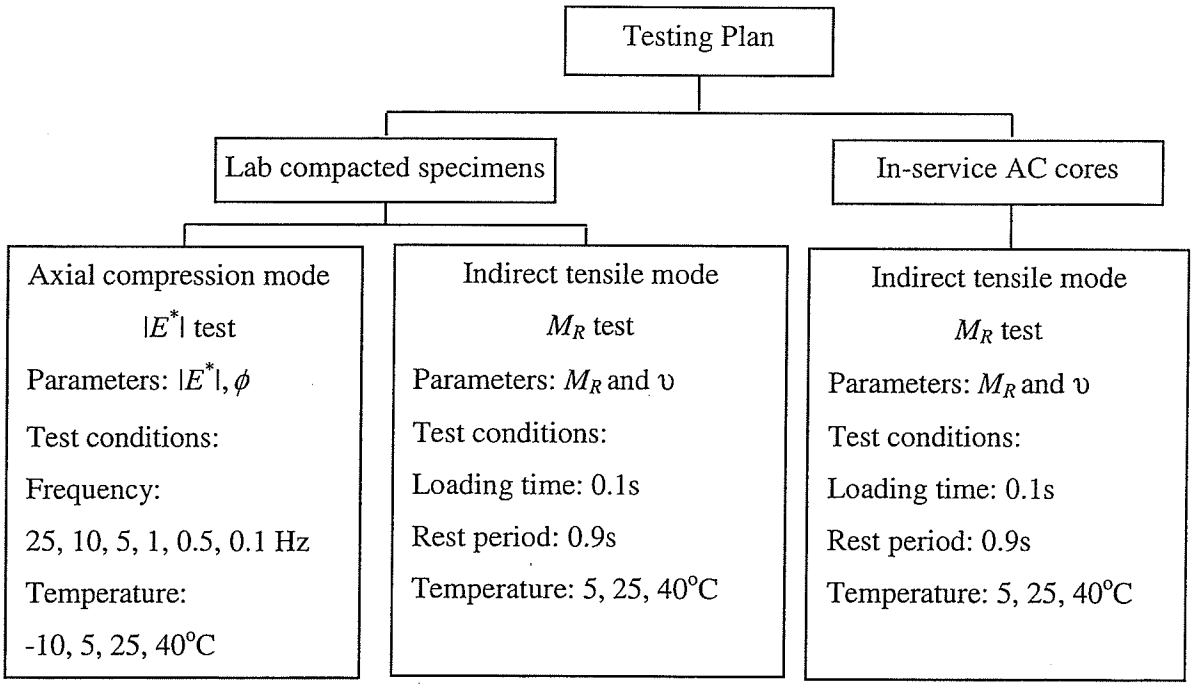

Figure 3.1: The experimental program

The sources of asphalt concrete consisted of AC mixtures prepared in the laboratory from loose aggregates and binders sampled from asphalt pavement projects and in-service AC extracted immediately after construction. The mixtures were tested in the axial compression mode to determine $|E^*|$ and ϕ and in the indirect tensile mode to determine M_R, $|E^*|$ and ϕ. The in-service AC cores were tested only in the indirect tensile mode to determine M_R, $|E^*|$ and ϕ.

3.2 Field Sampling

Field samples consisted of loose aggregates, loose binders, and the in-service AC cores taken from pavement projects constructed in Manitoba, Canada during the period from 2001 and 2004. Generally, the asphalt concrete layer of asphalt pavement constructed in Manitoba consists of surface and binder courses, as shown in Figure 3.2.

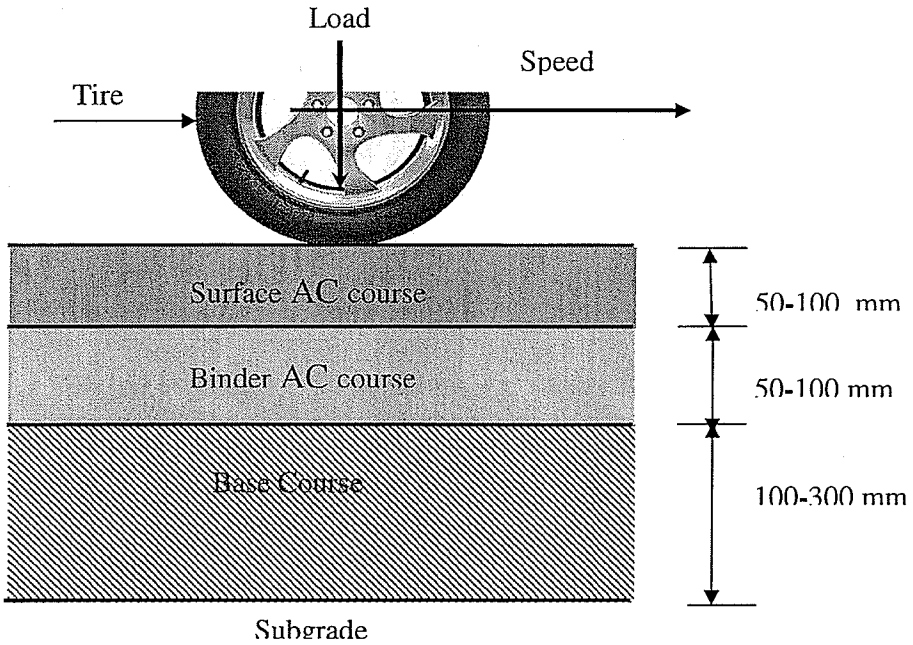

Figure 3.2: Typical cross section of asphalt pavement (not to scale).

The surface mixtures, denoted by S followed by a project number, contained crushed stone to meet the surface layer requirements. On the other hand, the binder mixtures, denoted by B followed by the project number, contained fine river gravel and may contain reclaimed asphalt pavement (RAP). Table 3.1 lists locations of pavement sections from which the loose aggregates and binders were collected and the field AC cores were extracted. Table 3.1 shows also whether the mixtures and cores from the surface course or the binder course. The samples were collected from Provincial Trunk Highways (PTH) and Provincial Roads (PR).

Table 3.1: Locations of pavement sections and source of the sampled materials

Highway	Project location	Construct-ion year	Materials			
			AC mixture		In-service AC	
			Surface course	Binder course	Surface course	Binder course
PTH[a] 8	PTH 68 Northerly	2004	S1	B1	S1	B1
PTH 20	PTH 20A Northerly	2004	S2	B2	S2	B2
PTH 18/ PTH 3	Killarney area	2004	S3	B3	S3	B3
PTH 83	Swan River by-pass	2004	S4	B4	--[b]	--
PTH 3	PTH 528 to PTH 31	2003/2004	--	--	S5	B5
PTH 83	Roblin Northerly	2003	--	--	--	B6
PTH 59	Seine river to Mondar road	2003	--	--	--	B7
PTH 3	West of Cartwright	2003	--	--	--	B8
PR[c] 248	PTH 2 to PTH 1	2002	--	--	--	B9
PTH 25	PR 259 to PTH 10	2002	--	--	--	B10
PTH 68	Poplar Field to Arborg	2002/2003	--	--	--	B11
PTH 8	PTH 17 to PR 229	2001	--	--	--	B12
PTH 5	Salt Creek to PTH 10	2001	--	--	--	B12
PTH 7	PR 231 to PTH 68	2001	--	--	--	B14

[a]Provincial Trunk Highway, [b] No material tested, and [c]Provincial road

These sites are a representative sample of AC mixtures selected in cooperation with MIT to characterize the asphalt concrete mixes used in Manitoba. Collecting the field samples and preparing the mixtures from the loose material were completed by MIT. The mechanical test program shown in Figure 3.1 was carried out in the Pavement Research Laboratory at the University of Manitoba. The loose aggregates and binders were sampled from materials specified for surface and binder courses of four projects constructed during 2004. The collected aggregates and the binders were stored in sealed containers until the day of preparation of test specimens.

The field AC cores were drilled through the whole depth of the bituminous layers from the 13 pavement sections immediately after construction. Thus, the cores were not exposed to damage from the traffic loads or from long-term aging. Twelve field AC cores were extracted from each pavement section in accordance with the test protocol of the LTPP project P07. The cores were taken from the between, outer and inner wheel paths. They were extracted using 150 mm diameter core drill with a water-soluble coolant. The field AC cores were put in plastic bags, wrapped with plastic sheets, and stored in freezers until testing to prevent the ambient effects on the core properties.

3.3 Properties of Sampled Aggregate and Binder

Eight mixtures, S1-S4 and B1-B4, were prepared in the laboratory by duplicating the proportions of the aggregates and the binders of the field mixtures. Table 3.2 lists properties of the sampled aggregates. B1 and B2 included RAP percentages of 15% and 46% respectively of the total weight of the aggregates but the shown gradations are for the

new aggregates only. The nominal maximum particle size (NMPS), according to SuperPave definition, is one sieve size larger than the first sieve to retain more than 10 percent. NMPS of all aggregates is 12.5 mm except for S4 and B2, NMPS is 19 mm and 9.5 mm respectively.

Table 3.2: Properties of the sampled loose aggregate

Mixture	Gradation							Specific Gravity	Water Absorption (%)
	Percent passing (%)								
	19 mm sieve	12.5 mm sieve	9.5 mm sieve	4.75 mm sieve	2 mm sieve	0.425 mm sieve	0.075 mm sieve		
S1	100	91.6	79.3	61.8	47.0	29.6	3.5	2.638	2.05
S2	100	90.2	79.0	61.9	49.0	26.9	3.6	2.667	0.93
S3	100	90.2	80.0	63.5	50.7	24.0	5.2	2.481	3.22
S4	100	86.7	77.3	61.8	49.6	28.9	3.7	2.66	1.16
B1, 15% RAP	100	94.4	86.3	71.9	53.0	25.5	4.1	2.634	1.62
B2, 46% RAP	100	96.0	91.9	77.1	60.3	34.4	6.9	2.652	1.58
B3	100	91.9	88.3	77.5	61.6	25.6	5.0	2.457	3.50
B4	100	93.2	85.6	69.9	56.8	30.7	4.2	2.642	1.01

Figures 3.3 and 3.4 show aggregate gradations plotted on the 0.45-power chart where the gradation charts are grouped by the aggregate type and NMPS. The mixtures were classified as fine-graded based on location of the gradation curves with respect to the maximum density line (MDL) of the 0.45-power chart. The gradations of fine-graded mixtures fall above MDL while those of the coarse-graded mixtures typically fall below MDL.

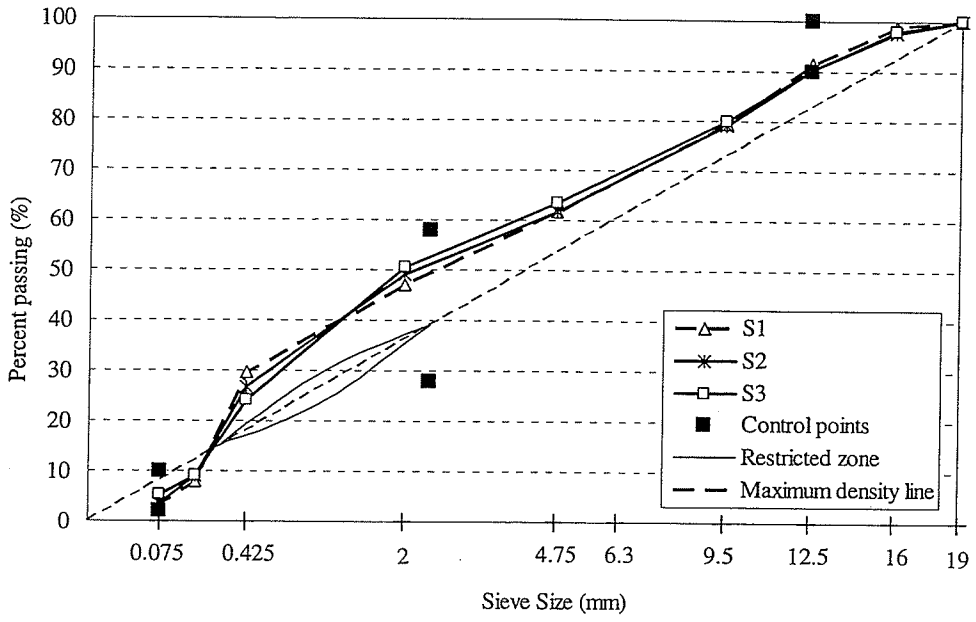

(a) S1-S3, nominal max particle size of 12.5 mm

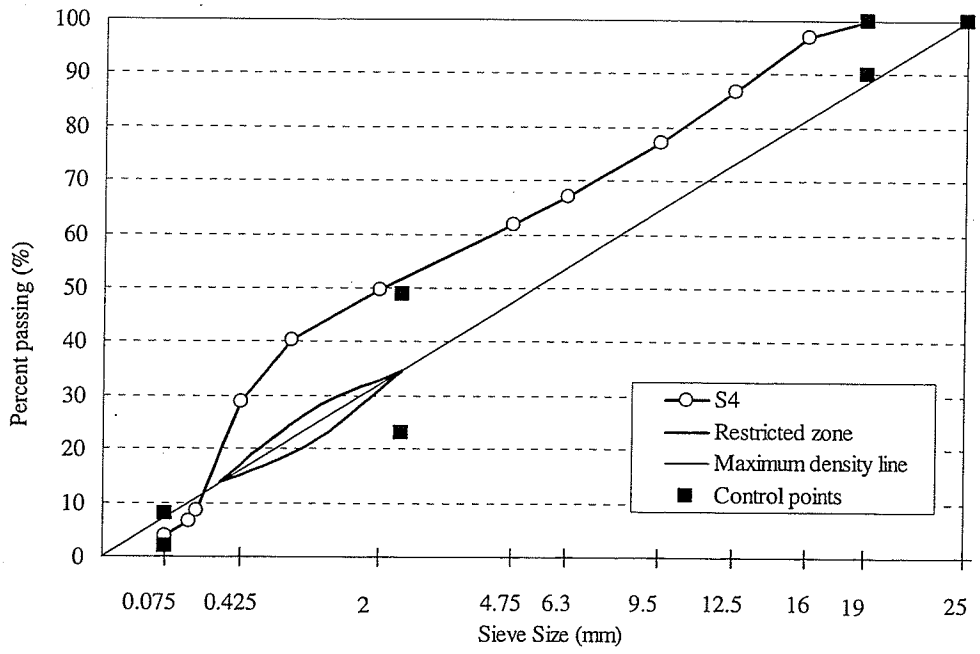

(b) S4, nominal max particle size of 19 mm

Figure 3.3: Aggregate gradation of surface mixtures

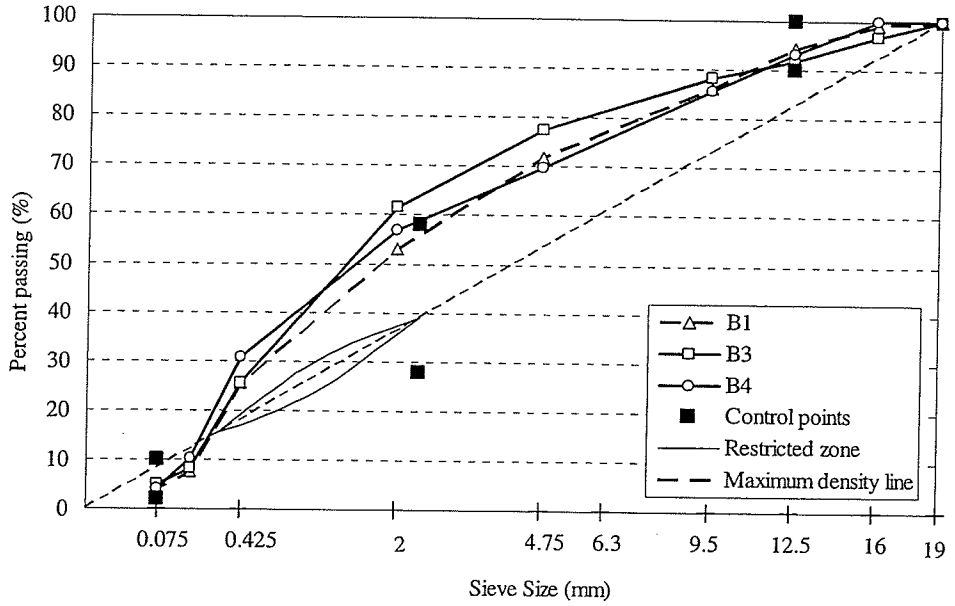

(a) B1, B3 and B4, nominal max particle size of 12.5 mm

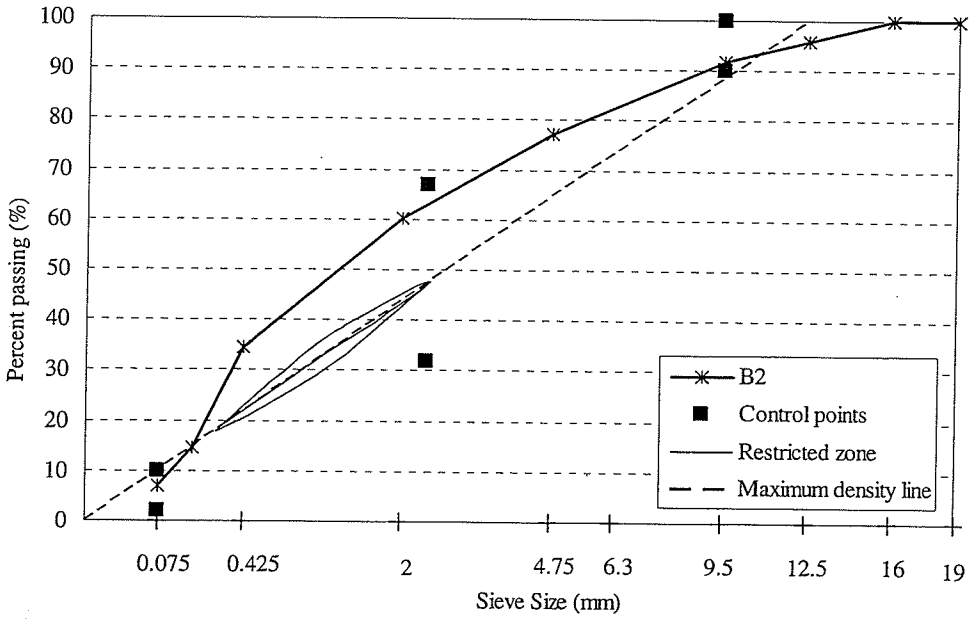

(b) B2, nominal max particle size of 9.5 mm

Figure 3.4: Aggregate gradation of binder mixtures

Table 3.3 lists performance grades (PG) of the binders and the average binder contents of the field mixtures. For mixtures that contain RAP, PG is for the unaged binders and the binder content is the sum of the contents of RAP binder (aged binder) and the unaged binders, which serve as a rejuvenator. The dynamic shear modulus ($|G^*|$) and the phase angle (δ) of the binders were obtained from published work (Shalaby, 2002) and were used, herein, to determine coefficients of the viscosity-temperature relationship (A and VTS). $|G^*|$ and δ were measured by the dynamic shear rheometer (DSR) test at a temperature range of 7°C to 70°C and a natural frequency (ω) of 10 rad/sec. Appendix A lists $|G^*|$ and δ.

Table 3.3: Binder performance grade and content of the laboratory prepared mixtures

Mixture	Performance grade (PG)	Binder content (%)
S1	58-28	5.5
S2	58-28	5.3
S3	52-28	6.5
S4	58-34	5.7
B1	52-34[a]	5.0[b]
B2	52-34[a]	5.0[b]
B3	52-28	6.2
B4	58-34	5.0

[a] added binder (rejuvenator)
[b] asphalt content including the aged RAP binder

3.4 Preparation of Test Specimens

3.4.1 Laboratory Compacted Specimens

The laboratory compacted specimens consists of those subjected to the axial compression $|E^*|$ test and the indirect tensile M_R and $|E^*|$ tests. All laboratory prepared mixtures, S1-S4 and B1-B4, were tested under the axial compression $|E^*|$ test while B2-B4 of these mixtures were subjected to indirect tensile testing to determine M_R.

The axial compression $|E^*|$ test specimens were prepared in according to AASHTO TP62-03 test method "Determining Dynamic Modulus of Hot-Mix Asphalt Concrete Mixtures". The specimens were prepared as follows:

1. Mixing an amount of aggregates and binder that is enough for one sample. The mix proportions are equal to those of the field mixture. The mixing temperature is 135°C.
2. Aging the mix for two hours in accordance with short-term oven aging procedure. The aging time is defined based on Manitoba practice considering the weather during the construction season and grade of the binder where Manitoba utilizes soft binder.
3. Compacting the mix with a gyratory compactor to obtain a 170 mm height specimen. The design number of gyrations (N_{des}) is 100 for S3 and B3 and 75 for the remaining mixtures.
4. Repeating steps 1 to 3 to generate three gyratory specimens. Table 3.4 lists the average volumetric properties of the gyratory samples prepared from each mixture. Figure 3.5 shows the densification curves of each mixture obtained during the compaction.

5. Extracting the test specimens from the centre of the gyratory specimens. First, core a 100 mm diameter specimens from the middle of the gyratory specimen and then cut equal amounts of the ends to obtain the test specimens with the nominal 150 mm height.

6. Checking the ends of the test specimens. The waviness height was checked for the target 0.05 mm using a feeler gauge and a straight edge. The specimen ends were checked to be perpendicular to the axis of the specimen with a mechanist square and feeler gauge.

7. Each test specimen was instrumented with three transducers to measure the axial deformation between gauge points 100 mm apart.

Table 3.4: Volumetric properties of the gyratory

Mixture	MTSG	Asphalt content (Ac) (%)	Asphalt Absorp. (%)	Bulk Density (kg/m3)	Air Voids (%)	VMA (%)	VFA (%)	P^a_{be} (%)
S1	2.504	5.5	0.75	2392	4.5	15.0	70.2	4.8
S2	2.505	5.3	1.07	2383	4.9	14.2	65.8	4.3
S3	2.394	6.5	2.21	2282	4.7	13.6	65.6	4.4
S4	2.480	5.7	0.54	2340	5.7	16.8	66.3	5.2
B1	2.512	5.0	0.81	2391	4.8	14.1	65.9	4.2
B2	2.513	5.0	1.07	2337	7.0	15.5	55.0	4
B3	2.342	6.2	1.44	2114	9.7	19.0	48.7	4.9
B4	2.494	5.0	0.65	2263	9.3	18.4	49.6	4.4

[a]P_{be} is the effective binder content (by weight)

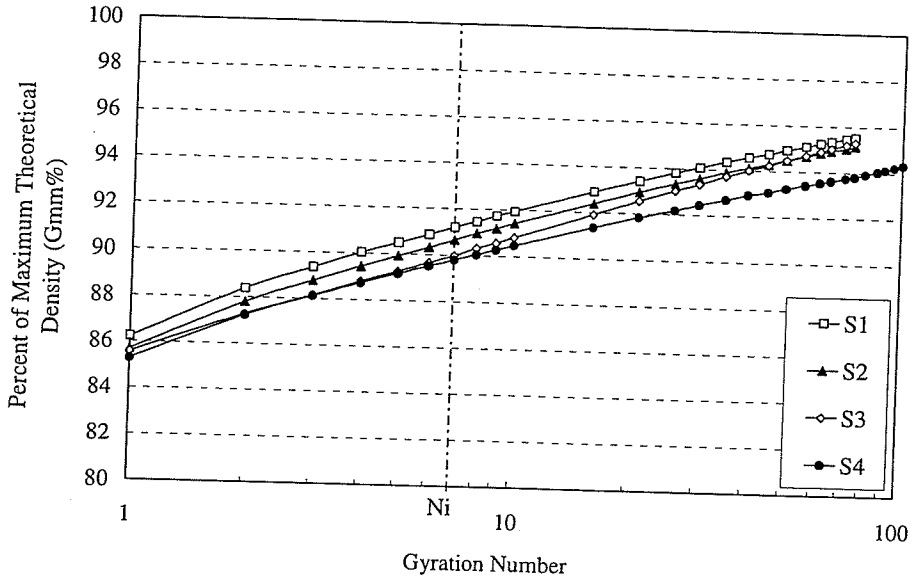

(a)

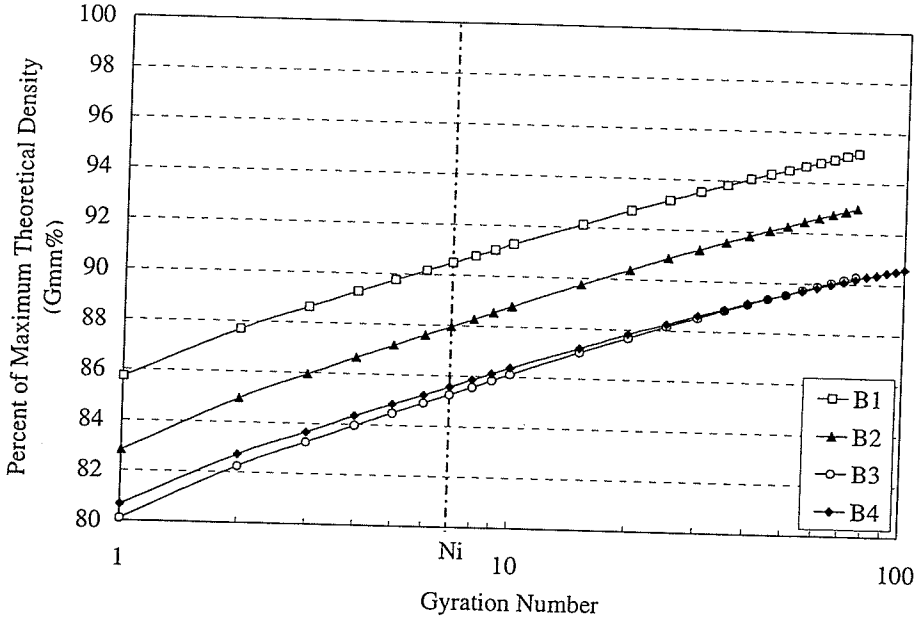

(b)

Figure 3.5: Percent of maximum theoretical density versus gyrations

(a) Surface mixtures, S1-S4; (b)Binder mixtures, B1-B4

The indirect tensile specimens were prepared from B2-B4 with the gyratory compactor by following the steps 1 to 4 from the procedure of preparing the axial compression test specimens. Three gyratory specimens with 120 mm height were prepared from each mixture. Each gyratory specimen was sawed into two test specimens of 51 mm thick. Table 3.5 lists properties of the gyratory specimens made from B2-B4 for indirect tensile test specimens. Comparing Table 3.5 and Table 3.4 for B2-B4, the density of the gyratory specimens that have 170 mm height is slightly higher (up to 4% difference) than for the ones that have 120 mm height since the density depends on the compaction effort per unit of volume.

Table 3.5: Properties of indirect tensile test specimens

Mixture	asphalt content (%)	Density (kg/m^3)	MTSG[a]	Air voids (%)
B2	5.0	2387	2.515	5.1
B3	6.2	2137	2.368	9.8
B4	5.0	2346	2.496	6.0

[a]Maximum Theoretical Specific Gravity

3.4.2 Field Compacted AC cores

The stored twelve whole field AC cores were split to layers to extract the test cores from the surface and binder courses. The test cores were prepared in accordance with the test protocol of the LTPP Project P07. Only three test cores from each layer were tested in the thesis test program. The other nine test cores were used to determine the indirect tension

strength of the material, to perform the volumetric analysis, and other three to substitute the damaged cores during the tests. Table 3.6 lists the properties of the test cores measured immediately after cutting. The properties consist of core height, bulk density, maximum theoretical specific gravity (MTSG) and in-place air voids.

Table 3.6: Properties of test AC cores

Mixt-ure	RAP %	Core height (mm)		In-place air voids (%)		Density (kg/m^3)		MTSG[b]
		Average	St. dev.[a]	Average	St. dev.	Average	St. dev.	
S1	None	35	0	6.1	1.5	2346	37	2.497
S2	None	40	5	3.9	1.2	2392	30	2.489
S3	None	43	3	10.5	1.0	2127	23	2.376
S5	None	39	2	4.9	0.5	2267	13	2.385
B1	15	40	5	6.7	0.4	2344	11	2.513
B2	46	31	4	9.3	2.1	2282	54	2.516
B3	None	44	3	11.8	1.7	2097	39	2.378
B5	26	44	7	9.8	1.2	2108	27	2.336
B6	None	50	7	7.7	0.3	2291	8	2.481
B7	None	45	6	10.3	0.4	2243	8	2.502
B8	None	43	5	10.4	2.7	2142	64	2.389
B9	None	48	4	8.1	1.5	2293	38	2.495
B10	None	34	7	9.5	1.3	2212	33	2.443
B11	None	53	3	10.1	0.5	2256	12	2.509
B12	57	40	5	5.5	2.0	2374	51	2.512
B13	46	40	4	9.3	1.7	2283	42	2.517
B14	25	44	3	7.5	2.0	2334	50	2.524

[a]Standard deviation
[b]Maximum Theoretical Specific Gravity

The percents of RAP, if present, are known from history of the field mixes. The test cores have thicknesses in the range of 31 mm to 53 mm, which meets the LTPP P07 required

range of 25 to 51 mm. The bitumen extraction was performed after completing the mechanical tests carried on the test cores as shown by Figure 3.1. Table 3.7 lists the binder contents and rheology of the extracted binder and Figure 3.5 illustrates the gradations of the recovered aggregates. The recovered aggregates of all mixtures have NMPS of 12.5 mm.

Table 3.7: Properties of the extracted binders from the field AC cores

Mixture	Asphalt Content (%)	Absolute Viscosity (Pa.s)	Kinematic Viscosity (centistokes)	Penetration (25°C, 0.1 mm)
S1	5.18	137.0	348	116
S2	5.12	202.4	401	88
S3	5.98	153.4	350	101
S5	6.05	273.9	480	73
B1	4.95	152.8	344	107
B2	5.32	335.6	451	61
B3	5.86	170.4	363	98
B5	6.14	472.4	589	57
B6	5.71	270.2	462	72
B7	5.33	240.7	412	75
B8	5.43	240.6	449	77
B9	5.37	235.4	398	75
B10	5.24	214.2	391	81
B11	4.92	262.6	430	73
B12	4.99	268.2	410	63
B13	4.49	333.3	431	59
B14	4.79	249.4	402	75

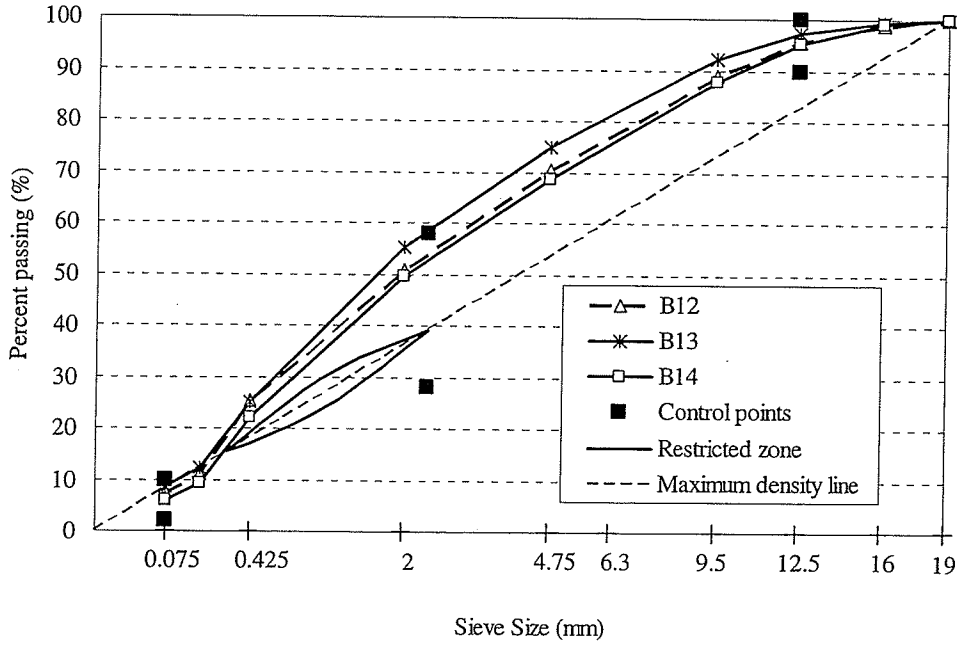

Figure 3.6: (a) Gradations of aggregate recovered from B12-B14

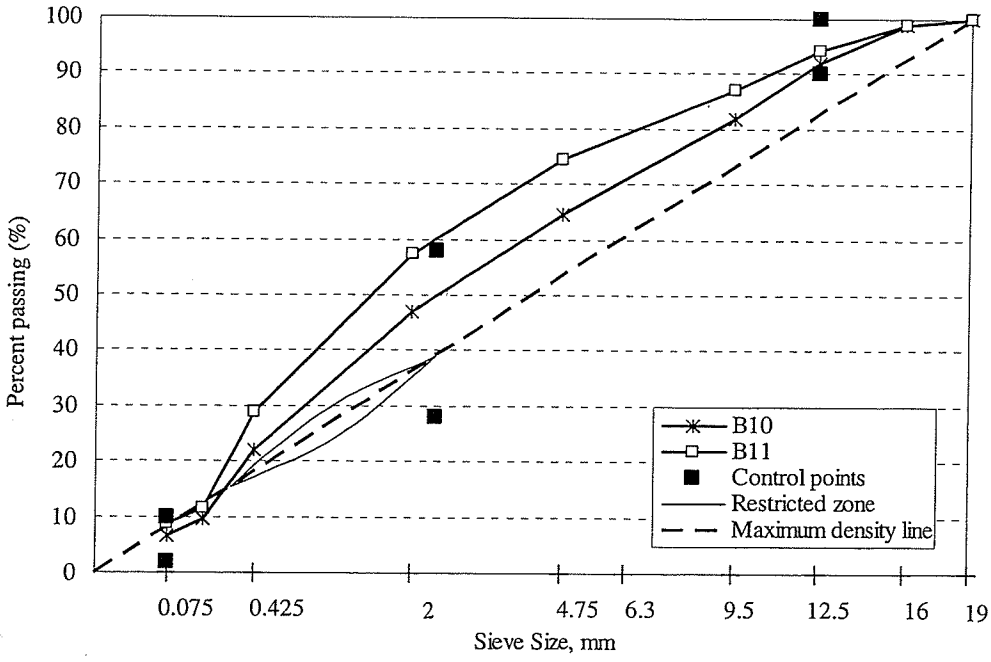

Figure 3.6: (b) Gradations of aggregate recovered from B10 and B11

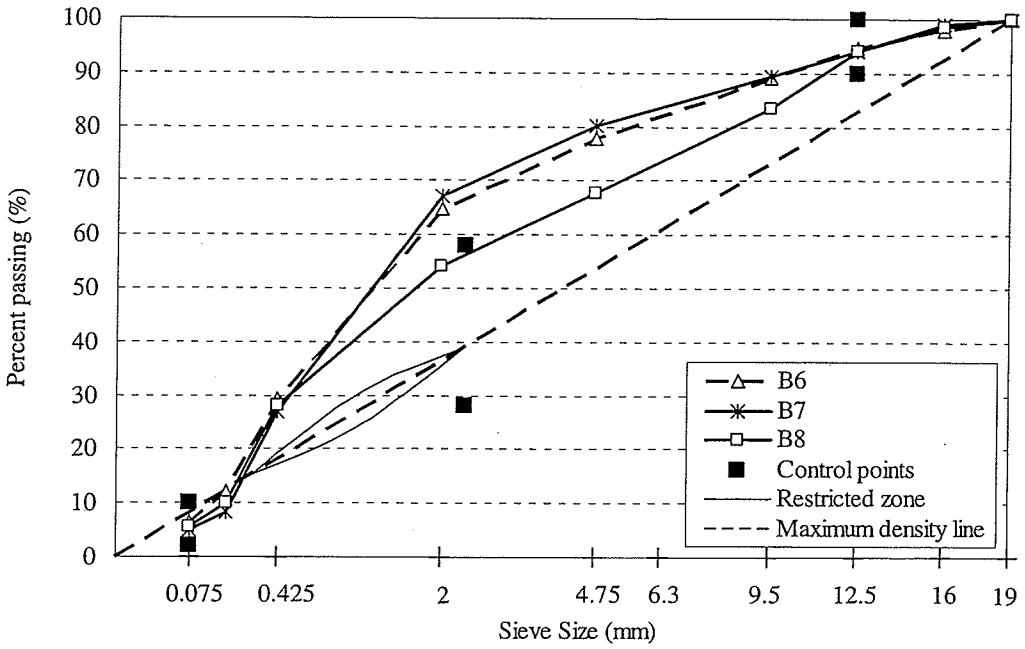

Figure 3.6: (c) Gradations of aggregate recovered from B6 and B8

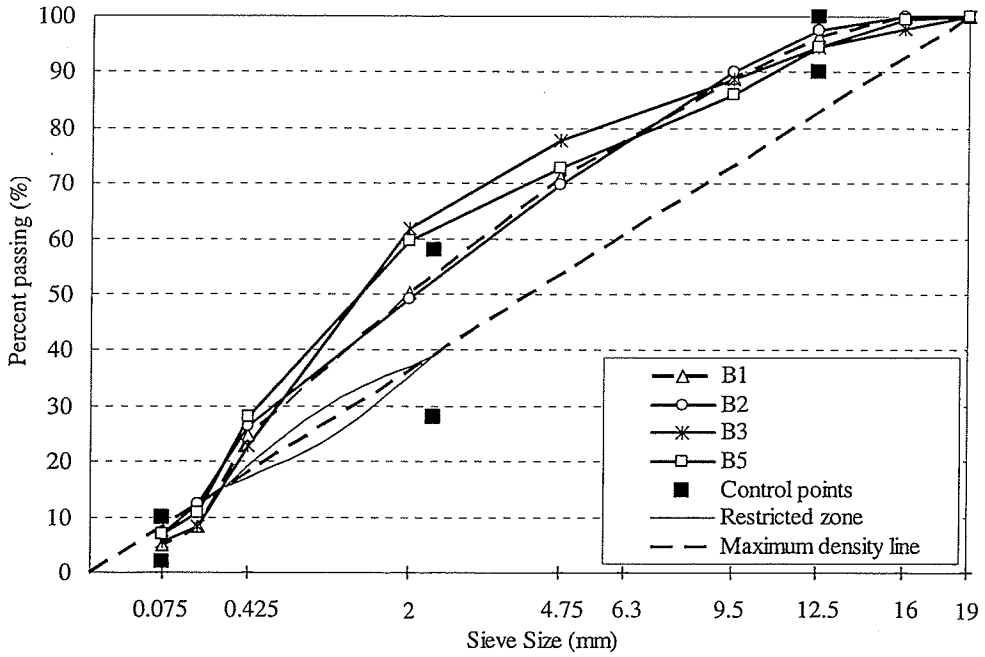

Figure 3.6: (d) Gradations of aggregate recovered from B1, B2, B3 and B5

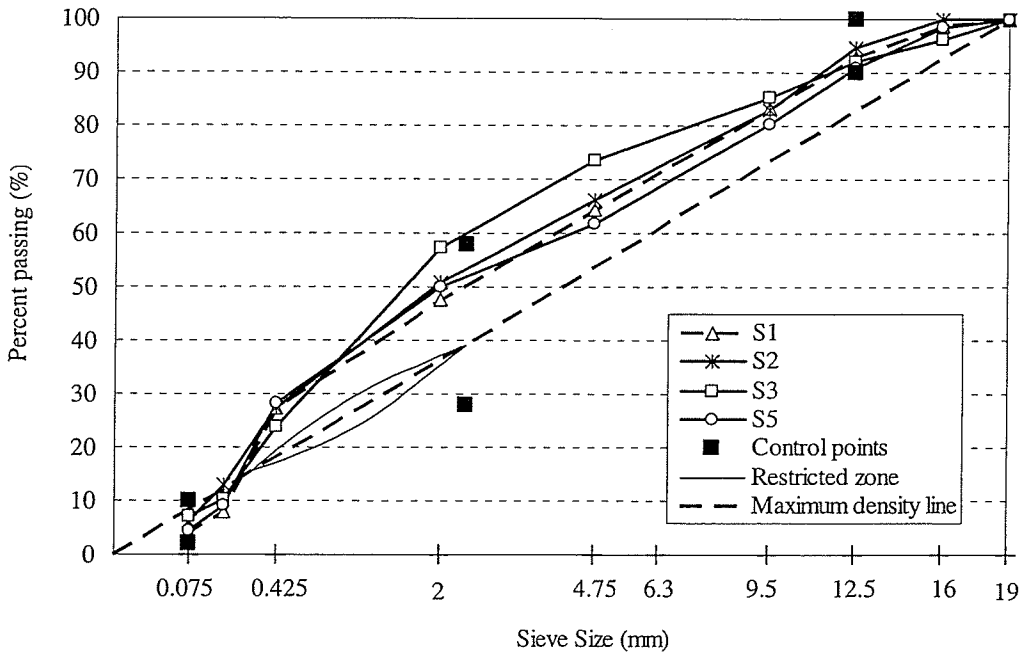

Figure 3.6: (e) Gradations of aggregate recovered from S1, S2, S3 and S5

3.5 Test Setup

Figure 3.7 shows the test setup used to carry out the test program including axial compression and indirect tensile testing. It consists of the following equipment and instruments:

a. A closed-loop servo-hydraulic testing machine. The capacity of the loading frame is 25 kN. The machine is capable of applying cyclic and static loads and can be adjusted to work under load or deformation control modes.

b. Load cell to measure the applied load, the cell was mounted on the stroke bar to measure the applied load.

c. Deformation measuring systems: two systems were calibrated and used in the test

program.

i. Linear Variable Displacement Transducer (LVDT), model Trans-TEK 0350-0010 with mechanical travel 3.5 mm (0.14 in) and internal carrier frequency greater than 1300 HZ.

ii. Extensometers with a 0.5 mm mechanical travel, model Epsilon 3910, with 4 inch axial conversion.

d. Controller to generate the loading waveform.

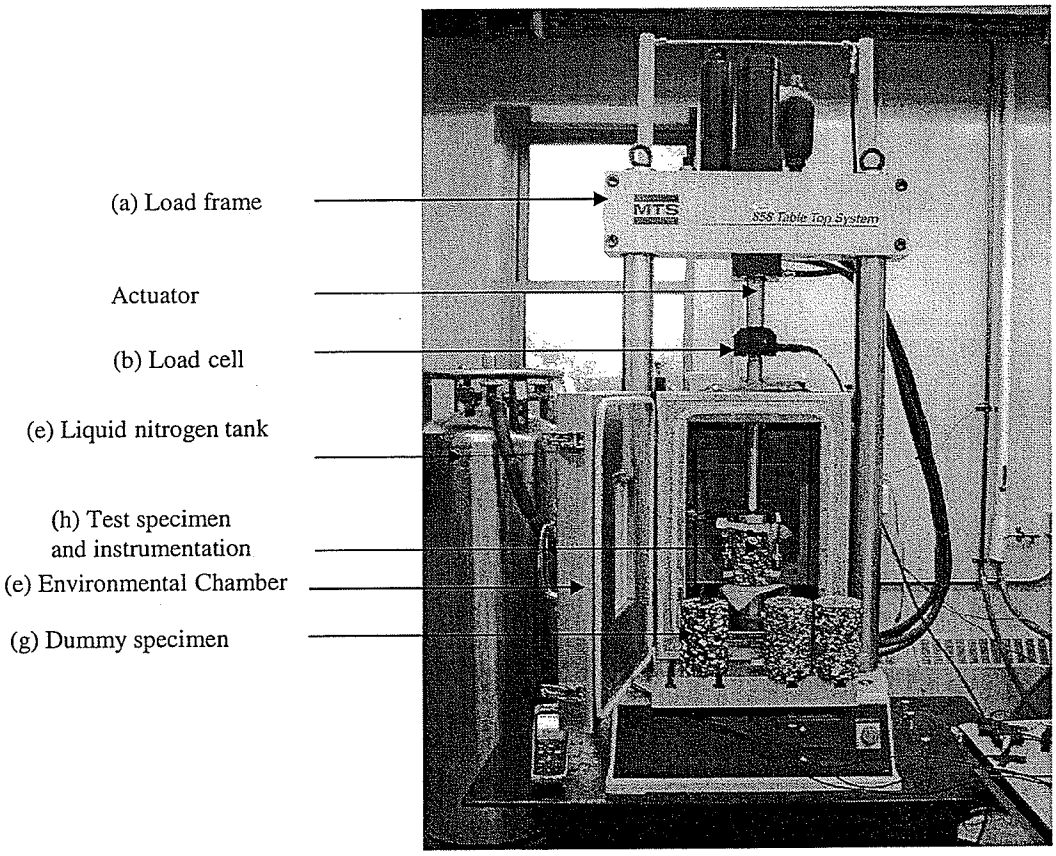

Figure 3.7: Test setup of the laboratory testing

d. Environmental chamber to condition and control the test specimens at the desired test temperatures. The chamber uses liquid nitrogen to condition the specimens at temperatures less than the room temperature, while high temperatures are generated by an electrical heating element.

e. Data acquisition system (DAQ) to capture the applied load and the specimen deformations. Nine data channels were acquired at a time consisting load, stroke bar movement, four extensometers and three LVDTs.

f. A dummy specimen with a thermocouple embedded in its middle to monitor the equilibrium temperature of the test specimens. The dummy specimen has dimensions equal to the dimensions of the $|E^*|$ specimens.

g. Loading plates: in the axial compression $|E^*|$ test, the load was transmitted via two circular plates to the specimen while, in IDT testing, the load was transmitted to the specimen with two 38 mm wide curved plates with curvature of 150 mm.

3.6 Specimen Instrumentation

Two specimen instrumentation methods were used in the test program for the axial compression $|E^*|$ testing and IDT testing. Figure 3.8 shows the instrumentation of the axial compression $|E^*|$ test specimen. The axial deformations were measured with LVDTs or extensometers at three locations on the specimen surface located 120° apart. The axial deformations were measured between gauge points glued to the specimen and located vertically at both ends of a gauge length (L_g) of 100 mm. LVDTs were mounted onto the gauge points with screws but the extensometers were mounted using a magnetic base.

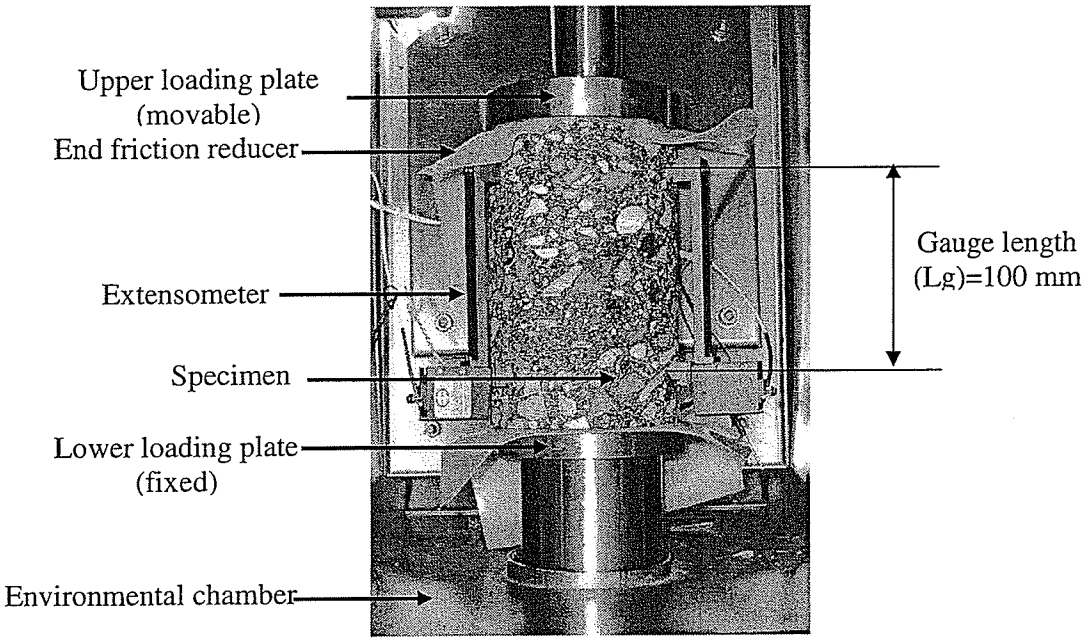

a)

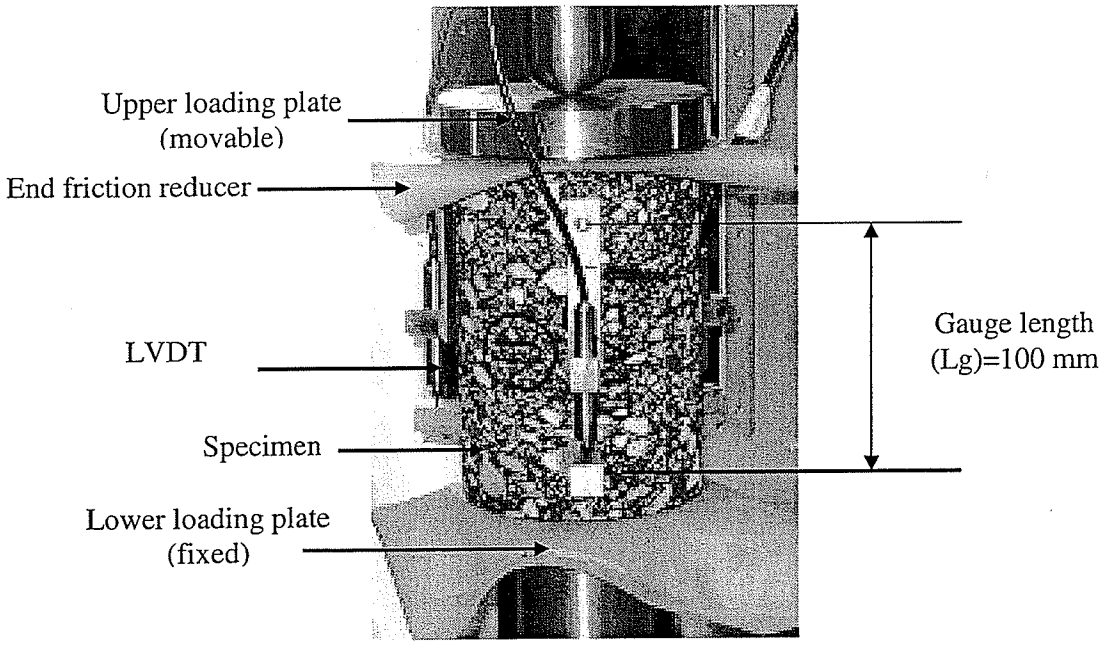

Figure 3.8: Specimen and instrumentation of the dynamic modulus test

(a) Extensometers, and (b)LVDTs

An end friction reducer (EFR) was used between the specimen and the circular loading plates. EFR consisted of two latex sheets filled with silicone grease. $|E^*|$ and ϕ measured using LVDTs and extensometers were compared, the results were documented in Appendix B. There was no significant difference between $|E^*|$ and ϕ obtained with the two instrumentations of the axial $|E^*|$ test. On the other hand, Figure 3.9 presents the specimen instrumentation of the IDT testing to measure M_R and the indirect tensile $|E^*|$. The load was transmitted to the specimen along the diameter via curved strips. The deformations were measured using four extensometers mounted on gauge points located 38 mm apart on the horizontal and vertical axis of the two specimen ends.

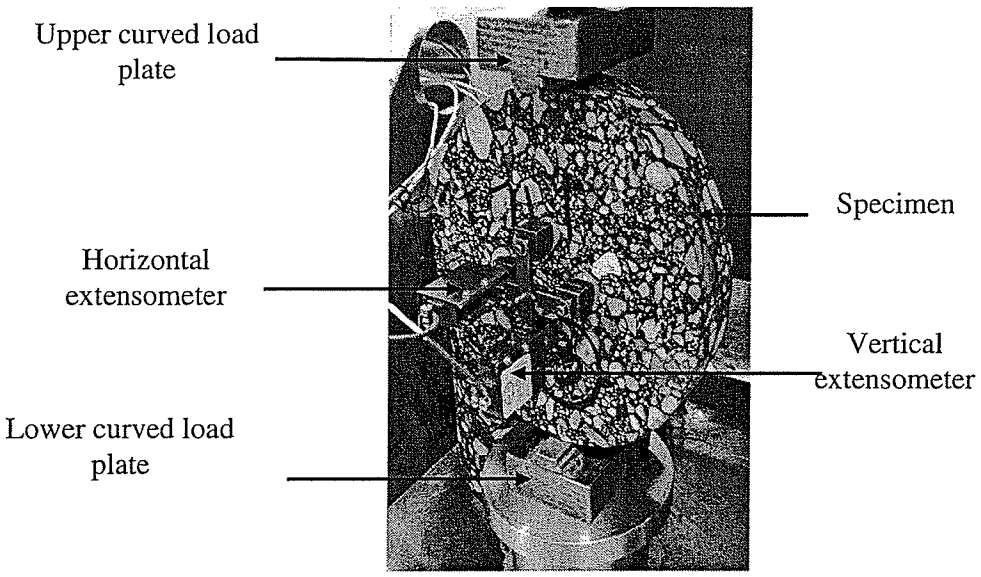

Figure 3.9: specimen and instrumentation of the indirect tensile testing

3.7 Procedure of Dynamic Modulus Test

The $|E^*|$ test was carried out in accordance with AASHTO TP 62-03 at four temperatures, -10, 5, 25 and 40°C, and six loading frequencies, 25, 10, 5, 1, 0.5 and 0.1 Hz, at each temperature. The tests proceeded from low to high temperature. At a given temperature, the testing began with high loading frequency and proceeded to low loading frequency. At each combination of temperature and frequency, the specimen was subjected to cyclic sinusoidal loads at a stress level adjusted to maintain axial resilient deformation within a range of 50 to 150 microstrains. The cumulative permanent deformation should not exceed 1500 microstrains at the end of a frequency sweep test at each temperature. The test procedure was as follows:

a. Conditioning the instrumented specimens in the environmental chamber at the given temperature. The temperature inside of the specimens was checked with the dummy specimen and the thermocouple.
b. Adjusting the LVDT to near the end of its linear range to allow the full range to be available for the accumulation of compressive permanent deformation.
c. Applying a contact load of 5 % of the cyclic load.
d. Adjusting and balancing the electronic measuring system as necessary.
e. At each temperature, the specimen is preconditioned first with 200 cycles at 25 Hz. Then specimen is loaded as specified in Table 3.8.
f. At each temperature, the test was carried at the highest frequency (25 Hz) and then proceeded to the lowest frequency (0.1 Hz).
g. Allowing at least 2 minutes rest period between testing between each of two

subsequent frequencies but not exceeding 30 minutes.

h. Repeating the test at the higher temperature with the same procedures a-g above.

Table 3.8: Number of applied load cycles at each test frequency

Frequency (Hz)	Number of Cycles
25	200
10	200
5	100
1	20
0.5	15
0.1	15

3.8 Test Measurements

The load- and deformation- time history of $|E^*|$ testing was collected in arrays consisting of the time, load, actuator position and the axial deformations at three positions. Table 3.9 lists the sampling rate of the collected data of $|E^*|$ test. The last five load cycles of each test were processed to determine the $|E^*|$ and ϕ. Figures 3.10 and 3.11 present a sample of the applied load and the resulting deformation at one transducer obtained at low and high temperatures, respectively.

Table 3.9: Data sampling rate of the dynamic modulus test

Frequency (Hz)	Sampling Rate (point/sec)
25, 10	1000
5, 1	500
0.5, 0.1	250

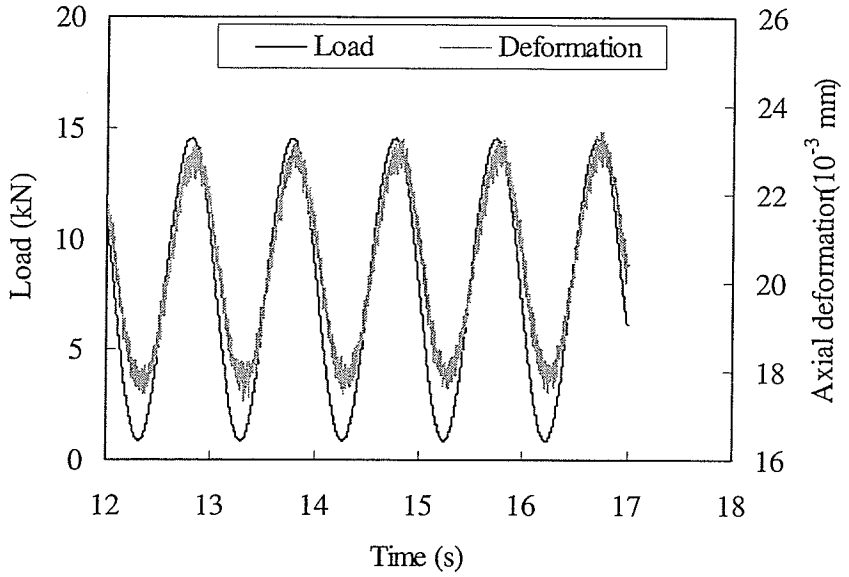

Figure 3.10: Typical load and deformation at low temperature (-10°C)

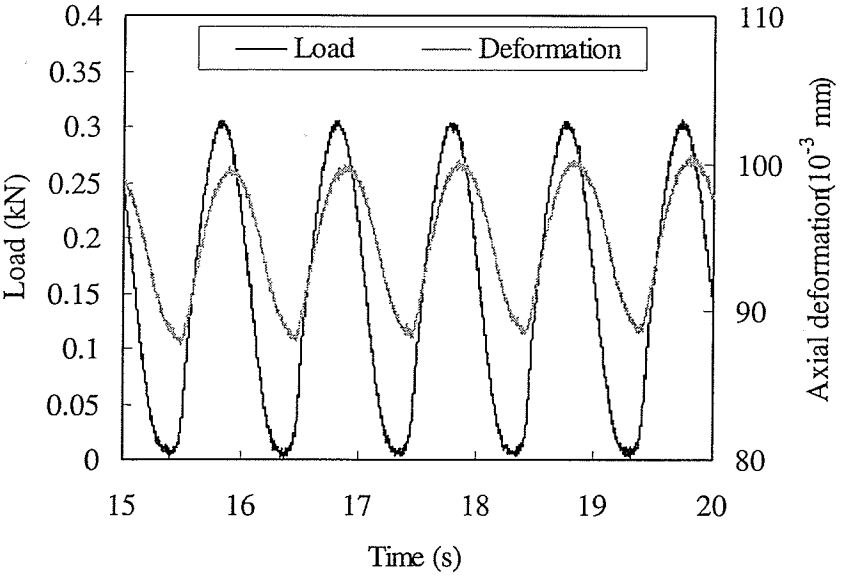

Figure 3.11: Typical load and deformation at high temperature (40°C)

The regression technique was used to smooth the measured data. Equations 3.1 and 3.2 were used to fit the load and deformation data, respectively.

$$P = P_0 + P_1 t + P_2 \cos(2\pi f t + \phi_P) \tag{3.1}$$

$$D = D_0 + D_1 t + D_2 \cos(2\pi f t + \phi_D) \tag{3.2}$$

where:

P and D = load and deformation respectively

t and f = time (s) and frequency (Hz).

$P_0, P_1, P_2, D_0, D_1, D_2, \phi_P, \phi_D$ = regression constants.

The cyclic stress applied on a specimen is obtained from Equation 3.3.

$$\hat{\sigma} = \frac{2P_2}{A} \tag{3.3}$$

where

A = cross section area of the specimen.

The recoverable strain at each transducer is obtained from Equation 3.4.

$$\hat{\varepsilon} = \frac{2D_2}{L_g} \tag{3.4}$$

$|E^*|$ at a transducer is calculated from the stress and strain by applying Equation 2.11 and ϕ is calculated using Equation 3.5.

$$\phi = \frac{\phi_D - \phi_P}{\pi} \times 180 \tag{3.5}$$

Appendix C consists of the following test results at each combination of temperature and frequency:

- peak stress of each specimen,

- strain, $|E^*|$ and ϕ at each transducer on the test specimen
- $|E^*|$ and ϕ of each test specimen
- $|E^*|$ and ϕ of the mixture, the average, standard deviation and coefficient of variation of the three LVDT/Extensometer positions (within the specimen) and those of the three replicates.

3.9 Indirect Tensile Testing

Laboratory and field compacted specimens were tested in the indirect tensile mode to determine M_R and $|E^*|$. The laboratory compacted specimens of B2-B4 and the field AC cores except B2 and B3 were subjected to M_R and 100 s creep compliance tests in accordance with the LTPP project P07. The tests were performed at -10, 5, 25 and 40°C proceeding from lower to higher temperatures. The M_R was measured by applying 0.1s haversine pulse load followed by 0.9 s rest period, as shown in Figure 2.11. The test sequence for the laboratory compacted specimen is as follows:

1. At -10°C, creep compliance,
2. At 5°C, resilient modulus followed by creep compliance,
3. At 25°C, resilient modulus followed by creep compliance, and
4. At 40°C, resilient modulus.

In chapter 6, an approach is introduced to predict $|E^*|$ from M_R.

The laboratory compacted B2 and B3 were subjected to further testing to determine indirect tensile $|E^*|$ at temperatures 5, 25 and 40°C and eight loading frequencies, 25, 10,

5, 1, 0.5, 0.1, 0.05 and 0.01 Hz, at each temperature. The Poisson's ratio calculated from M_R measurements showed that specimens behave in the linear stage where the frequency is less than 0.5. The field AC cores of B2 and B3 were subjected at 5, 25, 40°C to determine the M_R and then determine the $|E^*|$ at 25, 10, 1, 0.1, 0.01 Hz. A rest period of at least 2 minute was applied between two subsequent tests. The cyclic load was adjusted to maintain horizontal displacements between the gauge points to be less than 0.038 mm.

A Matlab code was developed based on an algorithm presented in LTPP P07 protocol "Test Method for Determining the Creep Compliance, Resilient Modulus and Strength of Asphalt Materials Using the Indirect Tensile Test Device". The raw data was processed using this code to obtain the instantaneous and total displacements, which were used to obtain instantaneous and total M_R and the Poisson Ratio.

4 Dynamic Modulus of Asphalt Concrete: Test Methods and Prediction Models

4.1 Introduction

Laboratory testing and predictive models are the two methods of determining $|E^*|$ of asphalt concrete. The aim of this chapter is to evaluate these methods for asphalt mixtures containing local aggregates and soft asphalt binders such as ones used in Manitoba, Canada and similar cold regions. $|E^*|$ and ϕ are evaluated in terms of the variability. The shifting methods for developing $|E^*|$ master curve from the measured $|E^*|$ are compared. The prediction accuracy of the Witczak $|E^*|$ model was assessed and the impact on the predicted pavement performance was examined.

4.2 Variability of Laboratory Measured Complex Modulus

The variability was measured with the standard error (S_e) calculated from between specimen and within specimen variabilities, Equation (2.20). Figures 4.1 and 4.2 show the average of S_e at each temperature calculated at the six loading frequency. Generally, the variability is more pronounced in $|E^*|$ than in ϕ especially at high service temperatures. The acceptance level of S_e of $|E^*|$ and ϕ is defined by AASHTO TP62-03 to be 15%. $|E^*|$ and ϕ of the mixtures except of those of B1 and B2 have limit of accuracy less than the acceptance level. $|E^*|$ of B1 and B2 has limits of accuracy that is slightly higher than 15 % at -10, 5°C. B1 and B2 contain high ratio of RAP and that may have increased the variability of $|E^*|$.

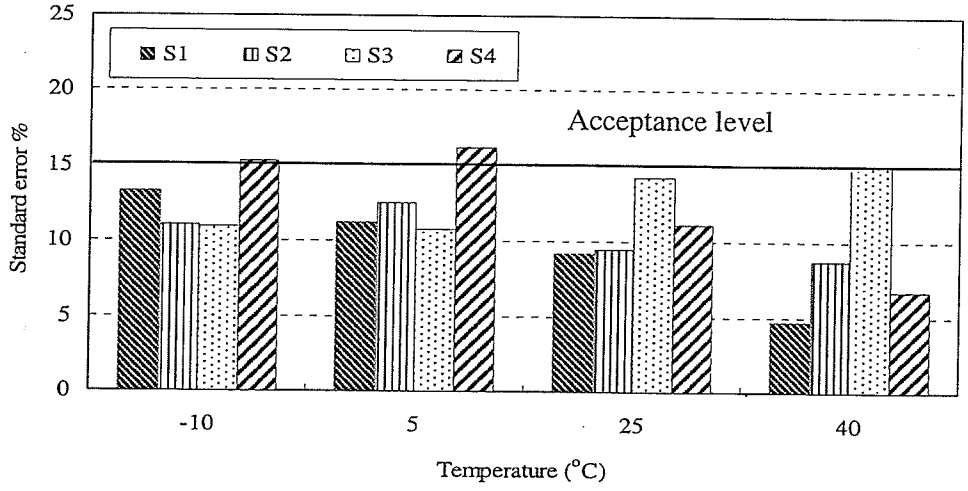

(a)

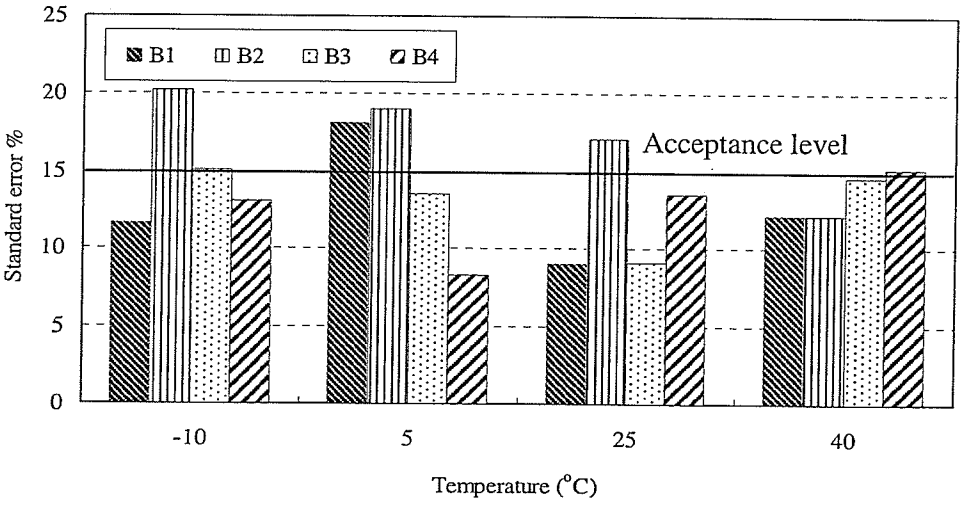

(b)

Figure 4.1: Standard error (S_e) of $|E^*|$ within mixtures

(a) S1-S4. (b) B1-B4

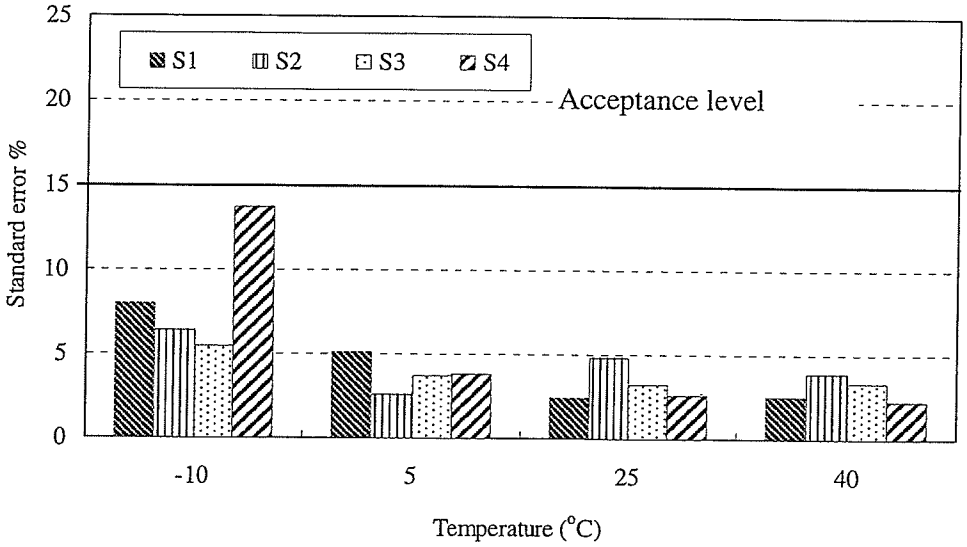

(a)

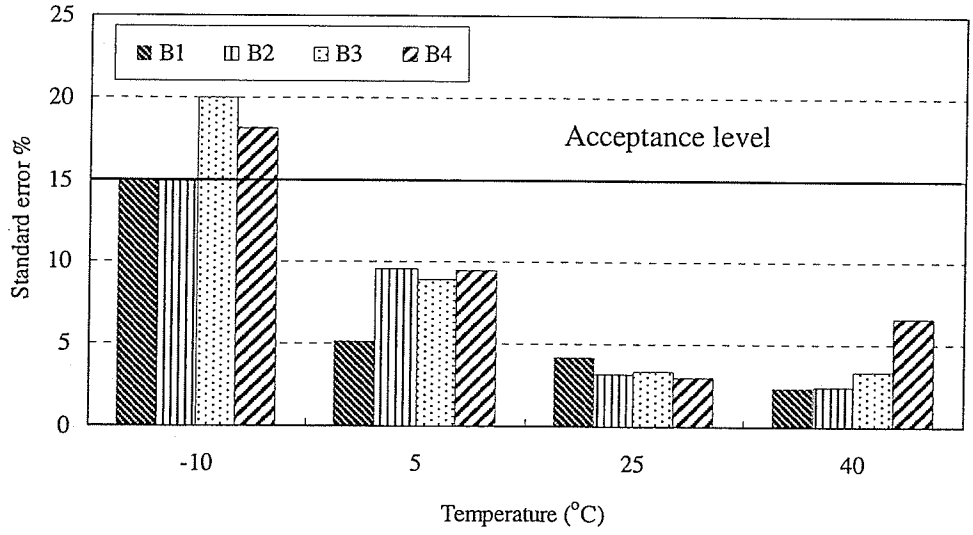

(b)

Figure 4.2: Standard error (S_e) of the phase angle within mixtures

(a)S1-S4. (b) B1-B4

Figure 4.3 shows the effect of test temperature on the variability in term of S_e of $|E^*|$ and ϕ between mixtures. S_e decreases with temperature and its decrease is more prominent in S_e of ϕ than in S_e of $|E^*|$. In addition to the variability in the measured data, the consistency of $|E^*|$ test data can be used to examine the data quality. Figures 4.4 and 4.5 show consistency of $|E^*|$ and ϕ illustrated by the complex plane (Cole-Cole) and the black space as explained in section 2.5.3.

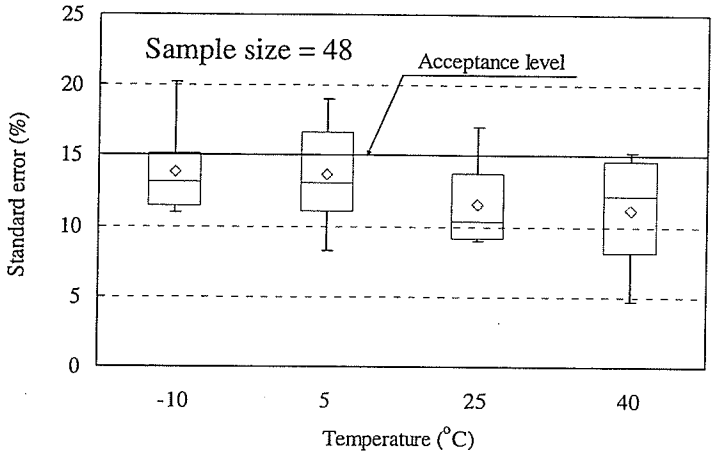

(a)

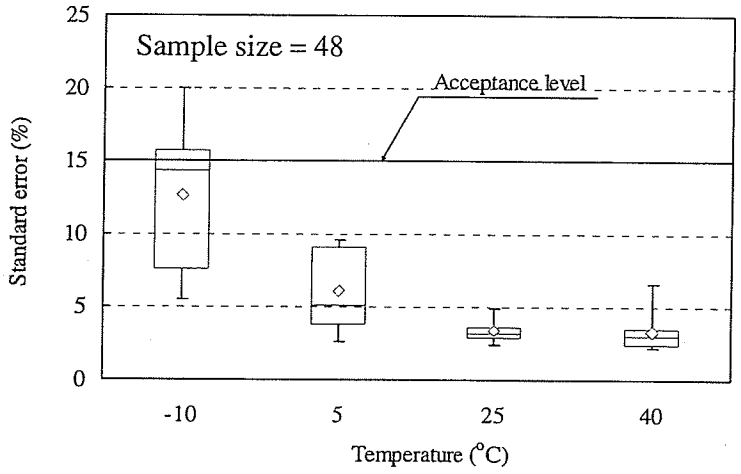

(b)

Figure 4.3: Standard error of measured $|E^*|$ and ϕ between mixtures at each temperature.

(a)Dynamic modulus. (b) Phase angle

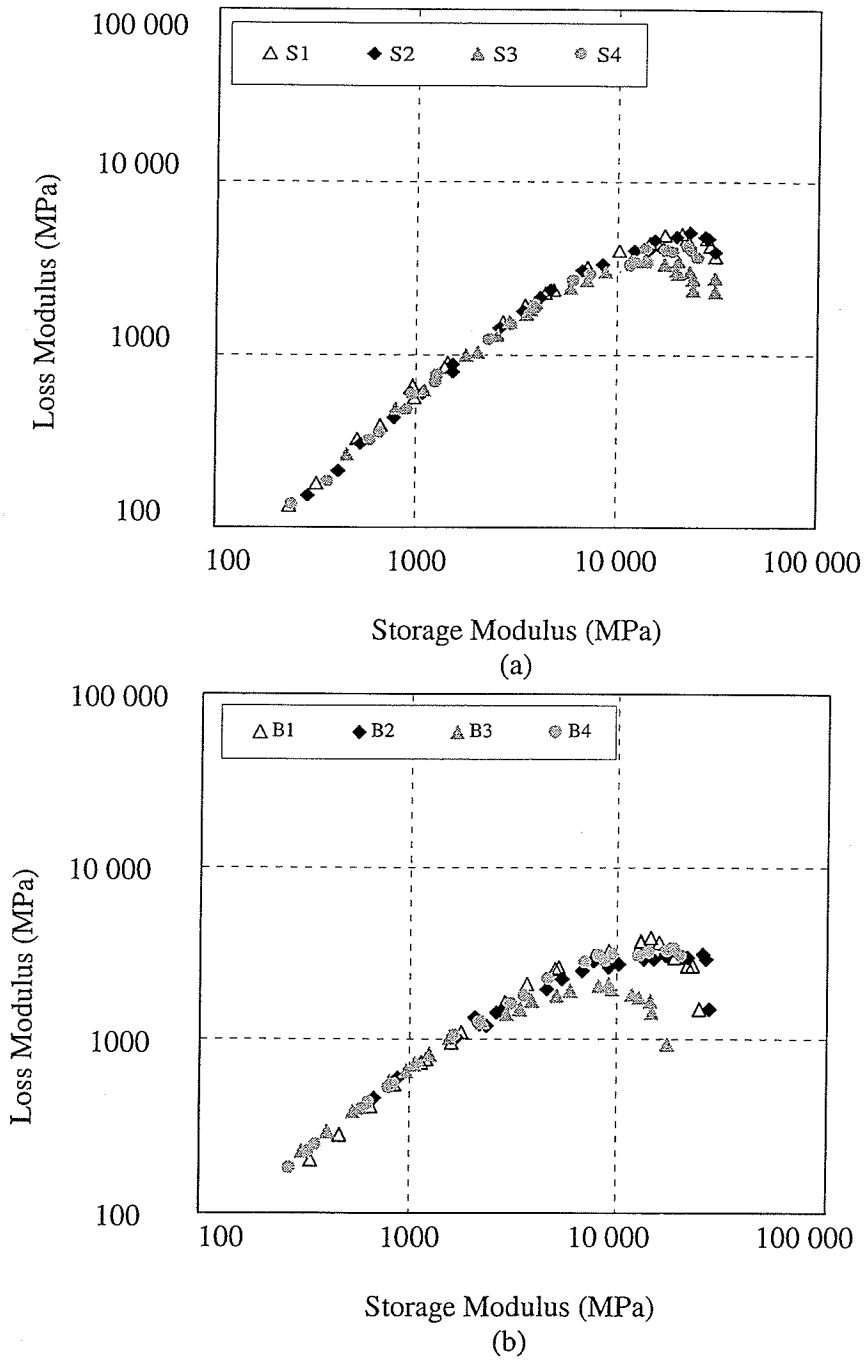

Figure 4.4: Complex plane, loss modulus versus the storage modulus

(a) Surface mixtures, (b) Binder mixtures

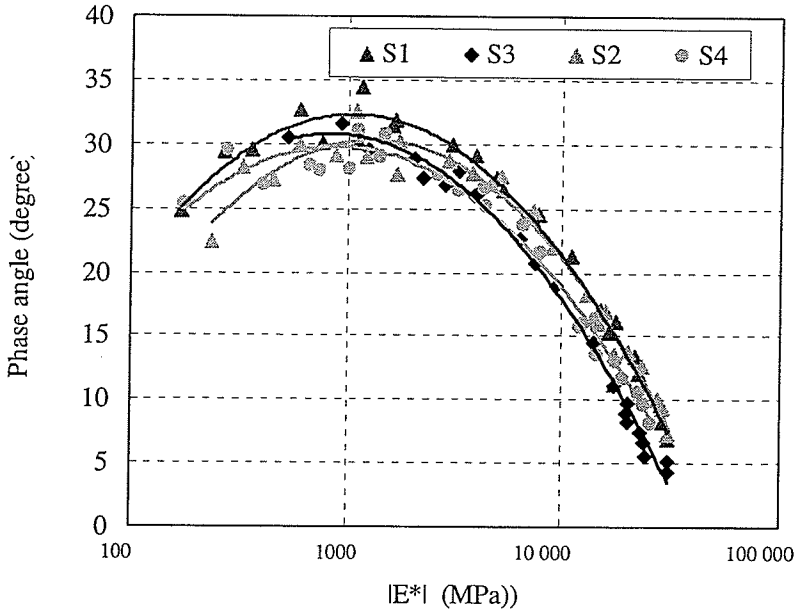

(a)

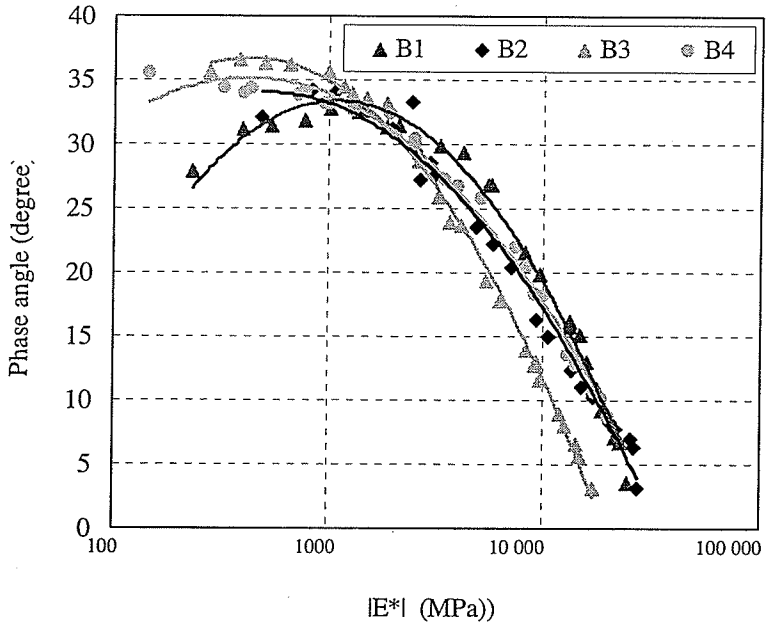

(b)

Figure 4.5: Black space, phase angle versus dynamic modulus

(a) Surface mixtures. (b) Binder mixtures

$|E^*|$ and ϕ at various temperatures and frequencies are consistent since the values are fitted by smooth curves in the black space at high stiffness and the complex plane at low stiffness. The black space and the complex plane can be used to compare $|E^*|$ and ϕ of specific mixtures measured by different testing methods since they do not depend on the test conditions.

4.3 Isothermal and Isochronal Curves of $|E^*|$ and ϕ

The $|E^*|$ and ϕ depend on two parameters: temperature and loading frequency. They are represented graphically by the isothermal and isochronal curves, Figures 4.6 and 4.7 respectively. The curves were used to find the deviated value from average data trends. They also illustrate the relationship between the measured data and the test conditions, temperature and frequency. They are simple ways to understand the effect of traffic speed and pavement temperature on AC stiffness since a constant design speed is allowed for a given highway. For a constant traffic speed, stiffness is best represented with the isochronal curve. The following observation are made:

- In general, isothermal and isochronal curves generated from $|E^*|$ data are more consistent than those curves generated from ϕ data.
- At a given temperature, $|E^*|$ increases with frequency while it decreases with temperature at a given frequency. The frequency has a large effect at high temperature than low temperature.
- On the contrary, ϕ decreases with frequency at low temperatures (-10 and 5°C).

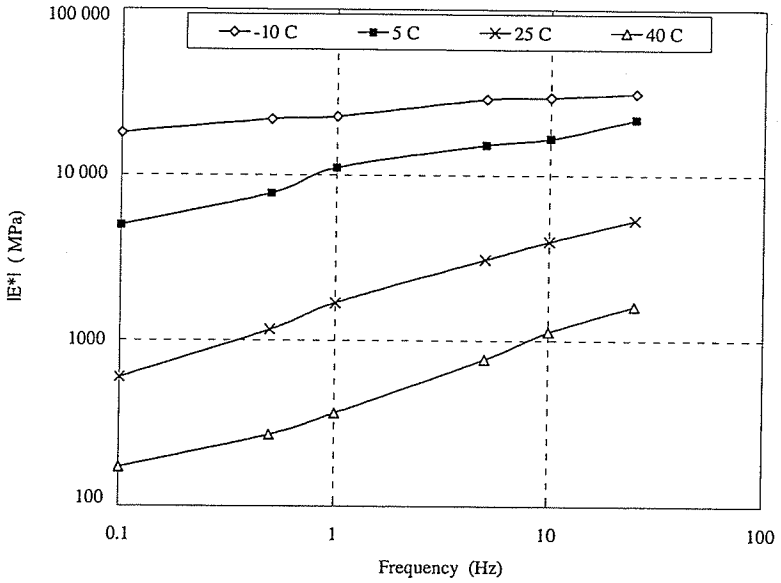

(a)

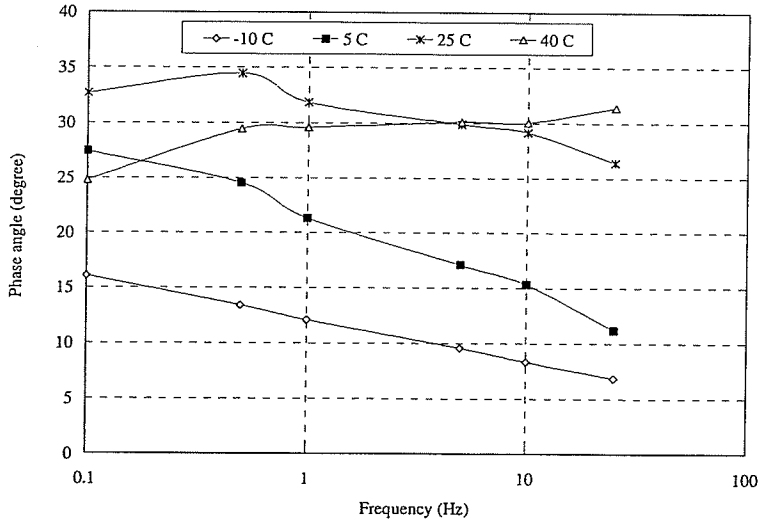

(b)

Figure 4.6: Isothermal curves for S1 mixture

(a) Dynamic modulus, (b) Phase angle

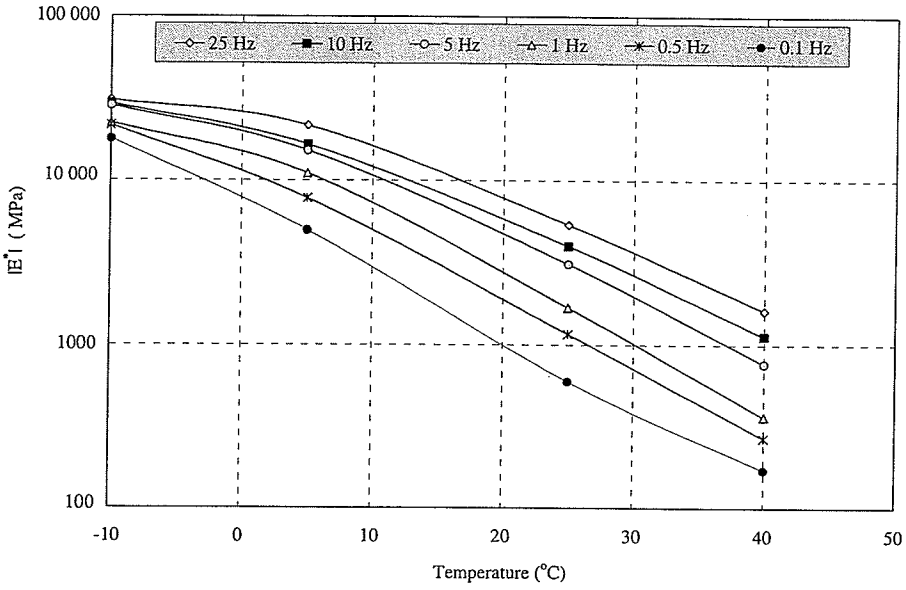

(a)

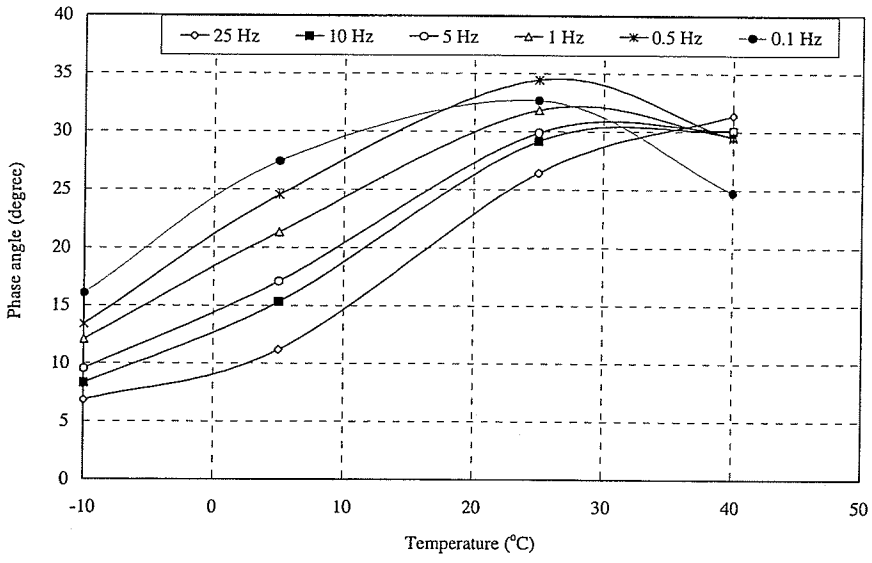

Figure 4.7: Isochronal curves for S1 mixture

a) Dynamic modulus, b) Phase angle

- At higher temperatures (25 and 40°C), the relationship between ϕ and frequency is not consistent. At 40°C, the phase angle is not sensitive to the loading frequency. The effect of aggregate on the rheology of mixtures increases in comparison with the effect of binder. Response (Kim and Lee 1996).

4.4 Evaluation of Shifting Techniques

Figure 4.8 illustrates the influence of the shift function on developing the $|E^*|$ master curve from measured $|E^*|$. Five techniques that are introduced in Section 2.4 are compared. The coefficients of the sigmoidal function, δ, α, β, γ, and shift factors have been obtained simultaneously by applying a non-linear fitting technique to minimize the sum of squared errors between the measured and fitted $|E^*|$. Figure 4.8 shows that different $|E^*|$ master curves at a reference temperature of 25°C have been obtained when different shift functions are applied producing different estimated $|E^*|$ and reduced frequency. It is important to note that the master curve should be analyzed with its associate shift function. For a reasonable visual comparison between AC mixtures using the master curve, it is preferable to use the same shift function for mixtures under comparison.

Table 4.1 lists the coefficients of master curves and shift factors that were obtained with the experimental method. These shift factors vary from mix to mix. Since they were obtained without constraints other than the minimum value of sum squared errors between measured $|E^*|$ and fitted $|E^*|$, they may be sensitive to the change in the testing program, for example testing at other temperatures and frequencies. Different shift factors of mixtures at a given temperature result in different reduced frequencies for a given loading frequency.

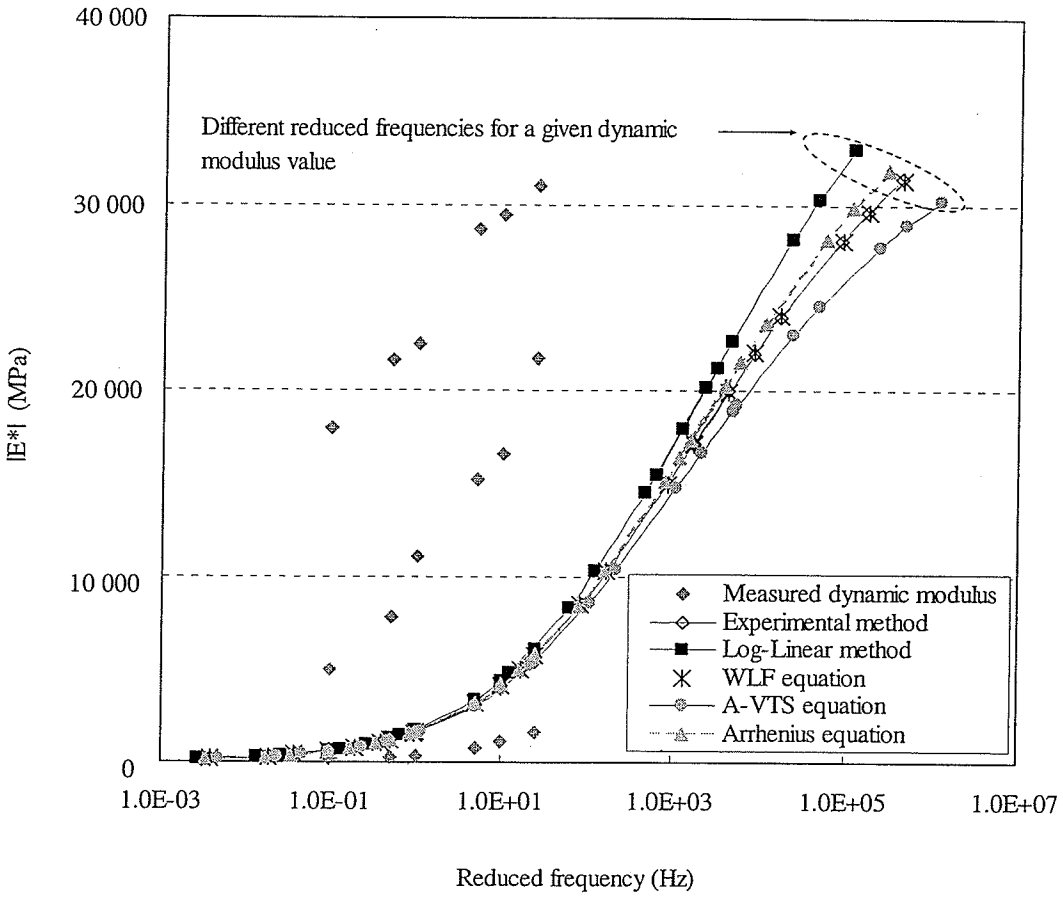

Figure 4.8: The master curve of S1 using the five shift functions

The shift functions have been examined using S1-S4 and B1-B4 to select a function that is less sensitive to mixture property. The coefficients of the shift functions, Equations (2.15 to 2.19), have been determined simultaneously with coefficients of the master curves for each mixture. Table 4.2 lists the viscosity-temperature susceptibility parameters, A and VTS, of the binders obtained from the complex shear modulus (G^*) and the phase angle (δ). These values have been used to generate the A-VTS shift function.

Table 4.1: Coefficients of $|E^*|$ master curves and shift factors of mixtures

Mixtures	Coefficients of $\|E^*\|$ master curves				Shift factor , Log *a(T)*		
	δ	α	β	γ	-10°C	5°C	40°C
S1	1.374	3.232	-0.264	0.547	4.234	2.242	-1.409
S2	1.549	3.054	-0.156	0.530	4.328	2.187	-1.304
S3	1.697	2.830	-0.778	0.534	4.007	2.187	-1.516
S4	1.009	3.549	-0.453	0.438	4.691	2.365	-1.495
B1	1.206	3.301	-0.514	0.494	4.176	2.392	-1.321
B2	1.500	3.002	-0.701	0.457	4.735	2.291	-1.423
B3	1.579	2.706	-0.371	0.539	4.185	2.122	-1.227
B4	0.597	3.909	-0.502	0.415	4.418	2.021	-1.113

Reference temperature = 25°C,

Table 4.3 lists statistics, the maximum value, the minimum value and the coefficient of variation (CV), of the coefficients of shift functions. These values have been obtained from the calculated coefficients of all mixtures. The activation energy (ΔE_a) is less sensitive to mixtures as shown by low CV. On the contrary, coefficients of WLF shift function are sensitive to the mixture property where CV is 25% for C1 and 21% for C2. Coefficients of Log linear and A-VTS functions have moderate sensitivity to mixtures.

Based on this comparison, the Arrhenius function with ΔE_a of 175 KJ/mol is recommended to construct the master curves of these mixtures for estimation of $|E^*|$ and for the visual comparison using the master curves of mixtures. Figure 4.9 presents the goodness of fit (S_e/S_y) of the master curves constructed using the five shift functions. The goodness of fit is the ratio of the standard error of the $|E^*|$ obtained from the master curve to the standard deviation of the measured $|E^*|$. The higher the S_e/S_y value is, the lower accuracy of the fitted master curve.

Table 4.2: Performance binder grades and parameters of viscosity-temperature susceptibility

Mixture	Binder grade (PG) .	A	VTS
S1	58-28	10.985	-3.693
S2	58-28	10.985	-3.693
S3	52-28	11.520	-3.890
S4	58-34	11.040	-3.715
B3	52-28	11.520	-3.890
B4	58-34	11.040	-3.715

Table 4.3: Coefficients of the shift functions

Statistics	Log-Linear	WLF		Arrhenius	A-VTS
	β	C1	C2	ΔE_a (kJ/mol)	C
Minimum value	-0.113	8.61	103	174.320	0.87
Maximum value	-0.097	21.44	209	175.066	1.08
Average value	-0.104	16.47	166	174.936	0.94
Coefficient of Variation (%)	4.98	24.47	21.20	0.14	6.81

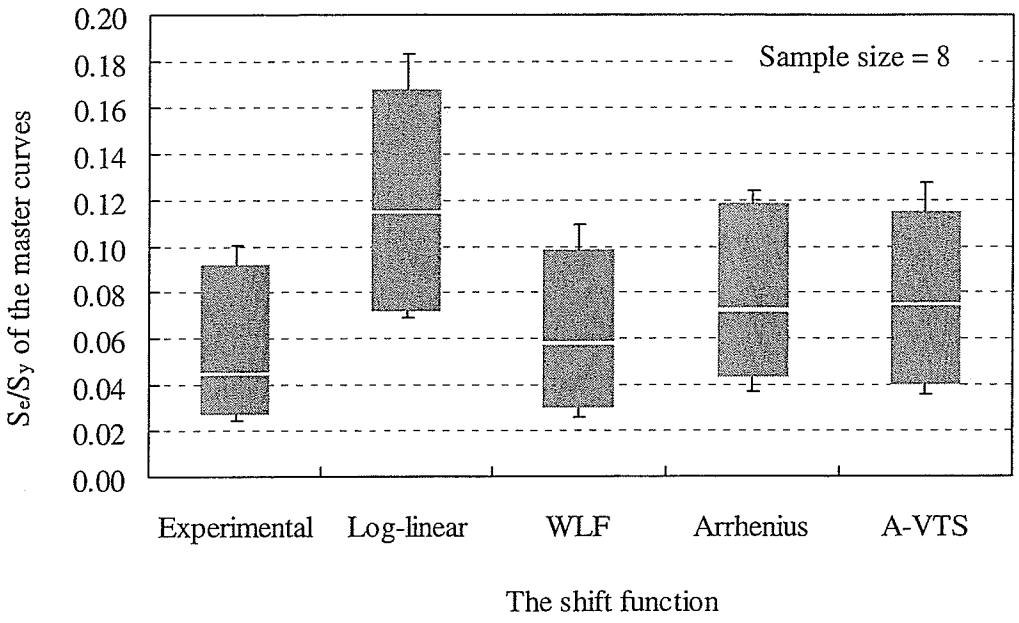

Figure 4.9: Goodness-of-fit of $|E^*|$ master curves using shift functions

The experimental shifting technique produces the most accurate master curves. On the contrary, Log-linear shift function produced the least accurate fitted master curves. The $|E^*|$ fitting errors were investigated at the test temperatures, Figure 4.10. The error increases slightly with temperature. The 10% of the sample at 25°C has errors up to 30%. This behaviour at 25 C, which is the reference temperature, can be explained by constraining the value of the shift factor at this temperature. All shift functions can reasonably be used to construct the $|E^*|$ master curves except the log-linear function where the error was within $\pm$ 20% at -10 and 25°C. The fitting errors produced by applying the experimental method and WLF function were within $\pm$10%, increase with temperature and are normally distributed since the median error is zero.

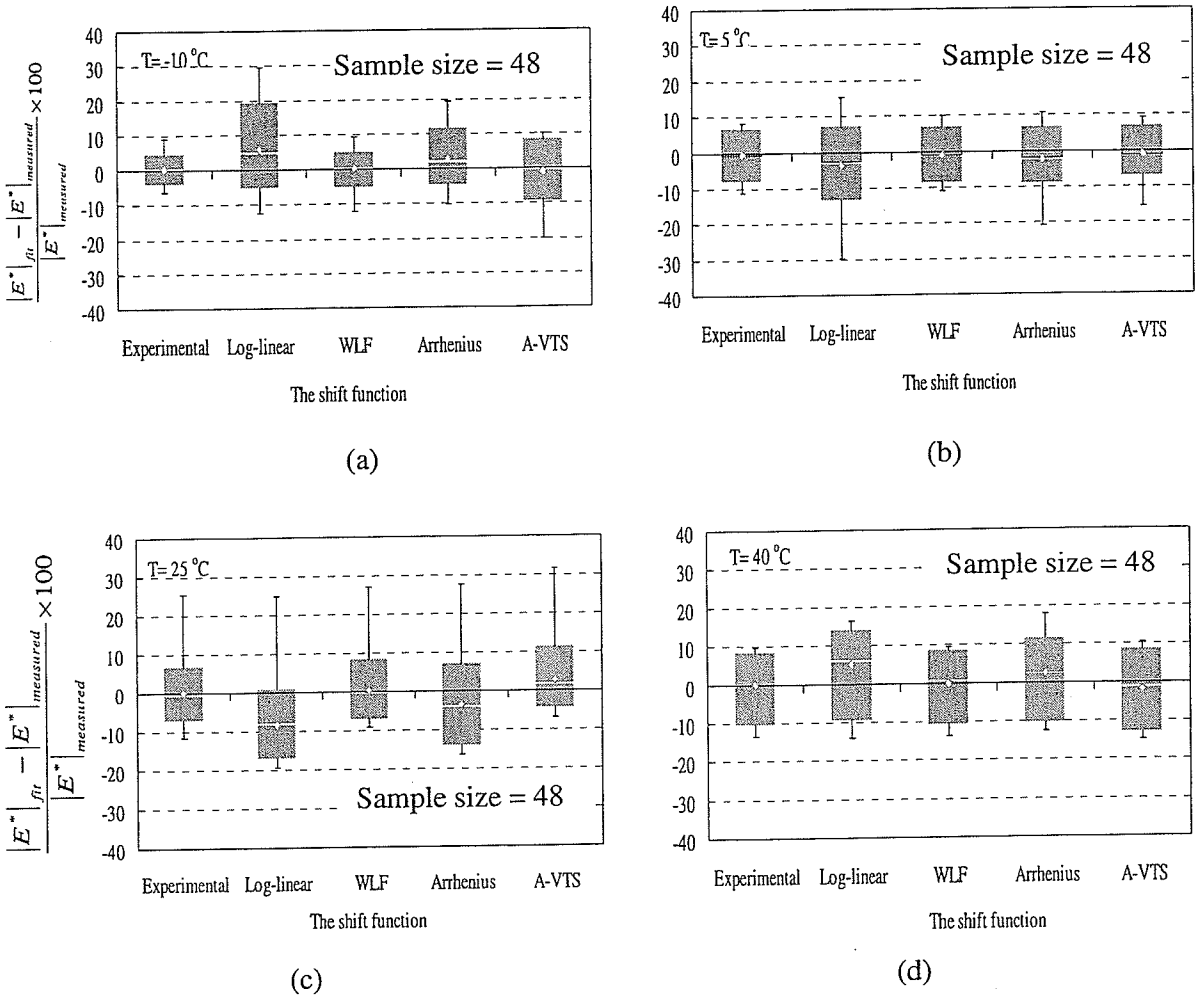

Figure 4.10: Distribution of $|E^*|$ fitting error of the master curves at temperatures (a)-10°C, (b) 5°C, (c) 25°C, and 40°C

A-VTS function can be used to obtain the shift factors from properties of binders allowing the rheology of binders to be incorporated. Although the WLF function produces small fitting errors and low S_e/S_y comparing to the other functions, the Arrhenius and A-VTS functions are recommended for constructing master curves because their constants are less sensitive, low CV, to the properties of the mixtures.

4.5 Evaluation of Witczak $|E^*|$ Prediction model

The Witczak $|E^*|$ model, Equation 2.49, was used to predict $|E^*|$ of S1-S4 and B3-B4 from the mixtures volumetric properties. Table 4.4(a) lists aggregate gradation parameters and volumetric properties of mixtures required to predict the modulus using the Witczak model at design level 2 and 3. At design level 2, the viscosity (η) of the binders was estimated from the DSR parameters measured at angular velocity (ω) of 10 rad/sec and temperature range from 7 to 70°C. The viscosity-temperature susceptibility model, Equation (2.20) was applied for each binder grade to obtain A and VTS to be used to calculate the viscosity at any temperature. Table 4.2 lists A and VTS obtained from the measured G^* and δ. At design level 3, where no laboratory measurements for the binder are required, typical values of A and VTS of a given binder grade can be obtained from NCHRP (2004). Table 4.4(b) lists the typical A and VTS for binder grades used in S1-S4 and B3 and B4 mixtures.

Figure 4.11 shows the comparison of the predicted and measured $|E^*|$ master curves of S1-S4 and B3 and B4 mixtures at the design levels 2 and 3. Generally, the Witczak model characterized the effect of the loading time quite well but it overpredicts $|E^*|$ especially at low stiffness/high temperatures. It is noticed that the prediction errors at design level 3 is slightly lower than those at level 2 for S1 to S3 while the opposite is true for the remaining mixtures. The higher reliability of the $|E^*|$ prediction does not guarantee low errors. For representative measurements, $|E^*|$ should be obtained from direct testing or high reliable prediction techniques.

At level 2 and 3, the predicted errors at low temperatures (-10 and 5°C) are lower than those at high temperatures. The predicted values for S1-S4 range from -0.65 to 2.5 times those

measured in the laboratory at intermediate and high temperatures (25 and 40°C). The prediction errors for B3-B4 range from -0.3 to 1.5 times of the measured $|E^*|$. $|E^*|$ at high temperature correlates significantly with the permanent deformation and rutting (Witczak et al. 2002a). Figures 4.12 and 4.13 show the distribution of the $|E^*|$ prediction errors at various measured $|E^*|$ values of S1-S4 and B3-B4 respectively.

Table 4.4(a): Inputs of the Witczak $|E^*|$ model of mixture properties, design level 2 and 3.

Mixture	Aggregate gradation (%)			Air voids (A_v) (%)	Effective volume binder content (V_{beff}) (%)
	Passing 0.075 mm sieve	Total retain 4.75 mm sieve	Total retain 9.5 mm sieve		
S1	3.5	38.2	20.7	4.5	4.68
S2	3.6	38.1	21.0	4.9	4.19
S3	5.2	36.5	20.0	4.7	4.33
S4	3.7	38.2	22.7	5.7	5.07
B3	5.0	22.5	11.7	9.7	4.74
B4	4.2	30.1	14.4	9.3	4.28

Table 4.4(b): Default MEPDG parameters of A and VTS for pavement design level 3

Mixture	Binder grade (PG)	A	VTS
S1	58-28	11.01	-3.70
S2	58-28	11.01	-3.70
S3	52-28	11.84	-4.01
S4	58-34	10.04	-3.35
B3	52-28	11.84	-4.01
B4	58-34	10.04	-3.35

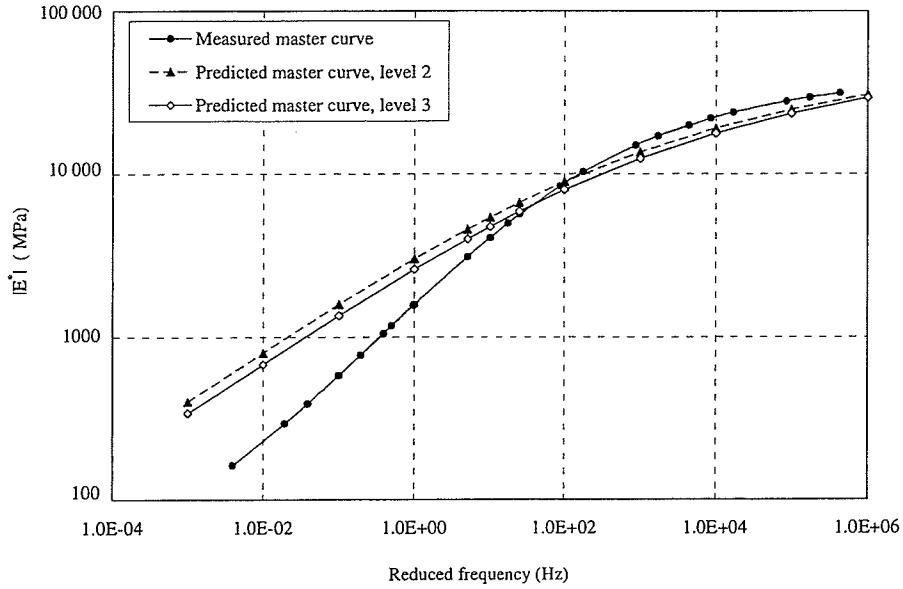
Measured master curve
Predicted master curve, level 2
Predicted master curve, level 3
100 000
10 000
1000
100
|E*| (MPa)
1.0E-04
1.0E-02
1.0E+00
1.0E+02
1.0E+04
1.0E+06
Reduced frequency (Hz)

(a) S1

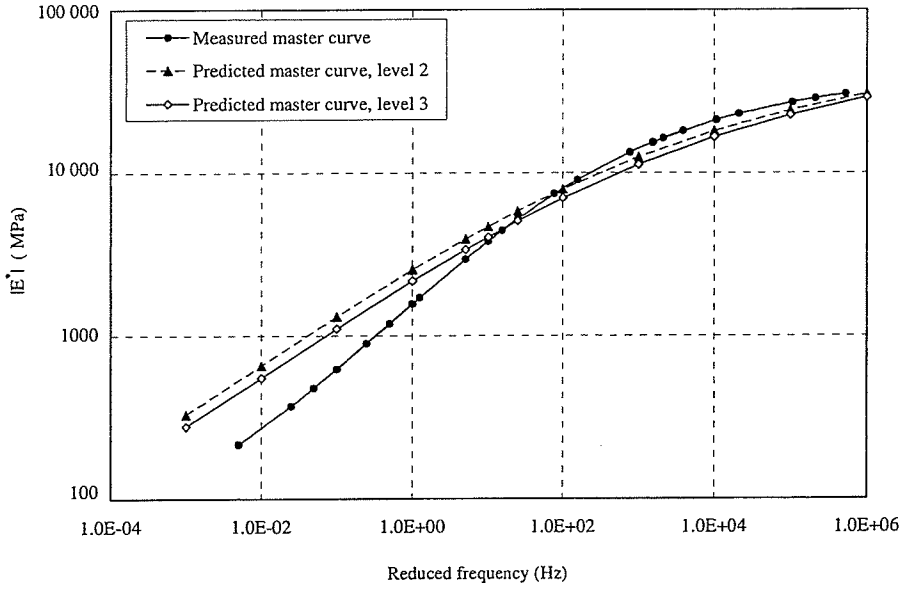
Measured master curve
Predicted master curve, level 2
Predicted master curve, level 3
100 000
10 000
1000
100
|E*| (MPa)
1.0E-04
1.0E-02
1.0E+00
1.0E+02
1.0E+04
1.0E+06
Reduced frequency (Hz)

(b) S2

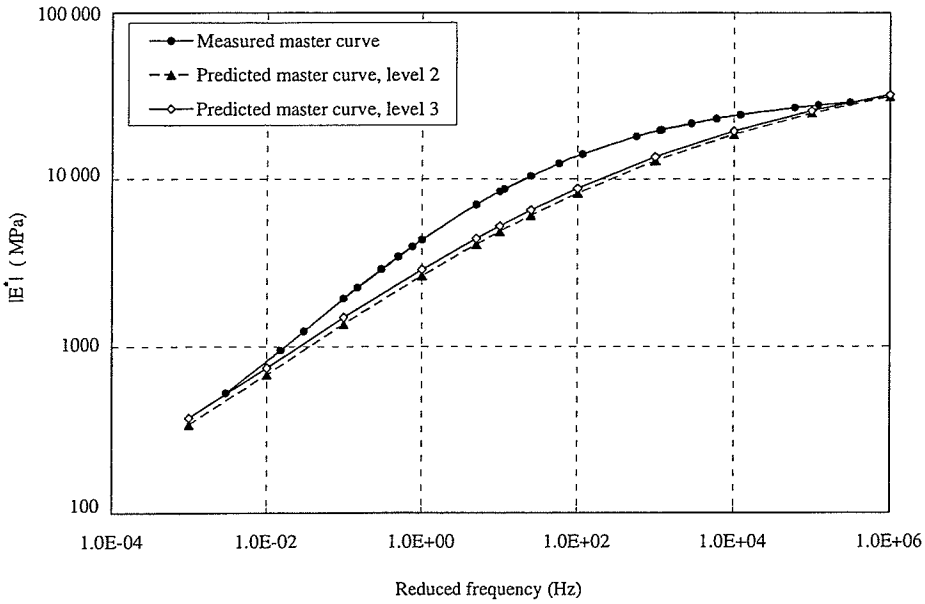
100 000
10 000
1000
100
|E*| (MPa)
Measured master curve
Predicted master curve, level 2
Predicted master curve, level 3
1.0E-04
1.0E-02
1.0E+00
1.0E+02
1.0E+04
1.0E+06
Reduced frequency (Hz)

(c) S3

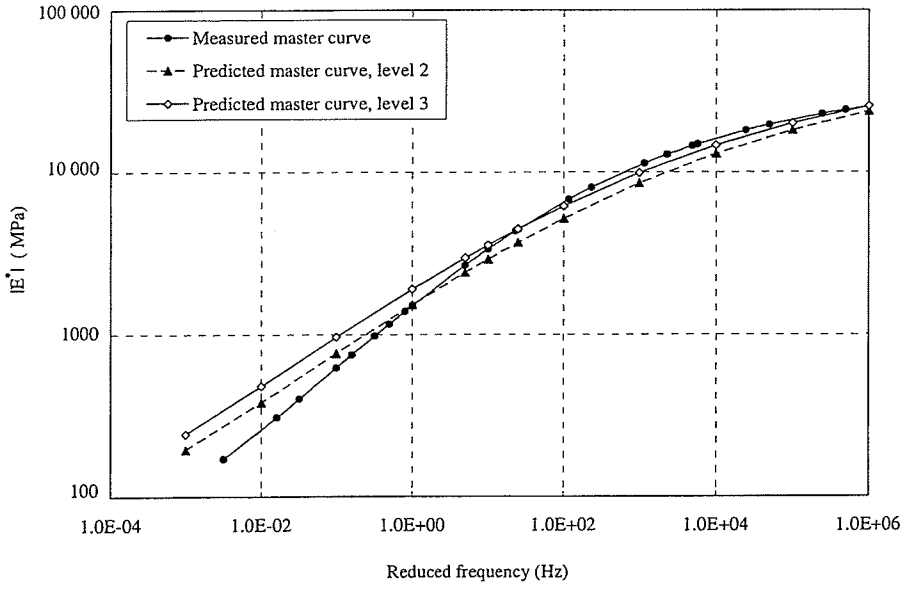
100 000
10 000
1000
100
|E*| (MPa)
Measured master curve
Predicted master curve, level 2
Predicted master curve, level 3
1.0E-04
1.0E-02
1.0E+00
1.0E+02
1.0E+04
1.0E+06
Reduced frequency (Hz)

(d) S4

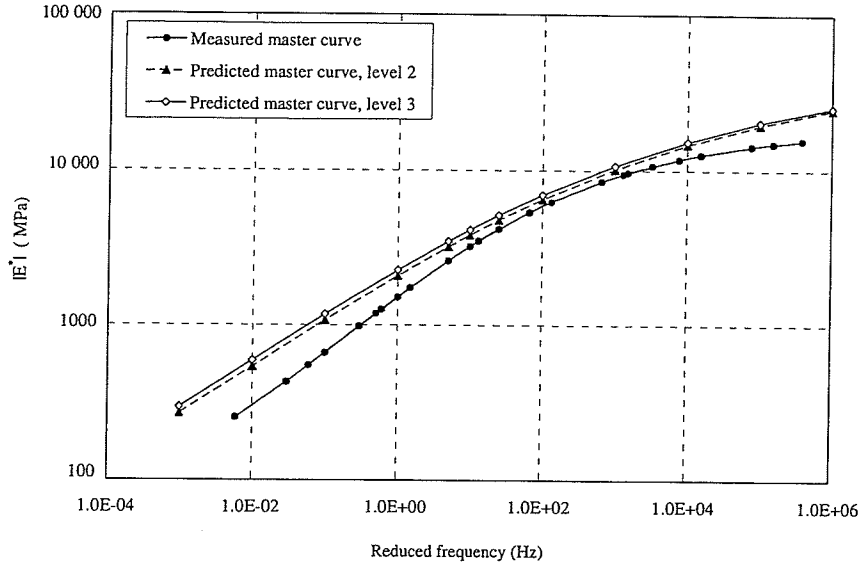

(e) B3

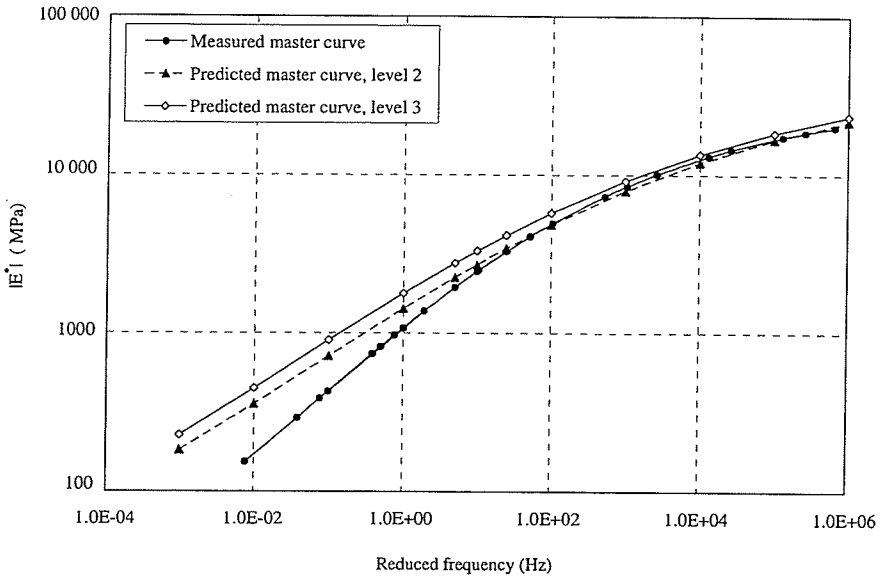

(f) B4

Figure 4.11: Measured $|E^*|$ master curves versus predicted at level 2 and level 3

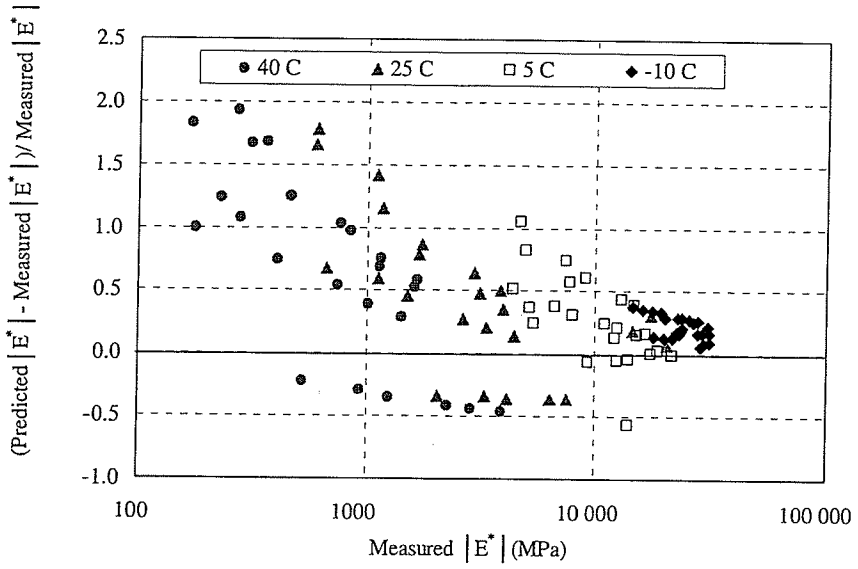

(a)

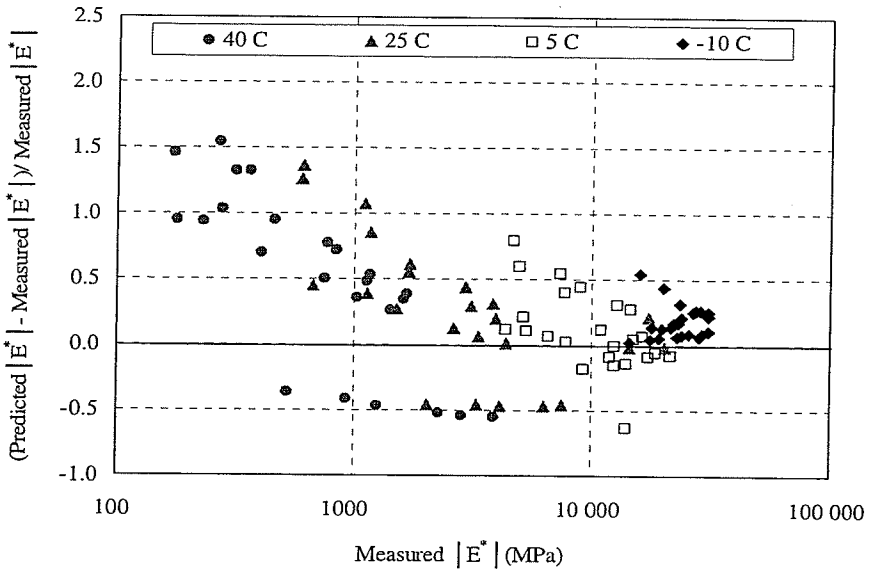

(b)

Figure 4.12: The $|E^*|$ prediction error at the measured $|E^*|$ value of S1-S4 mixtures

(a) design level 2 (b) design level 3.

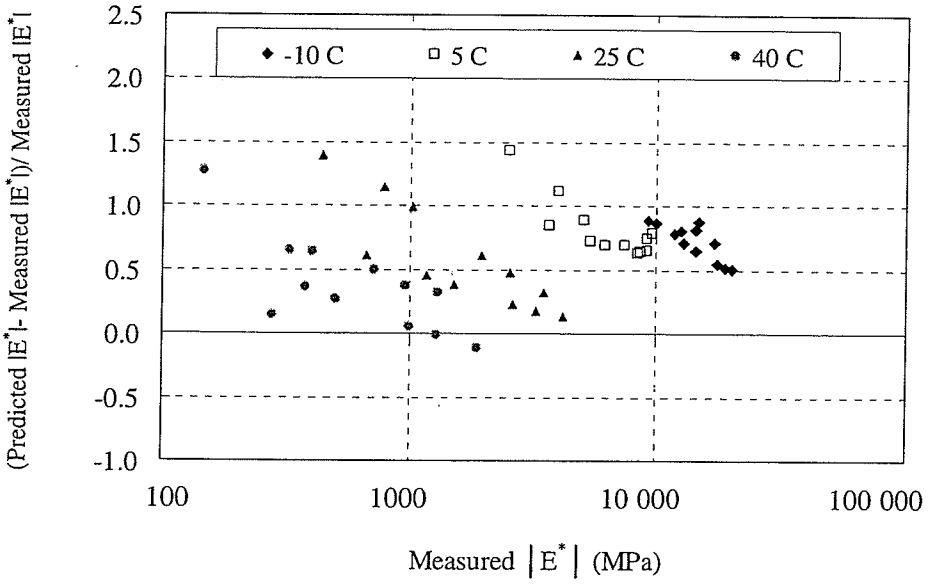

(a)

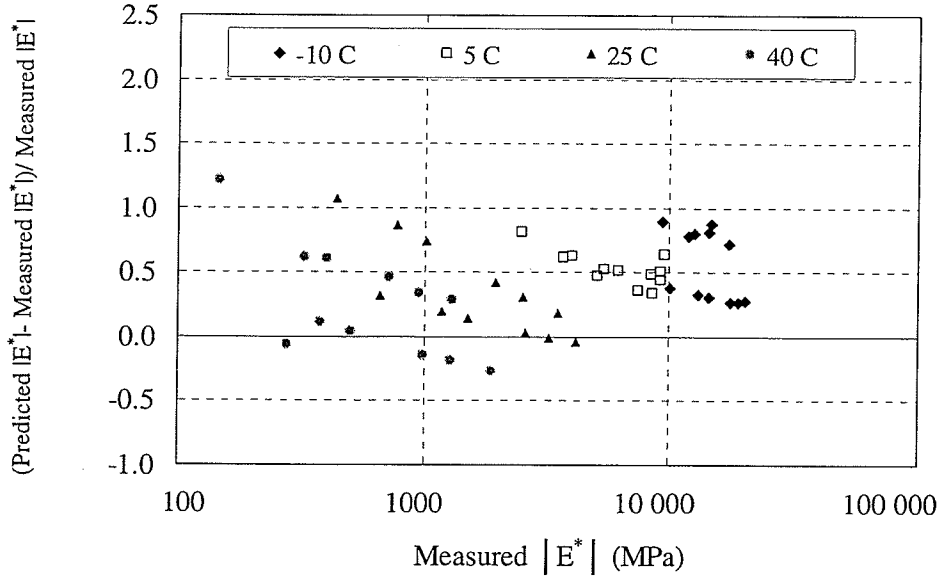

(b)

Figure 4.13: The $|E^*|$ prediction errors versus the measured $|E^*|$values of B3 and B4:

(a) design level 2 (b) design level 3.

4.6 Impact of $|E^*|$ prediction error

The significance of $|E^*|$ prediction errors is best evaluated with their impact on the predicted pavement performance and the mixture comparison. A pavement cross section has been analysed to evaluate the impact of the prediction errors on the predicted pavement performance.

The $|E^*|$ errors of the mixtures tested in this study have almost the same pattern. At high stiffness/low temperatures, the errors are small in comparison to the errors at low stiffness/high temperatures. Neglecting the error at the high stiffness, the predicted $|E^*|$ of this pattern at various prediction levels of error at high temperature can be represented numerically using the sigmoidal function, Equation (2.22), by changing the minimum $|E^*|$ value while holding constant the maximum $|E^*|$ value in the following modified sigmoidal function.

$$\log|E^*| = \log|E^*|_{min} + \frac{\log|E^*|_{max} - \log|E^*|_{min}}{1 - e^{\alpha - \gamma \log(f_r)}} \tag{4.1}$$

where

$|E^*|_{min}$: minimum dynamic modulus of a mixture,

$|E^*|_{max}$: maximum dynamic modulus

Comparing with Equation 2.22, it can be noticed that

$\delta = \log|E^*|_{min}$ and

$\delta + \alpha = \log|E^*|_{max}$

The maximum $|E^*|$ and the minimum $|E^*|$ values obtained from δ and α depend not only on the mixture property but also on the $|E^*|$ test conditions, temperature and frequency; therefore

they are not pure material properties. Figure 4.14 shows $|E^*|$ master curves generated from coefficients from S1, shown in Table 4.1, with changing δ to produce $|E^*|$ values at 40°C and 1Hz, $|E^*_{40}|$, that are 0.5, 1, 1.5, 2.0 and 3.0 times of the actual value of $|E^*_{40}|$.

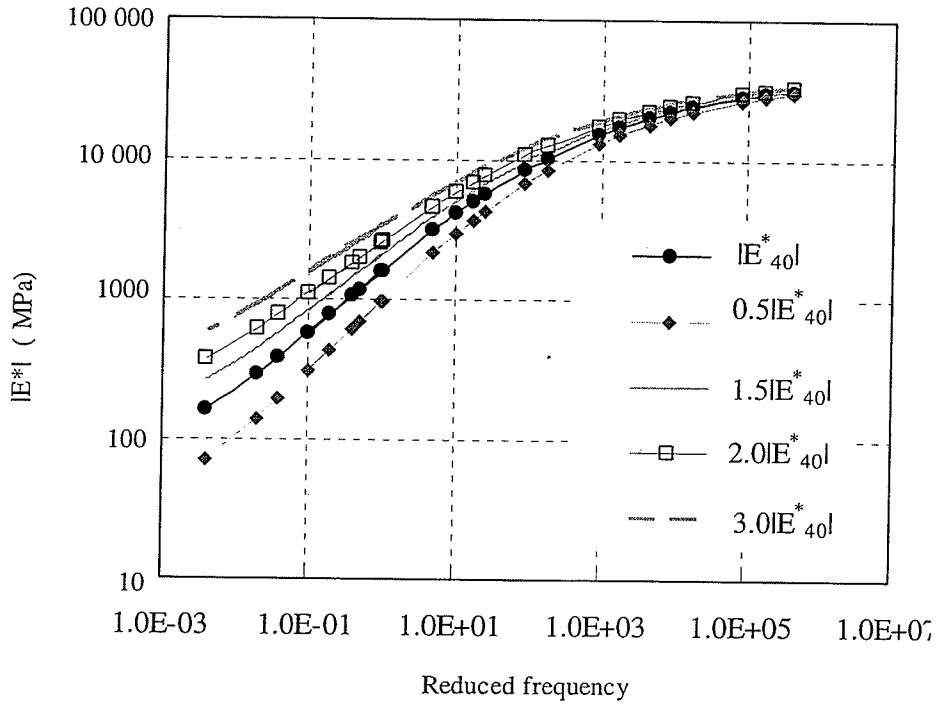

Figure 4.14: $|E^*|$ master curves of S1 generated at various prediction errors at low stiffness

S1 is a surface asphalt mixture for PTH 8 located in Manitoba. The road is 4 lane divided highway. Based on 2005 traffic count at station number 1 that located 1.4 Km south of PR 321, the annual average daily traffic (AADT) of PTH 8 is 10900. The count station is classified as regular permanent count station (PCS) where no weight or vehicle classification data was collected. The assumed average annual daily truck traffic (AADTT) is 2000, which

is about 18% of AADT, and it contains mainly class 9 trucks. The percent of AADTT of 2005 traffic counts in Manitoba was up to 30% of AADT.

The cross section consists of subgrade classified as A-6 AASHTO soil with stiffness of 100 MPa, a 500 mm base course from crushed gravel with stiffness of 170 MPa, and 200 mm asphalt concrete. The thickness of the asphalt layer constructed from S1 was determined using the MEPDG software of NCHRP project 1-37A to support the AADTT with annual growth of 2% and design service life of 20 years. The default design criteria of fatigue and rutting at a reliability level of 90% were applied. The criteria were 25% fatigue cracking, 6 mm asphalt layer rutting and 18 mm total rutting.

Figure 4.15 shows the predicted pavement performance, rutting, fatigue cracking and longitudinal cracking, over a design life. The rutting of the asphalt layer and total rutting of pavement are 7 and 19 mm respectively and the maximum fatigue cracking is 25%.

Sensitivity of the predicted pavement performance to the variation in $|E^*|$ at high temperature has been examined. Figure 4.16 shows the sensitivity of rutting and fatigue cracking. Although the pavement cross section lies in a cold region, the cold temperature distresses has been excluded from the sensitivity analysis since its model does not depend directly on $|E^*|$. The predicted pavement performance is sensitive to the variation of $|E^*|$ at low stiffness/high temperatures and overprediction of $|E^*|$ leads to underestimate the pavement performance and unconservative pavement design.

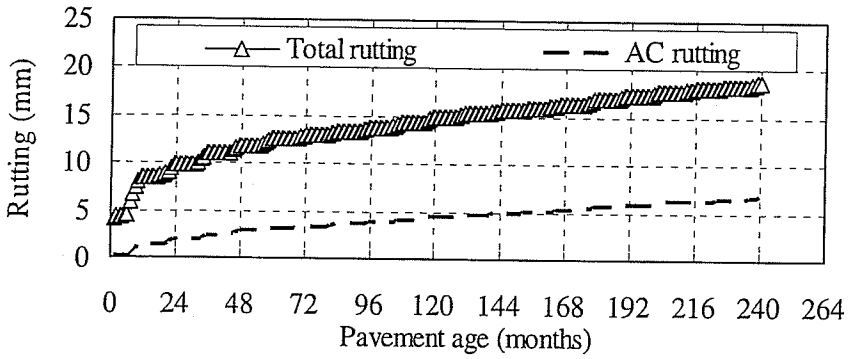

(a)

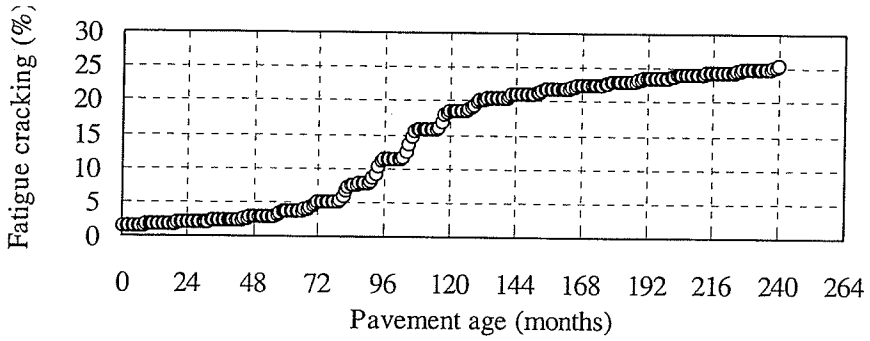

(b)

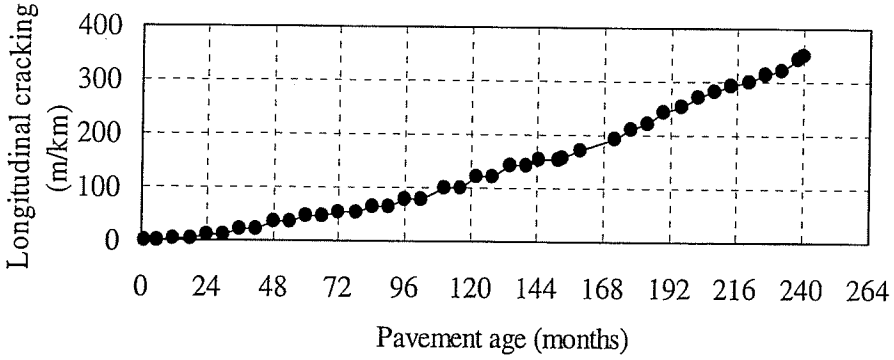

(c)

Figure 4.15: The predicted pavement performance:

(a) Rutting, (b) Fatigue cracking, c) Longitudinal cracking

For the given pavement section, the $|E^*|$ variation has an identical effect on the fatigue cracking and total rutting. It was noticed that the effect on rutting of asphalt concrete is higher than the effect on total rutting. Underpredicting $|E^*|$ by 50% overestimates the total rutting, fatigue cracking, AC rutting and longitudinal cracking by 20%, 20%, 30%, 70% respectively. Overpredicting $|E^*|$ by 250% underestimates the total rutting, fatigue cracking, AC rutting and longitudinal cracking by 25%, 25%, 40% and 100% respectively.

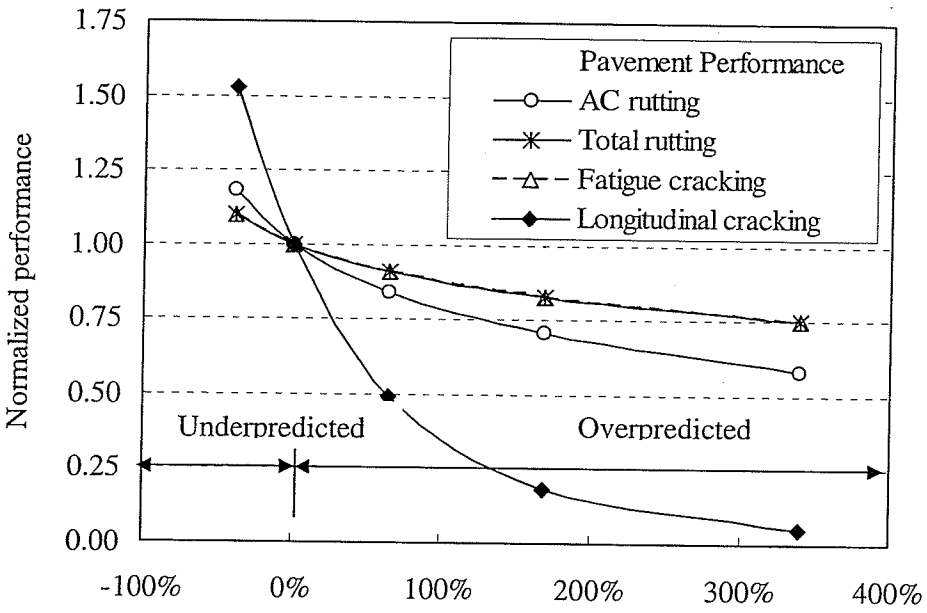

Figure 4.16: Sensitivity of the pavement performance to AC stiffness

4.7 Summary

The chapter evaluates the determination of $|E^*|$ of AC mixtures used in Manitoba and similar cold regions. The variability in $|E^*|$ and ϕ has been evaluated within a mixture and at the test

temperatures. The shift techniques applied to develop $|E^*|$ from measurements have been compared. The prediction of $|E^*|$ from the volumetric properties has been carried out using the Witczak model and the impact of prediction errors on the pavement performance have been evaluated.

The variability of $|E^*|$ within a mixture does not change significantly from a mixture to another and with test conditions. Therefore the variability of $|E^*|$ may be used to examine the variability in AC. The Arrhenius' function has been recommended as a shift factor function to develop master curves when the experimental method can not be applied and a visual comparison between mixtures is required (Pellinen et al., 2004). The Witczak model overpredicts $|E^*|$ at high temperature and the prediction error has a significant impact on the pavement performance.

5 Improving the Prediction of the Dynamic Modulus of Fine-Graded Asphalt Concrete Mixtures at High Temperatures

5.1 Introduction

A linear model is developed to predict $|E^*|$ at 40°C using a gradation parameter. The model is used to improve the reliability in the prediction of $|E^*|$ at high temperatures and to adjust the $|E^*|$ master curve constructed using the Witczak $|E^*|$ predictive model. The approach presented in this chapter was presented in Harran and Shalaby (2009).

5.2 Dynamic Modulus-Gradation Relationship

The relationship between $|E^*|$ at high temperature and aggregate gradations is examined using the following gradation parameters: the percent passing the 0.075 mm sieve, the percent passing the 4.75 mm sieve and a gradation ratio (GR). The gradation ratio is proposed in the thesis and can be defined as follow:

$$GR = \frac{\%\ \text{Passing 4.75 mm sieve}}{\%\ \text{Passing 0.075 mm sieve}} \tag{5.1}$$

The 4.75 mm sieve and the 0.075 mm sieve are selected since they are typically used to split the aggregate into three portions, coarse aggregate (CA), fine aggregate (FA) and mineral filler. GR measures the ratio of the FA portion to the mineral filler portion. The

dynamic modulus at 40°C and 1 Hz, $|E^*_{40}|$, is selected to capture the influence of the aggregate gradation (Birgisson and Roque, 2005). A statistical analysis is carried out to test the relationship between $|E^*_{40}|$ and the gradation parameters at a threshold significance level (ρ) of 0.05.

The analysis is conducted using four mixture groups that included a total of 24 mixtures, Table 5.1. Table 5.2 lists properties of the mixtures that are used to study the relationship between the gradation parameters and the dynamic modulus at high 40°C. The first group, G1, consisted of six mixtures, S1-S4, B3 and B4. B1 and B2 are not considered because they contain percents of RAP. More information about S1-S4 and B1-B4 can be found in chapter 3. The second group, G2, consists of 6 fine-graded mixtures and the third group, G3, consists of 7 coarse-graded mixtures.

Table 5.1: Characteristics of the mixture groups

Mixture group	Mixture source	Aggregate classification	Number of mixtures	Binder grade
G1	University of Manitoba	Fine-graded	6	PG58-28, PG 52-28 PG 58-34
G2	Florida	Fine-graded	6	PG 67-22 (AC- 30)
G3	Florida	Coarse-graded	7	PG 67-22 (AC- 30)
G4	MnRoad, Minnesota	Fine-graded	5	AC- 30, Pen 120-150
			Total 24	

Table 5.2: Gradation parameters, volumetric properties and measured $|E^*_{40}|$, $|E^*|$ at 40°C and 1Hz.

Mix	Gradation			GR	Level of Compaction	Mix properties		Meas. $|E^*_{40}|$ (MPa)
	Percent passing (%)					Air voids (%)	Effective binder content (%), by volume	
	0.075 mm sieve	4.75 mm sieve	9.5 mm sieve					
G1								
S1	3.5	61.8	79.3	17.7	75 gyrations	4.5	4.68	363
S2	3.6	61.9	79.0	17.2	75 gyrations	4.9	4.19	460
S3	5.2	63.5	80.0	12.3	100 gyrations	4.7	4.33	1257
S4	3.7	61.8	77.3	16.6	75 gyrations	5.7	5.07	407
B3	5.0	77.5	88.3	15.5	100 gyrations	9.7	4.74	504
B4	4.2	69.9	85.6	16.5	75 gyrations	9.3	4.28	401
G2								
F1	4.8	69.3	85.1	14.4	109 gyrations	4.0	5.09	850
F2	6.3	61.3	78.0	9.7	109 gyrations	3.9	4.12	1076
F4	6.3	69.3	85.1	11.0	109 gyrations	4.0	4.41	1044
F5	4.8	61.3	85.1	12.8	109 gyrations	4.0	5.39	727
F6	6.3	69.3	85.1	11.0	109 gyrations	4.2	4.99	880
P7	4.2	70.0	88.0	16.7	84 gyrations	4.5	4.35	550
G3								
C1	4.8	60.2	90.0	12.5	109 gyrations	4.0	5.12	526
C2	4.8	47.1	73.5	9.8	109 gyrations	3.9	4.44	759
C3	6.3	57.4	89.3	9.1	109 gyrations	4.0	4.35	801
P1	5.1	64.0	99.0	12.5	96 gyrations	4.1	4.73	524
P2	4.9	45.0	89.0	9.2	96 gyrations	4.4	4.35	607
P3	4.4	67.0	90.0	15.2	96 gyrations	4.2	5.50	459
P5	3.9	64.0	94.0	16.4	96 gyrations	4.4	4.40	638
G4								
Cell16	4.6	68.3	84.5	14.8	N.A gyrations	8.2	9.60	794[a]
Cell17	4.2	68.8	85.0	16.4	75 blows	7.7	10.30	751[a]
Cell18	4.4	68.8	84.5	15.6	50 blows	5.6	11.40	641[a]
Cell20	4.8	69.3	85.0	14.4	35 blows	6.3	11.80	350[a]
Cell22	4.3	69.5	85.0	16.2	75 blows	6.5	10.20	421[a]

[a]Interpolated value using measured dynamic moduli at 37.8°C and 54.4°C,

The G2 and G3 mixtures were used in a project at the University of Florida to develop the gradation-based mixture design guideline that is described in section 2.6.5. They consisted of laboratory and field mixtures containing limestone and granite aggregates and a single binder grade of PG 67-22. G2 and G3 were prepared based on the SuperPave mix design. Additional information about these mixtures can be found in Birgisson and Roque (2005). The available information included volumetric properties and dynamic modulus at 40°C and 1 Hz, $|E^*_{40}|$.

The fourth group, G4, is used to validate the proposed model. It consists of the five mixtures of the Minnesota Road research project (MnRoad) experimental test site, cells 16-18, 20 and 22, as reported by Pellinen (2001). The MnRoad mixtures were prepared from materials sampled from the experimental test site and contained various aggregate gradations and two binder grades. Cells 16-18 contained an AC-20 binder while cells 20 and 22 contained a 120-150 penetration grade binder. A SuperPave gyratory compactor was used to duplicate the field-compacted mixture properties. G4 mixtures were prepared according to the Marshall mix design except for cell 16 mixture which was designed according to the SuperPave mix design.

The dynamic modulus-aggregate gradation relationship is tested within five dataset groups, G1, G2, (G1 and G2), G3 and (G2 and G3). The first three datasets are fine-graded mixtures. The G1 and (G1 and G2) contain various binder grades to test the relation in mixtures that include different binder grades. The G2, G3 and (G2 and G3) contain a single binder grade, PG 76-22, as such the effect of the binder rheology on the

relationship is neutralized. The fourth dataset, G3, contains coarse-graded mixtures and the fifth dataset, (G2 and G3), contains combined fine- and coarse-graded mixtures. The relationship is tested at two sample size levels of the fine-graded mixtures that include various binder grades. The G1 dataset has a sample size of 6 and a GR range of 12.3-17.7 and the (G1 and G2) has a sample size of 12 and a GR range of 9.7-17.7. The relationship is considered significant if the correlation coefficient (r) is higher than or equals the critical correlation coefficient (r_{crt}) at a significance level of 0.05 or less.

Table 5.3(a) lists the correlation coefficients between $|E^*_{40}|$ and the gradation parameters. The data shows that the GR has the potential to describe the relationship between $|E^*_{40}|$ and aggregate gradation. Table 5.3(b) summarizes the relationship between GR and $|E^*_{40}|$ in the various datasets, G1, G2, (G1 and G2), G3, and (G2 and G3).

The following observations can be made for the relationship between the GR and $|E^*_{40}|$:

- In fine-graded mixtures, the relationship is significant regardless of the binder grade.
- The relationship is not significant in coarse-graded mixtures.
- The relationship is also not significant in the combination of coarse-graded and fine-graded mixtures.

For the fine-graded aggregates, G1 and G2, the correlation between $|E^*_{40}|$ and the asphalt binder content, the effective volume binder content (V_{eff}), the air voids (V_a) and the voids in mineral aggregates has shown weak correlations where it was found 0.25, –0.20, –0.29 and –0.54 respectively

Table 5.3(a): Correlation coefficients (r) between $|E_{40}^{*}|$ and aggregate gradation parameters

Gradation parameters	Mixture groups				
	G1	G2	G1 and G2	G3	G2 and G3
Passing 4.75 mm sieve	-0.101	-0.231	-0.085	-0.546	0.120
Passing 0.075 mm sieve	0.721	0.888[c]	0.805[c]	0.520	0.762[c]
Gradation Ratio (GR)	-0.957[c]	-0.883[c]	-0.887[c]	-0.598	-0.504

[c]Significance level (ρ) < 0.05

Table 5.3(b): Significance of the relationship between $|E_{40}^{*}|$ and GR in the mixture groups

Statistical criteria	Mixture groups				
	G1	G2	G1 and G2	G3	G2 and G3
Sample size (N)	6	6	12	7	13
Critical coefficient ($r_{crt.}$) at (N-2) and $\rho \leq 0.05$	0.811	0.811	0.576	0.754	0.553
Correlation ($r \geq r_{crt.}$)	Yes	Yes	Yes	No	No
Level ρ	0.003	0.020	0.0001	0.156	0.079
Significant ($\rho \leq 0.05$)	Yes	Yes	Yes	No	No

5.3 $|E_{40}^{*}|$-GR Regression Model

Figure 5.1 shows the relationship between $|E_{40}^{*}|$ and GR for both fine-graded and coarse-graded mixtures respectively. Figure 5.1(a) shows the 95% confidence limits based on G1 and G2 datasets and suggests a linear relationship for fine-graded mixtures. The confidence limits suggest that S3 data point is an outlier.

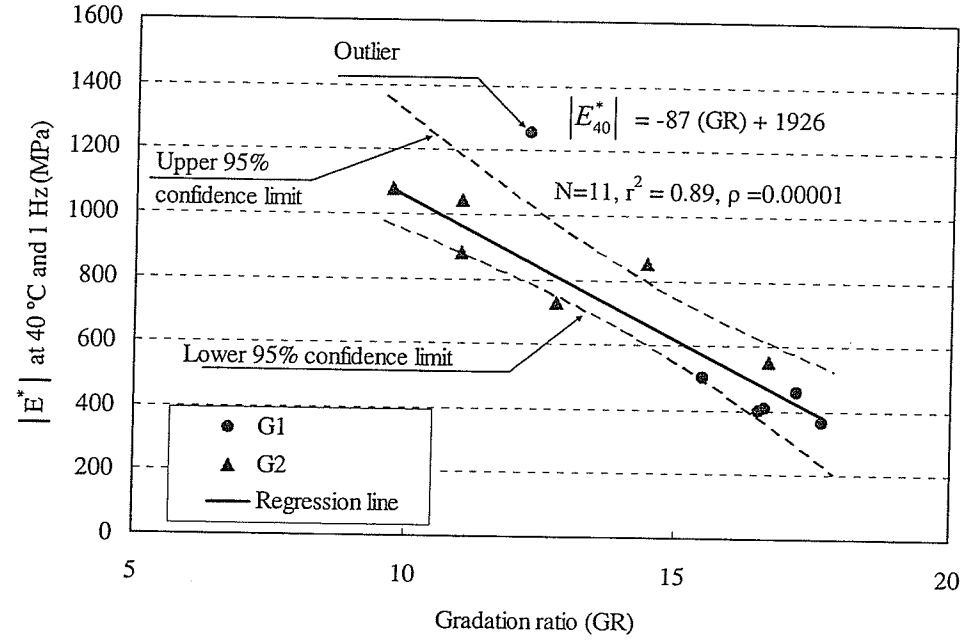

(a)

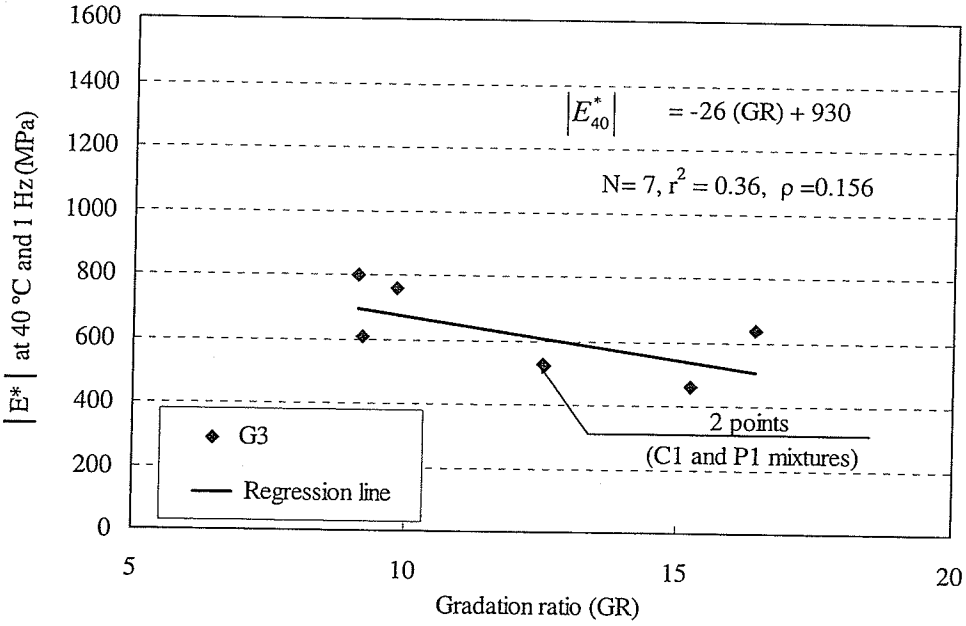

(b)

Figure 5.1: Dynamic modulus at high temperature versus the gradation ratio (GR)

(a) Fine-graded mixtures. (b) Coarse-graded mixtures.

It can be noticed that $|E^*_{40}|$ of S3 is relatively high compared to $|E^*_{40}|$ of G1 and G2 mixtures that have similar GR values. Accordingly, S3 data was excluded from the regression model. The model, as shown by Equation 5.2, was found to be statistically significant for the range of GR values of 9.7 to 17.7.

$$|E^*_{40}| = -87\ (GR) + 1926 \tag{5.2}$$

where

$|E^*_{40}|$ = the dynamic modulus at 40°C and 1 Hz, in MPa

The statistics of the model shown by Equation (5.2) is as follows:

N = 11 (based on G1 and G2 mixtures, S3 excluded)

$r^2 = 0.89$, the adjusted $r^2 = 0.87$

S_e = the standard error of estimate = 93.00 MPa

S_y = the standard deviation = 265.00 MPa

$S_e/S_y = 0.35$ and $\rho = 0.00001 < 0.05$

The statistics of the model confirm a significant relationship between $|E^*_{40}|$ and GR for fine-graded mixtures. The data consists of 11 fine-graded mixtures with different aggregate gradations, aggregate sources, and binder grades. The aggregates passing both the 0.075 mm and the 4.75 mm sieves are in the range of 3.5% –6.3% and 61.3% –77.5% respectively. The model is simple since it includes one independent variable (GR) and it is rational since $|E^*_{40}|$ decreases as GR increases. Figure 5.1(b) shows the relationship between $|E^*_{40}|$ and GR in coarse-graded mixtures.

5.4 Validation of the $|E_{40}^*|$-GR Model

The model was validated with the datasets used for the calibration, G1 and G2, and with an independent dataset, G4. The validation with G1 and G2 illustrates the accuracy of the model when applied to its calibration data. Figure 5.2 shows the $|E_{40}^*|$ prediction errors of G1 and G2 using the proposed model shown by Equation (5.2) and the Witczak model. The proposed model predicts $|E_{40}^*|$ of G1 and G2 reasonably well where the prediction errors range between –32% and +20%. These prediction errors are much lower than those of the Witczak model, which were in the range of –50% and +210%. The comparison demonstrates the potential of using GR to adjust the predicted $|E^*|$ master curve generated by the Witczak model.

The predicted $|E_{40}^*|$ values of G1 with the Witczak model are obtained at design level 2 and level 3 and those of G2 are obtained at design level 3 only. The typical binder values, A and VTS, for design level 3 are provided by the MEPDG (NCHRP 2004). The Witczak model mostly tends to overpredict $|E_{40}^*|$ at the two reliability levels.

The proposed model is verified using the independent dataset, G4. Figure 5.3 shows the prediction errors of $|E_{40}^*|$ for G4. The $|E_{40}^*|$ values of G4 mixtures are interpolated using measured values at 37.8°C and 54.4°C (100°F and 130°F).The model predicted $|E_{40}^*|$ of four mixtures of G4 reasonably well with an error range of –34% to +21%, and over-predicted $|E_{40}^*|$ of Cell 20 by almost 90%. Cell 20 has low $|E_{40}^*|$ in comparison with the other G4 mixtures and that may result from the low compaction of its specimens.

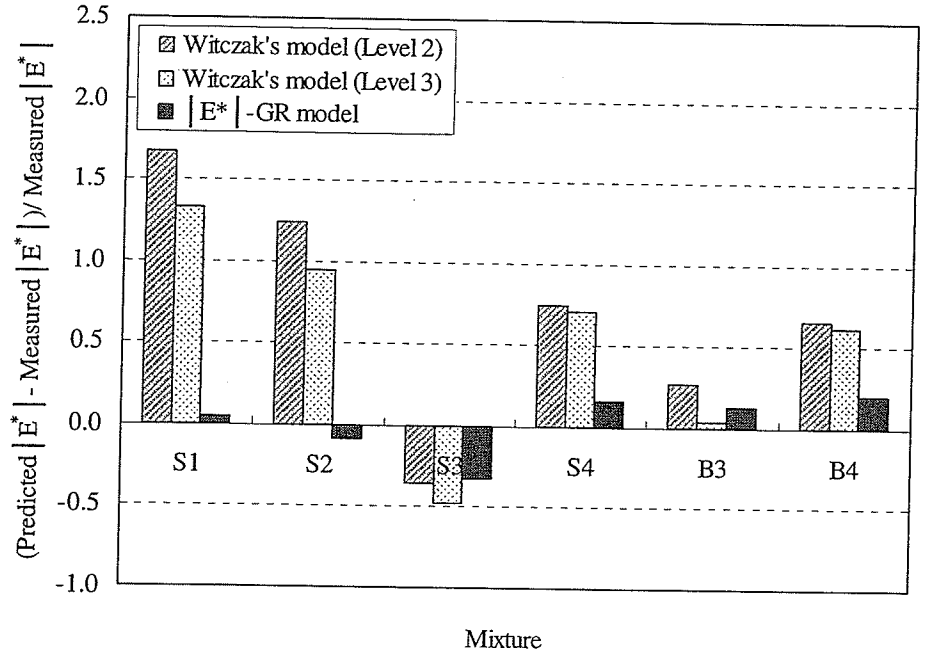

(a)

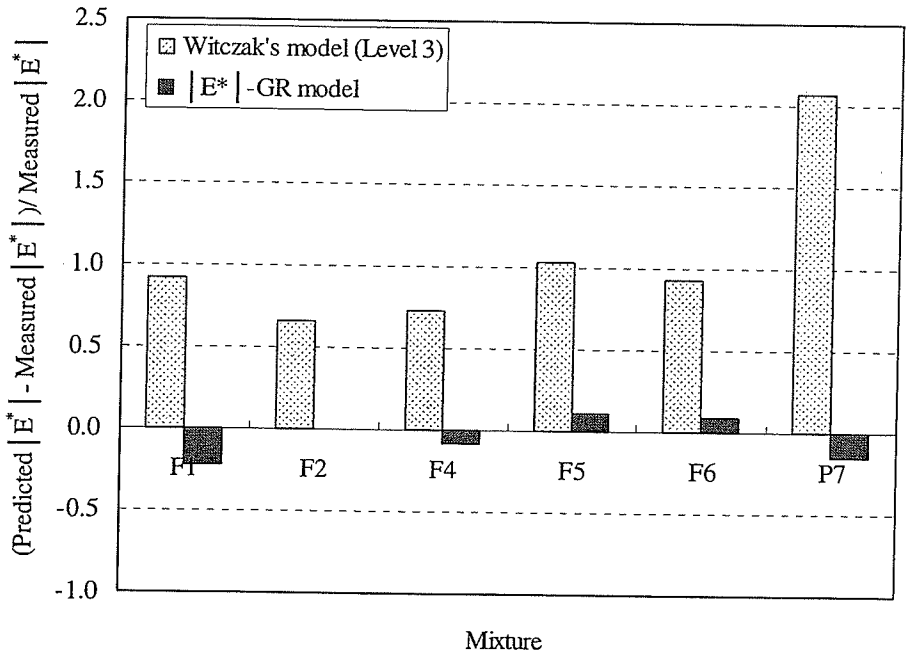

(b)

Figure 5.2: Comparison of the prediction error in $|E_{40}^{*}|$ using the proposed and Witczak models (a) G1 and (b) G2.

Schwartz (2005) used the MnRoad mixtures, G4, to validate the Witczak model and reported $|E^*|$ prediction errors up to 350% at low stiffness/high temperatures. In comparison with the $|E^*|$ prediction by using the Witczak model, the GR model predicts $|E_{40}^*|$ reasonably well for the independent mixtures, G4, and the calibration mixtures, G1 and G2. It can be noticed that the effective binder content by volume and air voids of G4 mixtures are higher than those of mixtures used to calibrate the model. The aggregate gradation confirms being the most dominant property at high temperatures, and the differences in the binder rheology and the volumetric properties of mixtures have small effect on the predicted $|E_{40}^*|$.

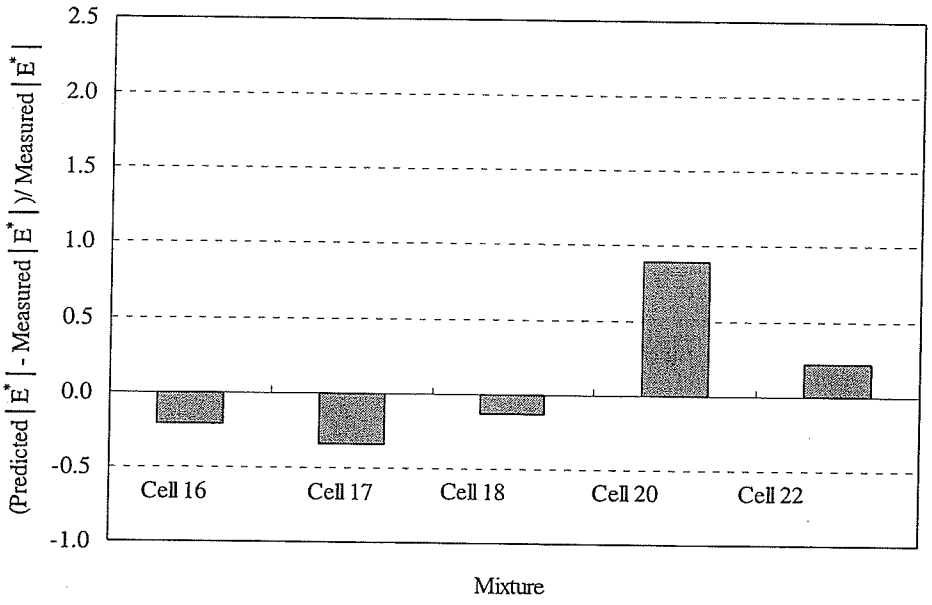

Figure 5.3: Verification of the $|E_{40}^*|$-GR model using G4 mixtures

5.5 Effect of Reclaimed Asphalt Pavement on Gradation Ratio-Stiffness Relationship

Figure 5.4 shows the relationship between M_R at 40°C and GR for field compacted AC cores that were extracted immediately after construction. The data is from 17 field mixtures extracted from 4 surface and 13 binder courses as shown in Table 3.1. Six binder mixtures contain RAP with a range of 15% to 57% as shown in Table 3.6. It can be noticed that M_R at 40°C of S5 and B12 is not within the M_R range of mixtures that have the same GR values. The Poisson's ratio at 40°C of S5 calculated according to LTPP 07 project was a negative value so the test specimens may have experienced damage leading to unreasonable M_R value.

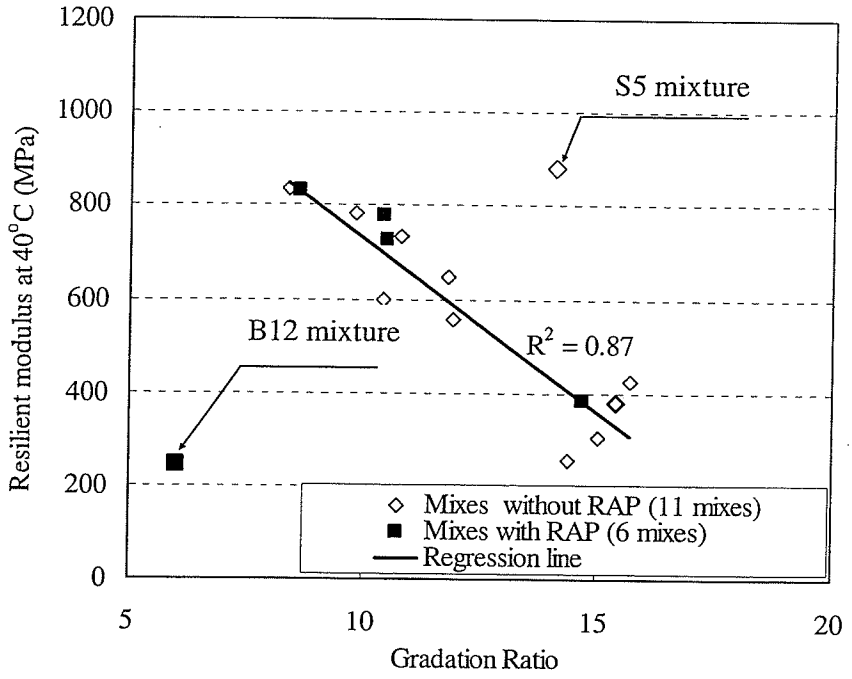

Figure 5.4: Effect of percent of reclaimed asphalt pavement on the relationship between aggregate gradation and stiffness of the mixture at 40°C

The low M_R value of B12 mixture may result from the high percent RAP in the mixture, which is 57%. Figure 5.4 confirms existing the relationship between the stiffness of fine-graded mixtures, which are represented with M_R or $|E^*|$, and the aggregate gradation represented with the proposed GR even in-service AC mixtures. Furthermore, it shows that RAP does not have a significant effect on the relationship.

5.6 Improving Witczak |E*| model at High Temperature

The model is used for adjusting the predicted $|E^*|$ master curve for fine-graded mixtures. The adjustment considers that the effect of aggregate gradation dominates $|E^*|$ at high temperature and this effect diminishes with decreasing temperature. The adjustment is performed in three steps. Firstly, the Witczak model is used to predict $|E^*|$ master curve using the volumetric properties of mixtures. Secondly, $|E_{40}^*|$ is predicted from the GR by applying the proposed model shown by Equation (5.2). Finally, the predicted $|E^*|$ master curve is pivoted at the highest reduced frequency ($f_r \approx 10^6$ Hz) and rotated to match the predicted $|E_{40}^*|$. Figure 5.5 illustrates the process of adjusting the predicted $|E^*|$ master curve of S1 and it compares the predicted $|E^*|$ master curves before and after the adjustment with the measured $|E^*|$ master curve. As illustrated in Figure 5.6, the predicted $|E^*|$ is improved at high and intermediate temperatures. Consequently, the predictions of rutting and fatigue cracking, which are relevant to the response at high and intermediate temperatures, are expected to be predicted more reliably. In addition, the model could be used as a preliminary mix design tool for optimizing stiffness of asphalt mixtures at high temperatures and accordingly reducing the potential of rutting. Higher stiffness mixtures can be achieved by lowering the GR.

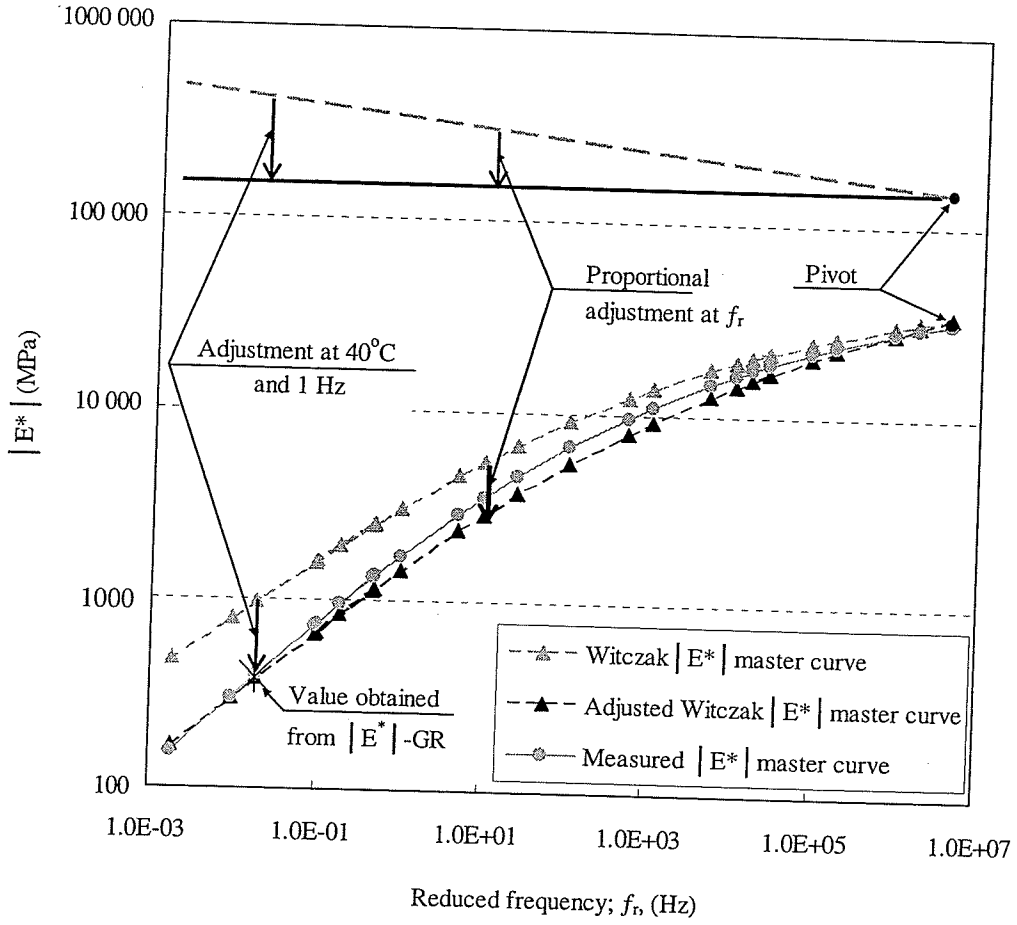

Figure 5.5: Adjusting of the Witczak predicted $|E^*|$ master curve using the $|E^*_{40}|$-GR model.

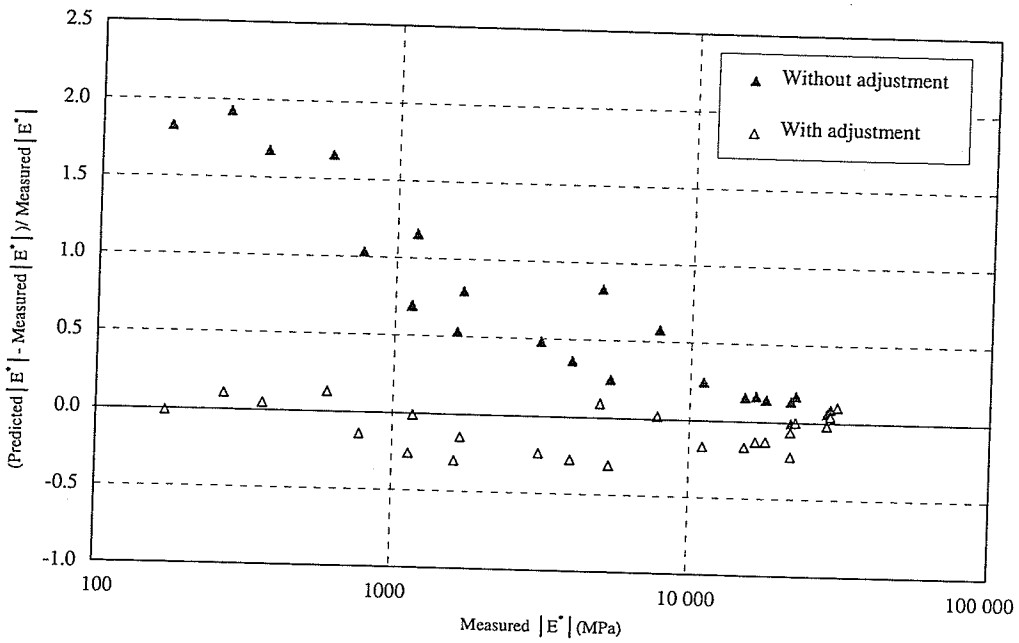

Figure 5.6: the Witczak $|E^*|$ master curve before and after adjusting with the $|E_{40}^*|$-GR mode

5.7 Discussion

The statistical analysis confirmed that aggregate gradation has a significant effect on the stiffness of asphalt concrete at high temperature and that GR appears to capture this effect adequately for fine-graded mixtures. This finding was validated in a relatively wide range of mixtures and aggregate blends. In mix design, a low GR should be desirable whenever possible, because it relates to a higher dynamic modulus. By definition, a lower GR is the result of a larger coarse fraction and a smaller fine fraction. A mixture with a low GR should have a higher percentage of interparticle contacts and crush counts than a mixture with a high GR.

These findings are consistent with the current mixture design practices which encourage stone-on-stone contact and better aggregate interlock with emphasis on aggregate shape and angularity. Excessive use of fines reduces the stiffness of the mixture and its ability to recover during unloading, thus leading to a more rapid rate of permanent deformations.

The Witczak model accounts for many aggregate, binder, and mixture properties and predicts performance reasonably well at low and intermediate temperatures; however at high temperature performance depends largely on the aggregate structure particularly with the soften types of asphalt used in cold regions. Using Witczak's model alone reduces the reliability of the modulus data at high temperature because the effect of aggregate structure may not be adequately represented in the model. The GR model, being statistically based on the GR and on laboratory tests performed at high temperature, can be used successfully to calibrate master curves produced by the more complex predictive models of dynamic modulus.

6 Pulse Time-Test Frequency Conversion Method

6.1 Introduction

Frequency (f) represents the time-dependent behaviour of AC under harmonic sinusoidal loading. On the other hand, pulse time (t_p) is the duration of the influence of the field or laboratory stress. In this chapter, an approach is proposed to convert the pulse time to frequency. The conversion method is required to assign $|E^*|$ as quasi-elastic AC modulus in the multilayered pavement system analysis, and to define the relationship between $|E^*|$ and AC stiffness under other loading forms. The approach is based on the viscoelastic theory and on equal recoverable strains resulting from both the pulse and sinusoidal stresses.

The field and laboratory pulse stresses can be represented with one of the symmetric shape forms listed in Table 2.1. In fact, the actual field stress shows delayed responses and has residual stresses due to the viscoelastic property (Al-Qadi et al., 2008b). The form of the field stress is best obtained from the analysis of the viscoelastic pavement system or measured directly from the field. Al-Qadi et al. (2002) found that the normalized bell-shape function shown by Equation (2.42) represents the measured vertical stress at various depths particularly for the loading side of the stress history. The difference between the field and laboratory stresses is that the rest period observed between load applications in the field is much greater than the rest period in the laboratory (Lytton et al., 1993). Consequently, almost all of the viscoelastic strain in the

field is recovered while the amount of recoverable resilient strain (ε_r) in laboratory tests depends on duration of the rest period. In this chapter, the equivalent frequency has been calculated for the loading pulse of the resilient modulus test by considering the instantaneous response.

In order to validate this method, $|E^*|$ and M_R are computed from the strains resulting from normalized continuous and pulse sinusoidal stresses, respectively. The results of the approach are compared with other methods from the literature.

6.2 Approach of the Pulse Time -Frequency Conversion

Figure 6.1 presents the proposed approach to calculate the test frequency of $|E^*|$ for a given normalized pulse stress. The controlling condition of the computation is that the recoverable strain (ε_0) of AC subjected to a normalized sinusoidal stress ($\sigma_0 = 1$) with f (Hz) is equal to the resilient pulse strain (ε_r) resulting from the normalized pulse stress. The ε_r for the field loading is assumed the maximum value of the strain history resulting from the normalized pulse stress. However, for the laboratory pulse loading, ε_r can be obtained from the strain history by applying definition of the resilient deformation, which is the instantaneous and total deformations, obtained from laboratory deformation plots.

The approach utilizes the linear viscoelastic theory represented by Equation (2.6) to determine the axial strain history, $\varepsilon(t)$, of AC subjected to an axial normalized pulse stress history, $\sigma(t)$.

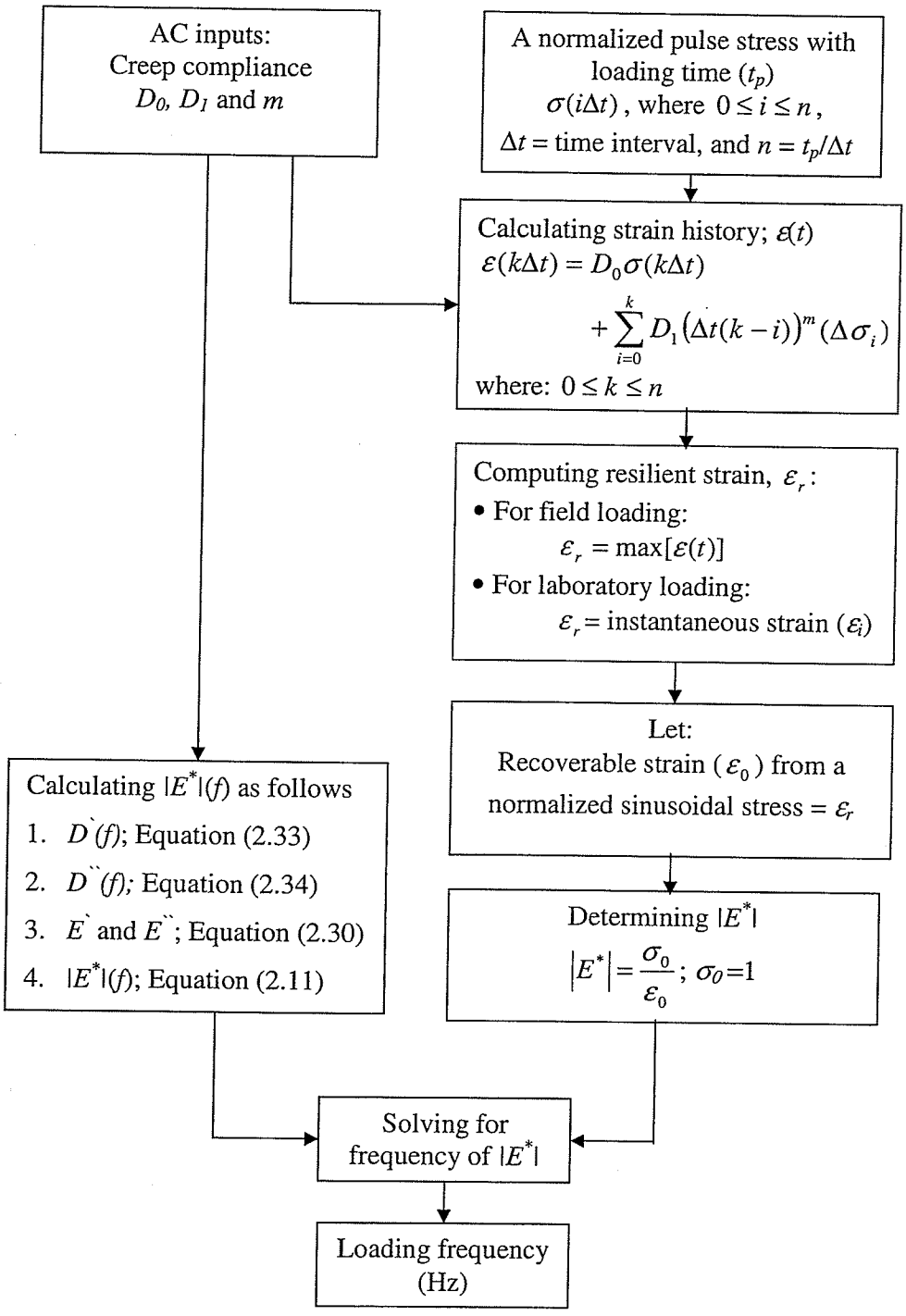

Figure 6.1: Proposed approach to determine the frequency equivalent to a pulse time

AC is characterized with GPL creep compliance parameters, D_0, D_1 and m, as shown by Equation (2.4). The integration shown by Equation (2.6) is carried out numerically and it can be represented with Equation (6.1).

$$\varepsilon(k\Delta t) = D_0\sigma(k\Delta t) + \sum_{i=0}^{k} D_1\left(\Delta t(k-i)\right)^m(\Delta\sigma_i) \tag{6.1}$$

where

$\Delta t = t_i - t_{i-1}$, the time interval,

$\Delta\sigma_i = \sigma_i - \sigma_{i-1}$, the change in stress and

k = the order of the time interval at which the strain is calculated.

Figures 6.2 and 6.3 illustrate computing of ε_r from $\varepsilon(t)$ for the pulse stress that represents the field loading and the laboratory M_R loading, respectively. Figure 6.2 shows that ε_r is the maximum value of the pulse strain history under field loading.

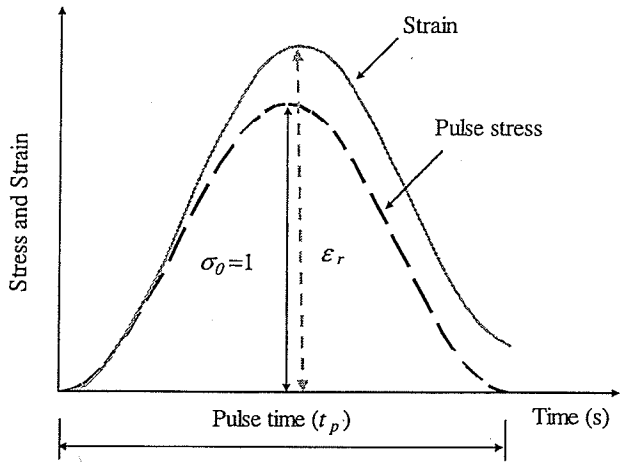

Figure 6.2: The resilient strain of the field pulse stress

An assumption is made that the rest duration between two consequent wheel loads is long enough to allow ε_r to be fully recovered. This assumption simplifies the frequency calculation since the rest duration depends on design traffic characteristics that are configuration of the axle load, traffic volume and traffic speed.

The recoverable strain of M_R whether it is the instantaneous (ε_i) or total (ε_t) strains is calculated for pulse with a total cycle period of one second consisting of loading time of t_p and a rest period of (1-t_p). ε_i is measured at the end of the unloading portion and ε_t is measured at the end of the rest period. Figure 6.3(a) shows process of computing of ε_i and ε_t following a procedure described by the test protocol of LTPP P07 for the determination of the instantaneous deformations from deformation-time plots. The LTPP P07 procedure is described for a sinusoidal pulse load of 0.1s followed by a rest period of 0.9s. To account for other loading times, this procedure has been re-defined in terms of t_p, as shown in Figure 6.3. Two regression lines are constituted from the strain history.

Figure 6.3(b) shows that regression line 1 is developed from the strain-time data of the unloading portion from $\frac{t_p}{6}$ to $\frac{t_p}{4}$ measured from the peak strain. Regression line 2 is developed from strain-time data of the last 0.2 s of the rest period. ε_i is measured between the peak strain and the strain at the intersecting point of the regression lines 1 and 2, and ε_t is the strain difference at the peak and the end of the rest period.

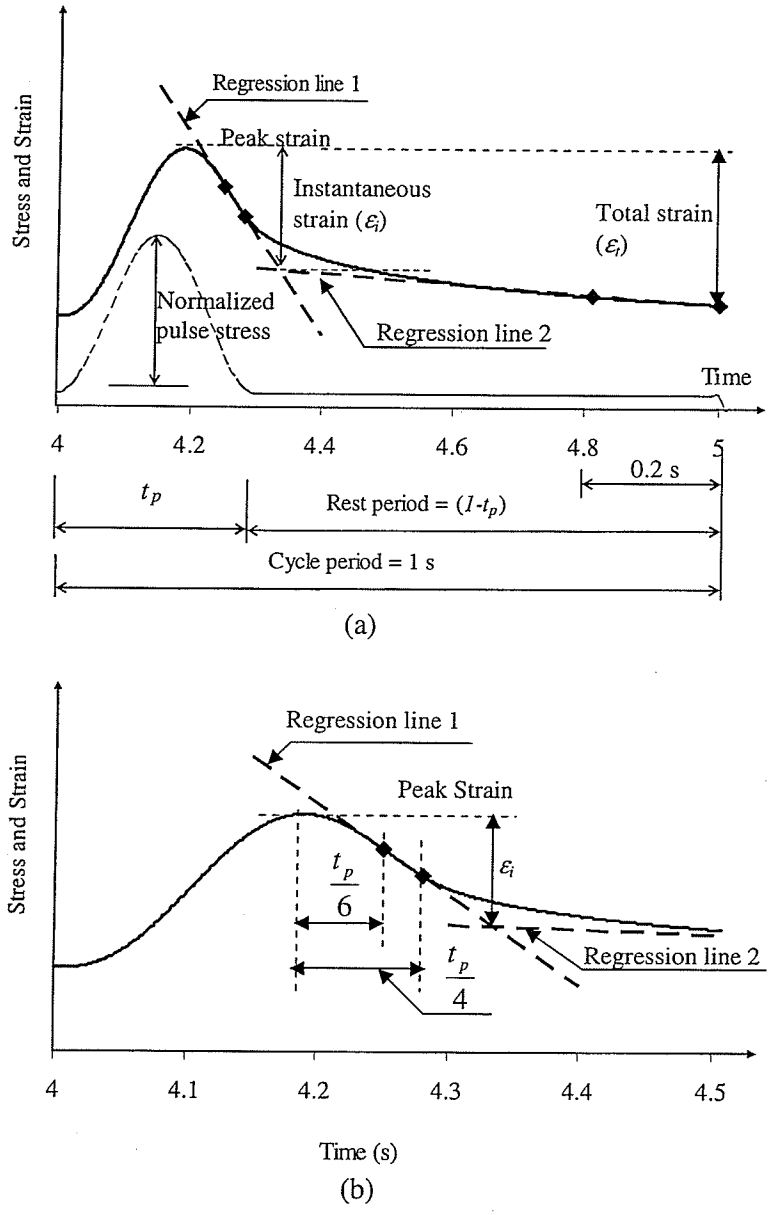

Figure 6.3. Definition of the resilient strain of M_R

(a) Constructing regression line 2. (b) Constructing regression line 1

f is the frequency of $|E^*|$, at which ε_0 resulting from subjecting AC to a normalized continuous sinusoidal stress is equivalent to ε_r. Knowing ε_r, f can be calculated as

follows. First, $|E^*|$ is calculated from ε_o and σ_o. Second, $|E^*|$ can be obtained as function of f for the given AC creep compliance parameters. Equations (2.23 and 2.24) are used to calculate the complex creep compliance (D^*) as a function of f. Then $|E^*|$ as a function of f can be obtained by applying Equations (2.11 and 2.30). Finally, f is determined by equating the $|E^*|$ value obtained from the first step and $|E^*|$ as a function of f.

6.2.1 Computing creep compliance parameters from the dynamic modulus

The creep compliance parameters, D_0, D_1 and m, can be determined from static creep, cyclic creep ($|D^*|$) and $|E^*|$ tests. Kim et al. (2005) concluded that the choice of the test method has a significant effect on the creep parameters. The effect results from the sensitivity of AC to loading rate. The cyclic tests can accurately characterize AC under short loading times while the static test can characterize it under long loading times. To determine a representative relationship between f and t_p, D_0, D_1 and m should be obtained from cyclic tests since the duration of the pavement pulse load is short with respect to the loading time of the static creep test, which at least is 100 seconds. These parameters have been determined for S1-S4 and B1-B4 at four temperatures from $|E^*|$ using Equations (2.27 to 2.34) by applying an approach described by Kim and Lee (1996) as follows:

1. Calculating $E`$ and $E``$ from measured $|E^*|$ and ϕ values at multiple frequencies using Equations (2.12 and 2.13).
2. Calculating $D`$ and $D``$ at $f$ using Equation (2.29). Table 6.1 lists $D`$ and $D``$ of S1.
3. Solving Equation (2.33) for D_0, D_1 and m using the least square technique.

Table 6.1(a): Storage complex creep compliance of S1

Temperature	Storage creep compliance (1/GPa)					
	25 Hz	10 Hz	5 Hz	1 Hz	0.5 Hz	0.1 Hz
-10	0.032	0.034	0.034	0.043	0.045	0.054
5	0.045	0.058	0.063	0.084	0.117	0.179
25	0.167	0.219	0.280	0.503	0.708	1.407
40	0.527	0.765	1.122	2.393	3.231	5.297

Table 6.1(b): Loss complex creep compliance of S1

Temperature	Loss creep compliance (1/GPa)					
	25 Hz	10 Hz	5 Hz	1 Hz	0.5 Hz	0.1 Hz
-10	0.004	0.005	0.006	0.009	0.011	0.015
5	0.009	0.016	0.019	0.033	0.053	0.093
25	0.083	0.122	0.161	0.312	0.486	0.902
40	0.322	0.442	0.651	1.359	1.823	2.444

Table 6.2 lists D_0, D_1 and m of S1-S4 and B1-B4. These values have been obtained by least square technique where initial values are assumed, and then the sum of the least square errors is minimized. D_0 at 40°C for most mixtures was a negative value so the solution was carried again forcing D_0 to be zero indicating fully viscous material. Table 6.2 has been used to validate the numerical integration shown by Equation (6.1) and to investigate the relationship between the loading time of the pulse stress and the loading frequency of the sinusoidal continuous stresses. Using the GPL model to represent the creep compliance of AC has some advantages. The GPL is a simple model since it has three parameters and each of them describes a material property where D_0 represents the response at very short loading time, D_1 represents the viscoelastic property at one second and m represents the viscous (creep) property. In addition, $|E^*|$ can be calculated exactly

for each set of parameters by applying Equations (2.27 to 2.34) without numerical integration. Furthermore, GPL parameters represent AC viscoelastic property at a specific temperature, so they can help in investigating the effects of temperature and AC stiffness on the relationship between the pulse loading time and frequency. Underwood and Kim (2009) used Prony series to represent the creep compliance of AC to determine $\varepsilon(t)$, and the number of the Prony series terms changed from a mixture to another.

Table 6.2: Calculated power model parameters of $D(t)$ from $|E^*|$ of laboratory mixtures

Mixture	Temp °C	D_0 1/GPa	D_1 1/GPa	m
S1	-10	0.018	0.037	0.183
	5	0.027	0.171	0.370
	25	0.114	1.909	0.566
	40	0.000	6.899	0.429
S2	-10	0.023	0.039	0.267
	5	0.034	0.175	0.352
	25	0.059	1.665	0.454
	40	0.000	5.053	0.379
S3	-10	0.000	0.049	0.072
	5	0.034	0.072	0.286
	25	0.000	0.463	0.299
	40	0.041	1.821	0.385
S4	-10	0.001	0.065	0.098
	5	0.041	0.185	0.348
	25	0.046	1.462	0.379
	40	0.000	6.158	0.390

Mixture	Temp °C	D_0 1/GPa	D_1 1/GPa	m
B1	-10	0.036	0.040	0.344
	5	0.042	0.126	0.330
	25	0.066	1.228	0.425
	40	0.000	4.478	0.399
B2	-10	0.031	0.027	0.266
	5	0.034	0.110	0.264
	25	0.039	0.517	0.300
	40	0.053	1.969	0.382
B3	-10	0.038	0.067	0.199
	5	0.076	0.195	0.368
	25	0.071	1.325	0.377
	40	0.000	3.616	0.349
B4	-10	0.032	0.066	0.248
	5	0.073	0.320	0.428
	25	0.023	2.091	0.382
	40	0.252	6.168	0.462

6.2.2 Validation of the Numerical Integration

The numerical convolution integral shown by Equation (6.1) has been validated through calculating $|E^*|$ and M_R of B2-B4. Figure 6.4 shows the comparison between the measured and calculated $|E^*|$. Figure 6.5 compares the calculated instantaneous and total resilient moduli with the measured values. The ε_0 of AC subjected to a normalized sinusoidal stress at various frequencies has been obtained from $\varepsilon(t)$ that is calculated numerically by using Equation 6.1 and then $|E^*|$ is calculated by applying Equation 2.11. Similarly, the instantaneous and total M_R values have been obtained by applying Equation 6.1 using a normalized sinusoidal pulse with loading time of 0.1s followed by a rest period of 0.9s.

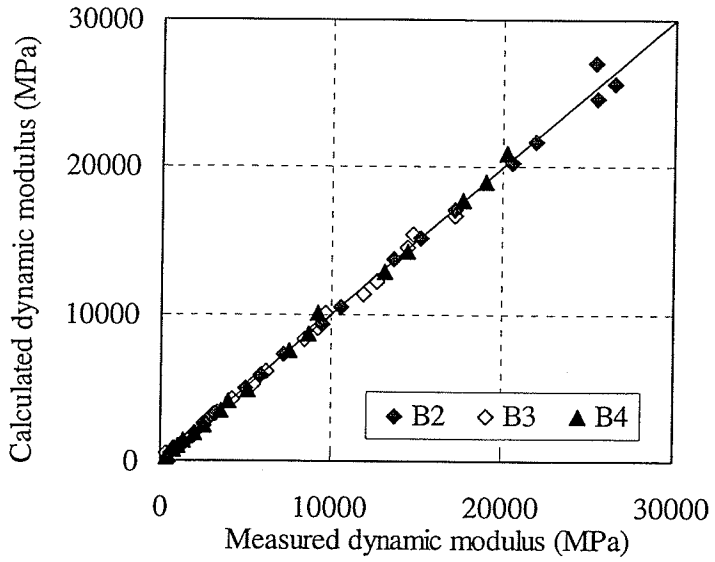

Figure 6.4: Comparison between measured and calculated dynamic modulus

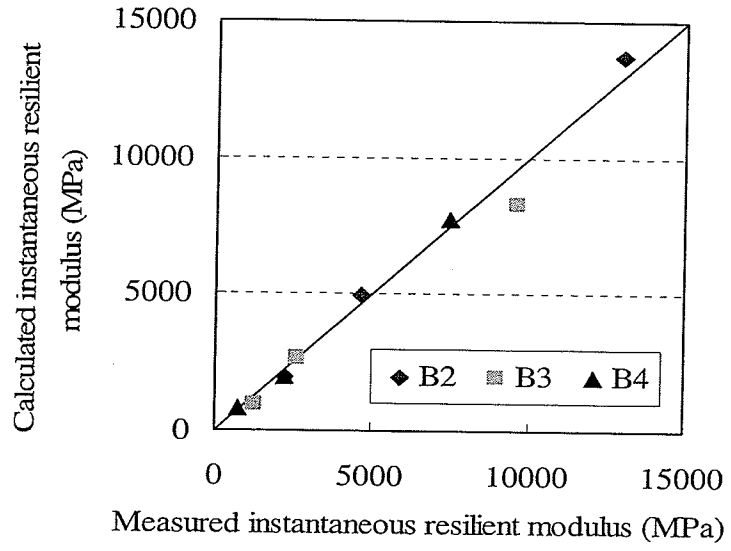

(a) Instantaneous resilient modulus

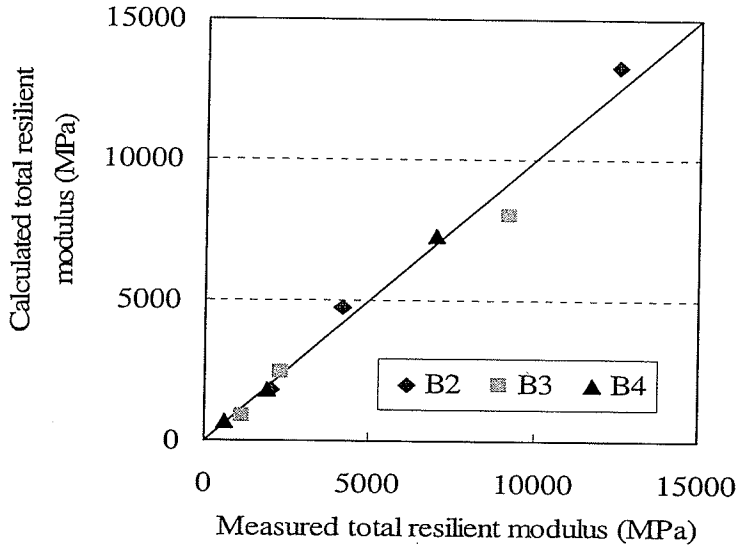

(b) Total resilient modulus

Figure 6.5: Comparison between the measured and calculated resilient modulus

The resilient strain including ε_i and ε_t has been obtained from $\varepsilon(t)$ using the procedure described with Figure 6.3. Then, the instantaneous and total M_R values are determined by applying Equation (2.54).

Figures 6.4 and 6.5 illustrate effectiveness of the proposed numerical convolution integral to calculate AC stiffness and consequently the strain from the parameters of the creep compliances. Since D_0, D_1 and m have been calculated from the measured $|E^*|$ values, high agreement is shown between the calculated and measured $|E^*|$ values are comparable. Figure 6.5 shows that the calculated M_R values from the axial loading are in good agreement with the measured M_R using the indirect tensile loading. This finding agrees with the literature where Kim et al. (2004) concluded that there is no significant difference between $|E^*|$ determined from both the axial loading and the indirect tensile loading within LVE range.

Performing the integration shown in Equation (6.1) numerically has many benefits. First, it facilitates applying the approach for asymmetric $\sigma(t)$ such as field-measured stresses even without knowing the pulse loading time. Symmetric $\sigma(t)$ can be represented with an equation such as haversine, bell-shape, sinusoidal and squared pulse shapes. While asymmetric $\sigma(t)$ could be measured from the field or obtained from a viscoelastic analysis. AC shows delayed response especially in the unloading portion. Second, numerical integration helps incorporating the rest period especially for laboratory-applied pulses to determine the resilient strain (ε_r). Finally, $\varepsilon(t)$ can be obtained without the need to perform complex integrations.

6.3 Time-Frequency Conversion Equations for Pulse Stresses

The proposed approach has been applied to determine the loading frequency (Hz) as a function of pulse loading time (s) for the following cases:

- Pulses used to represent the field pavement stress such as haversine (Equation 2.41), the bell-shape (Equation 2.42), sinusoidal ($0.5\left[1-\cos(\frac{2\pi}{t_p}t)\right]$) and square forms.
- Sinusoidal pulse used for laboratory M_R testing.
- The load history of the Falling Weight Deflectometer (FWD).

Table 6.3 lists the average of the frequencies (Hz) at selected pulse loading time (second) of the field pulse stress. The frequency has been calculated at each loading time for B1-B4 at -10, 5, 25 and 40°C. The percent coefficient of variation (CV) has been calculated at each loading time. Generally, CV is low and it increases with the shift of the pulse from the sinusoidal stress form of $|E^*|$. The CV is the highest for the squared pulse. In contrast, CV decreases with the loading time. The frequency of the bell-shape pulse is not presented in Table 6.3 since this pulse is controlled with the standard deviation (s) as shown in Equation (2.42).

Figure 6.6 shows the relationship between the frequency and the loading time for the sinusoidal pulse stresses. The relationship is well represented with a straight line on the log-log chart. There is strong relationship between the frequency and the loading time.

Table 6.3: Mean and coefficient of variation (CV) of the frequency at various loading times of pulse stresses

Loading time (s)	Sinusoidal pulse		Haversine pulse	
	Frequency (Hz)	CV (%)	Frequency (Hz)	CV (%)
1.00	0.37	2.3	0.30	7.5
0.50	0.74	2.6	0.58	8.2
0.40	0.92	2.7	0.73	8.5
0.30	1.23	2.8	0.97	8.8
0.20	1.83	3.2	1.44	9.3
0.10	3.65	3.5	2.83	10.0
0.05	7.25	3.9	5.58	10.6
0.02	18.02	4.3	13.69	11.3

Loading time (s)	Triangular pulse		Squared pulse	
	Frequency (Hz)	CV (%)	Frequency (Hz)	CV (%)
1.00	0.45	3.5	0.11	9.0
0.50	0.90	3.8	0.21	9.5
0.40	1.12	3.9	0.26	9.7
0.30	1.50	4.1	0.35	9.9
0.20	2.24	4.3	0.52	10.2
0.10	4.41	5.4	1.03	10.9
0.05	8.77	6.1	2.03	11.5
0.02	21.81	6.8	4.97	12.1

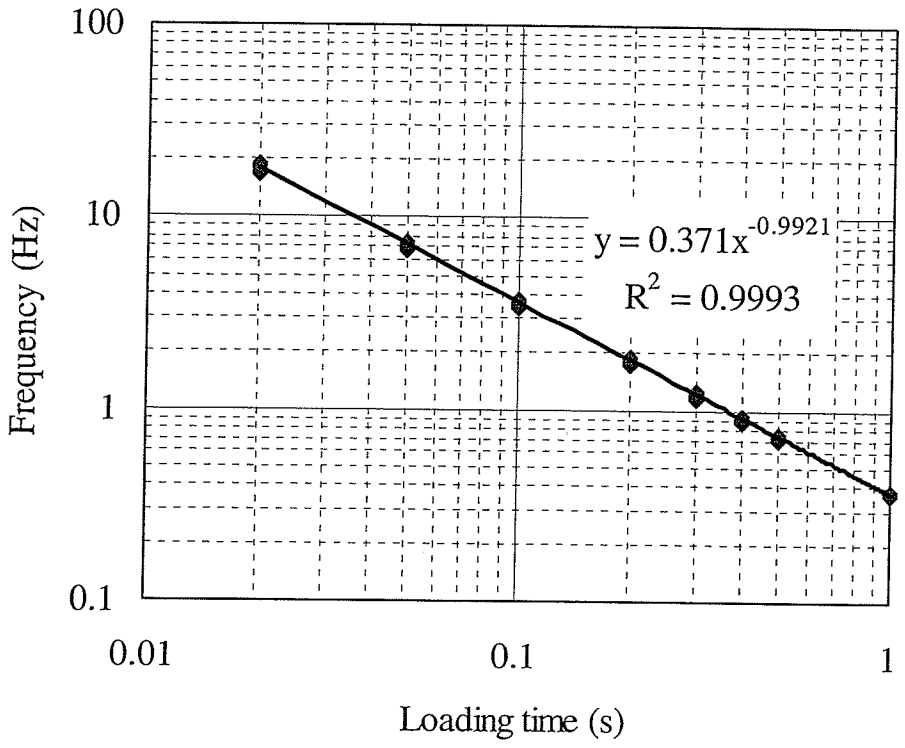

Figure 6.6: Loading time-frequency relationship for the sinusoidal pulse stress

The relationship can be represented with the following equation form.

$$f = \frac{k}{t_p} \tag{6.3}$$

where

k = constant depends of the pulse shape form.

Table 6.4 lists the conversion equations and their coefficients of determination (R^2) for the pulse forms under investigation. For the bell-shape function, it has been assumed that t_p is four times of the standard deviation (s) that controls the curve. It is clear that each of

these equations has k-value less than one. This means that using Equation (2.35) overestimates the loading frequency whatever is the pulse stress form. Overestimating the frequency leads to a higher $|E^*|$ and consequently un-conservative pavement design where the pavement performance is expected to be underestimated. Al-Qadi et al. (2008b) found that the field stress can be represented with the normalized bell-shape. Equation (2.35) overestimates the frequency with 131% error, and Equation (2.36) underestimates the frequency with 63% error.

Table 6.4: Pulse time-frequency equivalences

Criteria	Sinusoidal pulse	Haversine pulse	Bell-shape pulse	Triangular pulse	Squared pulse
Equivalent frequency	$\frac{0.366}{t_p}$	$\frac{0.368}{t_p}$	$\frac{0.432}{t_p}$	$\frac{0.449}{t_p}$	$\frac{0.105}{t_p}$
Coefficient of determination (R^2)	0.997	0.981	0.997	0.994	0.979

The equivalent frequency for the sinusoidal pulse loading time of the M_R testing is determined by applying the approach including the procedure of computing ε_i and ε_t. Table 6.5 lists the equivalent frequency at selected pulse loading times where the frequency has been determined based on ε_i. Table 6.5 can be represented with the following equation.

$$f = \frac{0.496}{t_p} \tag{6.4}$$

From comparing Equation (6.4) with the conversion equation for the sinusoidal pulse shown in Table 6.4, the definition of the resilient strain has significant effect on the determined frequency. Figure 6.2 and Figure 6.3 show the determination of the resilient

strain from the strain-time history for calculating the equivalent frequency of field pulse loading and the equivalent frequency of the resilient modulus, respectively. Furthermore, Equation (6.4) indicates that both the approaches represented with Equation (2.35 and 2.36) are incorrect. Equation (2.35) overestimates the frequency by 50.4% while Equation (2.36) underestimates the frequency by 68%.

Table 6.5: Equivalent frequencies for loading pulse for instantaneous resilient modulus

Loading time (s)	Frequency (Hz)	CV (%)
0.03	13.30	0.93
0.05	8.32	0.48
0.10	4.70	0.77
0.20	3.04	1.71
0.30	2.32	1.75
0.40	1.92	1.25

The equivalent frequency of the FWD load history has been obtained by the proposed approach. Figure 6.7 shows the normalized FWD load and deformation histories. It can be seen that the deformation was collected over a short period compared to the M_R pulse load that allows a rest period with nine times of the pulse time. Consequently, the calculation of pavement stiffness including AC stiffness is based on the instantaneous response of FWD loading. Herein, the equivalent frequency of the normalized FWD pulse stress is calculated by applying the same procedure of determining the equivalent frequency of M_R pulse loading. It has been found that the equivalent frequency is 15.7 Hz with CV of 7%. If the deformation collected over a long time that is enough to catch the

delayed response of the pavement and the FWD backcalculated stiffness is determined based on the maximum resilient deformation, the equivalent frequency will be 13 Hz with CV of 5%.

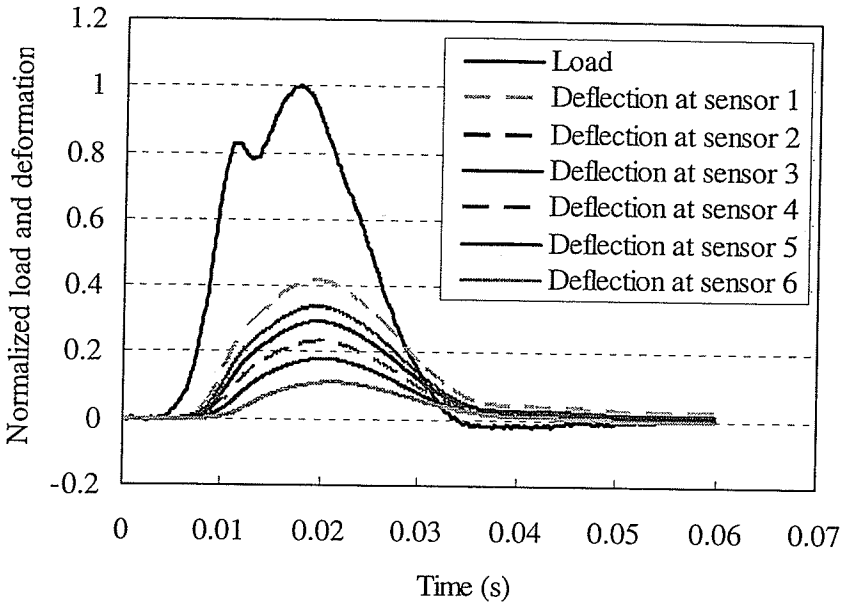

Figure 6.7: Normalized load and deformations of FWD load drop

6.4 Impact the Loading Time-Testing Frequency Conversion

Figure 6.8 shows the $|E^*|$ master curve of B2 plotted as a function of the reduced time that is calculated based on the current MEPDG approach with Equation 2.35 and on the proposed approach considering field haversine pulse stress. Figure 6.8 shows that the MEPDG approach overestimates $|E^*|$ at all frequencies and the difference increases at low $|E^*|$ leading to overdesigned pavement structure. Rutting is sensitive to low stiffness and it may be underestimated in this manner.

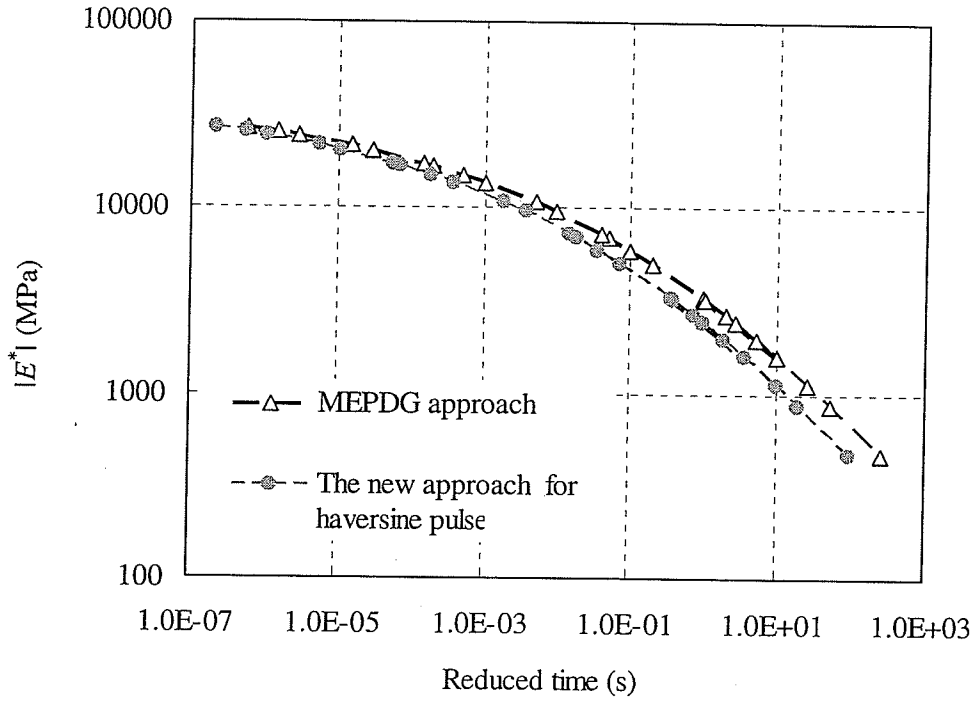

Figure 6.8: Dynamic modulus master curve of B2 as a function of the loading time

6.5 Discussion of Frequency-Time Conversion

The f-t_p conversion is consistent with findings from literature. Kim and Lee (1996) found experimentally that the backcalculated FWD moduli are equivalent to measured $|E^*|$ of field cores values at 16 Hz, which is close to the calculated mean of 15.7 Hz with CV of 7%. In the same research, it was found that the measured M_R values is higher than $|E^*|$ at 5 Hz and generally lower than $|E^*|$ at 10 Hz. According the proposed approach, the equivalent frequency of M_R measured at 0.1s pulse time is 5 Hz.

The proposed conversion equations indicate that the MEPDG approach overestimates the frequency by up to 173% of the value calculated based on the viscoelastic theory. The

overestimation of the frequency depends on the pulse shape of the field stress.

Since the approach applies the viscoelastic theory and uses a numerical computation to determine the strain history, it can be applied to determine the frequency of field pulse stress without the need to determine the loading time. The field stress shows delayed response and residual stresses and consequently the symmetric pulse form may not fit it well (Al-Qadi et al., 2008b) so the actual stress should be used to obtain the exact equivalent frequency.

The Fast Fourier Transform (FFT) analysis has been carried out to determine the equivalent frequency of the FWD pulse load. The dominant frequency according to the approach proposed by AL-Qadi et al. (2008-b) is 15.83 Hz. This frequency is the same as the frequency calculated according to the proposed approach and considering the instantaneous strain. This strain neglects the delayed response of AC; so it is close to the elastic response. According to the proposed approach and considering the delayed response, the frequency was 13 Hz. Consequently, FFT approach in its current form may overestimate the frequency of the field pulse stresses.

6.6 Summary

An approach has been introduced to convert the pulse loading time to frequency at which the dynamic modulus can be used in multilayer elastic analysis. The conversion utilizes the viscoelastic theory to calculate the recoverable strains of AC subjected to the normalized sinusoidal continuous stress and the normalized pulse stresses. The frequency

is calculated at a given loading time when both the recoverable strains are equivalent. The numerical computation of the strain histories made easy incorporating different pulse shapes and the rest periods and AC has been modeled with the creep compliance that is represented with general power law. The creep compliance parameters have been obtained from the dynamic modulus and phase angle to represent accurately the short loading time of traffic. The approach differentiates between the field pulse stress and the laboratory applied pulse stress used for AC characterization since both of them are followed with different rest periods.

The numerical integration shows the ability to calculate with significant accuracy both the measured dynamic and resilient moduli. The approach can calculate the frequency for any pulse shape whether it is collected from the field or from the pavement analysis. It can be applied to determine the frequency for special AC mixtures such as Stone Matrix Asphalt (SMA) if the creep compliance of a mixture is represented by the Equation (2.4).

Conversion equations have been developed based on the proposed approach to convert the loading time of the common pulse shape forms in pavement analysis to the frequency. It has been showed that the current approach of MEPDG overestimates the frequency with up to 171% depending on the pulse form. Furthermore, FFT method to determine the frequency content of the pulse and the dominant frequency has been shown to overestimate the frequency slightly.

The approach has been applied to determine the equivalent frequency for M_R and FWD

backcalculated stiffness. Both M_R and FWD stiffness are used in pavement evaluation and rehabilitation along with the dynamic modulus. Finding the equivalent frequency increases the reliability of pavement evaluation and design.

7 Predicting the Dynamic Modulus from Resilient Modulus Tests

7.1 Approach of Predicting |E*| from MR

Figure 7.1 illustrates the proposed approach to predict $|E^*|$ from M_R. The approach uses three relationships: the pulse loading time (t_p) and its equivalent frequency (f_{eq}), $|E^*|$ and temperature at a given frequency, and the shift factor and temperature. Equation 6.4 is used to determine f_{eq} for a given t_p of sinusoidal pulse load. For a pulse form other than the sinusoid, the approach presented in chapter 6 can be followed to calculate the equivalent frequency. At f_{eq}, $|E^*|$ is equivalent to the measured M_R at 5, 25, 40°C.

$|E^*|$ at any temperature can be interpolated from the equivalent $|E^*|$ at three temperatures using a function that represents reasonably the $|E^*|$ isochronal curve, Figure 2.5(b), at f_{eq}. The isochronal curve function can be used to predict $|E^*|$ at any temperature. Three functions have been examined to represent the isochronal curve and interpolate $|E^*|$. Applying the time-temperature superposition, $|E^*|$ at f_{eq} as a function of temperature can be generated from master curves. The process of selecting an interpolation function for $|E^*|$ at f_{eq} of 5 Hz is introduced and it can be followed to determine another interpolation function for $|E^*|$ at different frequencies. For f_{eq} of 5 Hz, the quadratic function represents reasonably well the $|E^*|$-temperature relationship using $|E^*|$ at 5 Hz and 5, 25 and 40°C. Furthermore, the quadratic function is assessed to interpolate $|E^*|$ from the three

equivalent values.

The required third relationship is the shift factor with temperature. One of shift techniques presented in section 2.4 can be used to determine this relationship.

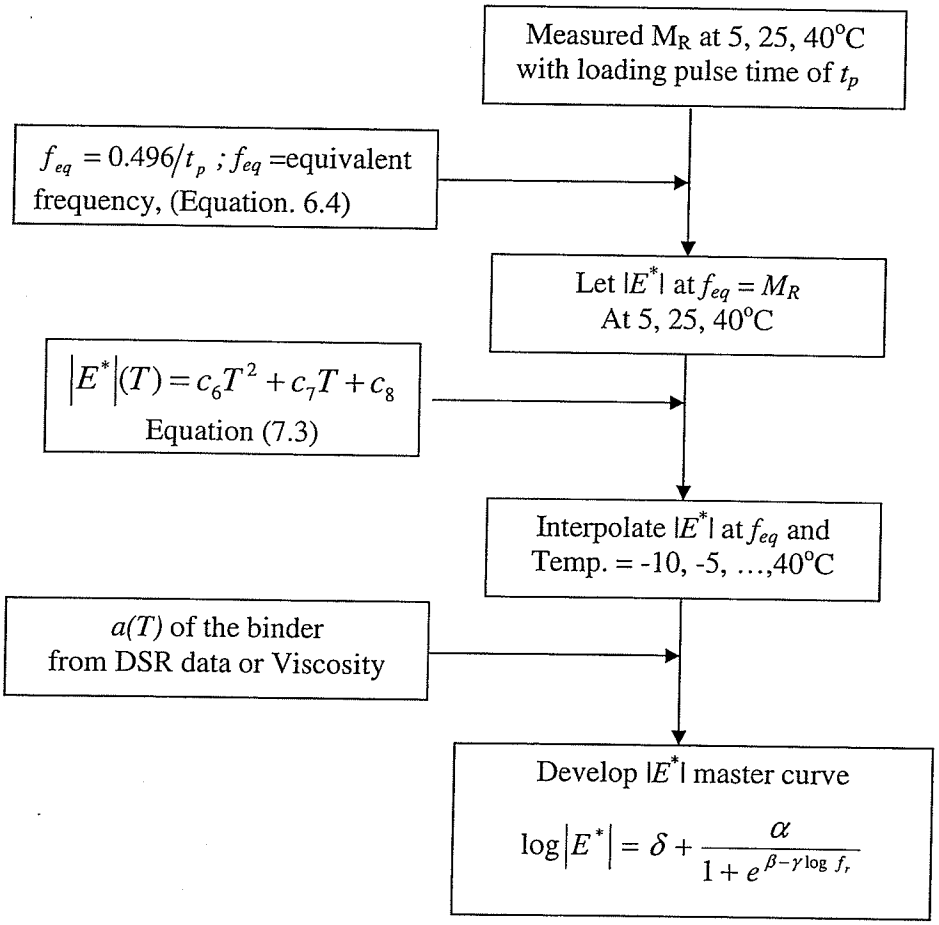

Figure 7.1: The proposed approach to predict $|E^*|$ from M_R

7.2 Predicting $|E^*|$ from M_R

7.2.1 Equivalent Frequency

For M_R pulse load of 0.1 s, f_{eq} is 5 Hz that is calculated using Equation 6.4. The B2-B4 and G5 mixtures are used to show that f_{eq} is practically the most reasonable value among the test frequencies. G5 consists of four mixtures, S12.5C, S12.5FE, S12.5CM and B25.0C. The G5 mixtures are used in North Carolina and documented in (Lacroix 2008). Aggregates of G5 were classified as coarse material with various gradations. Dataset of these mixtures consisted of $|E^*|$ and M_R values obtained in IDT test mode. Figure 7.2 shows the boxplot of the ratio of $|E^*|$ to M_R calculated at five frequencies (0.1, 1, 5, 10 and 25 Hz).

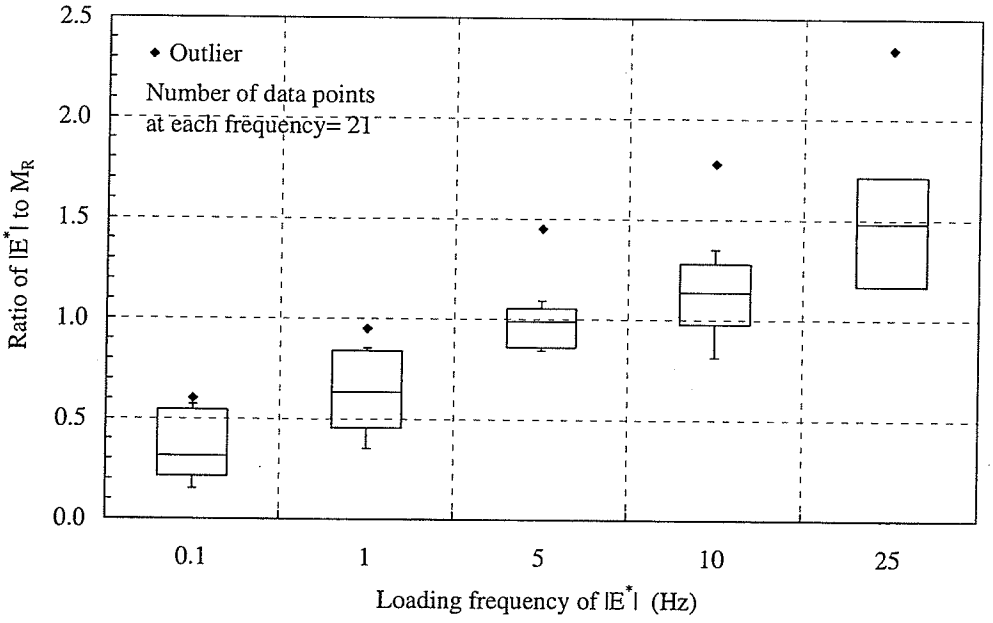

Figure 7.2: The ratio of $|E^*|$ to M_R at the loading frequency, B2-B4 and G5 mixtures

For each boxplot, the centre horizontal line represents the median value of the ratio, and the upper and lower horizontal lines that outline the box represent the 90^{th} and 10^{th} percentiles, respectively. The vertical lines extending above and below the box indicate the spread of the ratio.

The values of the ratio at each frequency are obtained from seven mixtures and three temperatures each. The ratio increases with frequency as expected as $|E^*|$ increases. The figure confirms the calculated f_{eq} of 5 Hz where the ratio has a median value of 0.99 with a spread of the ratio increasing with moving far away from 5 Hz. The frequency calculated based on the MEPDG approach shown by Equation (2.35) is 10 Hz. On the other hand, the frequency calculated based on the angular frequency approach shown by Equation (2.36) is 1.67 Hz. Figure 4.10 indicates that the first approach overestimates the ratio of $|E^*|$ to M_R with 15% and that the second approach underestimates the ratio with 35%. Furthermore, Figure 7.3 shows a strong relationship (R^2 >0.99) between M_R and $|E^*|$ at 5 Hz.

Lacroix et al. (2007) determined M_R from $|E^*|$ using the elastic-viscoelastic corresponding principle. For G5, the difference of both the calculated M_R using Lacroix et al. (2007) and $|E^*|$ at 5 Hz from the measured M_R is presented in Figure 7.4. It is noticed that $|E^*|$ at 5 Hz is almost as good as M_R. From Figures 7.2 to 7.4, Equation 6.4 gives f_{eq} comparable with the laboratory measurements and analytical approach of Lacroix et al. (2007).

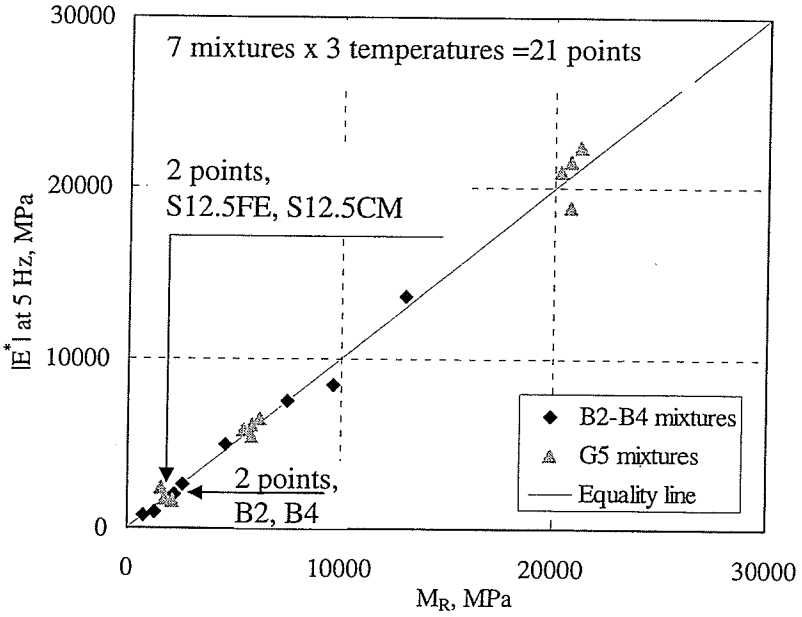

Figure 7.3: $|E^*|$ at 5 Hz versus M_R

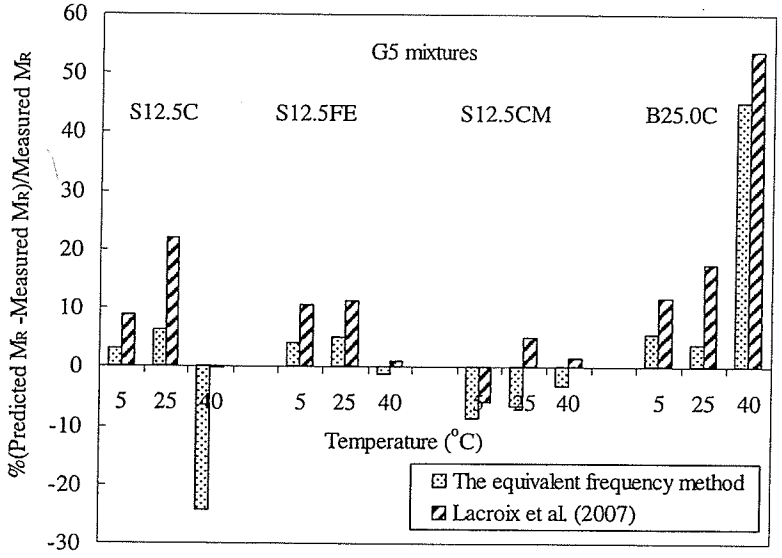

Figure 7.4 The accuracy of the proposed method of f_{eq} against the accuracy of the Lacroix et al. (2007) approach

7.2.2 Interpolation Function of $|E^*|$

M_R of the laboratory and field compacted AC specimens shown in Table 3.1 has been used to select the function that reasonably represents the M_R-temperature relationship. The power, exponential and quadratic functions, Equations 7.1-7.3 respectively, represented the relationship between M_R and temperature with $R^2>0.98$. The accuracy of these functions is examined to interpolate $|E^*|$.

$$|E^*|(T) = c_1(T + c_2)^{c_3} \tag{7.1}$$

$$|E^*|(T) = c_4 e^{c_5 T} \tag{7.2}$$

$$|E^*|(T) = c_6 T^2 + c_7 T + c_8 \tag{7.3}$$

where,

T = temperature (°C)

$c_1 - c_8$ = regression constants

The accuracy of the interpolation is represented by the percent difference and the percent Root Mean Square Error *(%RMSE),* which are obtained as follows:

$$\text{Percent difference } (T) = \frac{\text{interpolated } |E^*| \ (T) - \text{measured} |E^*|(T)}{\text{measured} |E^*|(T)} \times 100 \tag{7.4}$$

$$\%RMSE = \sqrt{\frac{\sum_{j}^{M}\sum_{i}^{N}\left(\text{Percent difference } (T_i)\right)_j^2}{NM}} \tag{7.5}$$

where N is number of temperatures and M is the number of mixtures.

$|E^*|$ of S1-S4 and B1-B4 has been used to evaluate the ability of Equations 7.1 to 7.3 to interpolate $|E^*|$ at any temperature. On one hand, the parameters of master curves and shift factors listed in Table 4.1 are used to generate $|E^*|$ at a set of temperatures (-10 to

40°C with a 5°C step). The shift factor at any temperature is interpolated from those shift factors using a quadratic function. On the other hand, $|E^*|$ at the set of temperatures has been interpolated from M_R at three temperatures using each one of Equation 7.1 to 7.3. Figure 7.5 shows the prediction error and *%RMSE*.

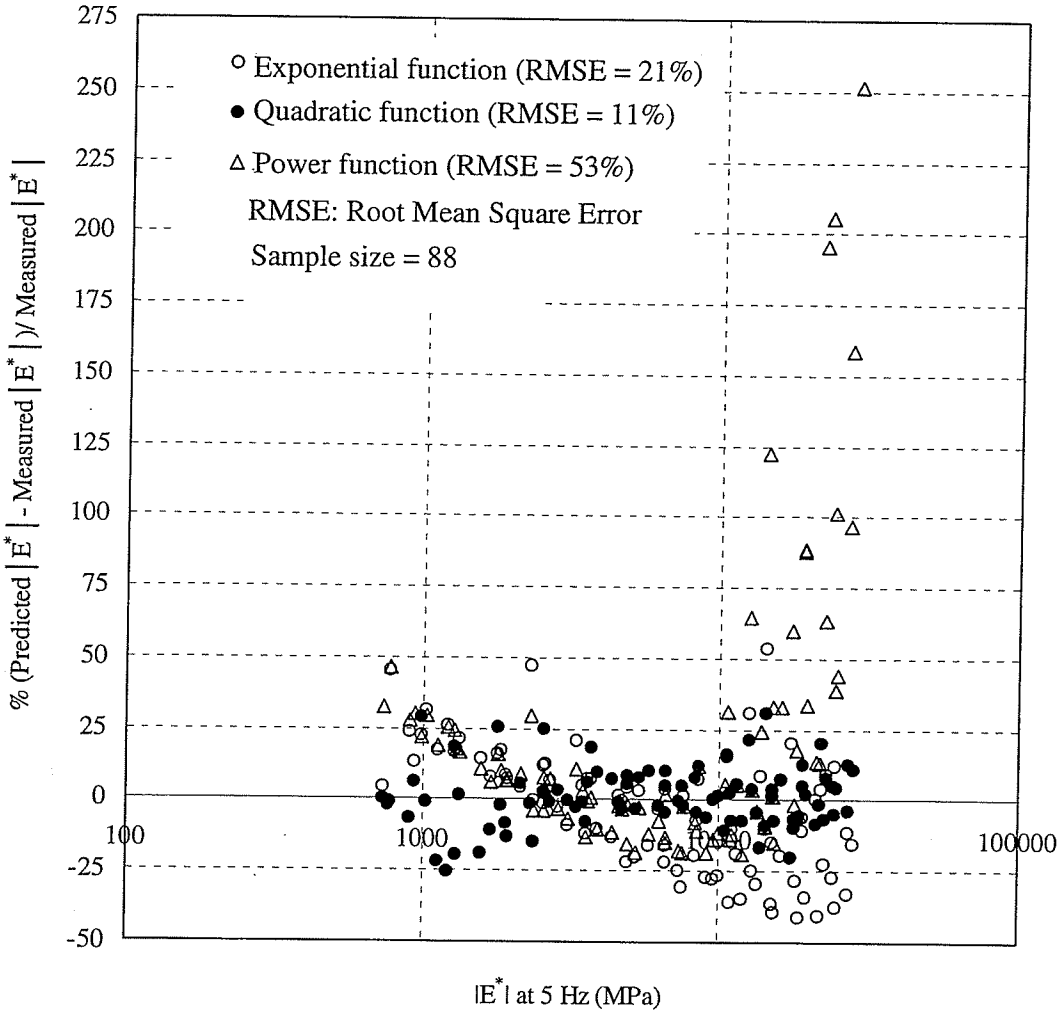

Figure 7.5: The accuracy of the functions proposed to interpolate $|E^*|$ of S1-S4 and B1-B4 from three equivalent $|E^*|$.

The quadratic function predicts $|E^*|$ with a percent difference up to 25%. The range of the percent difference is ± 10 % of the measured values at the intermediate stiffness (2000 – 10000 MPa) and ± 25 % at higher and lower stiffness. Furthermore, the *%RMSE* for the quadratic function is 11 % while it is 21 % and 53 % for the exponential and power law functions respectively. The power function overpredicts $|E^*|$ at high stiffness with up to 275% of the measured values. The exponential function underestimates mostly $|E^*|$ at high stiffness with -50 % and higher while overpredicts $|E^*|$ at low stiffness with up to 50%. Accordingly, the quadratic function is the best choice among the examined functions to interpolate the $|E^*|$ at f_{eq} at any temperature from M_R.

7.3 Predicted |E*| Master Curve

Figure 7.6 shows the predicted and the measured $|E^*|$ master curves of B2-B4 mixtures. The predicted master curves were developed from M_R at 5, 25 and 40°C according to the proposed approach shown in Figure 7.1 as follows:

1. Given the pulse duration of M_R of 0.1s, f_{eq} can be calculated using Equation 6.4. Consequently $|E^*|$ at 5 Hz is equivalent to M_R.
2. The quadratic function shown in Equation 7.3 is used to interpolate the equivalent $|E^*|$ from M_R at temperatures (-10 to 40°C with 5°C).
3. Developing the shift factor-temperature relationship. Lacroix et al. 2008 found that the shift factor of binder can be used to construct the $|E^*|$ master curve. Herein, the shift factors listed in Table 4.1 of B2-B4 mixtures are applied.
4. Constructing the $|E^*|$ master curve by shifting the interpolated $|E^*|$. Coefficients of the sigmoidal function can be determined from the shifted values using the non-linear

fitting technique. Figure 7.6 shows that the proposed approach can predict $|E^*|$ master curves of B2-B4 from M_R. Figure 7.7 compares the predicted and the measured $|E^*|$ of B2-B4 and G5 mixtures. The predicted master curves are as accurate as those developed from measured values and can efficiently differentiate between B2-B4 based on their load response. The approach predicts $|E^*|$ at middle and low frequencies where AC is sensitive to rutting and fatigue cracking.

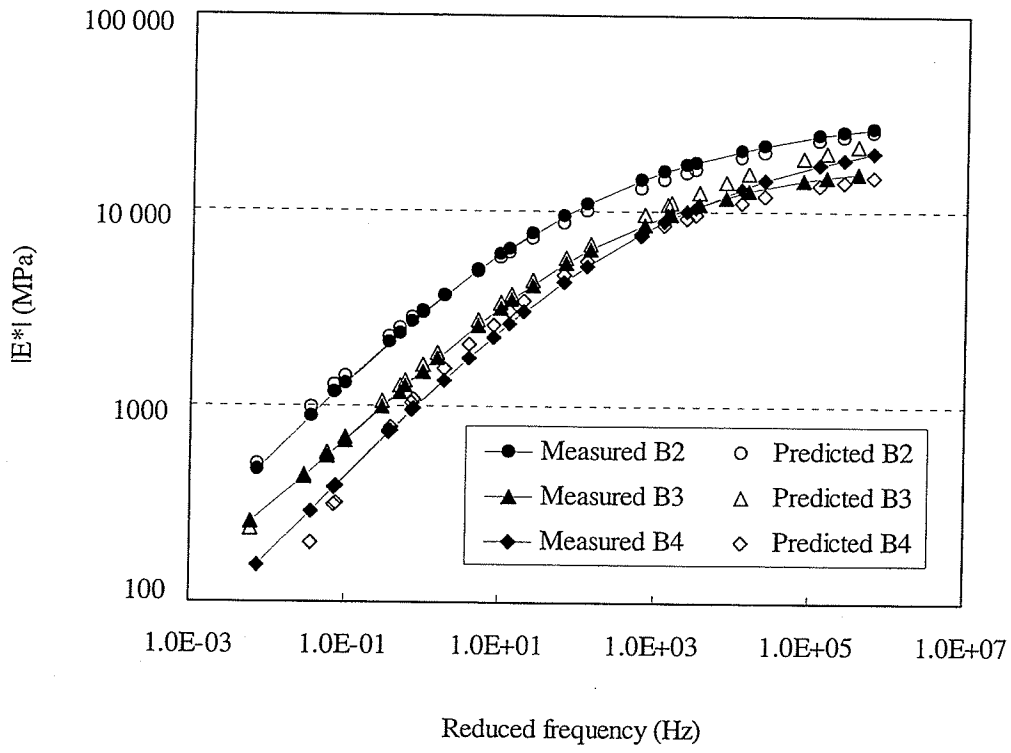

Figure 7.6: Comparison of the predicted and the measured $|E^*|$ master curves

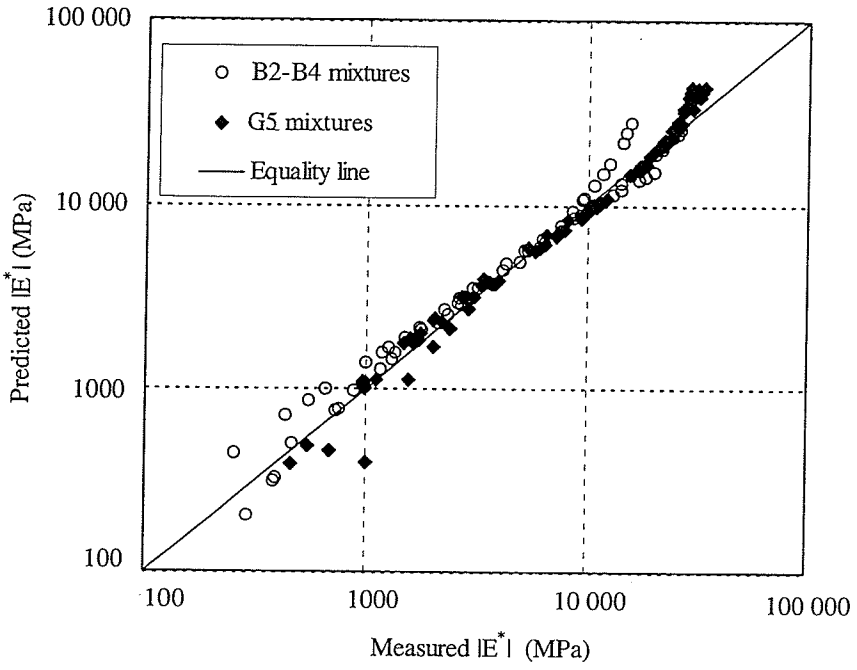

Figure 7.7: The accuracy of the proposed approach to predict $|E^*|$ from M_R of B2-B4 mixtures and G5 mixtures

7.4 Summary

An approach has been introduced to predict $|E^*|$ from M_R using three relationships, pulse loading time and frequency, $|E^*|$ and temperature, and the shift factor and temperatures. In this chapter, the relationship between $|E^*|$ and temperature has been investigated and the quadratic function that has three constants has been introduced and investigated to represent this relationship.

The approach has been used to predict $|E^*|$ of seven mixtures from M_R that is measured at

three temperatures. The predicted and measured $|E^*|$ have good agreement. The predicted $|E^*|$ master curve has the ability to differentiate between mixtures similarly as the measured $|E^*|$ master curve. The approach can be used to predict $|E^*|$ of field cores from M_R since it does not depend on properties AC mixtures such as the Witczak $|E^*|$ prediction model. $|E^*|$ of field cores can be used to evaluate in-service pavement and in construction quality control.

8 Conclusions, Limitations and Recommendations

8.1 Summary and Conclusions

One of the major advancements in the mechanistic-empirical pavement design is using $|E^*|$ that, in contrast of other stiffness parameters, is a fundamental stiffness describing the actual viscoelastic behaviour of asphalt concrete. Through $|E^*|$, factors that affect behaviour of asphalt pavement such as traffic speed, temperature and aging are incorporated in pavement design. In addition, $|E^*|$ is an SPT parameter that can compare asphalt mixtures against the pavement performance. Therefore, an accurate determination of $|E^*|$ is essential for improving the reliability of pavement design and for evaluating the asphalt mixtures. The thesis contributes research on improving the reliability of prediction of $|E^*|$ at high temperature, improving the determination of the quasi-elastic modulus of asphalt concrete for pavement design, and predicting $|E^*|$ from M_R of asphalt concrete to determine in-service stiffness.

Current methods for predicting $|E^*|$ are less reliable at high temperatures which increases uncertainty in the forecasted pavement performance and the estimated service life. Aggregate gradation has a dominant effect particularly at high temperature where the binder stiffness is low. A gradation ratio, GR, that is the ratio of passing 4.75 mm sieve to 0.075 mm sieve has been used to describe the relationship between aggregate gradation and $|E^*|$ at 40^0C, $\left|E^*_{40}\right|$. The $\left|E^*_{40}\right|$-GR model has been developed by the linear regression analysis to adjust the

predicted $|E^*|$ master curves. Data of twenty-four mixtures prepared from various aggregate types and gradation, and various binder grade has been used to investigate the relationship and to develop the model.

Furthermore, to determine the appropriate $|E^*|$ for the multilayered elastic analysis of asphalt pavement system, the frequency of the applied load is calculated as a function of the loading time that depends on the traffic speed and the pavement thickness and stiffness. Therefore, the reliability of load representation in pavement design depends on correctness of the loading frequency. The pulse time-frequency conversion approach, based on viscoelastic theory, has been introduced to determine the equivalent frequency for a given loading pulse. The approach calculates a quasi-elastic modulus of asphalt concrete under a pulse load. Similar to $|E^*|$, the quasi-elastic modulus is the ratio of the maximum stress to the maximum strain under the pulse load. Then, the frequency of the applied load is calculated from the $|E^*|$-frequency relationship when the quasi-elastic modulus is equivalent to $|E^*|$. Asphalt concrete has been characterized with the creep compliance represented by parameters of the general power law, D_0, D_1 and m, to determine numerically the quasi-elastic modulus and to define the $|E^*|$-frequency relationship. Conversion equations have been developed to calculate frequency from pulse time of field loading and laboratory pulses.

Finally, the method of predicting $|E^*|$ from M_R has been introduced to develop the entire $|E^*|$ master curve from M_R. The equivalent frequency, f_{eq}, at which $|E^*|$ is equivalent to M_R is calculated by applying the pulse time-frequency conversion approach. Then, the parabolic function is used to interpolate $|E^*|$ at f_{eq} and a wide range of temperature from M_R at three

temperatures. The interpolation is carried out to generate sufficient $|E^*|$ values to substitute the measured $|E^*|$ at various frequencies and temperatures. Finally, the interpolated values at f_{eq} are shifted with the shift factor of the binder. The method has been verified with measured $|E^*|$ and M_R from mixtures tested during the experimental program and other mixtures from literature.

Conclusions are drawn:

1. Improving the prediction of $|E^*|$ at high temperature

- The relationship between $\left|E_{40}^*\right|$ and aggregate gradation represented by GR should be studied independently in fine-graded and coarse-graded mixtures.
- For fine-graded mixtures, the relationship is statistically significant regardless of the binder grade.
- The $\left|E_{40}^*\right|$-GR model has been developed to adjust the predicted $|E^*|$ at high temperature for fine-graded mixtures. The model, Equation 5.2, is calibrated with data from 11 fine-graded mixtures and has goodness of fit of $R^2 = 0.89$ and $S_e/S_y = 0.35$.
- $|E^*|$ master curves predicted using the Witczak model have been adjusted using $\left|E_{40}^*\right|$ calculated from GR of mixtures. The adjustment improves the prediction of $|E^*|$ especially at high temperatures.
- The relationship between stiffness at high temperature and GR is examined in as-constructed AC mixtures using M_R at 40°C. The relationship is significant even within mixtures containing RAP.

- The relationship between $|E^*|$ at high temperature and GR can be used as a guide to optimize aggregate gradation of fine-graded mixtures for higher $|E^*|$. It can also be used for construction quality control by defining M_R that should be reached as a function of gradation.

2. Pulse Time-Test frequency conversion

- The factors affecting pulse time-frequency conversion have been investigated. It was found that the equivalent loading frequency depends significantly on the pulse load form and to a lesser extent on the viscoelastic property of asphalt concrete and temperature. Conversion equations, Table 6.4, were developed for the following field loading forms: haversine, bell-shape form, triangular and square.

- The MEPDG approach overestimates the loading frequency by up to 173% depending on the shape of the field stress. On the other hand, the approach that applies the angular frequency underestimates it by up to 65%. Since $|E^*|$ increases with the frequency, MEPDG overestimates the design value of $|E^*|$.

- The equivalent frequency of the M_R pulse load, for instantaneous resilient modulus, is the one-half inverse of pulse time. For example, the frequency of a 0.1s pulse load is 5 Hz. In addition, the equivalent frequency of FWD loading history is 15.7 Hz. Both M_R and backcalculated FWD stiffness are used in pavement evaluation and rehabilitation. The determination of their equivalent frequencies increases the reliability of pavement evaluation and design.

- Since the conversion approach applies a numerical integration scheme, the loading frequency of any pulse stress can be calculated even for asymmetric pulses. In addition,

the approach can be applied to determine the loading frequency when special mixtures such as Stone Matrix Asphalt (SMA) or mixtures that containing modified binders are used. The creep compliance of a mixture must be represented accurately by the power function to apply the approach.

3. Predicting $|E^*|$ from M_R

- The method of predicting $|E^*|$ from M_R has been successfully verified for the laboratory compacted mixtures. The parabolic function has interpolated $|E^*|$ at various temperatures and 5 Hz, which is f_{eq} of 0.1 pulse load, from M_R at 5, 25, 40°C. The function was verified by using $|E^*|$ at f_{eq} generated from $|E^*|$ master curves. The predicted $|E^*|$ master curves match significantly the master curves developed from measured $|E^*|$. The method does not carry any constant value from materials, so it can be applied to predict $|E^*|$ of in-service asphalt concrete.

- The $|E^*|$ master curve can be predicted from a cheaper and faster test like the M_R test. The approach can be applied to predict $|E^*|$ from M_R measured under any pulse load after determination f_{eq} by applying the pulse time-frequency conversion approach. The method is useful for testing as-built and in-service pavements. In addition, the method can support using the M_R test for quality control (QC). Furthermore, the method can be beneficial for adapting the existing asphalt pavement databases, such as the LTPP database, to MEPDG.

8.2 Limitations and Recommendations

- The $|E^*_{40}|$-GR mode has been developed for fine-graded mixtures. For coarse-graded

mixtures, the relationship needs further investigation.

- The conversion equations of the pulse loading time to the frequency are obtained for AC tested in this thesis. Further investigation is required when they are used with AC mixtures containing modified binders or with special mixtures such as SMA.

- The conversion equations are developed for symmetric loading forms. The stress pulses from field pressure cells and those pulses from the viscoelastic analysis are asymmetric since the unloading portion of the pulse may contain residual stresses. The maximum pulse strain is mostly developed during the loading portion; therefore, the conversion equations may not be sensitive to the unloading portion. Further examination is required to evaluate the effect of the asymmetry of the loading and unloading portions.

- The conversion equations have been developed for forms used to represent vertical pulse stresses. The effect of adopting these equations in pavement design on the resulting tensile strain at bottom of the asphalt layer and the vertical stress on the base course should be examined by comparing results of viscoelastic and elastic analysis. The reliability of the fatigue cracking and rutting of the pavement foundation depends on the accuracy of the calculated tensile strain of asphalt concrete and the vertical stresses on the base course. Adopting the approach in pavement design requires recalibrating the pavement performance models.

- Equation (6.4) has been developed for instantaneous M_R obtained under sinusoidal pulse stress. For other pulse forms or for the total M_R, the equivalent frequency can be determined by applying the pulse time-frequency approach.

- The frequency of square loading pulse equals $\frac{0.105}{t_p}$ and it can be useful for determining

$|E^*|$ from an easy and fast test like the *D(t)* test that can be carried out on laboratory and field specimens.

- The proposed approach to predict $|E^*|$ from M_R requires determination of the shift factor of the binder. For unaged binder, methods are available to calculate the shift factor from the binder rheology while, for in-service AC, the shift factor from field-extracted binders needs further investigation.

- Adapting the measured $|E^*|$ values is recommended for comparing between mixtures when small differences are expected between mixtures. M_R specimens can be damaged more easily due to cracking at the contact area between loading strips and the specimen affecting the accuracy of the predicted $|E^*|$ from M_R. In addition, the variability of $|E^*|$ test is generally smaller than the variability of M_R test.

References

1. AASHTO 2003. Standard method of test for determining dynamic modulus of hot-mix asphalt concrete mixtures. AASHTO TP 62-03. American Association of State Highway and Transportation Officials, Washington, DC.

2. ASTM 4123. 1982. Standard test method for indirect tension test for resilient modulus of bituminous mixture. ASTM International, West Conshohocken, PA.

3. ASTM D3497. 2003. Test method for dynamic modulus of asphalt concrete. American Society for Testing and Materials. ASTM International, West Conshohocken, PA.

4. Al-Qadi, I. L., Elseifi, M. A., Yo, P. J. 2008a. Accuracy of current complex modulus selection procedure from vehicular load pulse: NCHRP project 1-37A mechanistic-empirical pavement design guide Source. Transportation Research Record, n 2087, pp 81-90.

5. Al-Qadi, I. L., Xie, W., Elseifi, M. A.. 2008b. Frequency determination from vehicular loading time pulse to predict appropriate complex modulus in MEPDG. Journal of the Association of Asphalt Paving Technologists, v 77, pp 739-771.

6. Birgisson, B., and Ruth, B.E. 2002. Development of tentative guidelines for the selection of aggregate gradation in hot-mix asphalt. *In* ASTM Aggregate Contribution to Hot Mix Asphalt (HMA) Performance, ASTM 1412(STP). Edited by T.D. White, S.R. Johnson, and JJ. Yzenas. American Society of Testing and Materials, West Conshohocken, Penn. pp.110-127.

7. Birgisson, B. and Roque R. 2005. Evaluation of the gradation effect on the dynamic modulus. Transportation Research Record, 1929, pp 193-199.

8. Birgisson, B., Sholar, G., and Roque, R. 2005. Evaluation of predicted dynamic modulus for Florida mixtures. Transportation Research Record, 1929, pp 200-207

9. Biswas, K. G. and Pellinen, T. K. 2007. Practical methodology of determining the in-situ dynamic (complex) moduli for engineering analysis. Journal of Materials in Civil Engineering, v 19, n 6, pp 508-514.

10. Chehab, G.R., Kim, Y.R., Schapery, R.A., Witczak, M.W., and Bonaquist, R., 2002. Time-temperature superposition for asphalt concrete mixtures with growing damage in tension state. Asphalt Paving Technology, Association of Asphalt Paving Technologists, Minneapolis, MN, U.S.A.

11. Chehab, G.R., Kim, Y.R., Schapery, R.A., Witczak, M.W., Bonaquist, R., Huang, B., Roque, R., Davis, R., Penia, J., Molenaar, A., and Masad, E. 2003. Characterization of asphalt concrete in uniaxial tension using a viscoelastoplastic continuum damage model. Journal of the Association of Asphalt Paving Technologists, v 72, pp.315-355.

12. Christensen, D.W., and Anderson, D.A. 1992. Interpretation of dynamic mechanical test data for paving grade asphalt cements. Journal of the Association of Asphalt Paving Technologists, v 61, pp 67-116.

13. Christensen, D.W., Jr, Pellinen, T., and Bonaquist, R.F. 2003. Hirsch model for estimating the modulus of asphalt concrete. Journal of the Association of Asphalt Paving Technologists, v 72, pp 97-121.

14. Di Benedetto, H., Franken, L. and De La Roche Saint Andre', C. 2001. Stiffness

testing for bituminous mixtures. Journal of Materials and Structures, v. 34, pp 66-70.

15. Dongré, R., Myers, L., D'Angelo, J., Paugh, C., and Gudimettla, J. 2005. Field evaluation of Witczak and Hirsch models for predicting dynamic modulus of hot-mix asphalt. Journal of the Association of Asphalt Paving Technologists, v 74, pp.381-442.

16. Dongré, R., Myers, L. and D'Angelo, J. 2006. Conversion of testing frequency to loading time: impact on performance predictions obtained from the M-E pavement design guide. *In* Proceedings of the 85th Annual Meeting of the Transportation Research Board, Washington, DC, No 06-2394.

17. Daniel, J.S. and Kim, Y.R. 1998. Relationships among rate-dependent stiffnesses of asphalt concrete using laboratory and field test methods. Journal of the Transportation Research Record, 1630, pp. 3-9.

18. ETG. 2006. Fundamental Properties and Advanced Modeling of Bituminous Materials. 2006 Expert Task Group Minutes. May 9 & 10th, Denver, CO Available from http://www.asphaltmodelsetg.org/index_1.htm.

19. ETG .2007. Fundamental Properties and Advanced Modeling of Bituminous Materials. 2007 Expert Task Group Minutes. February 7 & 8th, Phoenix, AZ. Available from http://www.asphaltmodelsetg.org/index_1.htm.

20. Goodrich, J.L. 1991. Asphalt binder rheology, asphalt concrete rheology and asphalt concrete mix properties. Journal of the Association of Asphalt Paving Technologies. v 57, pp.81-121.

21. Harran, G. and Shalaby, A. 2007a. Dynamic modulus of asphalt concrete in uniaxial

compression and indirect tension modes. *In* proceedings of the Annual Conference of the Canadian Society for Civil Engineering 2007: Where the Road Ends, Ingenuity Begins, v 1, pp 581-590.

22. Harran, G. and Shalaby, A. 2007b. Variability of dynamic modulus of asphalt concrete measured in uniaxial compression and indirect tension. *In* proceedings of the Annual Conference of the Canadian Society for Civil Engineering 2007: Where the Road Ends, Ingenuity Begins, v2, pp. 681-689.

23. Harran, G. and Shalaby, A. 2008. Representative values for resilient and dynamic moduli of asphalt mixtures in Manitoba. A final project report submitted to Manitoba Infrastructure and Transportation, Materials Engineering Branch, Winnipeg, Manitoba.

24. Harran, G. and Shalaby, A. 2009. Improving the prediction of the dynamic modulus of fine-graded asphalt concrete mixtures at high temperatures. Canadian Journal of Civil Engineering, v 36, n 2, pp 180-190.

25. Kim, J. R., Roque and B. Birgisson. 2005. Obtaining creep compliance parameters accurately from static or cyclic creep tests. Journal of ASTM International. v 2, n 8, , pp 113-133.

26. Kim, Y.R., Lee, Y.C. and Lee, H.J. 1995. Correspondence principle for characterization of asphalt concrete. Journal of Materials in Civil Engineering, v 7, n1, pp 59-68.

27. Kim, Y.R. and Y.C. Lee. 1996. Interrelationships among stiffnesses of Asphalt-Aggregate Mixtures. Journal of Association of Asphalt Paving Technologists, v 64,

pp. 575-609.

28. Kim, R.Y., S. Youngguk, K.M., and Mostafa, M. 2004. Dynamic modulus testing of asphalt concrete in indirect tension mode. Journal of the Transportation Research record. n 1891, pp. 163-173.

29. Lacroix, A.. 2007. Evaluation of different methods for populating the LTPP materials database with the dynamic modulus. Master thesis. North Carolina State University, Raleigh.

30. Lacroix, A., Khandan, A. A. M., and Kim, Y. R. 2007. Predicting the resilient modulus of asphalt concrete from the dynamic modulus. Journal of the Transportation Research Board, n. 2001, pp132-140.

31. Lacroix, A.; Kim, Y. R. and Ranjithan, S.R. 2008. Back calculation of the dynamic modulus from the resilient modulus of asphalt concrete using an artificial neural network. Journal of the Transportation Research Board, n. 2057, pp 107-113.

32. Loulizi, A.; Flintsch, G. W.; Al-Qadi I.L.; and Mokarem D. 2006. Comparing resilient modulus and dynamic modulus of hot-mix asphalt as material properties for flexible pavement design. Journal of the Transportation Research Board, n 1970, pp161-170.

33. Lytton, R. L., Uzan, J, Fernando, E.G., Roque, R., Hiltunen, D., and Stoffels, S. 1993. Development and validation of performance prediction models and specifications for asphalt binders and paving mixes. SHRP A-357, National Research Council, Washington, D.C.

34. NCHRP. 2002. Simple performance test for SuperPave mix design. NCHRP project

9-19. Transportation Research Board, National Research Council, Washington, DC. Available from http://onlinepubs.trb.org/Onlinepubs/nchrp/nchrp_rpt_465.pdf

35. NCHRP. 2004. Mechanistic-Empirical Design of New and Rehabilitated Pavement Structures, NCHRP Project 1-37A Final Report, Transportation Research Board, National Research Council, Washington, DC. Available from http://www.trb.org/mepdg.

36. NCHRP. 2005 Simple performance tests: Summary of recommended methods and database. NCHRP project 9-19 final report. Transportation Research Board, National Research Council, Washington, DC. Available from http://onlinepubs.trb.org/onlinepubs/nchrp/nchrp_rpt_547.pdf.

37. NCHRP. 2006. Independent review of the mechanistic–empirical pavement design guide and software. Report NCHRP 1–40 A, Research Results Digest 307. National Cooperative Highway Research Program, Transportation Research Board, Washington, D.C.

38. NCHRP. 2007. Specification criteria for simple performance tests for rutting. NCHRP Report 580. Transportation Research Board, National Research Council, Washington, DC. http://onlinepubs.trb.org/onlinepubs/nchrp/ nchrp_rpt_580.pdf.

39. Nunn, M. E. 1996. The characterization of bituminous macadam by indirect tensile stiffness modulus. Transport research laboratory Report 160

40. Pellinen, T.K. 2001. Investigation of the use of the dynamic modulus as an indicator of hot-mix asphalt performance. Ph.D. thesis. Arizona State University.

41. Pellinen, T.K.; Witczak, M.W. Marasteanu, Mihai ; Chehab, Ghassan ; Alavi, Sirous;

Dongré, Raj. 2002. "Stress Dependent Master Curve Construction for Dynamic (Complex) Modulus." Journal of the Association of Asphalt Paving Technologists, Volume 71. Colorado Spring, CO., pp. 281-309.

42. Pellinen, T.K., Witczak, M.W., and Bonaquist, R.F. 2004. Asphalt mix master curve construction using sigmoidal fitting function with non-linear least squares optimization. Geotechnical special publication, v 123, pp 83-101.

43. Pellinen, T.K., Xiao, Shangzhi; R. and Sunil Y. 2006. Dynamic modulus testing of thin pavement cores. Journal of ASTM International, v 3, n 4.

44. Peterson, R. L., Mahboub, K. C; R. Anderson, M., Masad Eyad; and Tashman L. 2004 Comparing SuperPave gyratory compactor data to field cores. Journal of Materials in Civil Engineering, v 16, n 1, pp 78-83.

45. Ruth, B.E., Roque, R., Nukunya, B., Davis, R., Marasteanu, M., Vavrik, W., Fee, F., Taylor M., Dukatz E. and Li Xus 2002. Aggregate gradation characterization factors and their relationship to fracture energy and failure strain of asphalt mixtures. Journal of Association of Asphalt Paving Technologists, v 71, pp 310-334.

46. Shalaby, A. 2002. Modeling short-term aging of asphalt binders using the rolling thin film oven test. Canadian Journal of Civil Engineering. v 29, pp 135-144.

47. Schwartz, C. W. 2005. Evaluation of the Witczak dynamic modulus prediction model. *In* Proceedings of the 84th Annual Meeting of the Transportation Research Board, Washington, DC, No. 05-2112.

48. SHRP. 2001. Test method for determining the creep compliance, resilient modulus, and strength of asphalt materials using the indirect tensile test device. Long Term

Pavement Performance Protocol P07. SHRP, National Research Council, Washington, D.C.

49. Shook, J.F., Kallas, B.F. and McLeod, B.F. 1969. Factors influencing dynamic modulus of asphalt concrete. Journal of the Asphalt Paving Technologists, v 38, pp 140-178.

50. Tran, N. H. and Hall, K. D. 2006. Evaluation of testing protocols for dynamic modulus of hot-mix asphalt. Journal of the Transportation Research record. n 1970. pp 126-132.

51. Uzan, Jacob. 1996. Asphalt concrete characterization for pavement performance prediction. Journal of the Asphalt Paving Technologists, v 65, pp 573-607.

52. Underwood, B.S. and Kim, Y.R. 2009. Determination of the appropriate representative elastic modulus for asphalt concrete. International Journal of Pavement Engineering, v 10, n 2, pp 77-86.

53. Witczak, M.W. and Fonseca1, O.A. 1996. Revised predictive model for dynamic modulus of asphalt mixtures. Journal of the Transportation Research Record, n 1540, pp 15-23.

54. Witczak, M.W., Pellinen, T.K., and El-Basyouny, M. M. 2002a. Pursuit of the simple performance test for asphalt concrete fracture/cracking. Journal of the Association of Asphalt Paving Technologists, v 71, pp 767-778.

55. Witczak M. W., K. E. Kaloush and H. Q. Von .2002b. Pursuit of the simple performance test for asphalt mixture rutting. Journal of the Asphalt Paving Technologists, v 71, pp. 671-691.

56. Yoder, E.J., and Witczak, M.W. 1975. Principles of Pavement Design. J. Wiley and Sons, Inc., Second Edition.

57. Zeghal, M, Adam, Y.E., and Mohamed E. H.. 2005. Effectiveness of predictive models for estimating asphalt concrete complex modulus, 6th Transportation Specialty Conference Toronto, Ontario, Canada June 2-4.

58. Zeghal, M. and Mohamed, E., Assessment of analytical tools to estimate the stiffness of asphalt concrete. Canadian Journal of Civil Engineering. v 35, pp 268-275.

59. Zapata, C. E. and Houston, W. N. 2008. Calibration and validation of the enhanced integrated climatic model for pavement design. Project NCHRP 9-23 report. available from http://onlinepubs.trb.org/onlinepubs/nchrp/nchrp_rpt_602.pdf

Appendix A: Dynamic Shear Rheometer Test Result

Table A.1: DSR Test results for 52-28 (150-200)

Temperature (°C)	Shear dynamic modulus, $\|G^*\|$ (Pascal)	Phase angle (δ) (degree)
7.1	10575000	51.3
10.2	5226900	56.9
13.0	3262800	60.1
15.9	1945200	63.2
19.0	1004100	66.3
22.0	597580	69.1
25.0	327190	71.7
28.0	203260	72.6
30.9	123290	74.6
34.2	64664	76.5
37.0	17198	78.1
40.0	12676	80.6
46.0	10914	81.5
49.0	7323	82.9
52.0	4675	83.3
54.9	3199	85.1
58.0	2120	86.2
60.9	1441	87.0
64.0	956	87.6
67.1	667	89.8
70.0	469	88.6

Table A.2: DSR Test results for 58-28 (150-200)

Temperature (°C)	Shear dynamic modulus $\|G^*\|$ (Pascal)	Phase angle (δ) (degree)
7.0	9927800	50.7
10.1	5909700	54.5
13.0	3669000	57.4
16.1	2172600	60.9
19.1	1275200	63.1
22.2	741540	65.4
25.1	459240	67.4
28.1	281300	69.4
30.9	183600	71.0
34.0	104760	72.6
37.0	19322	74.8
46.0	13968	78.4
49.0	9578	79.5
52.0	6105.9	81.1
55.1	4120.4	82.0
58.0	2747.1	83.8
61.1	1806	84.3
64.0	1372	85.3
67.0	904	86.4
70.0	638	87.2

Table A.3: DSR Test results for 52-34 (200-300)

Temperature (°C)	Shear dynamic modulus $\|G^*\|$ (Pascal)	Phase angle (δ) (degree)
7.0	6388400	46.1
10.0	4621900	49.4
13.0	2929100	52.3
16.0	1797800	54.7
19.0	1129700	57.6
22.0	664860	60.4
25.0	374750	63.1
28.0	228980	65.4
31.0	130200	67.7
34.0	73719	70.2
46.0	9667	77.7
49.0	6548	78.8
52.0	3766	80.4
55.0	2477	82.0
58.0	1680	83.6
61.0	1140	84.6
64.0	786	85.4
67.0	546	86.2
70.0	377	86.6

Table A.4: DSR Test results for 58-34 (150-200)

Temperature (°C)	Shear dynamic modulus $\|G^*\|$ (Pascal)	Phase angle (δ) (degree)
7.0	8885700	51.1
10.1	4994000	55.5
13.2	2876500	58.9
16.2	1874300	61.3
19.1	1151000	63.4
22.1	692760	66.1
25.0	385560	68.7
28.1	232040	69.7
31.2	145030	71.8
34.1	87178	72.8
46.0	13682	78.6
49.0	9368	80.1
52.0	6094	81.5
55.0	3984	82.3
58.0	2741	83.5
61.0	1825	84.6
64.0	1238	85.7
67.0	899	86.4
69.9	630	87.1

Appendix B: Calibration of Testing Setup

This appendix presents calibration of the LVDTs and the extensometers, which are used in the testing program of the thesis. In addition, the dynamic modulus and the phase angle obtained by the two deformation measuring systems are compared. Both LVDT and extensometer measuring systems are discussed in 3.6. Since these systems are used to determine response of asphalt concrete, both collected displacement and the lag between the load and displacement have been calibrated.

Calibration of deformation measuring systems

Connected to the data acquisition, DAQ, each deformation measuring system is calibrated for displacement and phase angle. LabView is used to correlate between displacement and voltage measurements of each transducer. For calibrating LVDTs for displacement, a micrometer with precession of 2×10^{-6} m was used to measure the displacement. On the other hand, shunt calibration modules are used to calibrate the extensometers. The systems are used after calibration to measure displacements defined with the micrometer. Figure B.1 shows comparison of measured displacements and readings of the LVDTs for them.

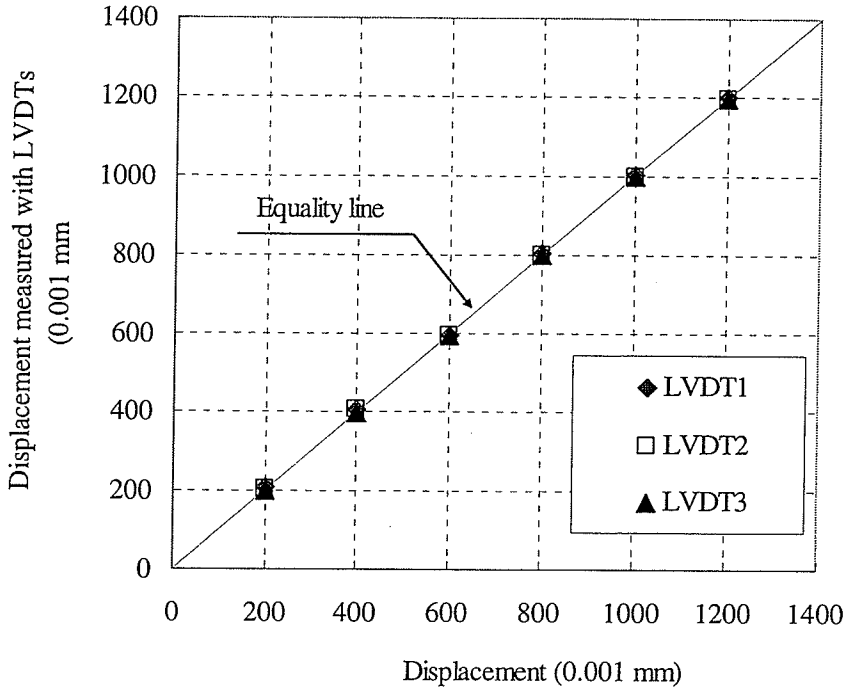

Figure B.1: the relationship between displacement determined with LVDTs and those measured with the micrometer

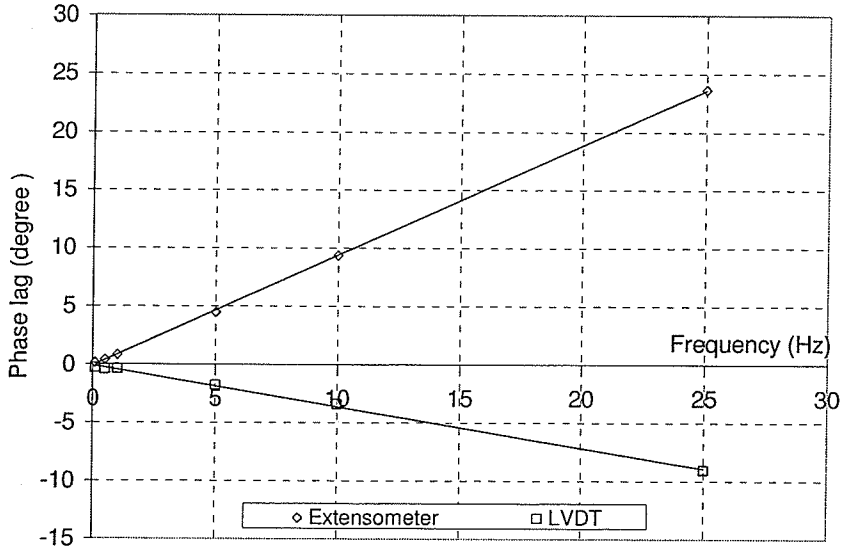

Figure B.2: Phase angle error between the applied load and displacement

A cylindrical aluminium specimen with thickness of 1 mm, 50.8 mm diameter, and 150 mm height has been used to determine the phase angle, if there, between the applied sinusoidal load and the collected sinusoidal displacement using LVDTs and extensometers. Figure B.2 shows the measured phase angle at various frequencies. Since Aluminium has elastic response, this phase angle represents the lag between the collected data of load and displacements. The measured phase angle with each of transducer suggests a linear relationship with frequency; therefore, the time lag between the load and displacements is constant and does not depend on the applied load. Phase angle of asphalt concrete is corrected from the time lag by taking off the measured phase angle shown in Figure B.2.

Comparison of LVDTs and Extensometers' measurements

Dynamic modulus test was carried out on B1 mixture and displacement of test specimens was collected simultaneously by both LVDTs and Extensometers. Figure B.3 shows the comparison between the measured dynamic modulus and phase angle with LVDTs and extensometers. There is no difference between dynamic modulus of B1 measured with LVDTs and that is measured with extensometers and for phase angle, there is small bias. Phase angle measured with LVDTs is slightly higher than phase angle measured with extensometers with about 1 degree.

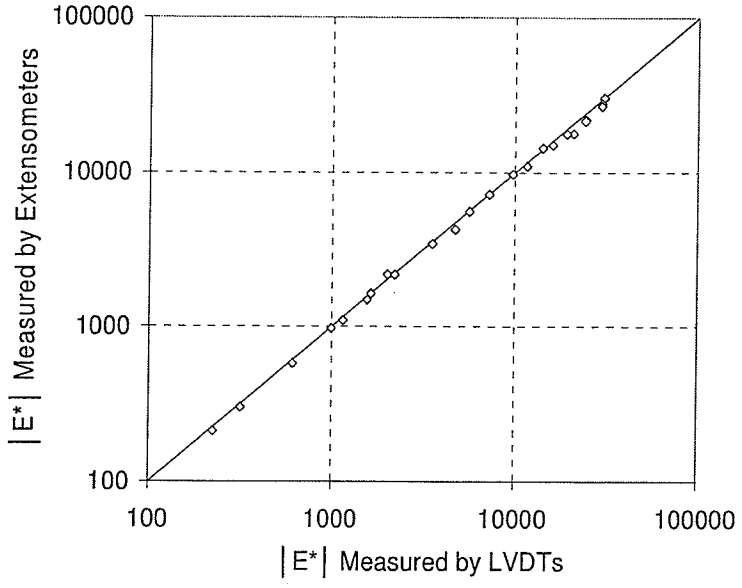

(a)

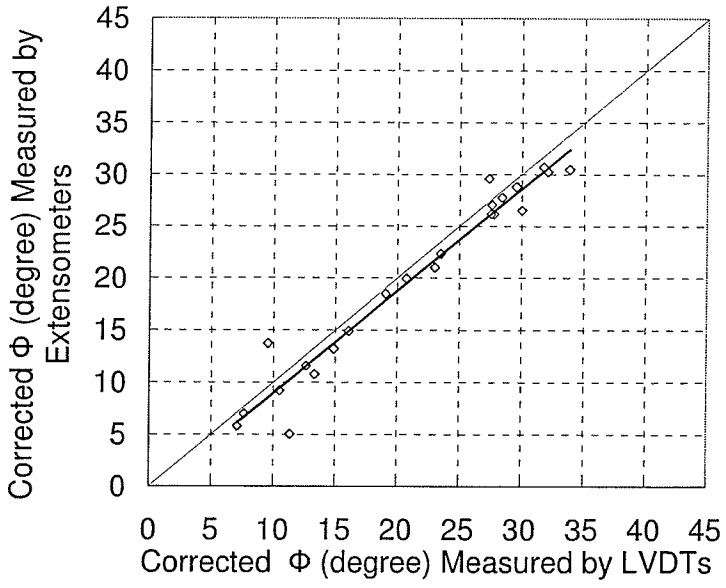

(b)

Figure B.3: Comparing LVDTs and extensometers' measurements for B1 mixture (a) Dynamic modulus. (b) Phase angle.

Appendix C: Measurements of the Dynamic Modulus Test

Table C.1: Strain, dynamic modulus and phase angle at each LVDT position on specimens of S1, -10°C

Frequency	Specimen	Test Temperature	Average Peak Load	Average Peak Stress	LVDT-1			LVDT-2			LVDT-3		
					Peak Strain (εo)	Dynamic Modulus	Phase angle	Peak Strain (εo)	Dynamic Modulus (MPa)	Phase angle	Peak Strain (εo)	Dynamic Modulus	Phase angle
		°C	KN	KPa	μs	MPa	Deg.	μs	MPa	Deg.	μs	MPa	Deg.
25	1	-9.7	16	1974	49	39878	7	75	26468	7	76	25807	9
	2	-9.7	16	1955	78	24968	8	51	38341	6	64	30642	4
10	1	-9.8	15	1879	54	34695	7	73	25631	8	80	23536	8
	2	-9.6	15	1831	87	21122	8	45	41009	7	60	30592	10
5	1	-9.9	15	1825	51	35956	9	84	21647	10	84	21650	10
	2	-9.6	14	1781	99	17912	9	38	46385	8	63	28363	11
1	1	-9.9	13	1656	50	33097	11	103	16106	13	91	18257	13
	2	-9.6	15	1891	106	17826	12	69	27332	10	84	22387	14
0.5	1	-9.9	12	1440	43	33692	12	104	13828	14	87	16514	14
	2	-9.6	13	1682	117	14318	13	54	31001	10	82	20600	17
0.1	1	-9.9	12	1452	52	27699	16	141	10261	18	116	12504	17
	2	-9.7	10	1219	126	9655	15	38	32160	12	80	15211	18

Table C.2: Strain, dynamic modulus and phase angle at each LVDT position on specimens of S1, 5°C

Frequency	Specimen	Test Temperature	Average Peak Load	Average Peak Stress	LVDT-1			LVDT-2			LVDT-3		
					Peak Strain (εo)	Dynamic Modulus	Phase angle	Peak Strain (εo)	Dynamic Modulus	Phase angle	Peak Strain (εo)	Dynamic Modulus	Phase angle
		°C	KN	KPa	μs	MPa	Deg.	μs	MPa	Deg.	μs	MPa	Deg.
25	1	4.9	10	1262	66	18978	12	78	16267	13	57	22279	13
	2	5	12	1508	124	12178	12	36	42175	10	81	18565	8
10	1	4.9	9	1154	74	15618	14	88	13163	15	62	18629	16
	2	4.8	11	1392	123	11360	15	59	23621	14	81	17202	17
5	1	5	7	917	66	13991	16	81	11381	16	56	16275	18
	2	5	7	917	103	8918	17	36	25561	16	60	15242	20
1	1	5	8	949	96	9895	20	119	8001	21	82	11580	22
	2	5	8	948	151	6290	21	48	19730	20	87	10857	24
0.5	1	5	4	483	59	8249	23	79	6114	24	53	9078	26
	2	5	4	482	79	6134	25	58	8328	22	55	8804	28
0.1	1	5	3	363	68	5302	27	95	3834	26	64	5673	30
	2	5	4	483	117	4130	27	85	5663	26	93	5220	29

Table C.3: Strain, dynamic modulus and phase angle at each LVDT position on specimens of S1, 25°C

Frequency	Specimen	Test Temperature	Average Peak Load	Average Peak Stress	LVDT-1			LVDT-2			LVDT-3		
					Peak Strain (εo)	Dynamic Modulus	Phase angle	Peak Strain (εo)	Dynamic Modulus	Phase angle	Peak Strain (εo)	Dynamic Modulus	Phase angle
		°C	KN	KPa	μs	MPa	Deg.	μs	MPa	Deg.	μs	MPa	Deg.
25	1	26.0	2.00	250	36	7027	28	56	4451	28	68	3675	26
	2	25.5	1.99	249	41	6108	26	55	4521	25	39	6426	26
10	1	26.0	1.94	242	44	5437	31	72	3347	29	89	2715	28
	2	25.3	1.88	235	53	4439	29	69	3391	29	51	4570	29
5	1	25.9	1.57	196	44	4457	32	75	2605	30	94	2090	29
	2	25.3	1.50	187	56	3316	29	71	2637	30	54	3485	30
1	1	25.7	1.17	146	58	2490	35	103	1418	31	127	1148	30
	2	25.2	1.18	147	86	1706	31	102	1446	31	76	1931	32
0.5	1	25.7	0.59	73	38	1919	39	78	944	33	94	779	33
	2	25.2	0.59	73	68	1083	35	73	1005	33	58	1259	34
0.1	1	25.6	0.29	36	34	1056	38	77	467	31	91	398	30
	2	25.0	0.29	37	64	571	33	74	497	32	61	602	32

Table C.4: Strain, dynamic modulus and phase angle at each LVDT position on specimens of S1, 40°C

Frequency	Specimen	Test Temperature	Average Peak Load	Average Peak Stress	LVDT-1			LVDT-2			LVDT-3		
					Peak Strain (εo)	Dynamic Modulus	Phase angle	Peak Strain (εo)	Dynamic Modulus	Phase angle	Peak Strain (εo)	Dynamic Modulus	Phase angle
		°C	KN	KPa	μs	MPa	Deg.	μs	MPa	Deg.	μs	MPa	Deg.
25	1	40.1	0.87	109.1	60	1827	32	69	1589	32	72	1525	31
	2	39.7	0.88	110.1	65	1686	32	79	1397	31	65	1695	30
10	1	40.0	0.81	101	78	1292	30	90	1117	30	95	1057	30
	2	39.8	0.91	113.4	97	1170	31	118	962	30	95	1194	29
5	1	40.2	0.55	69.2	78	890	31	94	736	30	96	718	29
	2	39.9	0.56	70.0	89	788	32	105	663	30	84	830	29
1	1	40.2	0.30	36.9	86	428	31	111	333	29	108	343	28
	2	39.9	0.30	37.7	100	378	30	127	298	31	94	400	28
0.5	1	40.2	0.16	19.8	67	295	31	67	295	30	80	248	26
	2	40.0	0.20	25.3	92	276	30	122	208	31	86	295	28
0.1	1	40.2	0.10	12.4	76	163	28	74	168	26	79	156	24
	2	40.0	0.15	19.1	99	192	24	141	136	26	89	214	22

Table C.5: Strain, dynamic modulus and phase angle at each LVDT position on specimens of S2, -10°C

Frequency	Specimen	Temperature °C	Average Peak Load KN	Average Peak Stress KPa	LVDT-1			LVDT-2			LVDT-3		
					Peak Strain (εo) μs	Dynamic Modulus MPa	Phase angle Deg	Peak Strain (εo) μs	Dynamic Modulus MPa	Phase angle Deg.	Peak Strain (εo) μs	Dynamic Modulus MPa	Phase angle Deg.
	1	-10	17.5	2186.9	83.1	26317.0	6.3	86.8	25188.0	7.6	52.4	41701.0	5.7
	2	-10.3	14.1	1755.1	80.2	21894.0	6.5	47.4	36990.0	7.0	51.6	33991.0	6.5
25	3	-9.9	17.4	2169.2	52.1	41628.0	8.2	88.2	24583.0	8.1	76.4	28392.0	9.7
	1	-9.9	16.206	2023	89	22840	8	90	22364	9	51	39804	8
10	2	-10.3	13.0	1629	85	19049	8	42	38487	8	44	37182	15
	3	-9.8	16.3	2031	63	32336	9	84	24150	8	79	25576	10
	1	-9.9	16.1	2014	97	20795	9	98	20653	10	50	40023	9
	2	-10.3	13.0	1619	97	16752	9	42	38319	9	44	36531	15
5	3	-9.9	16.2	2025	72	27977	10	86	23628	9	83	24495	11
	1	-10.0	16.9	2110	129	16351	12	125	16918	12	59	35648	12
1	2	-10.4	9.5	1181	93	12677	12	33	35350	10	35	33552	18
	3	-9.9	17.0	2116	101	20949	13	102	20792	11	104	20411	13
	1	-10.0	13.5	1682	120	14045	14	112	14982	14	48	34889	13
0.5	2	-10.0	9.6	1202	66	18176	13	68	17791	12	47	25548	17
	3	-9.9	15.4	1920	109	17606	14	96	19967	12	101	18993	15
	1	-10.0	9.7	1205	113	10631	16	105	11512	18	41	29381	17
0.1	2	-10.0	9.8	1223	94	12979	16	79	15482	15	60	20241	19
	3	-10.0	13.5	1689	133	12709	17	103	16398	16	113	14887	18

Table C.6: Strain, dynamic modulus and phase angle at each LVDT position on specimens of S2, 5°C

Frequency	Specimen	Temperature °C	Average Peak Load KN	Average Peak Stress KPa	LVDT-1			LVDT-2			LVDT-3		
					Peak Strain (εo) μs	Dynamic Modulus MPa	Phase angle Deg	Peak Strain (εo) μs	Dynamic Modulus MPa	Phase angle Deg.	Peak Strain (εo) μs	Dynamic Modulus MPa	Phase angle Deg.
25	1	5.0	8.130	1015	59	17134	14	87	11702	13	39	26203	12
	2	5.1	8.2	1022	75	13697	14	51	20186	13	67	15274	16
	3	4.6	16.2	2018	166	12173	13	94	21378	12	106	19046	15
10	1	5.0	7.561	944	65	14609	15	94	10055	15	41	22920	15
	2	5.2	7.5	934	82	11410	16	56	16660	16	73	12791	18
	3	0.0	0.0	0	0	0	0	0	0	0	0	0	0
5	1	5.0	5.6	695	55	12539	18	80	8731	18	34	20366	18
	2	5.1	7.4	922	92	9998	18	64	14403	18	81	11327	19
	3	4.8	7.4	930	109	8566	17	53	17420	18	70	13362	20
1	1	5.0	5.8	726	82	8864	22	119	6104	22	51	14301	22
	2	5.0	7.8	968	137	7077	21	96	10050	21	122	7930	22
	3	4.8	7.7	956	155	6172	21	81	11830	21	103	9303	23
0.5	1	5.0	3.9	485	69	7056	24	97	5002	25	39	12324	26
	2	5.0	5.8	729	126	5804	24	87	8416	24	118	6192	25
	3	4.9	4.8	604	124	4883	25	60	10072	25	83	7288	26
0.1	1	5.1	3.9	488	104	4683	27	149	3277	28	63	7731	28
	2	4.9	3.9	483	130	3717	25	89	5413	24	130	3728	26
	3	5.0	2.9	363	120	3030	28	58	6303	27	83	4356	30

Table C.7: Strain, dynamic modulus and phase angle at each LVDT position on specimens of S2, 25°C

Frequency	Specimen	Temperature °C	Average Peak Load KN	Average Peak Stress KPa	LVDT-1			LVDT-2			LVDT-3		
					Peak Strain (εo) μs	Dynamic Modulus MPa	Phase angle Deg	Peak Strain (εo) μs	Dynamic Modulus MPa	Phase angle Deg.	Peak Strain (εo) μs	Dynamic Modulus MPa	Phase angle Deg.
25	1	25.8	2.366	295	66	4496	25	61	4858	29	44	6744	27
	2	26.0	2.4	304	61	4967	25	55	5551	28	62	4882	28
	3	25.7	2.3	293	41	7182	31	72	4043	26	72	4042	29
10	1	25.7	2.278	284	89	3191	25	79	3606	30	59	4847	27
	2	26.0	2.3	291	77	3803	27	69	4249	28	79	3667	29
	3	25.7	2.1	257	48	5395	29	89	2872	26	89	2888	28
5	1	25.8	1.5	188	81	2332	27	68	2771	31	51	3701	29
	2	26.0	1.9	240	81	2975	26	72	3330	28	85	2836	29
	3	25.7	1.5	184	43	4274	31	83	2205	28	83	2227	30
1	1	25.7	0.1	18	12	1478	20	10	1843	23	8	2384	21
	2	26.0	1.6	194	113	1718	27	103	1874	32	121	1594	31
	3	25.7	1.0	121	53	2280	34	102	1192	30	108	1122	32
0.5	1	25.7	0.6	73	87	840	31	69	1057	34	52	1393	35
	2	25.9	0.8	97	91	1069	29	72	1342	34	85	1138	32
	3	25.7	0.6	73	48	1527	34	92	796	32	94	776	33
0.1	1	25.7	0.3	36	80	449	29	66	546	31	50	725	34
	2	25.9	0.6	73	108	670	25	91	794	29	105	691	27
	3	25.7	0.3	36	47	776	33	86	422	31	94	384	31

Table C.8: Strain, dynamic modulus and phase angle at each LVDT position on specimens of S2, 40°C

Frequency	Specimen	Temperature °C	Average Peak Load KN	Average Peak Stress KPa	LVDT-1			LVDT-2			LVDT-3		
					Peak Strain (εo) μs	Dynamic Modulus MPa	Phase angle Deg	Peak Strain (εo) μs	Dynamic Modulus MPa	Phase angle Deg.	Peak Strain (εo) μs	Dynamic Modulus MPa	Phase angle Deg.
25	1	40.8	1.0	130	72	1805	28	78	1674	31	70	1857	29
	2	39.7	0.9	109	42	2584	31	54	2027	31	76	1422	29
	3	41.7	0.6	72	34	2114	32	61	1186	29	62	1154	31
10	1	40.7	0.9	111	88	1263	26	94	1174	29	88	1251	28
	2	39.6	0.7	89	49	1801	29	64	1391	31	88	1003	27
	3	41.6	0.6	75	51	1486	32	91	831	28	92	824	30
5	1	40.5	0.5	67	76	882	28	82	822	29	80	840	30
	2	39.6	0.5	67	50	1341	30	67	1008	31	88	758	27
	3	41.6	0.5	67	62	1095	32	105	644	27	106	636	29
1	1	40.4	0.4	49	103	472	26	110	444	26	111	438	29
	2	39.6	0.3	36	57	638	28	76	476	31	90	402	25
	3	41.5	0.4	49	86	566	29	138	354	25	140	349	26
0.5	1	40.2	0.3	37	105	350	26	106	345	25	109	335	28
	2	39.5	0.2	25	53	468	27	69	359	29	78	320	24
	3	41.4	0.2	20	55	355	34	93	211	30	96	204	30
0.1	1	40.2	0.1	14	60	238	23	68	210	23	59	245	22
	2	39.5	0.2	23	72	322	21	93	248	22	92	252	18
	3	41.3	0.2	24	122	200	26	109	225	23	119	205	25

Table C.9: Strain, dynamic modulus and phase angle at each LVDT position on specimens of S3, -10°C

Frequency	Specimen	Temperature °C	Average Peak Load KN	Average Peak Stress KPa	LVDT-1			LVDT-2			LVDT-3		
					Peak Strain (εo) μs	Dynamic Modulus MPa	Phase angle Deg	Peak Strain (εo) μs	Dynamic Modulus MPa	Phase angle Deg.	Peak Strain (εo) μs	Dynamic Modulus MPa	Phase angle Deg.
25	1	-9.7	16.071	1967	36	55321	5	75	26266	3	92	21486	4
	2	-10.2	16.2	1983	53	37374	7	93	21328	3	61	32324	3
	3	-9.7	17.4	2171	60	36412	4	99	21950	5	85	25636	4
10	1	-9.7	14.879	1821	27	66955	6	81	22422	5	89	20370	5
	2	-10.1	15.0	1831	57	32108	7	86	21414	5	58	31473	5
	3	-9.9	16.3	2038	61	33605	5	104	19619	5	70	29039	4
5	1	-9.7	14.9	1822	20	90785	5	93	19666	6	96	18963	5
	2	-10.1	14.8	1806	63	28768	7	85	21168	5	59	30670	6
	3	-10.0	14.7	1840	60	30926	5	104	17770	5	59	31118	5
1	1	-9.8	13.6	1664	62	26790	6	78	21444	7	72	23075	7
	2	-10.0	15.2	1864	76	24650	7	95	19562	6	67	27841	7
	3	-10.1	15.1	1890	69	27257	7	120	15734	7	64	29457	6
0.5	1	-9.8	13.5	1655	51	32455	8	93	17732	8	81	20529	8
	2	-10.0	13.5	1649	73	22727	8	87	18909	7	62	26668	7
	3	-10.2	11.5	1436	56	25734	7	101	14286	7	49	29471	7
0.1	1	-9.8	11.7	1426	57	25167	10	87	16443	10	82	17407	10
	2	-10.0	13.6	1669	86	19470	9	101	16566	9	70	23788	9
	3	-10.3	11.8	1471	66	22293	9	116	12654	8	56	26117	8

Table C.10: Strain, dynamic modulus and phase angle at each LVDT position on specimens of S3, 5°C

Frequency	Specimen	Temperature °C	Average Peak Load KN	Average Peak Stress KPa	LVDT-1			LVDT-2			LVDT-3		
					Peak Strain (εo) μs	Dynamic Modulus MPa	Phase angle Deg	Peak Strain (εo) μs	Dynamic Modulus MPa	Phase angle Deg.	Peak Strain (εo) μs	Dynamic Modulus MPa	Phase angle Deg.
25	1	4.7	10.459	1280	72	17887	8	66	19315	9	55	23291	8
	2	4.6	12.0	1467	74	19804	8	51	28601	9	89	16428	11
	3	4.6	12.1	1506	82	18460	7	95	15823	8	62	24229	7
10	1	4.7	9.681	1185	71	16688	10	62	19038	10	61	19528	10
	2	4.8	11.1	1358	80	17017	10	46	29827	10	86	15754	9
	3	4.7	11.1	1382	90	15367	10	95	14581	10	63	21952	9
5	1	4.6	9.5	1160	73	15869	11	65	17950	12	69	16785	12
	2	4.8	11.0	1347	91	14876	10	46	29471	12	93	14487	11
	3	4.7	11.1	1381	100	13764	11	101	13670	11	67	20578	10
1	1	4.6	9.6	1172	90	13089	15	81	14397	16	94	12440	15
	2	4.8	11.4	1392	120	11587	14	55	25194	15	124	11230	15
	3	4.8	11.6	1446	133	10856	14	129	11199	14	87	16700	13
0.5	1	4.6	7.7	945	80	11803	16	72	13068	17	89	10613	17
	2	4.9	9.7	1182	116	10234	15	51	23297	16	122	9707	16
	3	5.0	9.6	1202	125	9586	16	121	9905	16	80	14940	15
0.1	1	4.6	7.8	960	107	8950	19	102	9416	20	126	7595	20
	2	4.9	7.7	941	123	7650	18	53	17666	19	136	6915	19
	3	5.0	7.8	979	137	7129	19	131	7500	18	88	11121	18

Table C.11: Strain, dynamic modulus and phase angle at each LVDT position on specimens of S3, 25°C

Frequency	Specime.n	Temperature °C	Average Peak Load KN	Average Peak Stress KPa	LVDT-1			LVDT-2			LVDT-3		
					Peak Strain (εo) μs	Dynamic Modulus MPa	Phase angle Deg	Peak Strain (εo) μs	Dynamic Modulus MPa	Phase angle Deg.	Peak Strain (εo) μs	Dynamic Modulus MPa	Phase angle Deg.
25	1	24.6	9.6	1172	90	13089	15	81	14397	16	94	12440	15
	2	25.0	11.4	1392	120	11587	14	55	25194	15	124	11230	15
	3	25.2	11.6	1446	133	10856	14	129	11199	14	87	16700	13
10	1	24.7	2.7	335	47	7167	22	62	5421	21	42	7924	23
	2	25.0	2.7	329	23	14512	22	59	5615	20	53	6199	19
	3	25.2	3.1	382	51	7427	20	59	6463	19	52	7413	21
5	1	24.8	2.3	283	48	5860	24	64	4425	22	41	6930	24
	2	25.0	2.3	277	22	12492	23	60	4644	22	55	5083	20
	3	25.2	2.6	326	59	5553	22	57	5700	22	51	6444	24
1	1	24.8	2.0	242	67	3619	27	87	2796	26	52	4697	29
	2	25.0	1.9	238	28	8547	27	80	2972	25	73	3279	24
	3	25.3	2.3	287	82	3496	26	81	3550	24	69	4184	28
0.5	1	24.8	1.6	190	69	2764	29	88	2162	28	51	3747	32
	2	25.0	1.5	190	27	6923	30	80	2370	26	72	2628	26
	3	25.3	1.9	241	87	2788	27	86	2812	25	70	3451	29
0.1	1	24.9	1.0	118	75	1574	29	94	1266	29	52	2285	32
	2	25.1	1.0	118	26	4591	32	83	1430	27	79	1496	28
	3	25.3	1.5	193	111	1738	27	111	1736	26	87	2222	30

Table C.12: Strain, dynamic modulus and phase angle at each LVDT position on specimens of S3, 40 °C

Frequency	Specimen	Temperature °C	Average Peak Load KN	Average Peak Stress KPa	LVDT-1			LVDT-2			LVDT-3		
					Peak Strain (εo) µs	Dynamic Modulus MPa	Phase angle Deg	Peak Strain (εo) µs	Dynamic Modulus MPa	Phase angle Deg.	Peak Strain (εo) µs	Dynamic Modulus MPa	Phase angle Deg.
25	1	40.1	2.7	335	100	3355	27	134	2498	26	68	4967	30
	2	39.9	2.7	333	49	6748	28	120	2766	26	91	3663	24
	3	40.1	1.4	173	52	3292	25	45	3867	22	41	4190	26
10	1	40.1	2.2	274	108	2526	27	151	1811	27	77	3547	30
	2	4.0	2.4	293	60	4850	29	143	2048	25	115	2550	25
	3	40.3	1.3	168	66	2555	26	61	2747	25	52	3263	27
5	1	40.1	1.9	228	115	1977	27	161	1412	27	81	2806	30
	2	40.0	1.8	225	57	3938	29	136	1648	25	110	2046	25
	3	40.3	0.9	118	62	1899	28	60	1972	28	44	2673	28
1	1	40.1	1.0	120	120	1000	28	162	741	29	80	1500	32
	2	40.1	1.0	117	49	2416	32	139	843	28	114	1032	29
	3	40.3	0.8	97	90	1086	30	89	1089	29	60	1610	30
0.5	1	40.1	0.4	48	78	609	33	93	514	33	45	1070	34
	2	40.1	0.4	48	25	1920	33	84	565	32	67	710	31
	3	40.3	0.6	73	87	838	30	90	815	29	56	1308	30
0.1	1	40.2	0.2	24	69	346	30	79	301	30	40	600	32
	2	40.1	0.2	24	23	1033	34	72	330	32	59	407	31
	3	40.3	0.3	36	76	479	29	84	433	26	45	803	29

Table C1.3: Strain, dynamic modulus and phase angle at each LVDT position on specimens of S4, -10 °C

Frequency	Specimen	Temperature °C	Average Peak Load KN	Average Peak Stress KPa	LVDT-1			LVDT-2			LVDT-3		
					Peak Strain (εo) μs	Dynamic Modulus MPa	Phase angle Deg	Peak Strain (εo) μs	Dynamic Modulus MPa	Phase angle Deg.	Peak Strain (εo) μs	Dynamic Modulus MPa	Phase angle Deg.
25	1	-10.5	18.5	2260	88	25708	9	93	24183	6	101	22385	7
	2	-10.1	18.1	2212	128	17290	7	77	28680	8	76	29020	12
	3	-9.7	15.8	1969	99	19835	9	105	18788	9	43	45280	8
10	1	-10.5	17.2	2108	90	23526	9	106	19827	9	97	21649	8
	2	-10.2	16.7	2049	143	14344	9	79	25953	8	60	34239	17
	3	-9.7	14.8	1842	98	18893	9	108	17072	9	45	40842	8
5	1	-10.4	15.2	1860	84	22133	10	105	17766	10	86	21561	9
	2	-10.2	13.2	1610	132	12210	9	63	25616	9	48	33237	18
	3	-9.8	12.9	1610	93	17345	10	101	15874	10	40	39933	9
1	1	-10.4	15.4	1880	98	19192	2	137	13748	12	100	18842	12
	2	-10.2	11.7	1428	149	9604	12	65	22020	11	49	29443	21
	3	-9.8	13.6	1693	118	14368	12	127	13284	12	51	33443	11
0.5	1	-10.4	11.7	1432	102	14062	2	116	12376	13	83	17280	13
	2	-10.2	9.7	1193	149	8034	13	59	20146	13	37	32338	24
	3	-9.9	11.5	1441	112	12866	14	120	11961	14	45	32065	12
0.1	1	-10.4	11.6	1417	141	10034	8	154	9211	17	99	14374	16
	2	-10.2	7.7	943	158	5985	16	59	16100	16	30	31556	27
	3	-9.9	9.7	1206	120	10047	16	128	9401	16	48	25165	15

Table C.14: Strain, dynamic modulus and phase angle at each LVDT position on specimens of S4, 5 °C

Frequency	Specimen	Temperature °C	Average Peak Load KN	Average Peak Stress KPa	LVDT-1			LVDT-2			LVDT-3		
					Peak Strain (εo) µs	Dynamic Modulus MPa	Phase angle Deg	Peak Strain (εo) µs	Dynamic Modulus MPa	Phase angle Deg.	Peak Strain (εo) µs	Dynamic Modulus MPa	Phase angle Deg.
25	1	5.3	8.3	1015	74	13757	14	104	9736	13	65	15713	13
	2	5.2	8.2	999	72	13927	14	55	18008	13	93	10709	13
	3	4.4	8.4	1052	91	11507	14	97	10882	14	38	27562	13
10	1	5.3	7.5	922	90	10259	17	118	7789	17	56	16334	16
	2	5.2	7.5	917	76	12110	17	60	15340	16	99	9265	16
	3	4.5	7.7	962	99	9695	16	100	9642	16	42	22927	15
5	1	5.3	5.7	696	97	7167	17	109	6379	18	27	26146	2
	2	5.2	5.6	681	68	10072	19	49	13797	17	87	7855	17
	3	4.7	5.7	713	88	8109	18	88	8142	17	33	21506	16
1	1	5.3	5.7	701	124	5668	22	148	4733	23	61	11440	22
	2	5.2	5.8	712	100	7140	22	72	9901	21	126	5662	21
	3	4.7	5.8	721	124	5828	22	122	5916	21	48	15141	21
0.5	1	5.3	3.9	474	107	4448	24	121	3923	25	53	8885	24
	2	5.3	3.9	482	88	5498	24	54	8924	23	103	4656	22
	3	4.8	3.9	482	107	4525	25	101	4794	23	34	14008	23
0.1	1	5.3	2.9	356	123	2893	26	138	2577	27	64	5521	28
	2	5.3	3.9	475	125	3808	26	83	5737	27	147	3229	25
	3	4.8	3.8	480	152	3169	27	144	3331	26	53	8987	28

Table C.15: Strain, dynamic modulus and phase angle at each LVDT position on specimens of S4, 25 °C

Frequency	Specimen	Temperature °C	Average Peak Load KN	Average Peak Stress KPa	LVDT-1			LVDT-2			LVDT-3		
					Peak Strain (εo) μs	Dynamic Modulus MPa	Phase angle Deg	Peak Strain (εo) μs	Dynamic Modulus MPa	Phase angle Deg.	Peak Strain (εo) μs	Dynamic Modulus MPa	Phase angle Deg.
25	1	25.3	3.0	370	81	4576	24	136	2729	27	88	4222	26
	2	25.0	2.0	241	66	3657	24	64	3760	26	36	6685	22
	3	24.8	1.9	234	59	3961	26	50	4674	25	42	5508	27
10	1	25.3	1.3	165	53	3089	27	79	2076	30	53	3102	26
	2	25.0	1.9	230	77	2973	26	75	3066	27	47	4893	26
	3	24.8	1.8	229	77	2969	26	62	3704	24	55	4157	27
5	1	25.2	1.3	165	67	2478	28	98	1686	31	65	2538	28
	2	25.0	1.3	159	69	2299	27	67	2368	28	43	3692	29
	3	24.8	1.5	183	77	2379	26	63	2890	25	54	3392	29
1	1	25.2	1.0	119	96	1246	31	131	909	33	87	1375	30
	2	24.8	1.3	164	108	1525	31	118	1396	31	81	2033	31
	3	24.9	1.1	143	104	1366	29	89	1600	28	71	2008	33
0.5	1	25.2	0.8	95	103	928	31	135	708	33	90	1061	30
	2	24.8	1.0	119	105	1131	31	112	1061	31	79	1507	32
	3	24.9	0.8	97	98	989	30	86	1125	29	60	1610	34
0.1	1	25.1	0.4	47	95	500	30	114	416	29	77	612	27
	2	24.8	0.6	71	111	640	29	116	612	28	82	867	31
	3	24.9	0.5	61	94	647	26	83	730	26	61	989	29

Table C.16: Strain, dynamic modulus and phase angle at each LVDT position on specimens of S4, 40 °C

Frequency	Specimen	Temperature °C	Average Peak Load KN	Average Peak Stress KPa	LVDT-1			LVDT-2			LVDT-3		
					Peak Strain (εo) µs	Dynamic Modulus MPa	Phase angle Deg	Peak Strain (εo) µs	Dynamic Modulus MPa	Phase angle Deg.	Peak Strain (εo) µs	Dynamic Modulus MPa	Phase angle Deg.
25	1	39.5	0.9	107	96	1121	28	76	1423	31	77	1400	28
	2	40.1	0.8	98	69	1420	29	64	1535	29	74	1327	29
	3	40.0	0.9	109	79	1383	28	67	1630	28	68	1613	31
10	1	39.5	0.7	89	114	779	27	91	971	29	88	1002	27
	2	40.0	0.6	78	77	1013	28	73	1071	28	82	948	28
	3	40.0	0.9	117	112	1043	28	99	1181	28	101	1156	31
5	1	39.6	0.6	69	122	569	27	97	711	29	92	749	26
	2	40.0	0.6	68	87	782	28	83	819	28	94	727	28
	3	40.0	0.6	71	98	722	28	87	814	28	84	843	30
1	1	39.7	0.4	48	154	312	25	128	376	29	117	412	25
	2	40.0	0.4	49	117	416	27	105	462	26	122	397	26
	3	40.0	0.4	50	133	372	29	112	442	26	104	477	29
0.5	1	39.8	0.2	19	101	192	29	77	250	34	69	279	28
	2	40.0	0.2	26	95	273	29	83	312	30	94	276	27
	3	40.1	0.2	25	107	234	31	85	293	26	65	385	30
0.1	1	39.9	0.1	12	89	134	24	74	162	29	63	189	24
	2	40.0	0.1	17	98	171	27	88	188	25	96	172	26
	3	40.1	0.2	19	139	138	28	96	200	21	77	249	26

Table C.17: Strain, dynamic modulus and phase angle at each LVDT position on specimens of B1, -10 °C

Frequency (Hz)	Specimen No.	Average Peak Load (KN)	Average Peak Stress (KPa)	LVDT-1			LVDT-2			LVDT-3		
				Peak Strain (εo) μs	Dynamic Modulus MPa	Phase angle Deg	Peak Strain (εo) μs	Dynamic Modulus MPa	Phase angle Deg.	Peak Strain (εo) μs	Dynamic Modulus MPa	Phase angle Deg.
25	1	11.1	1352	70	19285	4	44	30992	1	35	39571	18
	2	11.1	1356	59	22951	0	68	19966	4	63	21614	2
	3	10.8	1324	50	26026	1	50	26450	10	88	15011	1
10	1	10.4	1268	65	19592	6	46	27588	6	39	33079	3
	2	10.3	1266	59	21371	5	61	20836	5	71	17929	7
	3	10.5	1282	47	27275	4	50	25289	6	84	15329	5
5	1	10.2	1245	68	18311	8	49	25600	7	39	32007	7
	2	10.3	1260	65	19390	7	64	19572	8	75	16952	8
	3	10.1	1240	47	26390	6	52	23560	8	84	14722	7
1	1	10.5	1286	81	15777	11	60	21556	10	45	28563	10
	2	10.5	1289	80	16040	11	77	16747	12	87	14935	11
	3	10.5	1283	56	22838	9	64	19798	10	99	13004	10
0.5	1	10.6	1303	87	15038	12	63	20745	12	46	28793	11
	2	10.7	1308	91	14449	12	85	15427	13	94	14101	12
	3	10.7	1307	58	22169	16	71	18258	12	107	12184	11
0.1	1	10.6	1303	88	14783	15	70	18574	14	103	12822	14
	2	10.7	1315	117	11272	15	105	12484	16	106	12569	15
	3	9.9	1215	98	12308	33	81	14891	14	119	10243	13

Table C.18: Strain, dynamic modulus and phase angle at each LVDT position on specimens of B1, 5 °C

Frequency (Hz)	Specimen No.	Average Peak Load (KN)	Average Peak Stress (KPa)	LVDT-1			LVDT-2			LVDT-3		
				Peak Strain (εo) μs	Dynamic Modulus MPa	Phase angle Deg	Peak Strain (εo) μs	Dynamic Modulus MPa	Phase angle Deg.	Peak Strain (εo) μs	Dynamic Modulus MPa	Phase angle Deg.
25	1	10.1	1238	83	14892	4	59	21014	9			
	2	11.1	1358	83	16317	5	136	9988	6			
	3	10.9	1332	92	14304	6	65	20258	10			
10	1	8.3	1019	52	19501	15	66	15337	14			
	2	10.2	1248	94	13233	13	142	8809	14			
	3	10.4	1274	88	14258	11	68	18686	14			
5	1	8.2	1009	58	17267	17	73	13885	16			
	2	9.2	1126	93	12078	16	145	7755	18			
	3	9.4	1146	89	12757	14	67	16882	17			
1	1	7.6	934	75	12429	22	93	10042	20			
	2	6.7	818	96	8496	21	152	5393	23			
	3	9.6	1171	122	9526	19	94	12372	22			
0.5	1	7.8	950	88	10765	23	109	8739	22			
	2	5.8	711	100	7109	23	157	4529	25			
	3	8.7	1067	130	8108	22	99	10667	24			
0.1	1	7.8	954	130	7343	26	158	6053	25			
	2	5.8	712	145	4912	26	220	3234	27			
	3	9.7	1186	204	5757	25	158	7429	27			

Table C.19: Strain, dynamic modulus and phase angle at each LVDT position on specimens of B1, 25 °C

Frequency (Hz)	Specimen No.	Average Peak Load (KN)	Average Peak Stress (KPa)	LVDT-1			LVDT-2			LVDT-3		
				Peak Strain (εo) μs	Dynamic Modulus MPa	Phase angle Deg	Peak Strain (εo) μs	Dynamic Modulus MPa	Phase angle Deg.	Peak Strain (εo) μs	Dynamic Modulus MPa	Phase angle Deg.
25	1	2.0	241	46	5248	20	42	5762	20	39	6281	23
	2	1.6	195	29	6782	22	46	4198	23	42	4638	24
	3	2.0	248	32	7757	18	40	6088	19	66	3768	16
10	1	1.9	229	56	4072	28	53	4334	26	50	4590	28
	2	1.1	136	26	5264	32	45	3057	30	41	3376	30
	3	1.5	186	33	5622	25	39	4760	27	60	3090	23
5	1	1.5	182	57	3167	30	54	3378	28	52	3528	30
	2	1.1	136	34	4022	34	57	2400	32	51	2706	32
	3	1.1	137	31	4373	28	38	3623	29	56	2471	26
1	1	1.5	187	104	1805	32	97	1932	31	94	2024	33
	2	1.0	118	54	2185	35	92	1289	35	81	1476	33
	3	1.2	143	56	2507	32	65	2186	32	98	1459	31
0.5	1	1.0	119	94	1267	33	87	1366	33	83	1453	35
	2	0.8	95	58	1640	35	98	970	34	86	1123	33
	3	0.8	95	52	1813	34	60	1564	35	88	1087	33
0.1	1	0.6	71	107	663	32	100	710	33	92	780	34
	2	0.8	95	99	956	31	157	605	30	142	676	29
	3	0.6	72	69	1029	33	76	939	32	114	635	31

Table C.20: Strain, dynamic modulus and phase angle at each LVDT position on specimens of B1, 40 °C

Frequency (Hz)	Specimen No.	Average Peak Load (KN)	Average Peak Stress (KPa)	LVDT-1			LVDT-2			LVDT-3		
				Peak Strain (εo) μs	Dynamic Modulus MPa	Phase angle Deg	Peak Strain (εo) μs	Dynamic Modulus MPa	Phase angle Deg.	Peak Strain (εo) μs	Dynamic Modulus MPa	Phase angle Deg.
25	1	0.7	90	55	1645	23	36	2495	30	56	1621	24
	2	0.6	77	42	1812	23	24	3265	29	60	1303	24
	3	1.0	119	44	2694	26	49	2426	24	71	1677	23
10	1	0.5	66	58	1133	30	39	1672	33	61	1097	30
	2	0.6	79	63	1259	30	34	2348	33	86	931	30
	3	0.5	66	35	1889	34	42	1546	30	61	1078	31
5	1	0.5	55	68	813	31	46	1202	35	70	792	32
	2	0.5	57	64	894	32	35	1605	33	90	638	32
	3	0.4	45	34	1317	35	38	1162	33	59	760	33
1	1	0.4	47	108	435	30	76	621	34	112	424	31
	2	0.4	48	101	477	31	56	863	33	145	335	31
	3	0.4	43	61	702	33	67	631	33	104	414	32
0.5	1	0.3	35	113	313	31	78	455	34	116	310	32
	2	0.3	36	103	351	31	56	643	34	151	240	31
	3	0.3	31	61	508	33	67	463	34	105	297	33
0.1	1	0.2	29	152	187	27	105	273	29	160	181	29
	2	0.2	24	116	207	29	66	361	33	185	131	28
	3	0.2	24	80	298	29	88	270	31	137	175	29

Table C.21: Strain, dynamic modulus and phase angle at each LVDT position on specimens of B2, -10 °C

Frequency (Hz)	Specimen No.	Temperature (°C)	Average Peak Load (KN)	Average Peak Stress (KPa)	LVDT-1			LVDT-2			LVDT-3		
					Peak Strain (εo) μs	Dynamic Modulus MPa	Phase angle Deg	Peak Strain (εo) μs	Dynamic Modulus MPa	Phase angle Deg.	Peak Strain (εo) μs	Dynamic Modulus MPa	Phase angle Deg.
25	1	-10.8	11.5	1403	74	19061	4	48	29484	5	41	34934	1
	2	-10.8	11.2	1367	59	23235	9	65	20879	4	51	27204	5
	3	-9.7	11.1	1355	32	42570	2	71	19013	2	120	11248	2
10	1	-10.6	10.4	1275	61	21013	7	63	20315	5	38	34334	5
	2	-10.9	10.4	1274	35	36844	5	68	18709	4	41	31446	4
	3	-9.9	10.5	1283	28	44917	1	69	18282	6	109	11785	6
5	1	-10.5	10.4	1278	63	20182	10	66	19218	6	39	33249	7
	2	-10.3	10.3	1265	36	34841	8	72	17623	6	42	30321	5
	3	-9.9	10.5	1279	28	45794	5	74	17101	8	115	11087	8
1	1	-10.4	10.5	1287	78	16540	11	77	16663	9	45	28712	11
	2	-10.1	10.6	1296	43	29836	10	85	15162	8	50	26352	8
	3	-10.1	10.7	1305	33	39506	6	87	14784	10	136	9574	10
0.5	1	-10.4	9.7	1183	78	15206	10	80	14848	10	44	26967	12
	2	-9.9	10.6	1300	46	28024	11	91	14346	9	53	24770	9
	3	-10.2	10.6	1303	34	37747	6	93	13913	11	146	8939	11
0.1	1	-10.4	9.8	1201	94	12779	10	90	13404	10	55	21878	13
	2	-9.7	10.7	1308	58	22386	21	107	12216	11	62	21246	11
	3	-10.2	10.9	1330	43	30789	8	111	11846	12	171	7793	12

Table C.22: Strain, dynamic modulus and phase angle at each LVDT position on specimens of B2, 5 °C

Frequency (Hz)	Specimen No.	Temperature (°C)	Average Peak Load (KN)	Average Peak Stress (KPa)	LVDT-1			LVDT-2			LVDT-3		
					Peak Strain (εo) μs	Dynamic Modulus MPa	Phase angle Deg	Peak Strain (εo) μs	Dynamic Modulus MPa	Phase angle Deg.	Peak Strain (εo) μs	Dynamic Modulus MPa	Phase angle Deg.
25	1	4.6	5.2	633	63	10042	6	36	17472	5	58	11046	5
	2	5.1	8.1	991	72	13670	3	69	14265	4	32	30999	4
	3	4.6	5.2	635	16	38098	8	52	11985	4	85	7478	5
10	1	4.4	4.8	593	60	9879	10	34	17461	11	61	9804	11
	2	5.1	7.6	930	81	11504	10	70	13325	11	35	26536	11
	3	4.7	5.8	710	23	30185	4	65	10851	9	97	7336	10
5	1	4.4	4.7	574	63	9040	14	35	16303	13	66	8781	14
	2	5.1	7.4	910	88	10384	13	75	12144	13	38	23983	14
	3	4.8	5.8	705	27	26061	7	71	9809	11	105	6685	12
1	1	4.5	4.8	589	84	6992	17	47	12525	16	90	6585	18
	2	5.1	7.7	942	120	7868	18	100	9412	17	53	17959	18
	3	4.8	5.8	712	34	20586	11	92	7630	16	137	5205	16
0.5	1	4.6	4.9	595	95	6267	18	53	11297	18	104	5768	20
	2	5.2	5.8	710	100	7104	20	89	7948	19	44	16163	19
	3	4.9	5.9	720	38	18884	12	106	6712	17	154	4664	18
0.1	1	4.6	4.9	597	125	4779	21	68	8780	20	144	4175	23
	2	5.2	5.9	726	141	5148	22	125	5786	22	62	11737	22
	3	4.9	4.9	597	39	15040	17	123	4808	21	177	3368	20

Table C.23: Strain, dynamic modulus and phase angle at each LVDT position on specimens of B2, 25 °C

Frequency (Hz)	Specimen No.	Temperature (°C)	Average Peak Load (KN)	Average Peak Stress (KPa)	LVDT-1			LVDT-2			LVDT-3		
					Peak Strain (εo) μs	Dynamic Modulus MPa	Phase angle Deg	Peak Strain (εo) μs	Dynamic Modulus MPa	Phase angle Deg.	Peak Strain (εo) μs	Dynamic Modulus MPa	Phase angle Deg.
25	1	24.5	2.2	266	33	8078	15	37	7215	12	70	3856	13
	2	24.9	2.2	263	50	5252	13	39	6829	17	30	8782	13
	3	24.8	2.1	261	17	15442	14	47	5537	14	68	3809	14
10	1	24.6	1.9	232	35	6598	23	39	5987	19	79	2981	19
	2	24.9	2.1	254	51	5007	22	44	5793	22	37	7017	20
	3	25.0	1.9	230	19	12194	21	53	4295	20	75	3060	19
5	1	25.0	1.5	183	33	5585	26	38	4797	22	76	2423	22
	2	24.9	1.8	226	54	4174	24	46	4964	24	39	5817	23
	3	25.0	1.5	180	16	10831	25	51	3503	24	74	2453	22
1	1	25.0	1.1	140	41	3451	30	50	2825	28	95	1487	27
	2	24.9	1.5	187	70	2662	29	62	3031	29	50	3756	28
	3	25.0	1.2	142	19	7574	32	66	2146	29	101	1413	27
0.5	1	24.8	0.8	95	34	2755	31	45	2128	31	82	1166	31
	2	24.9	1.2	144	67	2134	30	64	2249	30	48	3015	30
	3	24.9	0.8	95	12	7667	37	56	1665	33	93	1024	30
0.1	1		0.6	71	43	1635	32	57	1239	32	102	705	31
	2		1.0	120	88	1368	31	82	1476	32	63	1929	31
	3		0.6	71	14	4948	41	70	1006	35	116	616	31

Table C.24: Strain, dynamic modulus and phase angle at each LVDT position on specimens of B2, 40 °C

Frequency (Hz)	Specimen No.	Temperature (°C)	Average Peak Load (KN)	Average Peak Stress (KPa)	LVDT-1			LVDT-2			LVDT-3		
					Peak Strain (εo) μs	Dynamic Modulus MPa	Phase angle Deg	Peak Strain (εo) μs	Dynamic Modulus MPa	Phase angle Deg.	Peak Strain (εo) μs	Dynamic Modulus MPa	Phase angle Deg.
25	1	39.7	0.9	111	23	4860	19	31	3543	22	48	2339	21
	2	39.6	1.0	128	41	3093	21	44	2922	22	33	3924	20
	3	40.1	1.2	142	33	4249	21	45	3124	20	63	2230	21
10	1	39.6	0.6	69	18	3859	27	27	2584	28	42	1670	28
	2	39.7	0.6	79	34	2295	28	37	2149	28	27	2940	28
	3	40.0	0.7	89	27	3224	29	40	2178	27	54	1646	26
5	1	39.6	0.4	47	14	3277	32	22	2094	32	37	1275	33
	2	39.8	0.5	56	30	1861	32	34	1652	31	25	2249	33
	3	40.1	0.6	68	28	2413	32	40	1654	29	52	1288	28
1	1	39.6	0.3	36	19	1839	41	31	1152	35	50	722	37
	2	39.9	0.3	41	41	982	36	46	886	35	33	1235	35
	3	40.2	0.4	48	37	1290	34	55	863	34	70	689	32
0.5	1	39.6	0.2	29	20	1426	39	31	925	35	51	573	36
	2	39.9	0.3	36	47	754	36	52	687	35	38	956	36
	3	40.2	0.3	36	37	956	36	55	642	35	69	518	33
0.1	1	39.5	0.2	24	30	785	37	45	529	34	72	333	35
	2	40.0	0.3	31	67	460	32	74	415	33	55	565	32
	3	40.3	0.3	31	55	549	33	81	375	33	97	317	31

Table C.25: Strain, dynamic modulus and phase angle at each LVDT position on specimens of B3, -10 °C

Frequency (Hz)	Specimen No.	Average Peak Load (KN)	Average Peak Stress (KPa)	LVDT-1			LVDT-2			LVDT-3		
				Peak Strain (εo) μs	Dynamic Modulus MPa	Phase angle Deg	Peak Strain (εo) μs	Dynamic Modulus MPa	Phase angle Deg.	Peak Strain (εo) μs	Dynamic Modulus MPa	Phase angle Deg.
25	1	10.1	1240	66	18834	3	86	14477	2	70	17865	10
	2	9.0	1100	30	36741	1	68	16108	5	121	9161	7
	3	8.1	994	65	15150	0	92	10649	1	61	16386	4
10	1	8.6	1052	61	17182	3	70	15065	4	66	16173	8
	2	6.7	816	32	25554	10	197	4135	18	95	8641	3
	3	7.7	947	62	15202	4	82	11465	6	48	19821	1
5	1	8.4	1033	61	16964	5	73	14128	6	67	15683	7
	2	5.7	700	28	25305	10	181	3871	7	83	8558	5
	3	7.5	923	63	14526	7	85	10715	9	45	20733	5
1	1	8.8	1076	71	15205	8	87	12389	9	77	14045	9
	2	5.5	676	32	21212	11	159	4250	4	88	7738	8
	3	6.7	825	66	12388	10	90	9103	11	47	17507	9
0.5	1	8.8	1075	74	14613	9	90	11947	10	82	13186	10
	2	5.4	665	34	19768	12	130	5105	1	92	7333	9
	3	5.8	716	64	11152	11	85	8380	12	45	15883	8
0.1	1	7.9	965	106	9085	26	154	6289	18	103	9490	18
	2	5.5	669	40	16713	13	82	8135	1	105	6428	12
	3	5.8	714	82	8578	15	105	6703	15	55	12903	11

Table C.26: Strain, dynamic modulus and phase angle at each LVDT position on specimens of B3, 5 °C

Frequency (Hz)	Specimen No.	Average Peak Load (KN)	Average Peak Stress (KPa)	LVDT-1			LVDT-2			LVDT-3		
				Peak Strain (εo) μs	Dynamic Modulus MPa	Phase angle Deg	Peak Strain (εo) μs	Dynamic Modulus MPa	Phase angle Deg.	Peak Strain (εo) μs	Dynamic Modulus MPa	Phase angle Deg.
25	1	5.0	607	60	10170	5	66	9131	7	98	6242	7
	2	6.0	735	76	9652	7	114	6436	5	46	16271	4
	3	4.1	496	51	9651	3	66	7409	7	42	11914	1
10	1	4.7	578	55	10566	11	69	8336	11	96	6085	9
	2	5.7	699	81	8617	12	129	5432	12	49	14406	13
	3	3.9	473	55	8522	10	61	7653	12	35	13495	7
5	1	4.7	577	61	9467	15	75	7690	13	104	5620	13
	2	4.7	576	75	7656	15	118	4883	15	44	13265	17
	3	3.8	468	61	7582	14	66	7011	14	37	12723	11
1	1	4.8	590	86	6847	19	104	5654	19	142	4208	18
	2	3.9	472	84	5635	21	131	3617	21	49	9822	22
	3	3.9	473	83	5622	18	87	5354	18	49	9659	16
0.5	1	4.9	600	101	5921	22	122	4936	21	162	3745	21
	2	3.5	429	88	4844	23	139	3092	23	51	8513	24
	3	3.5	434	89	4824	19	91	4723	19	51	8442	17
0.1	1	3.9	476	125	3802	29	147	3228	25	186	2586	25
	2	3.5	431	131	3295	27	215	2009	28	80	5455	28
	3	3.0	363	109	3314	24	104	3443	23	60	6101	22

Table C.27: Strain, dynamic modulus and phase angle at each LVDT position on specimens of B3, 25 °C

Frequency (Hz)	Specimen No.	Average Peak Load (KN)	Average Peak Stress (KPa)	LVDT-1			LVDT-2			LVDT-3		
				Peak Strain (εo) μs	Dynamic Modulus MPa	Phase angle Deg	Peak Strain (εo) μs	Dynamic Modulus MPa	Phase angle Deg	Peak Strain (εo) μs	Dynamic Modulus MPa	Phase angle Deg
25	1	1.5	186	51	3665	19	31	5998	19	65	2885	15
	2	1.3	155	39	3960	18	49	3156	20	62	2524	18
	3	1.3	155	54	2853	15	45	3433	17	17	9369	18
10	1	1.5	185	73	2522	25	45	4069	27	85	2205	21
	2	1.3	154	46	3336	28	63	2451	26	77	2038	24
	3	1.1	132	57	2295	22	48	2706	25	17	7589	22
5	1	0.9	114	57	2015	29	36	3154	29	63	1828	29
	2	0.9	112	45	2505	31	59	1902	30	68	1646	30
	3	0.9	115	59	1930	25	52	2213	28	18	6257	28
1	1	1.0	118	102	1155	35	67	1771	35	109	1094	34
	2	1.0	119	81	1463	35	111	1073	34	128	937	34
	3	1.0	121	106	1126	30	96	1239	33	33	3687	32
0.5	1	1.0	119	131	905	37	87	1359	39	140	858	34
	2	0.7	84	77	1088	37	105	801	35	113	750	35
	3	0.7	84	91	920	34	87	953	37	29	2934	37
0.1	1	1.0	120	227	528	36	156	769	37	239	507	33
	2	0.5	59	96	620	38	133	447	35	137	437	36
	3	0.5	60	114	517	34	115	511	38	37	1626	39

Table C.28: Strain, dynamic modulus and phase angle at each LVDT position on specimens of B3, 40 °C

Frequency (Hz)	Specimen No.	Average Peak Load (KN)	Average Peak Stress (KPa)	LVDT-1			LVDT-2			LVDT-3		
				Peak Strain (εo) μs	Dynamic Modulus MPa	Phase angle Deg	Peak Strain (εo) μs	Dynamic Modulus MPa	Phase angle Deg.	Peak Strain (εo) μs	Dynamic Modulus MPa	Phase angle Deg.
25	1	0.3	36	21	1727	27	24	1522	31	28	1299	23
	2	0.2	27	15	1796	20	29	940	25	10	2679	30
	3	0.2	28	15	1807	26	19	1435	26	8	3654	31
10	1	0.4	45	37	1220	31	42	1079	34	48	947	29
	2	0.3	38	33	1135	33	55	689	31	24	1590	34
	3	0.3	40	27	1465	33	41	954	32	16	2478	31
5	1	0.3	34	37	902	33	40	831	37	47	717	33
	2	0.3	32	34	940	36	61	519	33	26	1242	36
	3	0.3	33	29	1106	38	48	676	36	16	1984	38
1	1	0.3	36	79	456	37	86	419	39	95	384	34
	2	0.3	37	80	463	38	135	273	35	58	638	37
	3	0.3	37	65	569	39	105	349	39	38	986	40
0.5	1	0.2	29	87	337	37	93	317	39	103	290	35
	2	0.2	30	85	350	37	150	198	35	59	505	38
	3	0.2	30	68	429	39	112	261	40	40	741	42
0.1	1	0.2	24	74	323	37	101	235	36	77	313	35
	2	0.2	19	108	175	37	110	171	40	122	156	34
	3	0.2	24	66	359	38	115	206	37	42	573	41

Table C.29: Strain, dynamic modulus and phase angle at each LVDT position on specimens of B4, -10 °C

Frequency (Hz)	Specimen No.	Average Peak Load (KN)	Average Peak Stress (KPa)	LVDT-1			LVDT-2			LVDT-3		
				Peak Strain (εo) μs	Dynamic Modulus MPa	Phase angle Deg.	Peak Strain (εo) μs	Dynamic Modulus MPa	Phase angle Deg.	Peak Strain (εo) μs	Dynamic Modulus MPa	Phase angle Deg.
25	1	10.9	1336	133	10030	2	37	36142	3	82	16417	5
	2	10.0	1229	74	16689	1	69	17877	1	36	34632	33
	3	10.0	1220	70	17374	3	59	20536	3	100	12217	2
10	1	9.3	1143	96	11895	8	43	26840	10	65	17670	8
	2	9.4	1152	67	17212	7	68	16867	7	39	29712	19
	3	9.3	1137	62	18262	5	52	21454	6	107	10643	7
5	1	9.4	1144	102	11231	11	46	24956	10	70	16588	11
	2	9.4	1146	70	16290	9	76	15088	10	45	25595	20
	3	9.4	1147	64	17863	8	54	21035	9	116	9876	10
1	1	8.6	1051	113	9286	15	51	20467	15	79	13503	15
	2	8.7	1066	79	13511	12	87	12248	13	54	19876	20
	3	9.5	1168	78	14882	12	65	17722	12	143	8145	14
0.5	1	7.7	946	113	8356	16	51	18591	16	79	12061	16
	2	7.8	955	79	12109	14	87	10921	14	55	17528	20
	3	9.7	1189	87	13516	13	70	16844	12	156	7603	14
0.1	1	6.8	830	128	6467	20	58	14221	20	91	9227	19
	2	7.8	951	102	9324	17	111	8554	18	74	12947	23
	3	8.8	1077	99	10817	17	81	13112	15	183	5887	17

Table C.30: Strain, dynamic modulus and phase angle at each LVDT position on specimens of B4, 5 °C

Frequency (Hz)	Specimen No.	Average Peak Load (KN)	Average Peak Stress (KPa)	LVDT-1			LVDT-2			LVDT-3		
				Peak Strain (μs)	Dynamic Modulus (MPa)	Phase angle (Deg)	Peak Strain (μs)	Dynamic Modulus (MPa)	Phase angle (Deg)	Peak Strain (μs)	Dynamic Modulus (MPa)	Phase angle (Deg)
25	1	3.9	473	75	6290	14	36	13164	12	57	8382	8
	2	3.9	480	45	10742	12	67	7178	10	47	10316	13
	3	3.9	471	47	9843	19	57	8236	9	54	8765	10
10	1	3.9	476	76	6238	18	41	11480	17	60	8058	15
	2	3.8	459	48	9548	16	70	6603	16	51	9174	18
	3	3.8	466	40	11410	34	61	7552	20	62	7520	17
5	1	3.8	467	86	5457	23	48	9680	22	66	7185	19
	2	3.7	457	54	8430	18	76	6013	19	57	8054	22
	3	3.8	467	47	9862	41	73	6357	17	70	6695	18
1	1	3.5	433	118	3657	26	66	6577	27	89	4915	25
	2	2.9	356	64	5597	24	90	3954	24	68	5277	26
	3	2.9	355	46	7587	47	78	4490	22	85	4153	24
0.5	1	2.9	358	122	2945	29	67	5363	30	92	3937	27
	2	2.5	308	65	4710	25	93	3329	26	71	4382	28
	3	3.0	367	80	4542	39	99	3690	24	110	3330	26
0.1	1	2.0	240	135	1772	30	73	3297	33	100	2410	30
	2	1.9	238	82	2909	28	113	2102	29	89	2716	31
	3	1.9	238	78	3006	44	107	2210	33	109	2187	30

Table C.31: Strain, dynamic modulus and phase angle at each LVDT position on specimens of B4, 25 °C

Frequency (Hz)	Specimen No.	Average Peak Load (KN)	Average Peak Stress KPa	LVDT-1			LVDT-2			LVDT-3		
				Peak Strain (μs)	Dynamic Modulus (MPa)	Phase angle (Deg)	Peak Strain (μs)	Dynamic Modulus (MPa)	Phase angle (Deg)	Peak Strain (μs)	Dynamic Modulus (MPa)	Phase angle (Deg)
25	1	1.0	117	41	2832	22	38	3040	22	39	3010	24
	2	1.5	182	36	5051	21	77	2356	19	57	3237	21
	3	1.2	141	46	3052	21	21	6540	19	55	2570	19
10	1	1.1	131	67	1960	29	59	2222	28	59	2241	30
	2	1.1	136	39	3465	28	77	1763	25	59	2319	28
	3	1.1	129	56	2304	29	28	4635	27	66	1948	25
5	1	0.6	68	48	1417	34	38	1790	32	39	1764	34
	2	0.6	69	27	2555	33	53	1297	29	39	1787	32
	3	0.5	66	35	1880	35	18	3546	32	44	1496	29
1	1	0.4	49	69	705	37	52	943	37	55	899	37
	2	0.4	49	36	1346	36	69	702	33	52	953	36
	3	0.4	49	46	1058	38	28	1749	37	59	827	34
0.5	1	0.3	36	69	524	38	48	756	39	55	659	38
	2	0.3	37	36	1005	37	70	525	34	50	744	38
	3	0.3	37	43	838	39	27	1324	38	58	638	35
0.1	1	0.2	24	82	295	35	57	427	36	66	368	34
	2	0.2	24	44	546	36	83	289	34	56	429	36
	3	0.2	24	48	495	38	33	722	39	66	363	35

Table C.32: Strain, dynamic modulus and phase angle at each LVDT position on specimens of B4, 40°C

Frequency (Hz)	Specimen No.	Average Peak Load (KN)	Average Peak Stress KPa	LVDT-1			LVDT-2			LVDT-3		
				Peak Strain (μs)	Dynamic Modulus (MPa)	Phase angle (Deg)	Peak Strain (μs)	Dynamic Modulus (MPa)	Phase angle (Deg.)	Peak Strain (μs)	Dynamic Modulus (MPa)	Phase angle Deg.
25	1	0.3	43	35	1214	24	46	926	28	37	1167	28
	2	0.6	74	37	1970	24	79	934	23	61	1218	24
	3	0.2	30	19	1554	27	19	1578	25	25	1193	29
10	1	0.1	17	17	1031	29	20	859	29	14	1291	31
	2	0.4	51	42	1203	31	79	642	28	67	763	30
	3	0.4	47	45	1018	29	44	1044	30	58	801	32
5	1	0.1	18	22	805	29	28	635	27	18	958	34
	2	0.3	33	39	830	33	73	448	30	60	544	34
	3	0.2	19	20	935	39	27	691	37	30	618	42
1	1	0.1	16	33	503	27	40	407	26	26	635	31
	2	0.2	25	63	405	35	111	230	31	91	283	35
	3	0.2	21	39	525	39	60	343	37	67	306	41
0.5	1	0.1	13	30	441	29	40	339	28	24	564	34
	2	0.1	15	52	287	38	96	154	34	73	206	38
	3	0.1	13	29	439	41	48	263	38	54	239	43
0.1	1	0.1	12	112	107	32	109	110	33	98	123	37
	2	0.1	7	41	176	38	82	88	35	56	130	38
	3	0.1	10	34	280	41	62	152	36	63	151	44

Table C.33: Dynamic modulus and phase angle of S1

Temperature (°C)	Frequency (Hz)	Dynamic modulus			Phase angle		
		Average (MPa)	σ [1] (MPa)	C V[2] (%)	Average (degree)	σ (degree)	C V (%)
-10	25	31017	424	1	6.9	1.2	18
-10	10	29431	2089	7	8.3	0.5	6
-10	5	28652	3160	11	9.6	0.5	6
-10	1	22501	20	0	12.1	0.1	1
-10	0.5	21659	444	2	13.4	0.0	0
-10	0.1	17915	1547	9	16.1	1.1	7
5	25	21740	3628	17	11.2	1.9	17
5	10	16599	1125	7	15.3	0.2	1
5	5	15228	1903	12	17.1	0.4	2
5	1	11059	1745	16	21.3	0.1	0
5	0.5	7784	41	1	24.5	0.5	2
5	0.1	4970	48	1	27.4	0.2	1
25	25	5368	448	8	26.4	1.4	5
25	10	3983	212	5	29.2	0.3	1
25	5	3098	67	2	29.9	0.1	0
25	1	1690	6	0	31.8	0.4	1
25	0.5	1165	69	6	34.4	0.5	1
25	0.1	598	59	10	32.7	0.4	1
40	25	1620	38	2	31.4	0.8	2
40	10	1132	33	3	30.1	0.2	1
40	5	771	15	2	30.1	0.2	1
40	1	363	6	2	29.6	0.2	1
40	0.5	270	14	5	29.4	0.5	2
40	0.1	171	13	8	24.8	1.6	6

[1]Standard deviation
[2]Coefficient of variation

Table C.34: Dynamic modulus and phase angle of S2

Temperature (°C)	Frequency (Hz)	Dynamic modulus			Phase angle		
		Average (MPa)	σ [1] (MPa)	C V[2] (%)	Average (degree)	σ (degree)	C V (%)
-10	25	31187	306	1	7.3	1.2	16
-10	10	29088	2207	8	9.3	1.1	11
-10	5	27686	2624	9	10.1	1.1	11
-10	1	23628	3287	14	12.6	0.7	5
-10	0.5	20222	1249	6	13.8	0.3	2
-10	0.1	16024	1268	8	16.9	0.3	2
5	25	17421	985	6	13.6	0.7	5
5	10	14741	1585	11	16.0	1.0	6
5	5	12968	993	8	18.3	0.2	1
5	1	9070	703	8	21.9	0.2	1
5	0.5	7448	936	13	24.8	0.6	2
5	0.1	4693	667	14	27.0	1.6	6
25	25	5196	149	3	27.5	1.1	4
25	10	3835	102	3	27.8	0.3	1
25	5	2961	76	3	28.7	0.9	3
25	1	1720	185	11	27.7	5.7	20
25	0.5	1104	75	7	32.6	1.1	3
25	0.1	606	99	16	30.0	2.8	9
40	25	1663	156	9	30.2	0.9	3
40	10	1158	97	8	29.0	1.3	4
40	5	841	46	5	29.1	0.1	0
40	1	460	42	9	27.3	0.7	3
40	0.5	313	49	16	28.2	2.9	10
40	0.1	230	20	9	22.4	2.3	10

[1]Standard deviation
[2]Coefficient of variation

Table C.35: Dynamic modulus and phase angle of S3

Temperature (°C)	Frequency (Hz)	Dynamic modulus			Phase angle		
		Average (MPa)	σ [1] (MPa)	C V[2] (%)	Average (degree)	σ (degree)	C V (%)
-10	25	30900	3216	10	4.3	0.2	4
-10	10	27876	5047	18	5.2	0.4	7
-10	5	26737	4287	16	5.6	0.8	14
-10	1	23979	193	1	6.6	0.2	3
-10	0.5	23168	402	2	7.5	0.4	5
-10	0.1	19989	344	2	8.9	0.7	8
5	25	20426	1078	5	8.3	1.0	12
5	10	18861	1824	10	9.8	0.3	3
5	5	17494	1883	11	11.1	0.6	5
5	1	14077	1680	12	14.5	1.0	7
5	0.5	12573	1603	13	16.0	0.6	4
5	0.1	9327	1478	16	19.0	0.7	4
25	25	14077	1680	12	14.5	1.0	7
25	10	7571	1051	14	20.7	0.9	4
25	5	6348	920	14	22.6	0.8	4
25	1	4127	698	17	26.3	0.9	3
25	0.5	3294	592	18	28.0	1.1	4
25	0.1	2038	416	20	28.9	1.1	4
40	25	3927	412	10	26.1	1.7	7
40	10	2878	261	9	26.8	0.9	3
40	5	2263	250	11	27.4	0.7	3
40	1	1257	175	14	29.6	0.1	0
40	0.5	928	175	19	31.6	2.1	7
40	0.1	526	96	18	30.5	2.2	7

[1]Standard deviation
[2]Coefficient of variation

Table C.36: Dynamic modulus and phase angle of S4

Temperature (°C)	Frequency (Hz)	Dynamic modulus			Phase angle		
		Average (MPa)	σ [1] (MPa)	C V[2] (%)	Average (degree)	σ (degree)	C V (%)
-10	25	25685	2028	8	8.1	0.8	10
-10	10	24038	2088	9	9.6	1.5	15
-10	5	22853	2078	9	10.6	1.5	14
-10	1	19327	1790	9	11.7	3.0	25
-10	0.5	17903	2947	16	13.0	3.6	28
-10	0.1	12937	4345	34	16.4	2.9	18
5	25	14645	1829	12	13.5	0.1	1
5	10	11849	550	5	16.0	0.4	2
5	5	10644	2553	24	15.7	2.7	17
5	1	7937	899	11	21.5	0.8	4
5	0.5	6629	429	6	23.7	0.8	3
5	0.1	4361	420	10	26.6	0.6	2
25	25	4419	500	11	25.2	0.9	4
25	10	3337	503	15	26.5	1.1	4
25	5	2636	351	13	27.7	1.3	5
25	1	1495	276	18	30.8	0.7	2
25	0.5	1124	195	17	31.1	0.1	0
25	0.1	668	143	21	28.4	1.2	4
40	25	1428	114	8	29.0	0.1	0
40	10	1018	105	10	28.1	0.6	2
40	5	748	63	8	28.0	0.4	2
40	1	407	35	9	26.8	0.7	3
40	0.5	277	33	12	29.5	0.9	3
40	0.1	178	17	10	25.4	0.4	2

[1]Standard deviation
[2]Coefficient of variation

Table C.37: Dynamic modulus and phase angle of B1

Temperature (°C)	Frequency (Hz)	Dynamic modulus			Phase angle		
		Average (MPa)	σ [1] (MPa)	C V[2] (%)	Average (degree)	σ (degree)	C V (%)
-10	25	24652	4614	19	3.5	0.9	25
-10	10	23143	3383	15	6.7	0.5	8
-10	5	21834	3343	15	7.1	0.7	10
-10	1	18806	3037	16	9.2	0.9	10
-10	0.5	17907	3448	19	10.9	0.7	6
-10	0.1	13327	1799	13	15.1	2.9	20
5	25	16129	2599	16	13.1	1.1	9
5	10	14220	4524	32	15.1	1.1	7
5	5	13437	3073	23	16.2	0.5	3
5	1	9710	2399	25	19.8	0.7	3
5	0.5	8319	2782	33	21.6	0.7	3
5	0.1	5788	1856	32	24.6	0.4	2
25	25	5614	357	6	26.9	2.5	9
25	10	4240	306	7	29.3	2.8	10
25	5	3296	229	7	29.9	2.4	8
25	1	1874	204	11	31.3	1.5	5
25	0.5	1365	122	9	32.4	0.3	1
25	0.1	777	80	10	30.0	1.4	5
40	25	2104	174	8	31.5	0.4	1
40	10	1439	120	8	32.7	0.5	2
40	5	1020	75	7	32.8	0.6	2
40	1	545	46	8	30.7	0.6	2
40	0.5	398	34	8	31.2	0.6	2
40	0.1	231	17	7	27.9	0.9	3

[1]Standard deviation
[2]Coefficient of variation

Table C.38: Dynamic modulus and phase angle of B2

Temperature (°C)	Frequency (Hz)	Dynamic modulus			Phase angle		
		Average (MPa)	σ [1] (MPa)	C V[2] (%)	Average (degree)	σ (degree)	C V (%)
-10	25	25292	2209	9	3.1	1.2	40
-10	10	26405	2250	9	6.3	0.6	9
-10	5	25491	1836	7	7.0	1.5	22
-10	1	21903	1660	8	7.8	0.9	12
-10	0.5	20529	1710	8	8.4	0.5	6
-10	0.1	17149	1331	8	10.5	2.1	20
5	25	17228	3796	22	11.4	1.3	11
5	10	15209	2499	16	11.1	1.8	17
5	5	13688	2109	15	12.3	1.9	16
5	1	10529	1612	15	15.0	1.8	12
5	0.5	9423	1434	15	16.3	2.2	13
5	0.1	7069	1007	14	19.3	1.4	7
25	25	7200	964	13	20.4	0.5	2
25	10	5881	666	11	22.2	0.7	3
25	5	4950	665	13	23.6	0.4	2
25	1	3150	562	18	27.6	0.3	1
25	0.5	2645	734	28	29.9	1.9	6
25	0.1	1658	502	30	31.3	2.3	7
40	25	3365	195	6	27.2	0.2	1
40	10	2505	181	7	29.5	0.3	1
40	5	1974	220	11	31.2	1.5	5
40	1	1073	149	14	34.0	2.1	6
40	0.5	826	137	17	34.3	0.9	3
40	0.1	481	68	14	32.1	1.7	5

[1]Standard deviation
[2]Coefficient of variation

Table C.39: Dynamic modulus and phase angle of B3

Temperature (°C)	Frequency (Hz)	Dynamic modulus			Phase angle		
		Average (MPa)	σ [1] (MPa)	C V[2] (%)	Average (degree)	σ (degree)	C V (%)
-10	25	17263	3309	19	3.1	0.5	17
-10	10	14804	1785	12	7.0	1.2	17
-10	5	14498	1668	12	6.6	1.2	18
-10	1	12649	1439	11	8.0	0.6	8
-10	0.5	11930	1261	11	7.7	1.7	21
-10	0.1	9369	1069	11	13.0	2.7	21
5	25	9653	1136	12	11.6	1.3	11
5	10	9235	810	9	12.2	1.5	13
5	5	8433	770	9	14.0	1.5	11
5	1	6269	659	11	17.8	2.0	11
5	0.5	5449	565	10	19.4	2.3	12
5	0.1	3692	548	15	23.9	2.3	10
25	25	4205	1003	24	24.2	1.1	5
25	10	3246	839	26	25.9	1.6	6
25	5	2605	762	29	28.7	1.8	6
25	1	1505	453	30	32.2	1.6	5
25	0.5	1174	379	32	34.5	0.4	1
25	0.1	663	199	30	34.8	0.9	3
40	25	1873	396	21	33.2	1.3	4
40	10	1284	303	24	33.6	0.7	2
40	5	991	233	24	35.6	1.6	5
40	1	504	115	23	36.3	1.4	4
40	0.5	381	85	22	36.5	2.0	6
40	0.1	279	106	38	35.7	1.5	4

[1]Standard deviation
[2]Coefficient of variation

Table C.40: Dynamic modulus and phase angle of IB4

Temperature (°C)	Frequency (Hz)	Dynamic modulus			Phase angle		
		Average (MPa)	σ [1] (MPa)	C V[2] (%)	Average (degree)	σ (degree)	C V (%)
-10	25	20213	3228	16	12.2	5.0	41
-10	10	18951	2242	12	10.2	2.6	25
-10	5	17614	1367	8	10.6	1.9	17
-10	1	14404	814	6	12.8	1.5	12
-10	0.5	13059	435	3	13.6	1.6	12
-10	0.1	10062	185	2	16.7	1.8	11
5	25	9213	239	3	18.2	0.7	4
5	10	8517	107	1	20.5	4.0	19
5	5	7526	101	1	22.0	3.0	14
5	1	5134	245	5	25.8	3.6	14
5	0.5	4025	41	1	26.7	1.7	6
5	0.1	2512	59	2	30.4	3.2	11
25	25	3521	547	16	27.3	1.7	6
25	10	2539	411	16	29.2	1.1	4
25	5	1948	331	17	32.4	1.3	4
25	1	1020	182	18	34.7	1.1	3
25	0.5	779	145	19	35.9	1.2	3
25	0.1	437	83	19	34.4	1.1	3
40	25	1306	180	14	32.0	1.9	6
40	10	961	96	10	31.6	0.3	1
40	5	718	99	14	33.8	4.8	14
40	1	404	105	26	32.3	5.6	17
40	0.5	326	117	36	34.4	5.2	15
40	0.1	146	43	29	35.5	3.2	9

[1]Standard deviation
[2]Coefficient of variation